SURFACE SCIENCE STUDIES OF THE REACTION OF MOLECULES OF RELEVANCE TO VAM SYNTHESIS USING Pd AND Pd/Au SINGLE CRYSTAL SURFACES

Christian Rory Morgan

Cardiff University

2005

ProQuest LLC
789 East Eisenhower Parkway
P.O. Box 1346
Ann Arbor, MI 48106-1346

ACKNOWLEDGEMENTS

Firstly I would like to thank Professor Mike Bowker of Cardiff University for his assistance and insight throughout the course of my studies. His experience in and enthusiasm for the subjects of surface science and industrial catalysis have been invaluable. I am very grateful for the faith he has shown in me over this time.

I would also like to thank BP Chemicals for providing the CASE award that helped to fund this project, and specifically Dr. John Couves, my industrial supervisor, for his advice and support, particularly in discussing the history of vinyl acetate synthesis, and the significance of gold in catalyst performance.

In addition, this project was funded by the EPSRC and I am grateful for their support.

For their advice regarding measurement of gold by spectroscopic methods in the catalysts used in this study the following deserve special mention: Tim Carney and Dave Milton at Thermovacuum Generators, Martyn Green at Omicron, Martin Seah at the NPL, and Elodie and Federico at Cardiff University. Discussion of results with other scientists was what made research doubly interesting!

Lastly, I thank every family member, friend and work colleague in Oxfordshire, Reading, Cambridge and Cardiff who contributed to this research, as well as my personal development, over the past four years. I am happy to say there are too many of these people to mention individually.

ABSTRACT

The adsorption, reaction and decomposition of a series of molecules (oxygen, ethene, acetic acid, carbon monoxide, acetaldehyde and vinyl acetate) associated with vinyl acetate synthesis were investigated using a combination of ultra-high vacuum surface science techniques, including molecular beam sticking and temperature programmed desorption. The catalysts were annealed single crystal Pd (110) surfaces and bimetallic Au/Pd (110) surfaces prepared by metal vapour deposition and annealing. All the molecules investigated adsorbed well to Pd (110) with a high sticking probability, and mechanisms for the reactions of each with the surface were suggested. The carbonaceous organic molecules all decomposed to deposit carbon at the surface at room temperature and above, blocking active sites to adsorption. Above a specific temperature, this carbon went subsurface and no longer inhibited subsequent adsorption of molecules. A residual carbon layer was often characterised by low energy electron diffraction and spectroscopy techniques, the exact structure varied with incident molecule type. The deposited carbon could often be removed in a facile manner by oxygen treatment. In the case of acetic acid, an acetate species was formed at room temperature and decomposed at higher temperatures with autocatalytic decomposition kinetics. Vinyl acetate reacted in a similar way to acetaldehyde under most conditions investigated, suggesting vinyl acetate decomposes primarily via a cleavage that produces acetyl groups under these conditions. An exceptional case occurred at 300-323 K at high coverages, where the formation of a template structure on the surface may stabilise acetate formation from vinyl-acetate cleavage. On Au/Pd (110) surfaces after annealing, the Au was determined to be partly subsurface in most cases. The uptake and sticking probability of each molecule were reduced often in a manner approximately proportional to Au content, in broad agreement with structural data on Au/Pd(110) published elsewhere.

CONTENTS

Chapter Sections and their associated page numbers are described on the contents pages at the beginning of each chapter.

1 INTRODUCTION: USING SURFACE SCIENCE TO INVESTIGATE VINYL ACETATE SYNTHESIS

1 INTRODUCTION: USING SURFACE SCIENCE TO INVESTIGATE VINYL ACETATE SYNTHESIS

1.1 Surface Science as an Aid to Catalysis

This thesis concerns studies of a particular type of gas-solid reaction, specifically on metal surfaces. Research into this area has developed mainly in terms of heterogeneous catalysis, due to its importance in the chemical industry. The role of surfaces in chemistry is fundamental and thus touches many important aspects of modern life. Catalysed synthesis of organic molecules, the main motivation for this thesis' project, is only one of these aspects. Semiconductors, computing, microelectronics, photography, car pollution control, oil refining, filament technology and gas separation also depend strongly on this branch of science. The focus of research in surface science has reflected advances in the disciplines of ultra-high vacuum (UHV) and solid state physics over the past fifty years. These developments allowed scientists to investigate model surfaces, such as single crystals and nanoparticulate arrays on an atomic scale, through a variety of analytical techniques. Today, surface science is at the forefront of research into nanoscale technology. However, arguably, in terms of gas-solid reactions, its origins date back to the early nineteenth century with the work of H. Davy [1], whose work on the reaction of coal gas and oxygen mixtures on the surface of a hot platinum wire led to the invention of the miners' safety lamp. Among many observations, he noticed that the activity of the platinum catalyst was depleted by formation of a carbide film on the wire. Others have made significant contributions to the principles of the field, including

Langmuir who performed the first research on atomic and molecular adsorption, relating the surface coverage of adsorbed gas and gas pressure at a fixed temperature (the Langmuir isotherm) [2], and defining dissociative chemisorption [3]. Other significant advances followed, for instance the Langmuir-Hinshelwood mechanism [4,5], the Rideal–Eley mechanism [6,7], physisorption vs. chemisorption [8] and activated adsorption [9]. These and many other findings have helped build the foundations of surface science.

Catalytic chemistry is an important part of nature and has been studied in natural and man-made processes for the past two hundred years. A catalyst affects the rate at which a chemical interaction reaches equilibrium. It is regenerated at the end of the mechanistic process, and does not affect the energy of reaction significantly. In recent times, catalysis has been harnessed to produce simple chemicals of industrial importance, such as ammonia production by the Haber process, which exploits finely divided iron as its catalyst [10]. It is of interest to control catalyst selectivity, activity and durability to arrive at an optimal catalyst for a process. This can be done macroscopically or by an understanding of the process on an atomic scale. The latter approach, through surface science in particular has had a great impact on research into heterogeneous catalysis. Surface science complements macroscopic analysis of catalytic, particularly heterogeneous catalytic, systems well by giving useful information on molecular and atomic processes at a surface. Processes such as adsorption and desorption, reaction and decomposition, redox and diffusion at surfaces can be investigated and help to explain macroscopic phenomena. This allows scientists to probe more accurately the atomic-

scale mechanisms and features of catalysis. This knowledge in turn may help to advance catalytic technology and optimise catalysed industrial processes. One of the many good examples of the application of surface science to heterogeneous catalysis is the production of ethylene oxide which is used in antifreeze, washing powder, cosmetics, fibres and pharmaceuticals. It was found macroscopically by chance that the addition of chlorine to the silver catalyst for ethylene oxidation enhanced the selectivity to ethylene oxide over combustion products significantly. The presence of chlorine atoms in an Ag surface on ethylene epoxidation was investigated by surface science techniques and has helped development of current commercial catalysts which incorporate enhancers such as vinyl chloride into the gas feed at the ppm level [11].

1.2 Reactions at a Surface under Vacuum

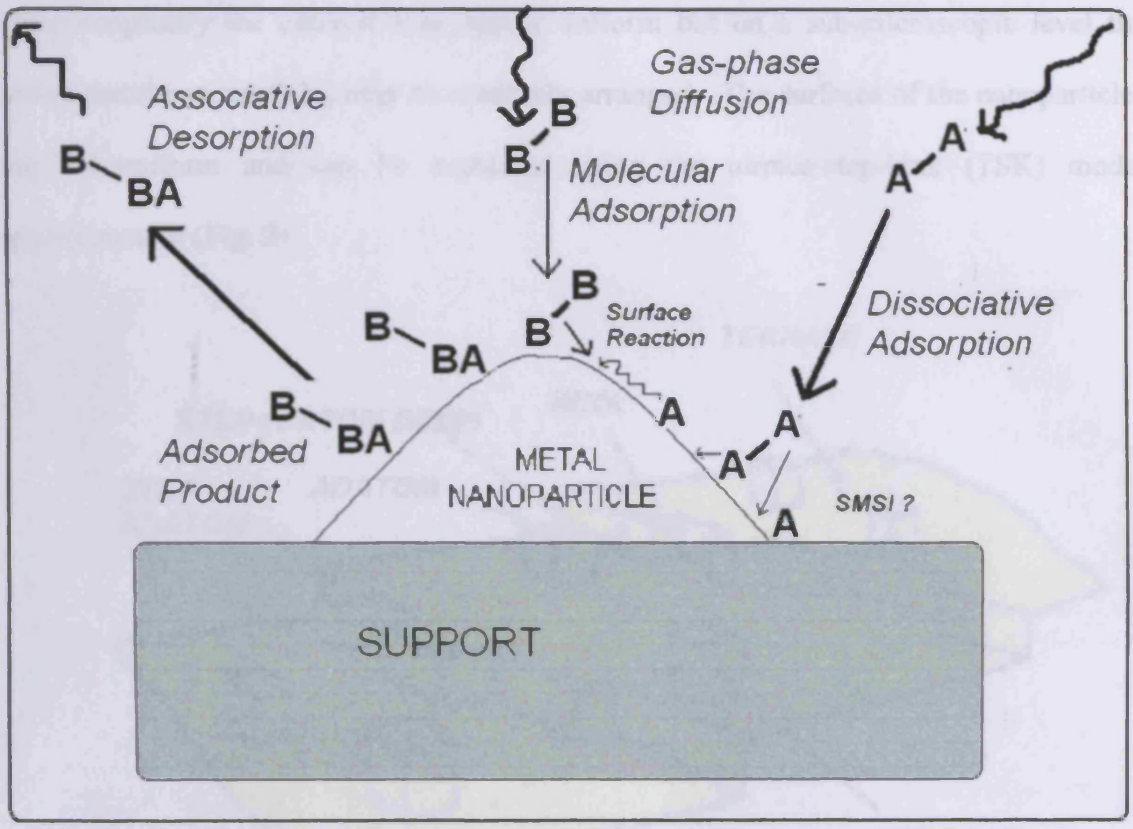

Fig. 1: Diagram of a metal nanoparticle on a metal oxide support showing adsorption and associative desorption of polyatomic molecules. Adapted from [12].

Any reaction can be reduced to a number of fundamental mechanistic steps which can involve many intermediates and transition states. In the case of surface catalytic reactions, these steps often involve a cycle of adsorption, diffusion, bond making and/or breaking in the adsorbates, and then desorption of products as shown in Fig. 1 for the interaction of two diatomic species on a supported metal nanoparticle catalyst [12]. The exact nature of the adsorbates and catalyst surface i.e. their chemical properties and morphology is crucial in determining the activity and selectivity of the process. Supported metal nanoparticle catalysts are very common forms of catalyst. Often it is not

just the metal surface but the metal-support interface that is an active site in catalysis. Macroscopically the catalyst may appear uniform but on a sub-microscopic level the active metal nanoparticles may be randomly arranged. The surfaces of the nanoparticles are non-uniform and can be explained using the terrace-step-kink (TSK) model approximation (Fig. 2).

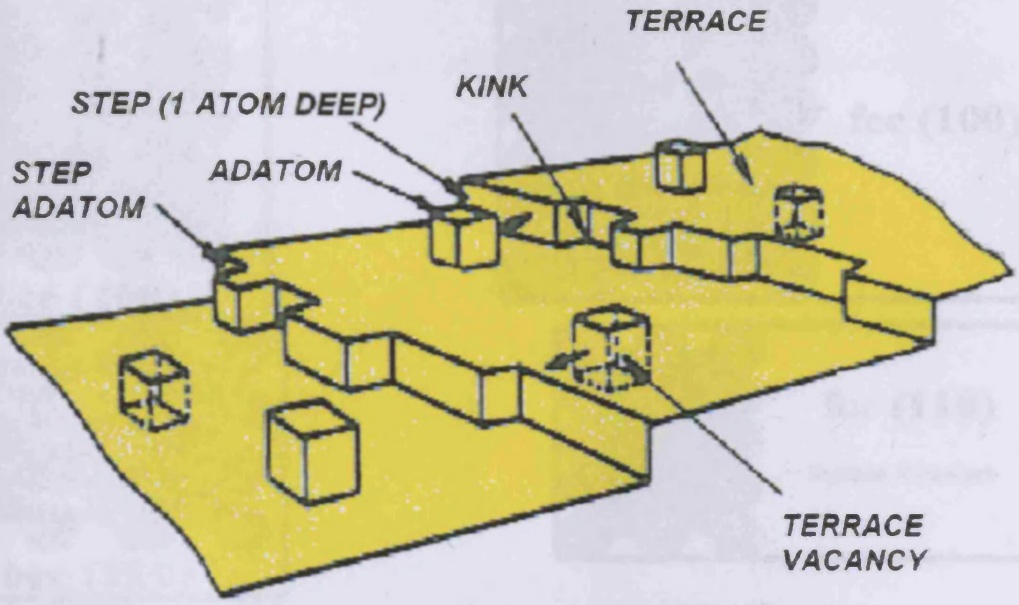

Fig. 2: An example TSK diagram showing various types of coordination sites on a stepped metal surface. Adapted from [13]

This model assumes a rigid lattice with surface atoms behaving as if they are in the bulk. Terrace atoms have the most nearest neighbours, atoms on kinks have the fewest. On a rough surface in equilibrium concentrations, up to 20 % of atoms may be in step sites and 5 % in kink sites [13-14]. This model is not so useful for microscopic surfaces on real and model catalysts [15-16], which often have sites that move from bulk atomic positions by adsorbate induced reconstructions, or contraction of the selvedge layers. Magnification of the TSK terrace system would give surface lattice planes described by

individual atoms. These 'single crystal surfaces' can be well defined and are thus used as uniform substrates for catalytic crystals in surface science. Many catalytic metals are body centred cubic (bcc) or face centred cubic (fcc) metals. The three fundamental surface planes for bcc and fcc are denoted (100), (110) and (111) by Miller Index notation and are shown in Fig. 3 [17].

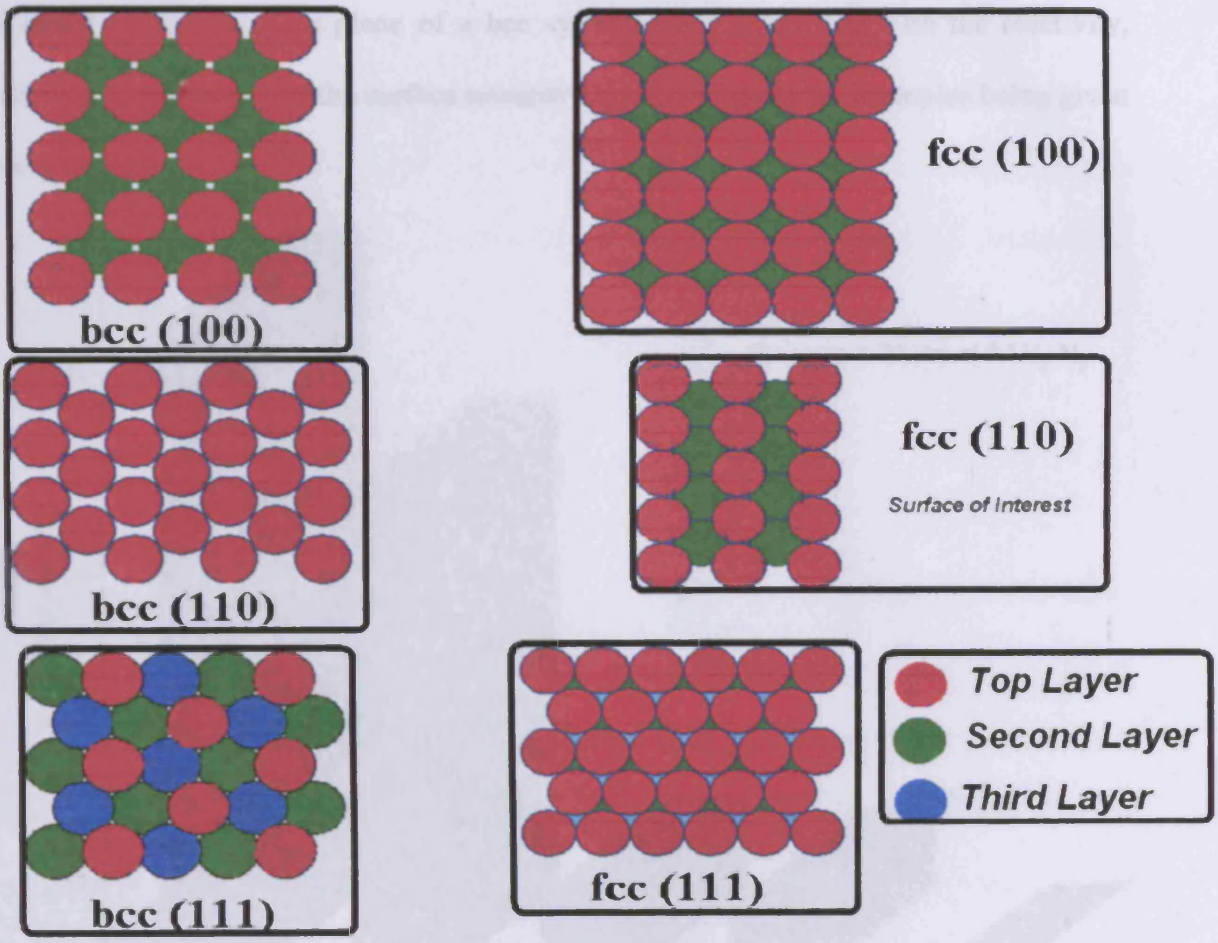

Fig. 3: Atomic arrangement unit cells of (110), (111) and (100) bcc and fcc surfaces. Note that the surface of interest in these studies is Pd (fcc) (110) which clearly displays top and second layer atoms in its selvedge.

These single crystal surface planes are the ones most commonly researched in surface science, although those with higher indices (and more complex surface structures) that may contain steps and kinks are also investigated. The (111) system is the most open, and thus usually the most reactive, surface for the bcc system. In the fcc system (for example Pd metal) the (110) is the most open surface and (111) the least open. The arrangement of atoms on each surface plane of a bcc system has a direct effect on the reactivity, activity and selectivity of the surface towards a particular reactant, examples being given in Fig. 4 [18].

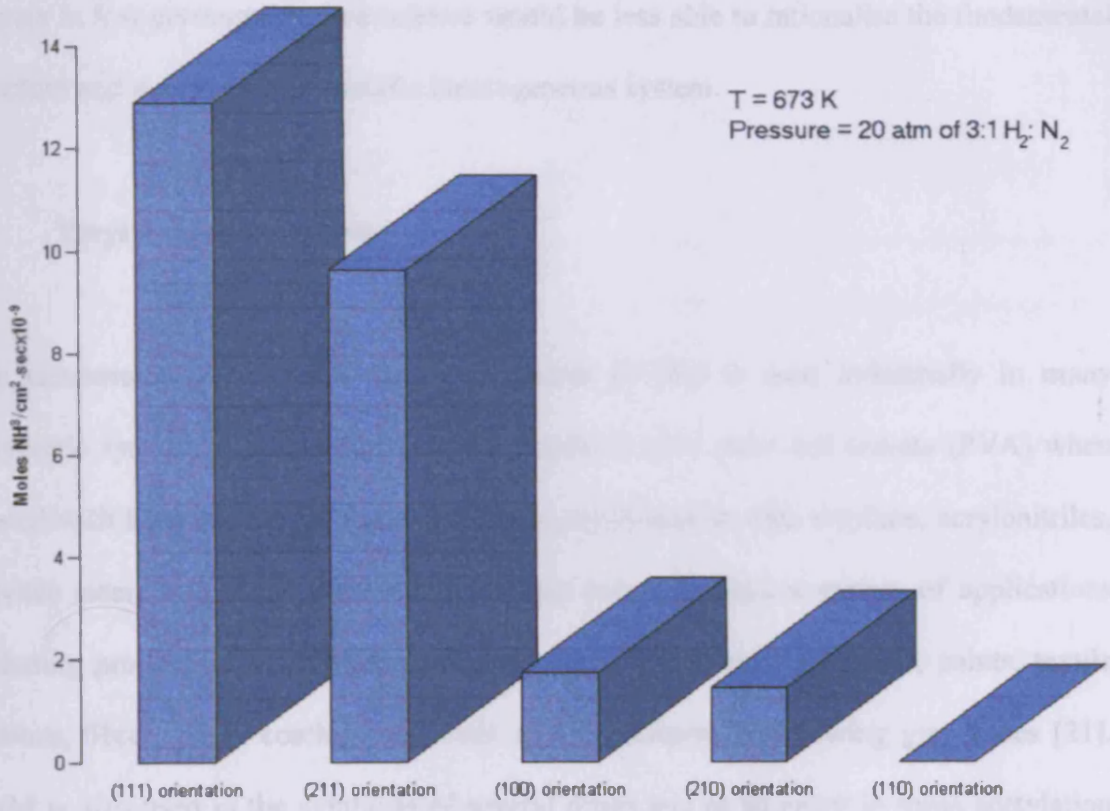

Fig. 4: Rates of ammonia synthesis over five iron (bcc) single-crystal surfaces with different orientations. Adaptation of data from [18]

Analysis of catalytic systems by either macroscopic or surface science techniques is often done under vacuum to minimise contamination of the process and/or poisoning of the

catalysts. Surface science commonly uses the above well defined surface indices in ultra high vacuum (UHV) conditions. The < 10^{-8} mbar pressure range is defined as the UHV range over which surface science experiments of the sort described in this thesis should be conducted [19-20]. These conditions are very different from those used in industrial processes which may involve very non-uniform catalysts in several atmospheres of overpressure. However, surface science tends to concentrate on investigating a reaction in a model system from elementary principles in order to relate them to more complex systems, making the use of UHV favourable. Without UHV and the techniques that operate in low pressure, surface science would be less able to rationalise the fundamental structure and reactivity of a specific heterogeneous system.

1.3 Vinyl Acetate Synthesis

The unsaturated ester, vinyl acetate monomer (VAM) is used industrially in many polymeric systems. It homopolymerises readily to give polyvinyl acetate (PVA) when treated with light or free radicals. VAM can copolymerise with ethylene, acrylonitriles, acrylate esters and other vinyl esters. These polymers have a variety of applications including production of architectural and decorative coatings, adhesives, paints, textile finishes, fibres, paper coatings and even as a constituent for chewing gum bases [21]. VAM is also used in the synthesis of several drugs and as an agent in some acetylation reactions. Examples of polymers derived from VAM and their uses [22] are shown in Fig. 5. There is extensive global capacity for VAM production: in 2002, 4.8 million metric tonnes were synthesised. Market development of VAM is growing at a global rate

of 3-4 % per year, particularly along with demand in North America and South East Asia [21]. BP Chemicals is an important developer of VAM synthesis catalysts.

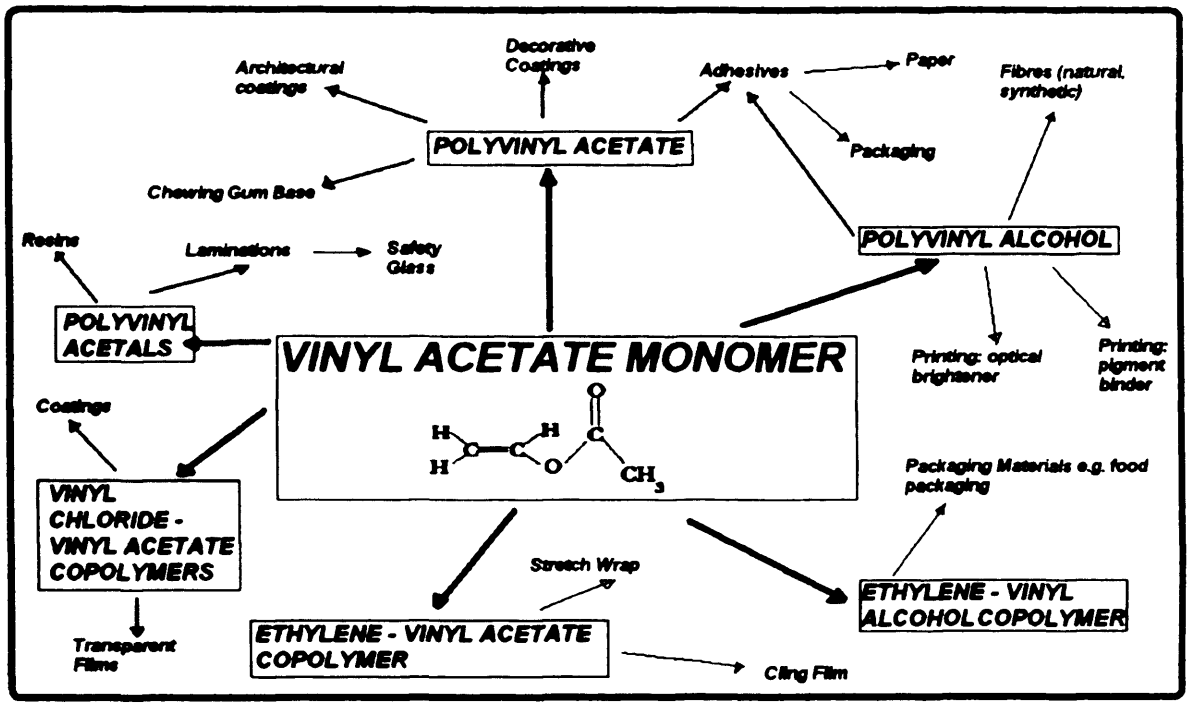

Fig. 5: A spider chart showing VAM, the main polymer groups derived from it, and their industrial and commercial uses.

In the past VAM has been synthesised via reaction of acetylene and acetic acid, originally by Klatte [23] in a homogeneous liquid phase reaction using Hg sulphate with a low VAM yield. A later homogeneous liquid phase conversion was developed by Wacker, using Zn acetate on a carbon support [24]. The Wacker process was found to be very selective (97% VAM yield), cheap and easy to control. Subsequently VAM has been prepared by acetoxylation of ethylene from acetic acid, due to the greater availability of ethylene over acetylene, from advances in the natural gas oxidation resulting in lower feedstock and conversion costs for ethylene [25-27]. These reactions are shown in Table 1.

METHOD	DESCRIPTION
Klatte (1912)	*Acetylene + Acetic Acid --> VAM* *Mercurous Sulphate/Acetic Acid Solution* *333 - 373 K* *Low Yield*
Moiseev (1960)	*Ethylene + Acetic Acid + Oxygen --> VAM + Water* *Homogenous Liquid Phase (Wacker-like)* *30:70 ethylene:oxygen mix* *Acetic Acid/ Na or K acetate/ Cu(I):Cu (II) redox couple slurry* *353 - 423 K* *Several atm overpressure* *70-90 % yield (by ethylene)*
Vapour Phase (1968) e.g. Hoescht-Bayer	*Ethylene + Acetic Acid + Oxygen --> VAM + Water* *Heterogeneous Pd/C catalyst* *Alternatives: Pd/silica or Pd/alumina* *Vapour phase reaction* *around 433 K* *5 atm overpressure* *91-95% yield (by ethylene)* *Many byproduct routes e.g. CO, acetaldehyde*

Table 1: The three main methods of VAM production and a comparison of their conditions, advantages and disadvantages.

The latter reaction is of interest to this thesis. It was first performed using Pd by Moiseev involving a 'Wacker-like' liquid phase conversion of reactants to products and redox of Pd (II) chloride by Cu (I) and (II) chlorides in acetic acid in the presence of the promoter sodium acetate [25].

$$Pd^{2+} + 2CH_3COO^- + C_2H_4 \rightarrow C_2H_3OOCCH_3 + Pd(0) + CH_3COOH \quad (1.1)$$

$$Pd(0) + 2Cu^{2+} = 2Cu^{+} + Pd^{2+} \quad (1.2)$$

The VAM yield was 90 % (bases on ethylene) with acetaldehyde and ethylidene diacetate as the major by-products. This homogeneous process was developed commercially [26-27]. Chloride-free catalyses were later developed which improved reactivity and

overcame many by-product poisoning and catalyst corrosion problems from chloride ions [28]. Despite these advances, a more favourable heterogeneous 'solid-gas phase' synthesis was discovered later [29,30] which minimised by-product formation and catalyst corrosion. It is still a matter of some debate whether the phase is truly 'solid-gas' or whether Pd acetate forms in a 'pseudo-liquid-phase' conversion. The heterogeneous process usually employs Pd metal, Pd/Au [31] or Pd/Cd [32] solid catalysts, and is the main pathway for VAM synthesis today [33]. Research into VAM synthesis by Pd/Pt, Pd/Ni [34], and Pd/Ag [35] catalysts has also been successful, but nowadays Pd/Au is considered a more favourable catalyst. Pd/Au is also more selective to VAM synthesis and ethylene conversion compared to Pd/Co, Pd/Rh, Pd/Ru and other bimetallic catalysts [36]. Most industrial (fixed-bed) reactors operate at around 440 K and 4-11 atmosphere overpressure [37-39] with feed compositions of ~65% ethylene, ~25% acetic acid and ~ 8% oxygen with the remainder being an inert species e.g. nitrogen. The percentage of oxygen present is limited by the explosive nature of the ethylene-oxygen mixture. However, the lower explosion limit can be increased by adding methane into the feedstream, allowing oxygen levels to be maximised and increasing the space-time yield of VAM [40]. The above system is very selective to VAM, with a yield of 90 - 96%, with carbon dioxide (the main by-product), acetic anhydride and acetaldehyde by-products as shown in Table 1. By-product synthesis is found to be strongly dependent on the primary VAM catalysed synthesis.

Pd/Au catalysts were developed by Bayer [29], Hoescht [41] and then DuPont [42] and usually consist of 'egg-shell type' Pd/Au catalyst nanoparticles (0.5-2 % Pd/ 0.2-1.2%

Au/1-4 % Group 1 metal acetate catalyst weight loading) on metal oxide supports such as silica (the most common) [29,41,42], alumina [43], titania [44], tin oxides [45] or metal silicates [46,47]. Silica is favoured for its relatively inert chemical behaviour, and is often used in the form of small pellets of high surface area. Au and Group 1 metal (usually potassium) acetates seem to act as moderators and promoters to the catalysis [48], improving factors such as catalyst durability, activity and selectivity to VAM synthesis. Potassium acetate is added to the catalyst by impregnation. The potassium to Pd & Au ratio is usually 0.7:1 to 2: 1. The exact structure and nature of the bimetallic particles on the surface, including how Au affects the active Pd component, is not yet fully understood.

1.4 Mechanisms of VAM Synthesis

Many questions concerning the mechanism of ethylene acetoxylation over Pd/Au catalysts are still outstanding, including:

- The nature of mechanism intermediates and rate determining steps.
- The effect of Au on the active catalytic sites, is it electronic, structural or both?
- The nature of the active catalytic sites, such as the size of particles and their structure.
- The nature of by-product formation mechanisms.
- The nature of the kinetics of the synthesis with respect to each reactant.

- The oxidation state of the palladium catalytic centres.

Published research into the catalysis has consisted mostly of studies of the 'real' system under industrial conditions, and mostly on supported Pd catalysts without the influence of Au. Although there have been many papers investigating 'model' single crystal catalysts and their interactions with the starting materials of VAM synthesis, none have published data on VAM synthesis, reaction or decomposition on these systems in UHV.

Essentially there are four schools of thought concerning the overall synthesis mechanism, which can be broadly defined by the disagreement concerning the exact phase of the catalysis: 'solid-gas phase, or 'pseudo liquid phase' as mentioned earlier. In the 'solid-gas' phase mechanism, the Pd surface remains essentially metallic Pd throughout, and in the 'pseudo liquid phase' the catalytic centres are Pd acetate particles. Which Pd (0-2) oxidation states occur in the mechanism is also a matter of debate. A fourth research group believes that all three oxidation states occur to an extent. Each hypothesis will be discussed in turn.

1.4.a. *Pd (0): VAM synthesis in solid-gas phase*

Moiseev reported that the active site consisted of Pd metal centres that remained in the same oxidation state throughout the mechanism [25]. The rate determining step was activation of a C-H bond in ethylene producing a vinyl intermediate which reacts rapidly with acetic acid to give the product.

1.4.b. *Pd (0) and Pd (I): The 'outer-sphere mechanism': VAM synthesis in solid-gas phase with a 'liquid phase' acetate intermediate*

In 1967, Kunugi et al. proposed that industrial VAM synthesis relied on a surface heterogeneous interaction [49], rather than a 'pseudo liquid phase' as described below. Nakamura and Yasui, investigating the gas phase interaction of propene, oxygen and acetic acid on metallic Pd [50], suggested their own data implied a Pd (II) 'pseudo liquid phase' mechanism for the same reactants [51-52]. The 'pseudo liquid phase' mechanism involves formation of iso-propenyl acetate, n-propenyl acetate and allyl acetate, whereas allyl acetate is the only product in the gas phase interaction. This led them to propose the following mechanism for VAM synthesis, with the active intermediate of VAM synthesis being a Pd^{+} complex of Pd(I) acetate:

$$2Pd + C_2H_4 = Pd(CHCH_2) + Pd(H) \quad (1.3)$$

$$2Pd + O_2 = 2Pd(O) \quad (1.4)$$

$$Pd + CH_3COOH = Pd(CH_3COOH)_{(a)} \quad (1.5)$$

$$Pd(CH_3COOH) + Pd(O) = Pd(OOCCH_3) + Pd(OH) \quad (1.6)$$

$$Pd(CHCH_2) + Pd(OOCCH_3) = Pd + Pd(CH_2CHOOCCH_3) \ (\textit{RDS}) \quad (1.7)$$

$$Pd(CH_2CHOOCH_3) = Pd + CH_2CHOOCH_3 \quad (1.8)$$

$$Pd(OH) + Pd(H) = Pd + Pd(H_2O) \quad (1.9)$$

$$Pd(H_2O) = Pd + H_2O \quad (1.10)$$

This mechanism suggests that dissociatively adsorbed ethylene and acetic acid combine to give Pd-vinyl and Pd-acetate species which form vinyl acetate in the gas phase. This process may occur as outlined in Fig. 6:

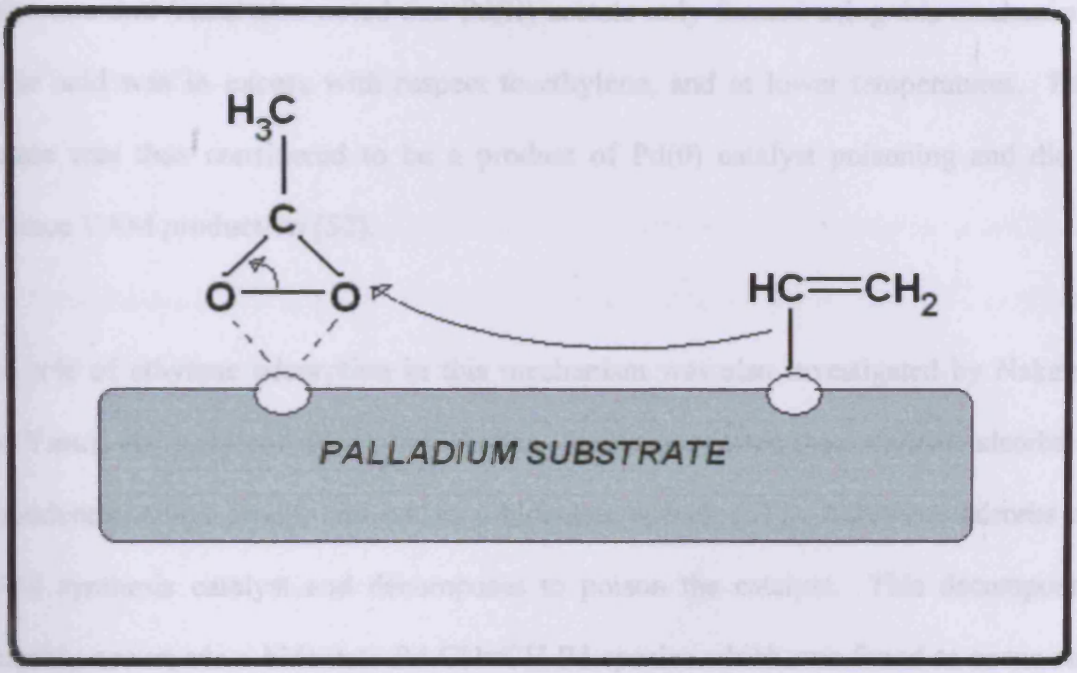

Fig. 6: The key step in the production of VAM from ethene and acetic acid, as suggested by Yasui and Nakamura's 'outer sphere mechanism'. The white circles indicate active sites in the crystal's selvedge.

Both starting materials dissociate by H abstraction and are thus active. In the case of acetic acid this requires the presence of dissociated oxygen. Potassium from K acetate acts as a promoter by facilitating the abstraction of H from acetic acid, and reducing the chemisorption strength in Pd acetate. Secondary reactions producing combustion products from vinyl and acetate groups also occur:

$$Pd(O) + Pd(CHCH_2) = Pd(H_2O) + Pd(CO_2) \quad (1.11)$$

$$Pd(OOCCH_3) + Pd(O) = Pd(H_2O) + Pd(CO_2) \quad (1.12)$$

$$Pd(CO_2) = CO_2 + Pd \quad (1.13)$$

$$Pd(H_2O) = H_2O + Pd \quad (1.14)$$

Nakamura and Yasui also noted that Pd(II) acetate only formed using this mechanism if acetic acid was in excess with respect to ethylene, and at lower temperatures. Pd(II) acetate was thus considered to be a product of Pd(0) catalyst poisoning and did not enhance VAM production [52].

The role of ethylene adsorption in this mechanism was also investigated by Nakamura and Yasui, via acetylene adsorption studies. It was suggested that ethylene adsorbs as a monodentate vinyl group, and not as a bidentate species [51]. Acetylene adsorbs on a VAM synthesis catalyst and decomposes to poison the catalyst. This decomposition probably occurs via a bidentate Pd-CH=CH-Pd species which was found to occur on Pd surfaces [53]. However, adsorption of ethylene on a VAM synthesis catalyst for over 100 hours has no poisoning effect, which led to the above hypothesis.

1.4.c *Pd(II): 'The inner sphere mechanism': VAM synthesis in 'pseudo liquid phase'*

Samanos [54] and Zaidi [55] suggest that the reaction occurs with Pd (II) acetate as the active catalyst. In this respect the proposed mechanism is similar to the Pd salt catalysed 'Wacker-like' homogeneous synthesis route mentioned above [24-25]. It is not fully

clear how VAM is produced by this homogeneous 'Wacker-like' method, and the following scheme has been suggested [56]:

$$Pd(OOCCH_3)_2 + CH_3COO^- = Pd(OOCCH_3)_3^- \quad (1.15)$$

$$Pd(OOCCH_3)_3^- + C_2H_4 = C_2H_4Pd(OOCCH_3)_3^- \quad (1.16)$$

$$C_2H_4Pd(OOCCH_3)_3^- \rightarrow C_2H_3OOCCH_3 + Pd(0) + CH_3COO^- + CH_3COOH \quad (1.17)$$

The final step is rate limiting and requires a coordinated ethylene species to insert into the coordinated Pd-$OOCCH_3$ bond. Note that in this homogeneous version, Pd^{2+} is provided by Pd (II) chloride, but in the heterogeneous version suggested by Samanos and Zaidi, Pd^{2+} is provided by oxidation of finely divided Pd metal to Pd(II)acetate. Using kinetic data, Samanos proposed a mechanism relying on the formation of Pd(II) acetate as an intermediate. It was proposed that two parallel reactions occur in this heterogeneous route, one of which is VAM production from palladium oxidation:

$$Pd + \tfrac{1}{2} O_2 + 2CH_3COOH \rightarrow Pd(OOCCH_3)_2 + H_2O \quad (1.18)$$

$$Pd(OOCCH_3)_2 + CH_3COO^- \rightarrow Pd(OOCCH_3)_3^- \quad (1.19)$$

$$Pd(OOCCH_3)_3^- + C_2H_4 \rightarrow C_2H_3OOCCH_3 + Pd(0) + CH_3COO^- + CH_3COOH \quad (1.20)$$

The in-depth mechanism of the first step, the oxidation of Pd, is not clear due to the strong adsorption of acetic acid over oxygen. Note that, in contrast to the homogeneous route, $Pd(OOCCH_3)_3^-$ reacts with gaseous ethylene to produce VAM and regenerate Pd(0). This is achieved by the presence of the promoter potassium (or sodium) acetate.

The secondary (parallel) reaction is Pd(0) catalysed combustion of ethylene, producing the major by-product carbon dioxide:

$$C_2H_4 + 3O_2 \rightarrow 2CO_2 + 2H_2O \qquad (1.21)$$

This acetate species in a similar system reacted with oxygen and ethylene to give VAM. Compared to the 'outer sphere mechanism' proposed by Yasui and Nakamura, the inner sphere mechanism has more supporting evidence and is probably prevalent in industrial VAM synthesis. For example, reports have shown that the catalyst surface supports a large multi-layered excess of adsorbed acetic acid during the reaction [54,57], which lowers the activation energy for VAM formation and increases the overall rate of VAM production [57]. Under the oxidising conditions of the reaction, adjacent Pd metal sites are unlikely to occur to allow the outer sphere mechanism to occur to a great extent. Diffuse reflectance infrared Fourier Transform spectroscopy and mass spectrometry (DRIFTS-MS) studies gave strong support for the formation of Pd(II) acetate as an intermediate [57]. Using silica supported Pd catalysts, Pd (II) acetate was formed from acetic acid and oxygen and detected by DRIFTS-MS. In a KCl matrix, which is similar to a silica support in DRIFTS, the Pd(II) acetate reacted with oxygen and ethylene to give VAM and acetic acid at 413 – 443 K. Kinetically the order of reaction with respect to acetic acid was found to be zero, suggesting it was in great excess, however, the order of reaction seems to vary significantly for acetic acid in other studies [51,54]. Isotope transient kinetics (ITK) studies have investigated both Pd/Cd and Pd/Au particles on silica using $^{18}O_2$ and $^{16}O_2$, and, by investigating the time taken for $H_2{}^{18}O$ and $H_2{}^{16}O$ to be

produced, have confirmed that a 'pseudo-liquid' acetic acid phase occurs in VAM synthesis [58]. Density functional theory (DFT) studies [59] investigated the inner sphere mechanism interaction of oxygen, acetic acid and ethylene on the clusters Pd_3O_3 and Pd-18, which were considered sufficiently similar to the larger stable trimer Pd_3OAc_6 [60]. VAM production was found to be feasible in these systems and gave very similar energies of reaction to those from real data. The rate determining step seemed to be cleavage of β-C-H species in ethylene acetate intermediates, which was likely to occur where Pd(OH) species formed from reaction of Pd(O) and cleaved hydrogen. Note that this RDS is in contrast to the ethylene insertion RDS suggested by Samanos et. al. [54].

Note that, in comparison to Nakamura and Yasui's observations for ethylene in this process, Samanos et. al. concluded that ethylene remains in the gas phase and does not adsorb and decompose to monodentate vinyl species [54]. This is supported by Augustine and Blitz, who stated that, in the oxidising conditions present, residence times of adsorbed ethylene and vinyl species would be very short. C-H stretches due to ethylene were not observed in DRIFTS spectra for VAM synthesis on silica supported Pd catalysts [57]. Dissociative adsorption of ethylene is unlikely in VAM synthesis conditions, as in UHV, as it is readily oxidised to combustion products on Pd single crystals with coadsorbed oxygen [61]. Hence ethylene is likely to occur either as a molecularly adsorbed species or in the gas phase in VAM synthesis.

Catalytic activity was measured against Pd particle dispersion for two support materials, alumina and silica by Samanos et al. [54]. Larger, less dispersed Pd particles gave a

greater activity, and alumina could remain active to a greater degree of Pd dispersion compared to silica. In addition, Samanos et. al. investigated the effects of catalyst supports on retention times for acetic acid, water, oxygen and ethylene. While oxygen and ethylene did not interact with supports, acetic acid was found to have a greater retention time compared to water for silica and alumina of the sort used as VAM catalyst supports [54]. Both water and acetic acid adsorb strongly on alumina and silica, which may explain why high Pd particle dispersion affects activity negatively. There are two possible reasons for this:

* There may be a metal-support interaction which changes Pd particle properties, dependent on the electronic properties of alumina and silica. This may in turn affect Pd dispersion against activity i.e. more dispersed particles maximise metal-support interactions which are more deactivating in the case of silica.

* Silica adsorbs water and acetic acid more strongly than alumina can. Adsorbed water and acetic acid might inhibit interactions between very dispersed Pd particles and gas phase oxygen and ethylene. Hence this inhibition has a greater effect in the case of silica.

Isotropic transient kinetics (ITK) data also suggested that oxygen and ethylene do not adsorb [62], and that acetic acid forms an aqueous 'pseudo-liquid' layer of acetic acid between two and three molecules deep on a silica support. In fact most of the acid present was associated with the support, and the thickness of the acid layer depended on

Pd and K levels present, and the support's surface area. Hence the acid layer is affected significantly by catalyst characteristics, and was therefore considered an important feature of the catalysed VAM synthesis.

1.4.d *Pd (0-2): a combination of the three models*

Augustine and Blitz [57], using Pd/α-Al_2O_3 catalysts, have reported that the ratio of VAM produced to catalyst Pd content is less than 1 in 40, suggesting that most of the Pd does not participate in the reaction. For Pd dispersion against catalyst activity, it was found that a maximum activity in fact occurs when the Pd is quite metallic in nature and not very dispersed [54]. In fact, minimum activity occurred in regions of low metallic nature. Augustine and Blitz thus proposed that in fact the active phase is a combination of Pd(0-2) in the form of islands of Pd(I) and Pd(II) acetate on Pd(0) metal and Pd(II) oxide. In conclusion, both the 'inner' and outer sphere mechanisms' may occur in industrial VAM synthesis, although most evidence suggests that the latter is dominant. In all of the above mechanisms, Group 1 metal acetates enhance palladium acetate formation which reacts with ethylene in the RDS. Ethylene always shows first order reaction kinetics and can be activated by H-abstraction with or without oxygen present. The kinetics of acetic acid vary from study to study, and its kinetic role is therefore unclear, however it requires oxygen to be activated to an acetate species in all cases. The order of reaction has been reported to be between zero and unity in several studies. Studies of acetic acid adsorption on single Pd crystal surfaces (63-66) shows that under these conditions it forms bidentate acetate species which bond to Pd via both oxygen

atoms, with a bond order of 3/2 each and extensive delocalisation. DRIFTS studies on silica supported Pd showed that increasing acetic acid pressure reduced the activation energy of the overall reaction. This was achieved supposedly by acid forming complexes (perhaps acetates) at the active site, thus affecting the active site's energetics. In addition, although acetic acid adsorbs strongly to Pd, it does not limit the reaction rate, and thus is capable of continually forming acetate and decomposing at the surface. It was also suggested that acetate binds both as a bidentate species and as a monodentate species, also described as a 'Pd ester' which produces a carbonyl absorption peak at 1735 cm^{-1} [57]. This has been supported recently by acetic acid adsorption studies on Pd (111) [65]. The above evidence suggests that acetate species form on the Pd surface in VAM synthesis, but the exact oxidation state of Pd, and hence the overall mechanism of VAM, has not been resolved.

1.5 By-Product Formation in VAM Synthesis

It is of interest industrially to minimise production of the main by-products of VAM synthesis: carbon dioxide, acetaldehyde and acetic anhydride. This can be achieved by a greater understanding of VAM decomposition on Pd catalysts. Most of the information from previous studies relies on microreactor homogeneous catalysis pathways, and decomposition of ethylene and acetic acid on Pd single crystals and supported catalysts also in UHV. Thus this information, while being useful, cannot be related directly to the industrial heterogeneous process. The principal by-product carbon dioxide is formed by oxidation of vinyl acetate, ethylene and acetic acid in the reactor, to different extents,

which is a matter of discussion in literature. Isotope labelling studies on the system performed by Davidson et al. implied that the main source of carbon dioxide was acetic acid oxidation [67]. However, ITK studies on $Pd/K/Cd/SiO_2$ systems indicated that carbon dioxide is formed significantly from the reactants to equal extents, and carbon dioxide production from VAM was not significant [62]. This suggested that VAM in the gas phase does not interact strongly with the catalyst surface to produce carbon dioxide, but may still produce carbon dioxide in significant amounts that can be detectable by other methods. Nakamura and Yasui [51,52] however, noticing that the selectivity for VAM increases with addition of acetic acid and that the rate of oxidation of individual molecules on Pd increased in the order acetic acid>VAM>ethylene, concluded that ethylene was the main source of carbon dioxide. This assumption was supported by Samanos et al. [54] who found that the oxidation of ethylene had the same activation energy as that for formation of carbon dioxide from oxygen, ethylene and acetic acid, suggesting that oxidation of ethylene is the main source of carbon dioxide production.

They also found that the activation energies of carbon dioxide and VAM formation were significantly different, and that, in contrast to VAM formation, the rate of carbon dioxide formation decreases with increasing ethylene partial pressure. These observations suggest that oxidation of ethylene is a reaction parallel to VAM formation. The oxidation mechanisms of dissociatively adsorbed ethylene and acetic acid, as suggested by Nakamura and Yasui are given below:

$$Pd(CHCH_2) + Pd(O) = Pd(CO_2) + Pd(H_2O) \quad (1.22)$$

$$Pd(CO_2) = Pd + CO_2 \quad (1.23)$$

$$Pd(H_2O) = Pd + H_2O \quad (1.24)$$

$$Pd(OOCH_3) + Pd(O) = Pd(CO_2) + Pd(H_2O) \quad (1.25)$$

$$Pd(CO_2) = Pd + CO_2 \quad (1.26)$$

$$Pd(H_2O) = Pd + H_2O \quad (1.27)$$

Another by-product, acetaldehyde only forms on Pd metal catalysts below 420 K under high acetic acid overpressures under industrial conditions [53]. Pd(II) acetate forms readily under these conditions. According to Nakamura and Yasui, acetaldehyde under these conditions can be formed by the interaction of ethylene and acetic acid, ethylene and water, VAM and water, and VAM and acetic acid, provided the reaction is catalysed by Pd (II) acetate [51]. Studies have shown that all of the above reactions will occur in the presence of a Pd(II) salt. The extent to which each of the above interactions occur is a matter of debate. Homogeneous reaction of ethylene and water in the presence of Pd (II) acetate and sodium acetate has been investigated in several studies [56,68,69], and have detected small amounts of acetaldehyde and acetic acid, with VAM as the major product. Sodium acetate appears to reduce the extent of acetaldehyde formation from ethylene oxidation [69]:

$$Pd(OH) + C_2H_4 \rightarrow Pd(CH_2CH_2OH) \quad (1.28)$$

$$Pd(CH_2CH_2OH) \rightarrow Pd(H) + CH_3CHO \quad (1.29)$$

$$Pd(H) + Pd(OOCCH_3) \rightarrow 2Pd + CH_3COOH \quad (1.30)$$

Homogeneous reaction of VAM and acetic acid catalysed by Pd(II) complexes has also been investigated [70] giving acetic anhydride and acetaldehyde as products. This reaction, along with the interaction of VAM and water, is considered to be the main contributor of acetaldehyde in the overall mechanism. It has been suggested that acetate ions are not necessary to catalyse the reaction [70], while other research groups state the opposite, using Pd(II) chlorides and Na acetate [71]. Schultz et al. suggest that acetate is needed for making the reactants soluble, rather than catalysis [70]. Schultz et al. also investigated VAM decomposition rates against water concentrations, and found that the rate of VAM decomposition decreases with increasing water concentration. This is of significance in the heterogeneous case, due to the aqueous 'pseudo-liquid' layer of acetic acid which was found on the support during ITK experiments [62].

1.6 Catalysis by Bimetallic Compounds

The above studies relate in the main to monometallic Pd systems. However, heterogeneous catalysed VAM synthesis relies on a bimetallic catalyst system on a metal oxide support. The presence of Au with Pd, and more generally a second metal with an already catalytically active metal in a system, can introduce valuable new catalytic properties including improved selectivity, longevity and activity. These changes can

occur by modification of surface electronic (ligand effect) properties or geometric (ensemble effect) properties. In a bimetallic alloy catalyst, the chemical composition of the surface can be very different to that in the bulk, which can have direct effects on catalysed adsorption and reaction at the surface. Bimetallic alloy catalysts are generally not very dispersed compared to supported catalysts, which often maximise surface area. Although the support is usually considered inactive, it provides a framework for the active phase and its dispersion and carries promoters such as K acetate. Thus it can have a major effect on the catalysed reaction.

Bimetallic cluster catalysts use principles from both bimetallic alloy and catalyst support research, and are discussed in more detail in many reviews [72]. When putting bimetallic catalysts on a support, how well the two metals form an alloy when dispersed comes into question. When the two metals have similar properties and form well defined alloys in the bulk and are dispersed on a support with a total metal concentration of around 1%, the metal particles often, but not always, form alloys in the catalyst particles. Hence not all bimetallic cluster systems are considered bimetallic alloys, as the immiscible Ru/Au supported system demonstrates [73]. However, the bimetallic system of interest in the studies in this thesis, Pd/Au is miscible at comparatively low temperatures [74]. In forming these Pd/Au bimetallic systems, it is important to consider how the composition of the surface changes with respect to the bulk as the alloy is formed. The component with the lower surface free energy and sublimation energy will tend to shift to the surface and enrich the first few atomic layers. In the case of Pd/Au, which have similar atomic radii, Au has the lower surface free energy and sublimation energy so is expected to

enrich the surface. This has been confirmed by some studies [75,76] and dismissed by others [77]. Alone, Au is not catalytically active in most reactions. However, when Au is combined with metals such as Pt and Pd, the activity and selectivity of the bimetallic catalyst can be affected greatly, depending on the system.

Pd and Au are both fcc metals that readily form alloys, with exothermic standard energies of formation over a complete range of compositions, a minimum occurring at 40% Pd /60 % Au [78]. Pd/Au alloys comprise a continuous range of fcc cubic solid solutions, with no solid state transformations across the whole range. Pd and Au have similar atomic radii, corresponding to a 4.8 % lattice mismatch, and similar lattice parameters across the whole range of compositions in Pd/Au wires at 298 K (4.0782 Å for 100% Au, 3.8896 Å for 100% Pd) [78]. Au (110) can show (1 x n) reconstructions in LEED, where n is 2 or above [79,80]. In contrast, Pd (110) does not reconstruct [81,82]. Pd/Au systems have been investigated extensively in UHV both with formation of films of one metal on the substrate of the other, and with pre-prepared alloy single crystals and supported systems. In addition, there is substantial information on the catalytic properties and structure of more 'real' supported Pd/Au catalysts, including references to VAM synthesis which has become of more interest to researchers in recent years. UHV studies of these bimetallic systems usually consider films of one metal deposited on a single crystal of the other. Schmitz et. al. [83,84] grew Au films of 1-10 ML by vapour deposition on a Pd (110) surface at 130 K, noting a Stranski-Krastanov (layers then islands) growth mode across this coverage region with a critical thickness of 2 ML (3D islands begin to grow on sequential layers after 2 ML Au deposition). The transition in phases was attributed to the

Pd/Au lattice mismatch inducing a strain energy affected by coverage. CO desorbed from these surfaces at 225 and 190 K which were attributed to desorption from the first and second Pd-modified Au surface respectively. On annealing between 300 -800 K, LEED analysis showed a series of (1 x z) diffraction patterns which were dependent on Au coverage, where z = 1, 2 or 3. These reconstructions were attributed to thermally activated Au-bulk-like missing row reconstructions. Below 1.5 ML coverage, only (1x1) patterns were observed. Above this coverage, the Au layer is sufficiently deep to support (1x2) reconstruction superstructures. Between 1.5 and 6 ML, the value of z changes gradually from 2 to 3, attributed to a mixture of small (1x2) and (1x3) domains, with the z=3 phase dominant at higher coverages. This behaviour was considered to be due to 3D clustering occurring which reduces surface area for reconstruction, making the LEED pattern fainter, and increasing surface roughness. Reannealing the surface above 640 K recovered a stronger (1x2) pattern which may have been due to Au layer depletion or re-ordering at this temperature. The Au/Pd surfaces were found to be stable up to 500 K, and the destabilisation was accounted for by intermixing of the film and bulk to reduce the Au/Pd ratio observed in AES. Kaukasoina et al. [85] investigated similar systems by AES and found that dissolution occurred at 740-770 K for coverages above 2ML, and at lower temperatures for lesser coverages. Later studies by Vos et al. using MEIS [86] implied a layer-by-layer rather than Stranski-Krastanov growth mode for Au films up to 24 ML thick deposited at 300 K, and a factor of 3x difference between lattice relaxation in the [100] and [111] directions. However, this data is not directly comparable to work by Schmitz et. al. due to the differences in analysis methodology and deposition temperatures. Theoretical analysis of Au on Pd(110) was performed by Nieminen [87]

using a model that explained the (1 x z) transitions and supported the growth mode inferred by Schmitz et. al. . Using dynamical LEED, Kaukasoina et al. [85] looked at a 2.5 ML (1x2) Au film on Pd (110), and found intermixed Pd/Au layers occurring below two layers of pure Au. The optimum geometry was a missing row top layer, followed by a row-paired second layer, then a rumpled third layer. This optimum geometry is different from that of (1x2) Au(110) and is attributed to conserving volume density due to the 4.8 % lattice mismatch. A significant difference between these results and those of Schmitz et al. was that a (1 x 2) pattern was not observed at 1.5 ML coverage, and the transition from (1x1) and (1x2) at higher coverages was continuous rather than a distinct single transition.

The analogous system of Pd deposited on Au (110) has been investigated using medium energy electron diffraction (MEED), x-ray diffraction (XRD), LEED, AES and low energy ion scattering (LEIS) by Dolle et al. [88]. With a 0.5 ML Pd layer on an Au (110) – (1 x 2), Au atoms covered much of the deposited Pd substrate, forming an ordered interface alloy covered by two incomplete Au layers, and the (1x2) LEED pattern was significantly reduced. The growth mode was found to be layer by layer from 0.5-3 ML, becoming a 3D SK growth mode between 3-4 ML. Similar results were obtained by Robach et al. using AES, LEED and STM with layer by layer growth between 2-3 ML and 3D growth above 4 ML. Both modes were considered to reduce strain between the Au substrate and deposited Pd layers [89]. Initially on deposition at low coverages, Pd fills the missing rows of the Au surface, and is then covered by Au, leaving holes in the surface to form a mixed Au-Pd interface. STM was also used by Martin et al. with

LEED and optical reflectance anisotropy (RA) on the same system, and Pd desposition and alloying induced significant changes in the Au RA response [90]. Using a very different method of deposition, cyclic voltammetry (CV) and STM studies of electrochemically adsorbed $[PdCl_4]^{2-}$ on Au(110) showed that layer by layer growth does not occur, and that epitaxial Pd film growth occurs above 3 ML of coverage [91].

Similar systems have also been studied, including Au/Pd(111) which displays layer by layer growth, grows as bulk Au below 3 ML and forms ($\sqrt{3}$ x 22 +/- 1) Au (111) reconstructions above 4 ML [92,93], and begins to intermix at about 400 K. Pd/Au (111) grows in a layer by layer mode for low coverages then random nucleation at higher coverages [94] to give a disordered surface film. This film becomes ordered between 300- 400 K and intermixes between 400-600 K. At coverages above 1 ML, an ordered Pd_2Au alloy forms at 500 K and is stable up to 700 K In contrast, the Pd/Au(100) system begins to intermix at 300 K [95].

1.7 Geometric and Electronic Effects of Gold in Bimetallic Catalyst Compounds

Addition of Au, which has a low activity as a bulk metal, to an active metal cluster ensemble can induce a reduction of catalytic activity due to disruption of the active clusters. In addition, changes in selectivity can occur which may be positive or negative, depending on the nature of the system. For instance, chemisorption of CO on bulk Au is virtually zero, and CO chemisorption decreases linearly with increasing Au concentration in Pd/Au alloys [96]. This can be interpreted in terms of the CO interacting with Pd, and

Au being inert to CO adsorption. Another example involves oxidation of ethylene on Pd/Au alloys, where complete oxidation of ethylene to CO_2 and H_2O occurs on adjacent Pd atoms [96,97]. Adding Au dilutes the concentration of Pd, reducing activity but improving selectivity to partial oxidation to acetic acid, acetaldehyde and acetic anhydride, which involves oxidation of ethylene on isolated Pd atoms. Hence maximum selectivity to partial oxidation products occurs at 80% Au 20 Pd% composition. This system has special relevance to VAM production from ethylene, oxygen and acetic acid, where Au is added in sufficient amounts to prevent total oxidation and is also in an amount that does not maximise partial oxidation to the by-products acetic anhydride and acetaldehyde.

There are several schools of thought as to the electronic behaviour of Pd/Au alloys. Bulk Au has a filled d-band and a half filled valence s-band, and it had been proposed that the Pd 4d-band overlaps with the Au 6s-band to form an alloy composite structure [97]. Also it has been suggested that in excited states Pd metal has a partially occupied d-band containing 0.6 holes per Pd atom [74]. In the alloy, Au s-electrons will shift to the unoccupied states in the Pd d-band. Hence it might be expected that at about an Au: Pd ratio of 3:2, the d-band will be filled and the catalytic properties would alter markedly. This hypothesis was supported in experiments involving conversion of para- to ortho-hydrogen on such surfaces [99]. However, studies involving magnetic susceptibility found that Pd metal had only 0.36 holes per Pd atom in the d-band [74], so the electronic model surface composition model, which considered only the surface atoms, [100] required adjustment. However, the surface and bulk compositions can be very different,

and the alloy composition and structure may change considerably during treatment and analysis. Hence models which consider both the surface and bulk were proposed [100]. However, it has been suggested that there is not a direct correlation between extent of d-band occupancy by Au content, and catalytic activity. Also, the Pd and Au atoms' electronic structure may remain virtually unchanged in the alloys, implying only local electronic effects in these systems [101]. The effects on CO chemisorption with alloy composition provide a useful method of characterising electronic effects on the alloy. CO chemisorption on pure Au is virtually zero [97]. Gerberich et al. [97] found that the chemisorption of CO decreased with increasing Au concentration in Pd/Au alloys, reaching zero chemisorption for pure Au. These finding were supported by studies on Pd/Au (111) in ultra high vacuum [102].

X-ray diffraction (XRD) has shown that alloys form on certain alumina-supported Au/Pd catalysts. Electron spin resonance (ESR) experiments on specific alumina-supported alloys have found that the surface of the particles is enriched with Au under most conditions [103]. However, on silica-supported Pd/Au nanoparticulate catalysts, alloy formation has been determined using Mossbauer spectroscopy, gas chemisorption and X-ray line broadening studies [104], with surface composition similar to bulk composition.

1.8 Thesis Synopsis

This work deals primarily with the adsorption, decomposition and reaction behaviour of small organic molecules associated with vinyl acetate synthesis on palladium and gold surfaces, and the characterisation of intermediates such as acetate, ethynyl and methyl groups. The aim is to understand the mechanism of vinyl acetate more, through the use of surface science and UHV conditions, as well as the effects of gold doping and alloying on palladium single crystals, on catalyst selectivity and reactivity. This first chapter has provided background history on vinyl acetate synthesis, and a consideration of gold and palladium surfaces and their potential effects on the reactions to be investigated. The significance of by-products from the synthesis is of great importance and will be considered in Chapters 4 to 6. Chapter 2 describes the apparatus that was used to obtain the data presented in the later chapters. In Chapters 3 and 4, results on a Pd (110) single crystal are presented. Chapter 3 involves work on the starting materials of VAM synthesis: oxygen, ethene and acetic acid, and their interaction with clean surfaces, and those dosed with small molecules such as carbon atoms or oxygen. Chapter 4 describes the interaction of vinyl acetate, and potential by-products acetaldehyde and carbon monoxide with clean Pd (110). There are similarities between these molecules and the intermediates of decompositions of other molecules described in the previous chapter, and these will be discussed.

Interest in bimetallic systems has increased greatly due to their activity and selectivity in certain industrial processes. In Chapter 5 a variety of such systems were obtained by

varying the exposure of a clean Pd (110) crystal to gold metal vapour. The surfaces obtained were studied with respect to their reactivity to the molecules described in the previous chapters. These results were then compared with those obtained for reactions on clean Pd (110). Chapter 6 gives a summary and conclusion to the findings of Chapters 3 to 5.

REFERENCES:

[1] H. Davy, *Phil. Trans. R Soc.*, **107** (1817) 77.

[2] I. Langmuir, *J. Chem. Soc.*, **38** (1916) 2221.

[3] I. Langmuir, *J. Chem. Soc.*, **34** (1912) 860 & 1310.

[4] I. Langmuir, *Trans. Faraday Soc.*, **17** (1922) 607 & 621.

[5] C. N. Hinshelwood, *Annual Reports Chemical Society*, London, **24** (1928) 335.

[6] D.D. Eley, E. K. Rideal, *Nature*, **146** (1940) 401.

[7] D.D. Eley, E. K. Rideal, *Proc. R. Soc.*, **A178** (1941) 429.

[8] H.S. Taylor, *J. Am. Chem. Soc*, **53** (1931) 578.

[9] J. E. Lennard-Jones, *Trans. Faraday Soc.*, **28** (1932) 333.

[10] See for example, J. Clark's description of the Haber Process on www.chemguide.co.uk/physical/equilibria/haber.html

[11] C. T. Campbell, *Appl. Surf. Sci.* **19** (1984) 32.

[12] M. Bowker, '*The Basis and Applications of Heterogeneous Catalysis*', Oxford University Press, (1998) 5.

[13] G. A. Somorjai, '*Introduction to Surface Chemistry and Catalysis*', J. Wiley & Sons Inc., (1994) 41.

[14] G. Attard, C. Barnes, '*Surfaces*', Oxford University Press, (1998) 17.

[15] P. J. F. Harris, *Nature*, **323** (1986) 792.

[16] H. Tanaka, J. Yoshinobu, M. Kawai, *Surf. Sci. Lett.*, **327** (1995) L505.

[17] A. Zangwill, *'Physics at Surfaces'*, Cambridge University Press, (1988).

[18] D. R. Strongin, J. Carrazza, S. R. Bare, G. A Somorjai. *'Iron single Crystals as Ammonia Synthesis Catalysts. The Effect of Surface Structure on Catalyst Activity.' J. Catal.* **74** (1982) 129.

[19] D. P. Woodruff, T. A. Delchar, *'Modern Techniques in Surface Science'*, CUP,(1994), 2nd Edition.

[20] A. Chambers et al., *'Vacuum Technology'*,2nd Edition, North-Holland, (1986).

[21] from Celanese Chemicals Corp. website: www.celanese.de

[22] R. E. Kirk & D. F. Othmer (Eds.), *'Encyclopaedia of Chemical Technology'*, Vol. **14**, (1955) 686, Interscience Encyclopaedia Inc., New York.

[23] F. Klatte, US Pat. No. 1084581 (1914).

[24] S. J. Wacker, *J. Am. Chem. Soc.*, **60** (1938) 440.

[25] I. I. Moiseev, M. N.Vargaftic, Y. K. Syrkin, *Dokl. Akad. Nauk. SSSR.*, **133** (1960) 377.

[26] Imperial Chemical Industries Co. Patent Nos. 964001, 969162, 975683, 975709, 1026594, 1061788. Also *Chem. Week* **101 (7)** (1967) 73.

[27] W. D. Shaeffer, Union Oil Co. of California, US Patent Nos, 3260739, 3253020.

[28] J. F. McKeon, P. S. Starcher, Union Carbide Corporation, US Patent No., 3221045.

[29] *World Pet. Cong. Proc.* **5** (1968) 41.

[30] *Eur. Chem. News* **11 (272)** (1967) 40, and also *Chem. Ind.* (1968) 1559.

[31] British Patent No. 1521652, US Patent Nos. 3775342, 3822308.

[32] British Patent No. 1220180, US Patent No. 3658888.

[33] see for example, *Chem. Week* **156** (1995) 44.

[34] National Distillers, British Patent No. 1146731 (1969).

[35] British Patent Nos. 1103125, 1107495, 1235632, US Patent No. 3432544.

[36] L. A. Sokolova, N. M. Popova, V. K. Eritsyan, B. S. Mukanova, V. K. Boyadzhyan, S. S. Khachatryan, *Izv. Akad. Nauk Kaz. SSR, Ser. Khim.* **28** (1978) 57.

[37] R. Haley, PhD Thesis, University of Cambridge, (1999).

[38] Hoescht, US Patent No. 4902823 (1990)

[39] Hoescht, EP Patent No. 403950 (1990).

[40] G. M. Severs Jr., Ger. Offen. 2 3 61 098 (1974).

[41] US Patent No. 3658888 (1967).

[42] US Patent No. 4048096 (1977).

[43] National Distillers, Ger. Offen. 1 9 44 933 (1970)

[44] Grace & Co. Corp., British Patent No., 1183672 (1967),9 44 933 (1970).

[45] C. W. Capp, French Patent No. 1566124 (1969).

[46] T Saito, M. Takano, S. Moriyama, H. Murayama, *Jap. Kokai*, **73-49** (1973) 711.

[47] BP, British Patent No., 1128993 (1966).

[48] W. D. Provine, G. W. Mills, J. J. Lerou, *Studies in Surface Science & Catalysis*, **101** (1996) 191.

[49] Kunugi, Fugimoto, Arai, Kon, Namatama, *Kogio-Kagaku-Zasshi*, **71** (1968) 2007.

[50] W. E. Stern, M. L. Spector, *Proc. Chem. Soc.*, **111** (1963).

[51] S. Nakamura, T. Yasui, *J. Catal.*, **17** (1970) 366.

[52] S. Nakamura, T. Yasui, *J. Catal.*, **23** (1971) 315.

[53] L. H. Little, N. Sheppard, P. J. C. Yates, *Proc. Roy. Soc.*, **242** (1960) A259.

[54] B. Samanos, P. Boutry, R. Montarnal, *J. Catal.*, **23** (1971) 19.

[55] S. A. H. Zaidi, *Appl. Catal.*, **38** (1988) 353.

[56] R. Van Helden, C. F.K Kohl, D. Medema, G. Verbag, T. Jonkhoff, *Receuil*, **87** (1968) 961.

[57] S. M. Augustine, J. P. Blitz, *J. Catal.*, **17** (1970) 366.

[58] N. F. Mott, *Advanced Physics*, **13** (1964) 325.

[59] M. Neurock, W. D. Provine, D. A. Dixon, G. W. Coulston, J. J. Lerou, R. A. van Santen, *Chem. Eng. Sci.*, **51** (1996) 1691.

[60] A. C. Skapski, M. L. Smart, *J. Chem. Comm.*, **531** (1970) 658.

[61] E. M. Stuve, R. J. Madix, *Surf. Sci.*, **160** (1985) 293.

[62] E. A. Crathorne, D. MacGowan, S. R. Morris, A. P. Rawlinson, *J. Catal.*, **149** (1994) 254.

[63] J. L. Davis, M. A. Barteau, *Langmuir*, **5** (1989) 1299.

[64] N. Aas, M. Bowker, *J. Chem. Soc. Farad. Trans.*, **89 (8)** (1993) 1249.

[65] R. D. Haley, M. S. Tikhov, R. M. Lambert, *Catal. Lett.*, **76** (2001) 125.

[66] M. Bowker, C. Morgan, J. Couves, *Surf. Sci.*, **555** (2004) 145.

[67] J. M. Davidson, P. M. Mitchell, N. S. Raghavan, *Front. Chem. React. Eng.*, **1** (1984) 300.

[68] D. Clark, P. Hayden, R. D. Smith, *Discuss Farad. Soc.*, **45** (1968) 98.

[69] S. Winstein, J. McCaskie, H. B. Lee, P. M. Henry, *J. Am. Chem. Soc.*, **98** (1976) 6913.

[70] R. G. Schultz, P. R. Rony, *J. Catal.*, **16** (1970) 133.

[71] W. H. Clement, C. M. Selwitz, *Tetrahedron Letters*, (1962) 1081.

[72] see for instance C. T. Campbell, *'Bimetallic Surface Chemistry'*, Annual Reviews Inc., 1990, or K. J. Klabunde et al., Chapter 7, *Am. Chem. Soc. (Review)*, (1993).

[73] J. H. Sinfelt, *J. Catal.*, **29** (1973) 308.

[74] E. G. Allison, G. C. Bond, *Cat. Rev.* **7** (1972) 233.

[75] G. Maire, L. Hilaire, P. Legare, F. G. Gault, A. O'Cinneide, *J. Catal.*, **44** (1976) 293.

[76] A. Jablonski, S. H. Overbury, G. A. Somorjai, *Surf. Sci.*, **65** (1977) 578.

[77] B. J. Wood, H. Wise, *Surf. Sci.*, **52** (1975) 151.

[78] J. B. Darby, *Acta. Met.*, **14** (1966) 265.

[79] G. Binnig, H. Rohrer, Ch. Gerber, E. Weibel, *Surf. Sci.*, **131** (1983) L379.

[80] W. Moritz, D. Wolf, *Surf. Sci.*, **88** (1979) L29.

[81] R. D. Diehl, M. Lindroos, A. Kearsley, C. J. Barnes, D. A. King, *J. Phys. C*, **18** (1985) 4069.

[82] M. Wolf, A. Goschnick, J. Loboda-Cackovic, M. Grunze, W. N. Unertl, J. H. Block, *Surf. Sci.*, **182** (1987) 489.

[83] P. J. Schmitz, W. Y. Leung, H. C. Kang, P. A. Thiel, *Phys. Rev. B*, **43** (1991) 8834.

[84] P. J. Schmitz, H. C. Kang, W. Y. Leung, P. A. Thiel, *Surf. Sci.*, **248** (1991) 287.

[85] P. Kaukasoina, M. Lindroos, O. L. Warren, P. A. Thiel, *Surf. Sci.*, **318** (1994) 243.

[86] M. Vos, I. V. Mitchell, *Phys. Rev. B*, **45** (1992) 9398.

[87] J. A. Nieminen, *Phys. Rev. Lett*, **74 (19)** (1995) 3856.

[88] P. Dolle, R. Baudoing-Savois, M. De Sanits, M. C. Saint-Lager, M. Abel, J. C. Bertolini, P. Delichere, *Surf. Sci.*, **518** (2002) 1.

[89] Y. Robach, M. Abel, L. Porte, *Surf. Sci.*, 526 (2003) 248.

[90] D. S. Martin, N. P. Blanchard, P Weightman, *Phys. Rev. B*, **69 (11)** (2004) 113409.

[91] L. A. Kibler, M. Kleinert, V. Lazarescu, D. M. Kolb, *Surf. Sci.*, **498** (2002) 175.

[92] R. C. Jacklevic, *Phys. Rev. B*, **27**(1983) 3308.

[93] Y. Kuk, L. C. Feldman, P. J. Silverman, *Phys. Rev. Lett.*, **50** (1983) 511.

[94] C. Baddeley, C. J. Barnes, A. Wander, R. M. Ormerod, D. A. King, R. M. Lambert, *Surf. Sci.*, **314** (1994) 1.

[95] Y. Matsushita, K. Yagi, T. Narasura, G. Honjo, *Jpn. J. Appl. Phys. Suppl.*, **2 (1)** (1974) 567.

[96] H. R. Gerberich, N. W. Cant, W. K. Hall, *J. Catal.*, **16** (1970) 204.

[97] H. R. Gerberich, W. K. Hall, *Nature*, **213** (1967) 1120.

[98] N. F. Mott, H. Jones, '*Theory of the Properties of Metals and Alloys*' (OUP, London, 1936) Chapter 6.

[99] A. Couper, D. D. Eley, *Disc. Farad. Soc.*, **8** (1950) 172.

[100] L. Whalley, D. H. Thomas, R. L. Moss, *J. Catal.*, **22** (1971) 302.

[101] J. A. Nicholson, J. D. Riley, R. C. G. Leckey, J. G. Jenkin, J. Liesegang, *J. Electron Spectrosc. Related Phenomenon.*, **15** (1979) 95.

[102] S. Xinyin, D. J. Frankel, J. C. Hermanson, G. J. Lapeyre, R. J. Smith, *Phys. Rev. B*, **32** (1985) 2120.

[103] K. M. Sancier, S. H. Imani, *J. Catal.*, **11** (1968) 135.

[104] Y. L. Lam, M. Boudart, *J. Catal.*, **55** (1977) 530.

[105] Y.Robach, M.Abel, L. Porte, *Surf.Sci.*, **314** (1994) 1.

2 EXPERIENTAL: SURFACE SCIENCE TECHNIQUES

2 EXPERIMENTAL: Surface Science Techniques

This chapter comprises an overview of the surface analytical techniques and apparatus that were used to obtain the experimental data shown in the following chapters. The many techniques available to the surface scientist have been developed progressively over the past forty years. No technique by itself can characterise a surface's structure and reactivity completely. However, when combined they are capable of giving useful information on surface and adsorbate structure, electronic and physical properties, oxidation states and chemical composition. Many techniques are spectroscopic in nature. Some rely on absorption and emission of fundamental particles such as atoms, charged ions, electrons and electromagnetic radiation. Others monitor adsorption and desorption of molecules involved in chemical reactions on the surface.

2.1 Reactions using Molecular Beams

2.1.1 Introduction to Molecular Beams

Molecular beams are an important means of investigating surface-adsorbate structure and reactivity. As a form of surface science experimentation, a beam is significant because it probes surfaces as part of the surface phenomenon itself. Effusive beams were first developed in 1911 by Dunnoyer using sodium atoms [1], and beams were first used on gas-surface systems four years later [2,3]. Gerlach and Stern developed a more comprehensive molecular beam methodology in the 1920's [4]. Today the method is

capable of determining microscopic features of surface reactions [see for instance 5-7]. Molecular beams consist of well defined, narrow, straight beams of atoms or molecules aimed at a crystal sample. In ultra-high vacuum conditions, the molecules in the beam can propagate without interacting with each other [8]. The quantum (translational, rotational and vibrational) states of beam molecules colliding with a surface will affect the nature of adsorption and surface reaction. Thus molecular beams are used to investigate surface reaction kinetics including sticking probabilities and activation energies of adsorption. Changing the direction of molecular beams can be difficult [8]. Like scanning tunnelling microscopy, molecular beams interact with the outermost surface layer only: they are thus very surface specific and are usually used on very well prepared surfaces. Compared to direct dosing for temperature programmed desorption, beams allow more control over dosing with respect to collision rate and spatial distribution [8,9]. Hence more accurate adsorption and reaction data can be obtained, even at temperatures higher than normal molecular desorption.

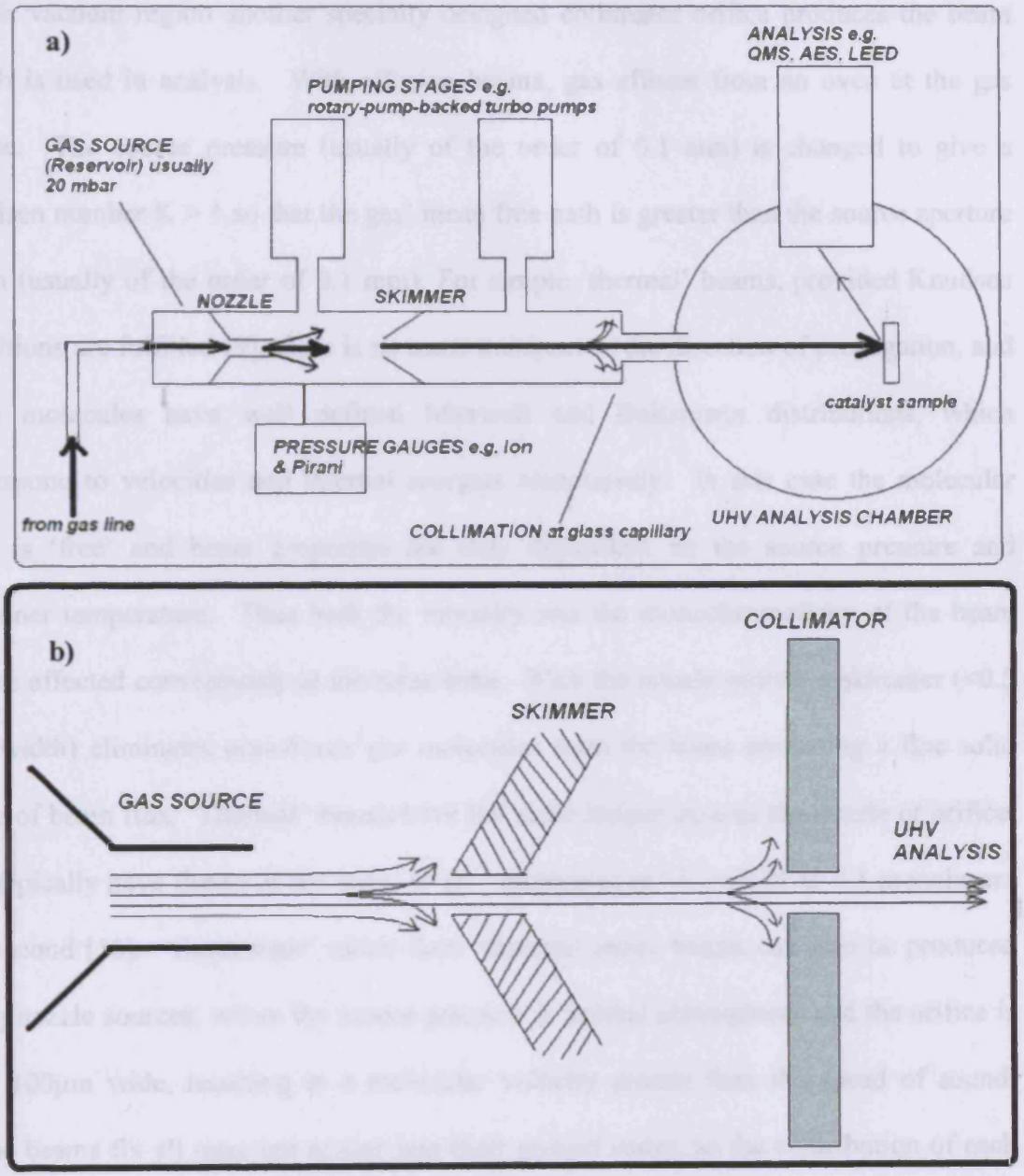

Fig 1: Schematic diagram of the apparatus used in a molecular beam system. (a) indicates the three chamber enclosure and the differentially pumped stages between the nozzle and skimmer. (b) indicates the collimation process which helps to define the beam by backscattering many incoming molecules from the gas line.

There are two classes of molecular beam: the effusive and nozzle sources. Fig. 1 shows a diagram of the typical molecular beam setup: a source container with an aperture or nozzle of specific dimensions through which molecules effuse into an evacuated region.

In this vacuum region another specially designed collimator orifice produces the beam which is used in analysis. With effusive beams, gas effuses from an oven at the gas source. The source pressure (usually of the order of 0.1 atm) is changed to give a Knudsen number K > 1 so that the gas' mean free path is greater than the source aperture width (usually of the order of 0.1 mm). For simple 'thermal' beams, provided Knudsen conditions are fulfilled [9], there is no mass transport in the direction of propagation, and these molecules have well defined Maxwell and Boltzmann distributions, which correspond to velocities and internal energies respectively. In this case the molecular flow is 'free' and beam properties are only dependent on the source pressure and container temperature. Thus both the intensity and the monochromaticity of the beam can be affected conveniently at the same time. With the nozzle source, a skimmer (<0.5 mm width) eliminates out-of-axis gas molecules from the beam producing a fine solid angle of beam flux. 'Thermal' beams have the same temperature as the nozzle or orifice, and typically have fluxes of the order of 10^{18} molecules m^{-2} s^{-1} = 0.01 to 0.1 monolayers per second [10]. 'Supersonic' rather than 'thermal' mode beams can also be produced using nozzle sources, where the source pressure is several atmospheres and the orifice is only 100μm wide, resulting in a molecular velocity greater than the speed of sound. These beams fix all quantum modes into their ground states, so the contribution of each mode to surface kinetics can be investigated [9,10]. They are often called 'cold' beams as their Maxwell-Boltzmann velocity distributions are very sharp and occur at a low temperature due to cooling on gas expansion, as shown in Fig. 2. 'Supersonic' beam fluxes are several orders of magnitude higher than those of 'thermal' beams. However,

only 'thermal' nozzle beams were used during the course of the experiments described in the following chapters.

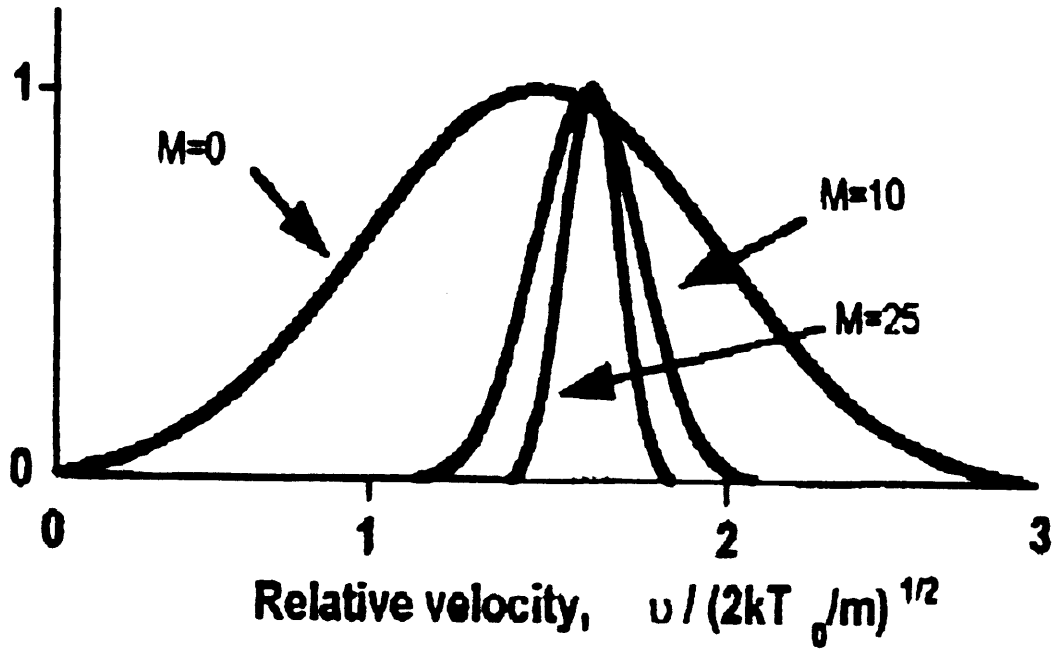

Fig. 2: Comparison of velocity dependence of velocity distributions of thermal and supersonic beams. M represents the 'Mach' number. Supersonic beams give high velocities with low velocity spreads [14].

2.1.2 Principles of Molecular Beam Experiments

The effect of Knudsen number on gas flow is shown in Fig. 3. At low source pressure, the source conductivity is constant, the flow is molecular (Knudsen flow, K >1) and beam flux is proportional to source pressure (P). At high source pressure where K<1, the flow is considered viscous, intermolecular collisions occur, the source conductivity now depends on pressure, and flux is now proportional to P^2. In the transitional region K lies between 0.01 and 1 and flow is a combination of the molecular and viscous regimes. In all these experiments the flow was of the molecular (Knudsen) type.

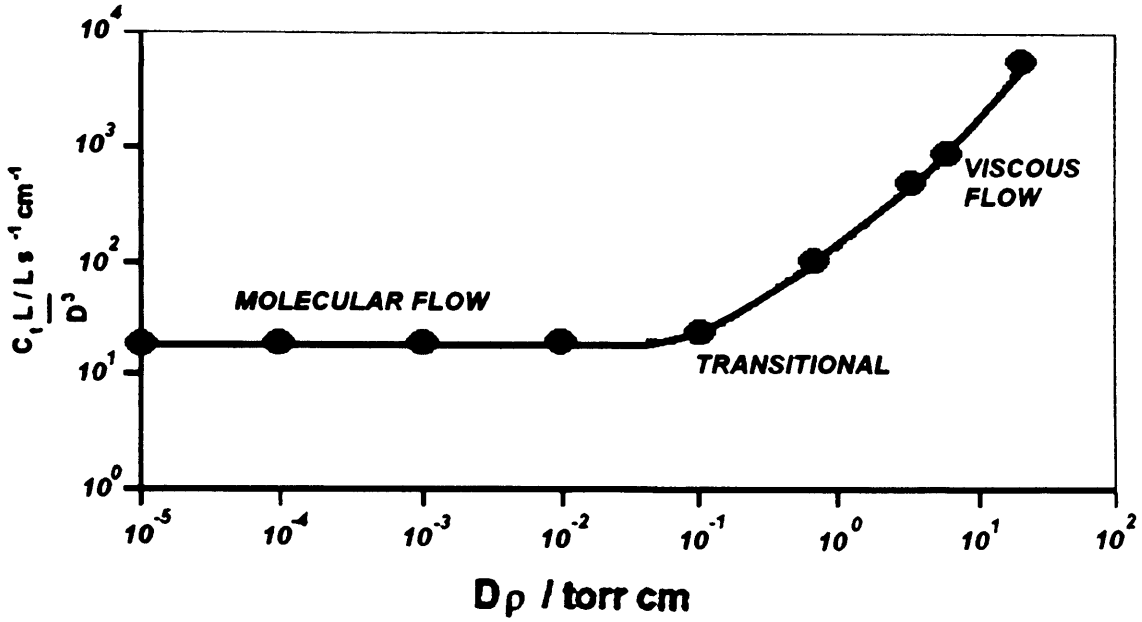

Fig. 3: Conductance dependence of average pressure across a capillary showing a constant value across the molecular flow region. Beam flux is proportional to the product of pressure and conductance [42]

In order to obtain good sticking measurements for varying surface coverage, it is essential that the molecular beam has a well defined solid angle of flux i.e. a sharp umbra (a few mm wide) of constant flux and a small penumbra where the flux falls off with increasing distance from the umbra as shown in Fig. 4. If the penumbra is too large (approximately greater than or equal to half the umbra width) then sticking measurements may not be accurate enough. The penumbra can be minimised by i) reducing the ratio of collimator-sample and source-sample distances or ii) reducing the nozzle or source aperture width. Thus it is important to have a good beam design, and to keep the sample as close to the collimator as possible.

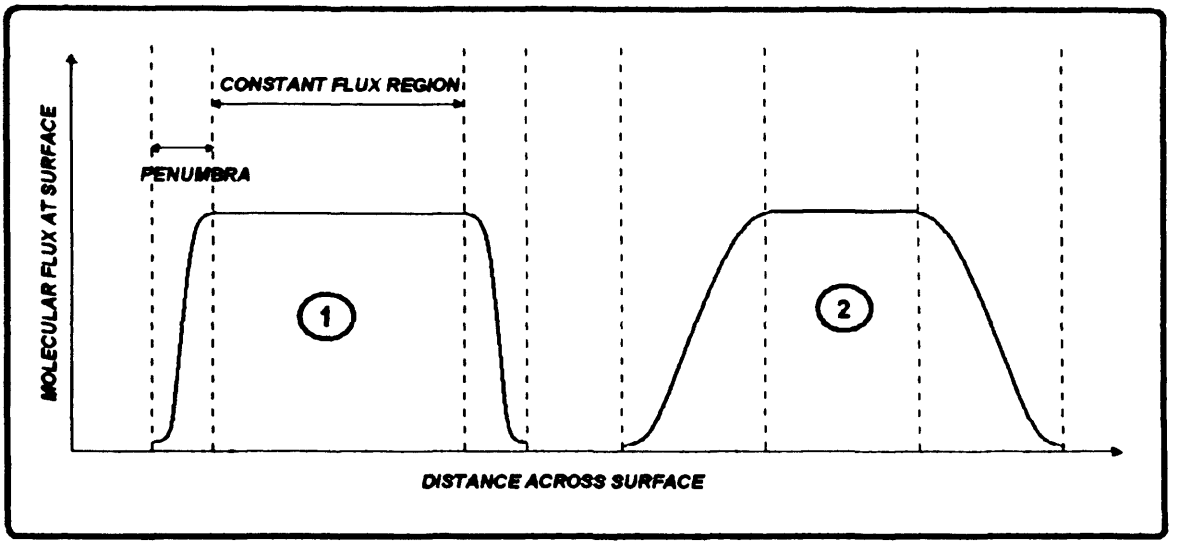

Fig. 4: Umbra and penumbra distances vs. flux for two different beams. Beam 1 would give more precise data, as its penumba:umbra ratio is significantly smaller.

2.1.3 Sticking Probability Measurements

Sticking Probability (S) is the tendency of a particular surface type to adsorb a particular incident molecule type. S also depends on a variety of additional factors, including the surface coverage and temperature and excitation of the particles' quantum (translational, vibrational, rotational) modes.:

$$S = \frac{\text{Rate of adsorption of molecules by the surface}}{\text{Rate of collision of molecules with the surface}}$$

If no incident particles stick, then S = 0, if every colliding particle adsorbs, then S = 1. Fig. 5 shows a sticking probability measurement obtained using a molecular beam reactor using the King and Wells chamber and beam flag technique [11,12]. The infinitesimally short changes between P_1 and P_2 are due to the beam being turned 'on' and 'off' by

manipulation of a flag between the skimmer and collimator. The curved red line shows the time dependent pressure P(t) of the particular incident molecule type. Hence the surface behaves as a pump, as some of the molecules adsorb to the surface and are removed from the chamber pressure. The integral of the shape in Fig. 5 gives the net amount of molecules entering the analysis chamber from the molecular beam over the course of the experiment. The integral of the shape in Fig. 6 b) shows the net number of molecules adsorbed to the surface during the experiment. For a simple reaction of type $X(g) \rightarrow X(a)$, this information can thus be converted to a more useful plot of sticking probability against surface coverage by the following equations [9]:

$$S(t) = \{P_2 - P(t)\}/\{P_2 - P_1\} \qquad (2.1)$$

$$\text{Surface coverage} = \theta(t) = N\int S(t)\,dt \qquad (2.2)$$

Where θ (t) is the surface coverage, N is the beam flux in molecules cm^{-2} s^{-1}. This information can then be converted to a plot of S versus coverage which can give information on the nature of the adsorption mechanism as shown in Fig. 6. This information allows adsorption trends of surface temperatures or molecule and/or surface types to be compared. In cases where there is an activation barrier to adsorption, S will be small. By varying the beam temperature, the value of this activation barrier, which may arise from the cleavage of bonds in the incident molecules, can be calculated. However, for all molecules investigated in the following chapters, the sticking

probabilities were sufficiently high to be measured at beam temperatures of about 298 K, and the effect of other beam temperatures on S was not investigated.

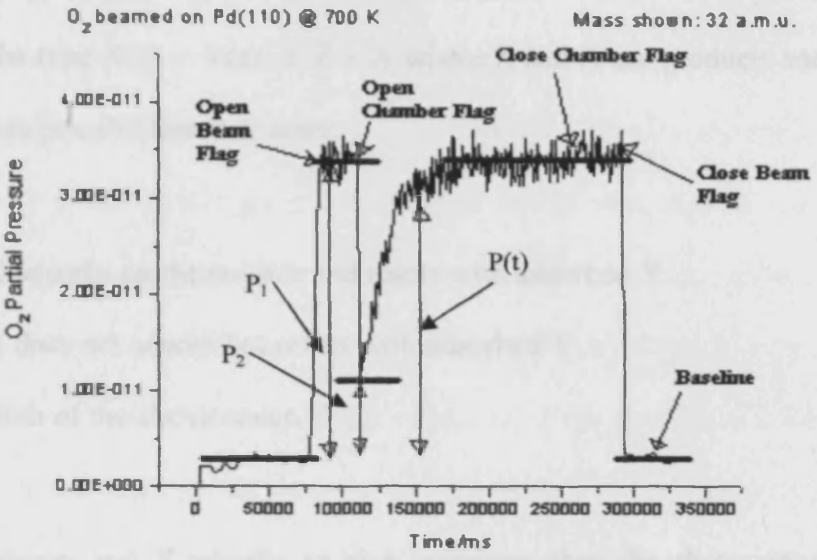

Fig. 5: A Typical raw data curve for oxygen sticking to clean Pd (110) at 700 K. The source pressure is 20 mbar.

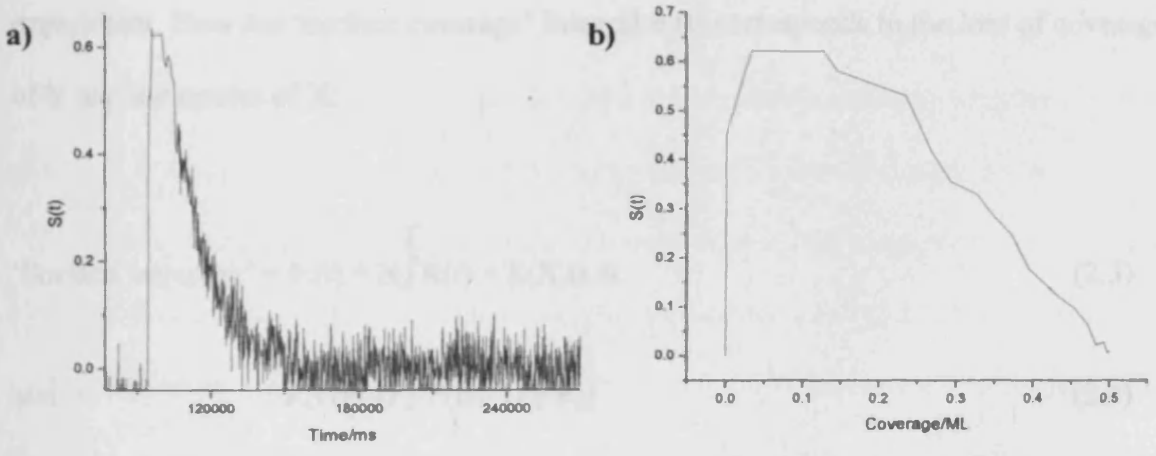

Fig. 6: a) an S(t) vs. time curve derived from Fig. 5 and Eqn. (2.1). b) an S(t) vs. coverage curve derived from Fig 6 a) and Eqn. (2.2). Fig. 6 b) gives the most useful information about the adsorption kinetics of the molecule under these conditions.

Molecular beams can also be used to investigate reactions between adsorbing molecules, either by i) preadsorbing known coverages of one reactant then beaming with another, or ii) by simultaneously beaming reactants that are already mixed in the gas line. In both cases, the rate of adsorption of starting molecules and emission of products can be monitored by quadrupole mass spectrometry (see Section 2.3). Thus, for a more complex reaction of the type X(g) + Y(a) → Z + A where Z and A are products and X and Y are reactants, three possibilities may arise:

i) X adsorbs on the surface and reacts with adsorbed Y.

ii) X does not adsorb but reacts with adsorbed Y

iii) Both of the above occur.

If i) or iii) occur, and X adsorbs to high coverage, then the above equations have to change to account for the additional uptake of X onto the surface at the end of the experiment. Now the 'surface coverage' integral θ (t) corresponds to the loss of coverage of Y and the uptake of X:

$$\text{'Surface coverage'} = \theta(t) = N\int R(t) + S(X,t)\,dt \qquad (2.3)$$

and

$$R(t) = \{P_2 - P(t)\}/\{P_2 - P_1\} \qquad (2.4)$$

Where R is the probability of X reacting with Y (on the preadsorbed surface), and S is the sticking probability of X (on the clean surface). The equation defining R(t) in terms of P

still holds, but θ (X) is now dependent on both the reaction with Y, and S(X,t). This equation works in theory, but it is often difficult to resolve the two processes sufficiently to use it in practice. The sticking curve shape gives an indication of the nature of the chemisorption occurring during adsorption. For example, precursor mediated adsorption has a characteristically high sticking probability due to the mobility of the precursor layer. A sticking curve would give a distinctive 'plateau' morphology with increasing coverage for this case. In the case of direct activated adsorption, the sticking probability is proportional to the coverage (or the square of the coverage if the adsorption is dissociative). Isothermal 'transient' measurements usually involve adsorption of a single beam of molecules onto a surface pre-dosed with another molecule type. The order in which the products are desorbed gives an indication of the strength of adsorption of each product. Also the integral of the product curves can give some information on the stoichiometric ratio of the products. Slopes of the curves give information on the rate of production at that temperature. Adsorption of a mixed beam of reactants can allow isothermal 'steady-state' measurements. For instance, both reactants could adsorb and introduce a transient region where the adsorption and desorption rates become constant and the coverages of the products and the reactants on the surface reach a steady state. These steady state processes can be repeated over several temperatures to determine a rate-temperature plot for the reaction, and measure true catalytic turnover, where it occurs. If the temperature is ramped while introducing a mixed beam to a surface, then the reaction will be continually perturbed. This 'pseudo-steady-state' process is generally more difficult to analyse than steady state measurements as it can contain transient

adsorption and desorption processes as well as reaction. However, it can achieve a rate-temperature relation much faster than via a steady-state measurement.

2.1.4 Temperature Programmed Desorption (TPD)

Temperature programmed desorption (TPD) is an invaluable technique for determining kinetic and thermodynamic parameters of desorption and decomposition. It is used on model and real catalysts to investigate both surface coverages of adsorbates and the strengths of surface-adsorbate interactions. Behaviour such as rate mechanisms and activation energies of desorption can be obtained. The methodology is shown in Fig. 7.

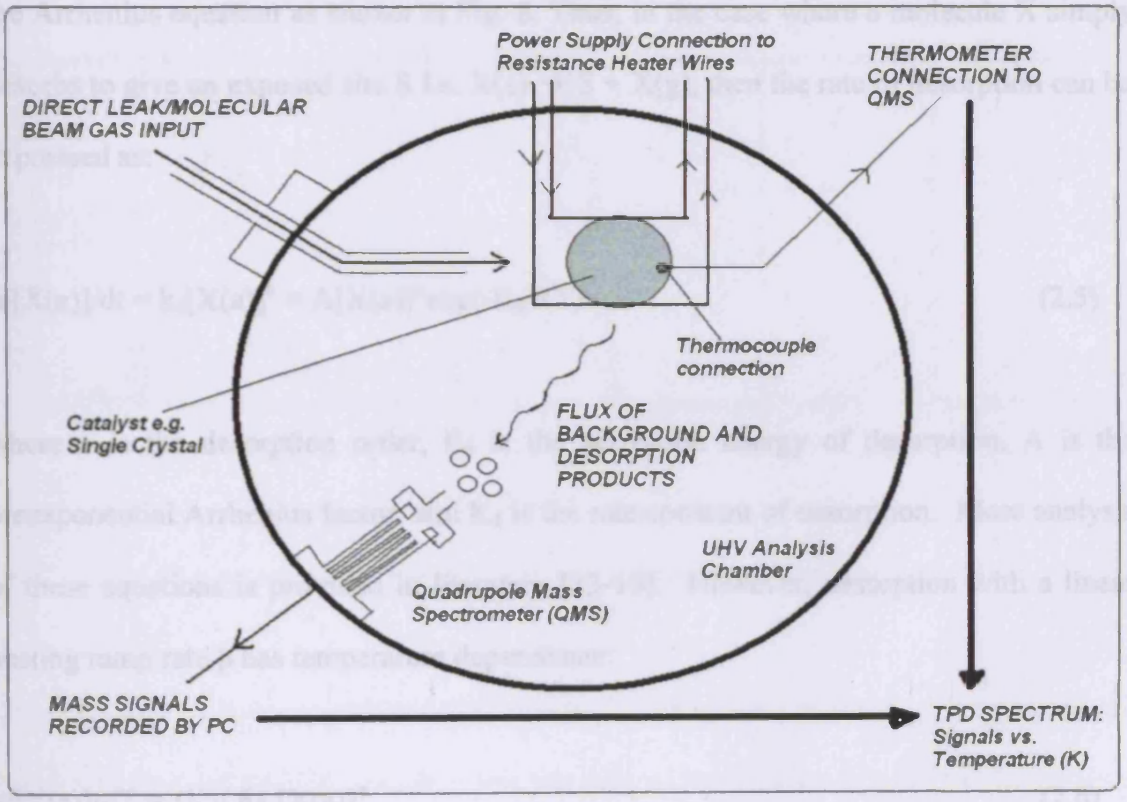

Fig. 7: Experimental apparatus for performing a TPD spectrum. Adapted from [10]

The sample is predosed with an exposure (measured in Langmuir, 1L = 1Torr s) of a molecule that is stable at the starting temperature. Thus the starting temperature is often below 273 K. A linear temperature ramp (usually between 1 and 100 Ks^{-1}) is then applied by measuring the amount of adsorbate desorbed vs. temperature. The amount of adsorbate desorbed can be measured in a variety of ways, but in these experiments it was monitored by ion pressure gauge and mass spectrometry. The temperature of evolution of desorbed species relates directly to their chemisorbed or physisorbed bond strength. Also, the temperature where maximum desorption occurs (T_p) relates to the maximum desorption rate. This is because, despite there being an Arrhenius dependency between desorption rate and temperature, surface coverage is also a factor and is convoluted with the Arrhenius equation as shown in Fig. 8. Thus, in the case where a molecule X simply desorbs to give an exposed site S i.e. $X(a) \rightarrow S + X(g)$, then the rate of desorption can be expressed as:

$$-d[X(a)]/dt = k_d[X(a)]^n = A[X(a)]^n \exp(-E_d/RT) \qquad (2.5)$$

where n is the desorption order, E_d is the activation energy of desorption, A is the preexponential Arrhenius factor, and K_d is the rate constant of desorption. More analysis of these equations is provided in literature [13-15]. However, desorption with a linear heating ramp rate β has temperature dependence:

$$-d[X(a)]/dT = \{K_d/\beta\}.[X(a)]^n \qquad (2.6)$$

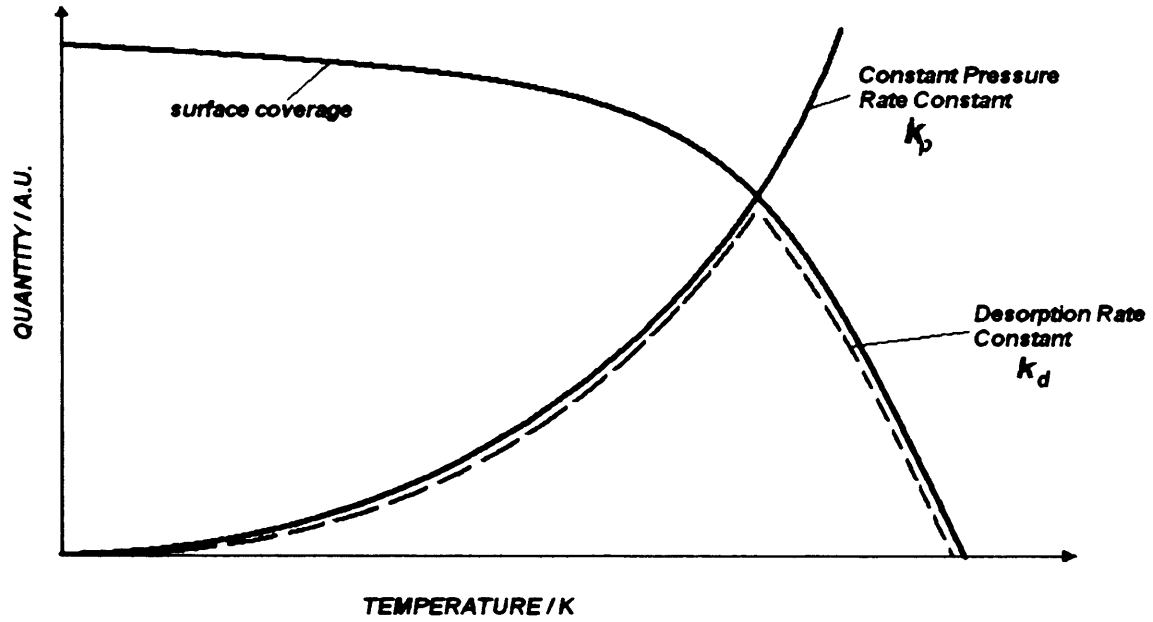

Fig. 8: A typical TPD profile showing the convolution of exponential and coverage contributions. Adapted from [10].

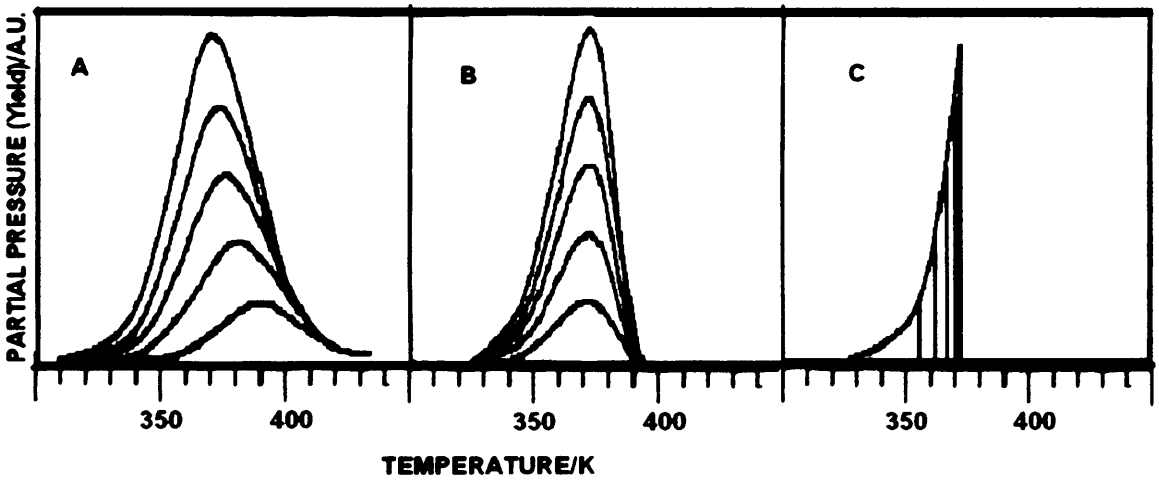

Fig. 9:Model second (A), first (B) and zeroth (C) order descompositions from a TPD.

If the analysis chamber is pumped sufficiently fast to remove products quickly then Eqn. 2.6 can be equated to P(X) which is the pressure of the product just above the surface-adsorbate layer. The order of desorption has an effect on desorption peak morphology as shown in Fig. 9 for three desorptions whose coverages are independent of E_a. Note the

variation in peak temperature with coverage for each desorption order type: this is direct consequence of desorption rate on N for a given value of n. In turn this is what affects peak shape for each order [16]. If there is a proportional Ea vs. coverage dependence, then a desorption that is first order with respect to coverage would resemble Fig. 9 c) rather than 9 b). More complex desorption peaks would have to be accounted for with more complicated E_a vs. coverage dependencies. Also, systems which show more complex desorption such as 'precursor state' adsorption behaviour do not undergo desorption in a single step and require more complex analysis to determine E_d. Other exceptional behaviour may arise due to multiple binding sites and coverage-dependent interactions between adsorbing molecules, as well as complex reactions occurring on the surface [10].

TPD can be used to investigate decomposition reaction mechanisms by monitoring the masses of several products at once by mass spectrometry, and this requires consideration of where products desorb with respect to temperature. This technique is often called temperature programmed reaction (TPR).

2.1.5 The Redhead Approximation

Differentiation of Eqn. F and setting the rate to zero for $T=T_p$ gives the following for a first order desorption:

$$\{E_d / RT_p^2\} = \{A/\beta\}. \exp(-E_d/RT_p) \qquad (2.7)$$

The ramp rate and T_p are easily obtained, and E_d can be found from an estimate of A (estimated at 10^{13} s^{-1} for first order desorptions [10]) or by an iterative process. As E_d and T_p are almost proportional to each other, it has been shown that Redhead's Approximation below is accurate to +/- 1.5 % when A/β lies within 10^8 and 10^{13} K^{-1}:

$$E_d = RT_p \ln (AT_p/\beta) - 3.46 \qquad (2.8)$$

This approximation is invaluable in simple determination of E_d in first order desorptions.

2.1.6 Surface Coverages from TPD

The area under a TPD desorption curve is directly proportional to the surface coverage, provided the pumping speed and other variables constant throughout the experiment. Thus relative surface coverages can be obtained for several TPD curves. Using LEED or AES for a known coverage with TPD data may help to provide absolute coverages using the following ratio:

$$\Theta = \frac{\text{(Integral of TPD curve with unknown coverage)} \times \theta}{\text{(Integral of TPD curve with known coverage)}} \qquad (2.9)$$

Where Θ is the absolute coverage to be determined, and θ is the absolute coverage for the system with the TPD curve of known coverage.

2.1.7 The Molecular Beam System

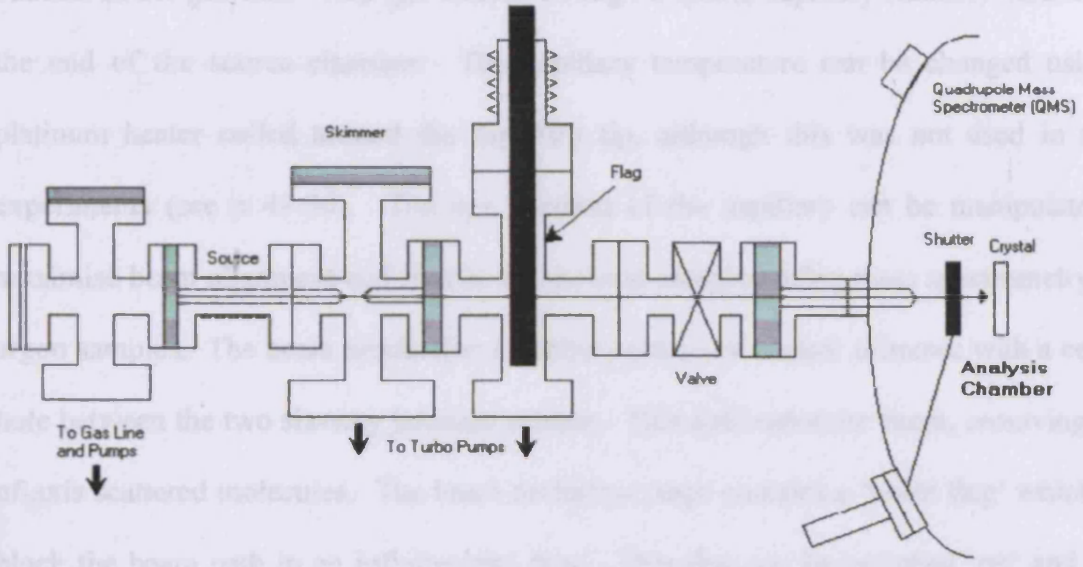

Fig. 10: Diagram of a flanged UHV enclosure housing the molecular beam system used in the experiments in this thesis. Adapted from work by M. Bowker.

The thermal, nozzle source molecular beam system described in Fig. 10 was designed and built by Dr. R. Bennett at Reading University and is based on earlier designs [9,11,17]. The beam housing comprises two stainless steel six way cross junctions and one four way cross junction (70 mm o.d. flanges). The four way cross is backed by an Edwards rotary pump and acts as a source chamber. One six way cross acts as a beam production chamber, the other six-way junction defines the beam. Both six way crosses are backed by Leybold turbomolecular pumps, which in turn are differentially backed by two Edwards rotary pumps. The pumping speed of the turbomolecular pumps has been calculated to be around 18 ls^{-1} [18]. The entire beam housing is bolted to the main chamber via a fast acting gate valve, allowing either region to be isolated from the other.

Gases entering the source chamber from the gas line were at a pressure of 20 mbar in all experiments. Gas can be stored in two glass reservoirs (5 L capacity) which also act as ballasts in the gas line. This gas effuses through a quartz capillary (nozzle) mounted at the end of the source chamber. The capillary temperature can be changed using a platinum heater coiled around the capillary tip, although this was not used in these experiments (see p 49-50). The xyz position of the capillary can be manipulated to maximise beam alignment and flux in the analysis chamber using mass spectrometry and argon samples. The beam production chamber contains a conical skimmer with a central hole between the two six-way junction crosses. This collimates the beam, removing out-of-axis scattered molecules. The beam definition stage contains a 'beam flag' which can block the beam path in an infinitesimal time. This flag can be switched 'on' and 'off' manually or by PC-controlled motors. Also in this stage a Pyrex tube acts as the final beam collimator. Its exit is 50 mm from the centre of the analysis chamber and the crystal sample. An ion gauge is also placed in this section to measure the pressure in this region. The effective pressure of the gases at the crystal surface (20 mbar source) is thus between 10^{-7} and 10^{-8} mbar e.g. 3.5 x 10^{-8} mbar for Ar. In the main chamber, between the crystal surface and the Pyrex tube, is a 'chamber flag' which can block the beam directly in front of the crystal face. It is controlled in the same way as the 'beam flag', and permits measurement of the sticking probability of incident beams in terms of pressure, and its coverage dependence.

Beam intensity changes with source pressure for this system. The plot in Fig. 11 a) indicates that from about 0-33 mbar, the curve is linear and flow is of the Knudsen

(molecular) type. The source pressure decays with time as shown in Fig. 11 b). This decay is mass dependent, and shows an almost linear dependence. Fig. 12 shows the variation in beam flux (arbitrary units) with the square root of the reciprocal of atomic mass $(1/M)^{1/2}$ for four noble gases. The linear dependence between these two quantities at constant temperature agrees with the relationship described in the literature for molecular flow [14].

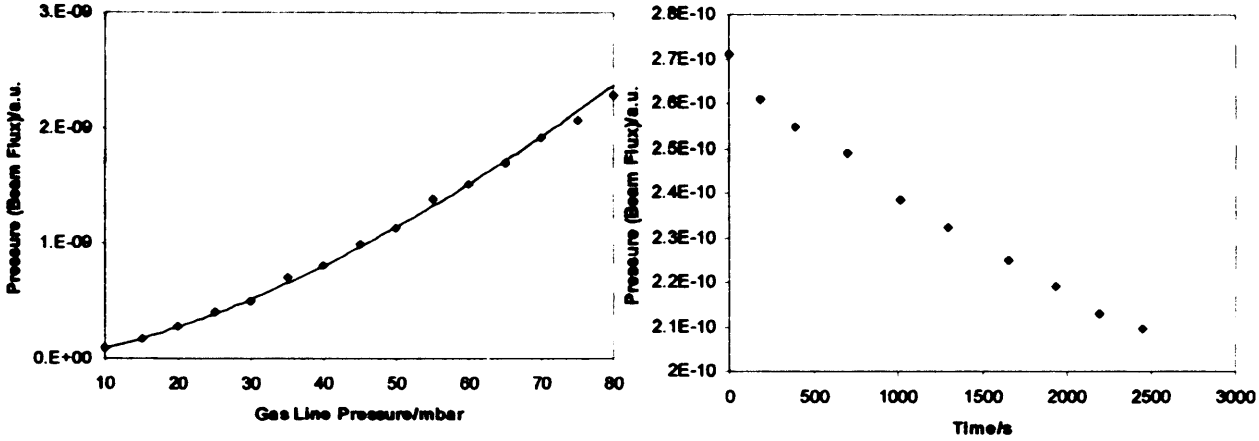

Fig. 10: a) The dependence of the beam flux as a function of source (gas line) pressure behind the capillary for a beam of argon. Pressure readings are accurate to +/- 0.5 mbar. b) The decay in source pressure with time for a 20 mbar argon beam.

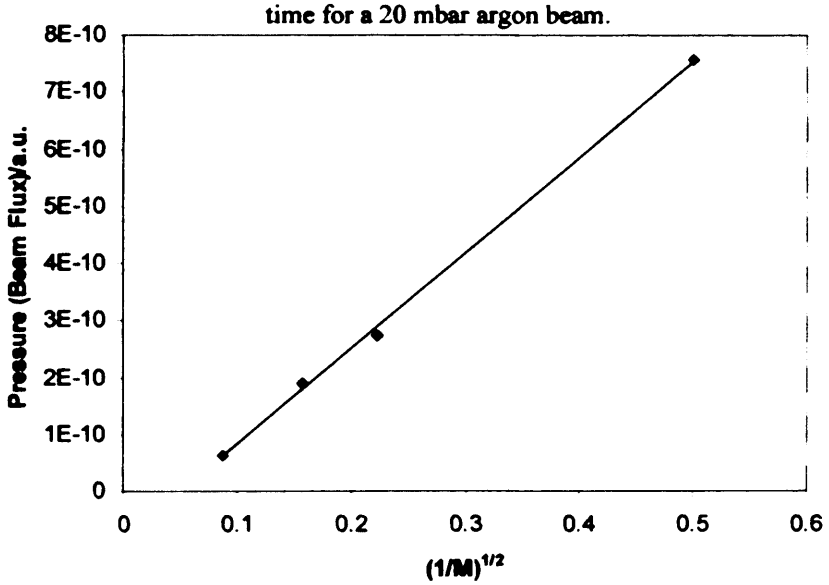

Fig. 11: The dependence of the initial beam flux on RMM in accordance with the literature [14] for Helium (mass 4), Neon (mass 20), Argon (mass 40) and Xenon (mass 131). The line of best fit is shown.

2.2 The Analysis Chamber

The experimental apparatus has been described previously in literature [19]. The analysis chamber is kept under ultra-high vacuum (UHV) and is pumped continuously using an oil diffusion pump and a Leybold turbomolecular pump. These pumps are both backed by Edwards rotary pumps. A Thermovacuum Generators titanium sublimation pump is also used to obtain base pressures below 1 x 10^{-10} mbar. The analysis chamber and molecular beam system are shown in Fig. 13. The main chamber has a Thermovacuum Generators reverse-view analyser used for low energy electron diffraction (LEED) and Auger electron spectroscopy (AES); a PSP argon bombardment ion gun (ISIS 3000) with fine leak valves; and a Hiden residual gas analysis quadrupole mass spectrometer (RGA-QMS) controlled by an RM personal computer used for molecular beam spectroscopy (MBS) and temperature programmed desorption (TPD) experiments.

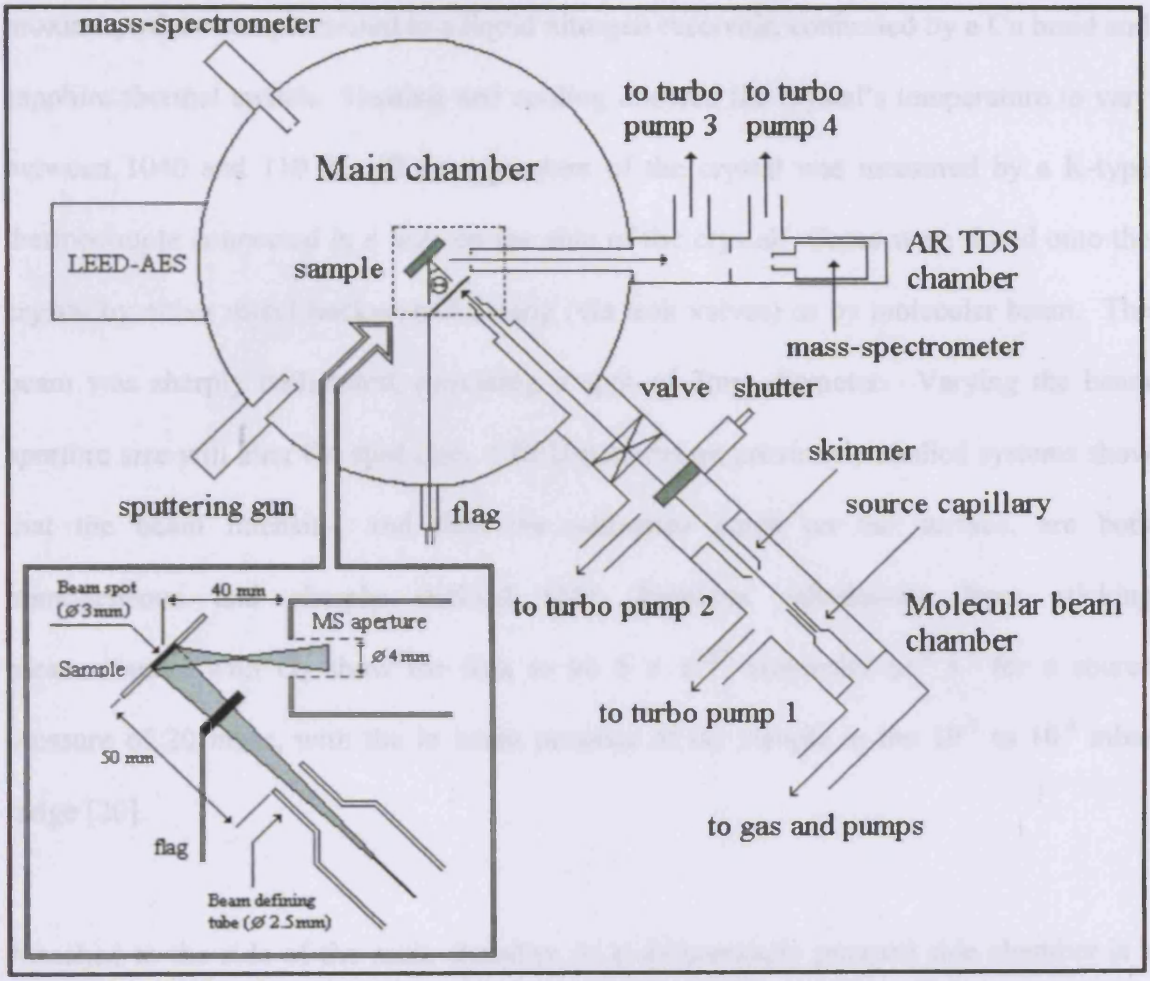

Fig. 13: Overview of the angle resolved analysis chamber and molecular beam system used during the experiments in this thesis.

The Pd (110) crystal is mounted centrally in the chamber on a manipulator capable of moving in the xyz directions as well as meridinal and azimuthal axes. Both axes have stepper motors to allow automated angle resolved experiments. However, all experiments described here were performed using normal incidence to the molecular beam (for sticking experiments) or the mass spectrometer (for TPD). The crystal sample was supported by direct contact with two tungsten wires (0.15 mm diameter), which passed through grooves in the edge of the crystal and were resistance heated. The heating rate was set at $1Ks^{-1}$ for most experiments. Sample cooling was performed by close

proximity of the sample mount to a liquid nitrogen reservoir, connected by a Cu braid and sapphire thermal switch. Heating and cooling allowed the crystal's temperature to vary between 1040 and 110 K. The temperature of the crystal was measured by a K-type thermocouple connected in a hole on the side of the crystal. Gases were dosed onto the crystal by either direct background dosing (via leak valves) or by molecular beam. The beam was sharply collimated, providing a spot of 3mm diameter. Varying the beam aperture size will alter the spot size. LEED patterns on previously studied systems show that the beam intensity, and thus the adsorbate patch on the surface, are both homogeneous and sharply defined [18]. Previous calculations from sticking measurements with O_2 show the flux to be 6 x 10^{17} molecules m^{-2} s^{-1} for a source pressure of 20 mbar, with the in beam pressure at the sample in the 10^{-7} to 10^{-8} mbar range [20].

Attached to the side of the main chamber, in a differentially pumped side chamber is a PIC-QMS without line of sight to the sample. This is set at an angle of 45° to the molecular beam behind two collimators. This mass spectrometer is used for angle-resolved molecular beam experiments but was not used in the following experiments.

2.3 Quadrupole Mass Spectrometry (QMS)

Mass Spectroscopy is an analytical technique for the identification of ions by way of measuring their mass-to-charge (m/e) ratios. While, in optical spectroscopy frequency and intensity are the most important parameters, in mass spectroscopy the parameters

number four: mass, charge, velocity, and intensity. However, fundamentally, any mass spectrometer determines only the m/e ratio.

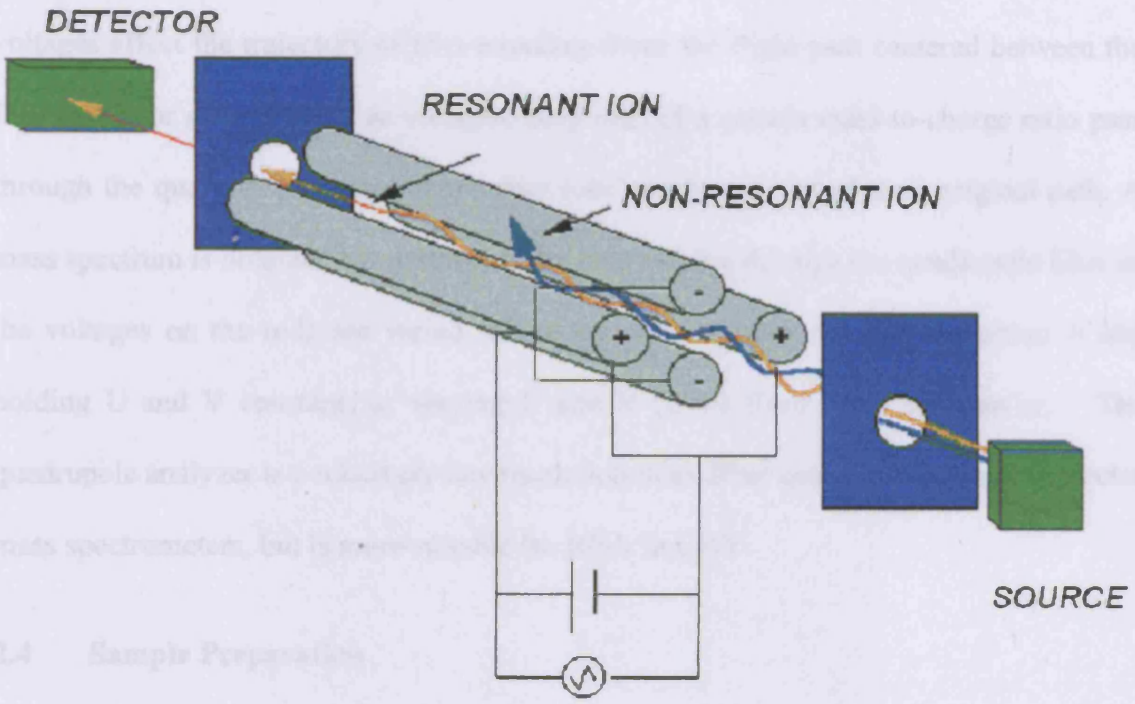

Fig. 14: A QMS analyser setup, showing two paths of incident ions – one with an (m/e) ratio allowing detection.

Mass spectrometers manipulate ionised gases with different masses and electric charges through specific spatial trajectories [21]. This is achieved in many ways, for instance, quadrupole mass spectrometry (QMS) uses an alternating E-field to separate ions by mass. QMS is a convenient method of mass spectrometry in UHV, and is especially convenient for RGA due to low cost and power requirements and ease of analysis. A QMS analyser is shown in Fig. 14. Quadrupole mass spectrometers consist of an ion source, ion optics to accelerate and focus the ions through an aperture into the quadrupole filter, the quadrupole filter itself with control voltage supplies, an exit aperture, an ion detector, detection electronics, and a high-vacuum system. A quadrupole mass filter

consists of four parallel metal rods arranged as in the figure above. Two opposite rods have an applied potential of (U+Vcos(wt)) and the other two rods have a potential of -(U+Vcos(wt)), where U is a dc voltage and Vcos(wt) is an ac voltage. The applied voltages affect the trajectory of ions traveling down the flight path centered between the four rods. For given dc and ac voltages, only ions of a certain mass-to-charge ratio pass through the quadrupole filter and all other ions are thrown out of their original path. A mass spectrum is obtained by monitoring the ions passing through the quadrupole filter as the voltages on the rods are varied. There are two methods: varying the phase w and holding U and V constant, or varying U and V (U/V) fixed for a constant w. The quadrupole analyzer is a relatively low resolution mass filter compared to magnetic sector mass spectrometers, but is more suitable for RGA in UHV.

2.4 Sample Preparation

The Pd (110) (5 N purity, Metal Crystals & Oxides Ltd.) surface was cleaned by cycles of Ar^+ bombardment ($1x10^{-5}$ mbar Ar, 500 eV, 6μA/cm^2, 30 min), annealing ($1x10^{-7}$ mbar O_2, 850 K, 20 min) and flashing (1020 K, 2 min) as documented elsewhere [19, 22-26]. The major elemental impurities in Pd(110), sulphur and carbon, were removed during the sputtering cycles. The absence of sulphur was determined by AES, but this was less useful for determining carbon contamination due to the overlap of C (KLL, 275 eV) and Pd (283 eV, MNN) Auger peaks. As an alternative, O_2 dosing, followed by TPD was used to check for the presence of CO and CO_2 in the desorption trace [27,28]. Also, CO TPD could be used for detecting C contamination through analysis of the α3 peak at low temperatures [29,30]. In addition, a sharp (1x1)-Pd (110) LEED pattern indicated a well-

ordered surface as shown in Fig. 15. For decomposition of C_2 and above organic molecules on Pd(110), surface carbon deposition was observed. This surface carbon was removed by annealing in $1x10^{-7}$ mbar O_2 at 500 K then flashing at 850 K after each C deposition.

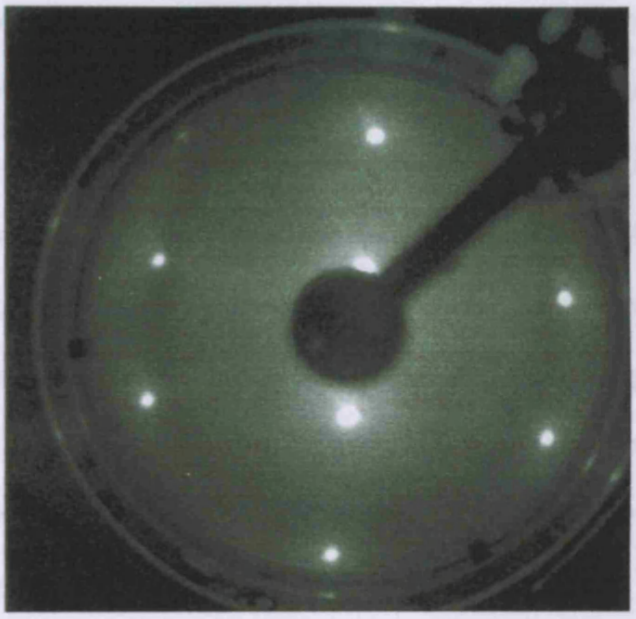

Fig. 15: LEED pattern for clean Pd (110) (1x1) observed at room temperature and at 58 eV beam energy.

2.5 Reactant Preparation

The gaseous chemicals used in these experiments: argon, oxygen, carbon monoxide, ethylene and ethylene oxide were used in lecture bottles provided by Argo Ltd, with purities of 99.999%, 99.6%, 99.5%, 99.5% and 99.9% respectively. The liquid chemicals used in these experiments: acetic acid, acetaldehyde and vinyl acetate were all of AnalR grade i.e. >99% purity. In spite of this, these samples contained trace impurities from isomerisation by exposure to UV radiation in sunlight. Thus they were in covered glass vials fitted with Youngs taps when used on the gas line, and below 273 K when in

storage. Before any experiment, liquid samples were subjected to rotary pumping and freeze-pump-thaw cycles to remove gaseous and high vapour pressure contaminants Samples were checked regularly by mass spectrometry for air leaks and isomerised contaminants (see Fig. 16 and Table 1). 'Multiplex' i.e. simultaneous monitoring of several masses by mass spectrometry was required for most TPD and MBS experiments. Often there is a large range of cracking fragments for reaction and/or decomposition of organic molecules. Thus, resolution of the products needs careful checking by consultation of mass spectrometry literature [31]. If reactants and products share the same cracking fragment masses, separation of the background of product masses from those of the reactants is required. The parent mass fragment, or fragment unaffected by product evolution is then normalized. This normalized value can then be used as a baseline for the fragment of interest. This baseline can then be removed from the recording trace to give a more useful reactant sticking curve.

Reactant Gas (RMM)	*Main Fragments (Highest first)*
ARGON (40)	*40, 20, 36, 38*
OXYGEN (32)	*32, 16*
CARBON MONOXIDE (28)	*28, 12, 16*
ETHENE (28)	*28, 27, 26, 25*
ACETIC ACID (60)	*43, 45, 60, 29, 42*
VINYL ACETATE (86)	*43, 15, 28, 27, 42*
ACETALDEHYDE (44)	*29, 44, 43, 42, 26*
ETHYLENE OXIDE (44)	*29, 44, 15, 14, 43*

Table 1: A list of the main fragments of interest during the studies of this thesis. The main fragments are listed, and several have to be monitored simultaneously to prevent confusion between molecules with the same RMM, as happens in the case of carbon dioxide, ethylene oxide and acetaldehyde.

2.6 Low Energy Electron Diffraction (LEED)

The first developments in this important aspect of surface crystallography took place in 1927 when Davisson and Germer diffracted electrons from 15-200 eV energy beams incident on nickel foil [32]. The process has been refined further [33] to produce a highly effective surface specific method of analyzing surface-adsorbate structure and ordering. Electrons interact strongly with the first 1-3 atomic layers but do not penetrate further significantly, having inelastic mean free paths of 5-20 Å. So electrons in a selected energy range of 20-1000 eV [10] are useful probes of crystal surface structure [34]. This is because their wavelengths, according to the de Broglie relationship:

$$\lambda = (150.6/E \text{ (in eV)})^{1/2} \qquad (2.10)$$

are similar in magnitude to the lattice spacing between atomic layers in most crystals (2.7 – 0.4 Å). Thus these electrons can be diffracted from regularly arranged crystals. Diffraction is possible via elastic back scattering from atoms parallel and perpendicular to the surface by momentum conservation. In regularly arranged crystals, scattering from each atom superposes to give large signals. For constructive interference diffraction in a one-dimensional lattice, this can be explained by the special case of the Bragg relationship for normal incidence:

$$\text{Path difference} = n\lambda = a \sin \theta \qquad (2.11)$$

Where λ is the electron de Broglie wavelength, a is the lattice constant, θ is the scattering angle from the surface normal and n is the order of diffraction (n= 0, +/- 1, +/- 2, +/- 3 etc.). Thus, the interference pattern consists of discrete diffracted beams of specific

scattering angles where interference is constructive. λ is constant for elastically scattered electrons of constant electron beam energy (so they are elastically scattered). The diffraction pattern will comprise lines of equal spacing perpendicular to the lattice. The lattice spacing is the reciprocal of the diffraction pattern line spacing. This can be deduced from the fact that $\sin\theta = n\lambda/a$.

LEED theory for 1-D and 2-D regularly arranged lattices can be explained either in terms of Bragg-like equations or reciprocal lattice (vector) analysis [14]. In the case of 2-D lattices, the latter method is more convenient to explain the phenomenon. It can be shown that an experimentally obtained LEED pattern is a scaled representation of the *reciprocal lattice* of the pseudo-2D surface structure of interest [14]. Laue's theory [35], based upon complex exponential phase factors, states that, for diffraction, the difference in the two wavevectors must be equal to a reciprocal lattice vector. Laue diffraction is shown in Fig. 17 for a 1-D array [35]. The Laue condition states that:

$$n\lambda = a(\sin\theta_n - \sin\theta_o) = a(X'_n - X_o) = a.\,\Delta S_n \qquad (2.12)$$

Where ΔSn is the path difference between the incident and scattered beams. The 2-D reciprocal lattice vector relating points in the reciprocal lattice can be expressed as:

$$G = pa_1^* + qa_2^* \qquad (2.13)$$

Where p and q are integers. The *reciprocal lattice* is defined by the reciprocal vectors $\mathbf{a}_1^*$,$\mathbf{a}_2^*$ for the substrate and $\mathbf{b}_1^*$,$\mathbf{b}_2^*$ for the adsorbate. Considering the simple case of the substrate alone, the reciprocal vectors are related to the real space unit cell vectors $\mathbf{a}_1$, $\mathbf{a}_2$ by the scalar product relations :

$\mathbf{a}_1 . \mathbf{a}_2^* = \mathbf{a}_1^* . \mathbf{a}_2 = 0$

$\mathbf{a}_1 . \mathbf{a}_1^* = \mathbf{a}_2 . \mathbf{a}_2^* = 1$

Thus $\mathbf{a}_1$ is perpendicular to $\mathbf{a}_2^*$, and $\mathbf{a}_2$ is perpendicular to $\mathbf{a}_1^*$. Also, there is an inverse relationship between $|\mathbf{a}_1|$and $|\mathbf{a}_1^*|$ where $|\mathbf{a}_1| = 1 / (|\mathbf{a}_1^*| \cos A)$, where A is the angle between the vectors $\mathbf{a}_1$ and $\mathbf{a}_1^*$ (similarly for $\mathbf{a}_2$ and $\mathbf{a}_2^*$). Analogous relations apply for the real space and reciprocal vectors of the adsorbate overlayer array: $\mathbf{b}_1$, $\mathbf{b}_1^*$, $\mathbf{b}_2$ and $\mathbf{b}_2^*$. If we apply a_1 and a_2 to the Laue condition and solve equation (2.12), then:

$$\Delta Sn = \lambda/|a| = \lambda (pa_1^* + qa_2^*) = \lambda G \qquad (2.14)$$

There is thus a relationship between the diffraction pattern and the surface reciprocal lattice. Also, the LEED pattern for a given surface structure may be obtained by superimposing the adsorbate reciprocal lattice (from $\mathbf{b}_1^*$ and $\mathbf{b}_2^*$) on the substrate reciprocal lattice (from $\mathbf{a}_1^*$ and $\mathbf{a}_2^*$). G-vector analysis can also predict the number and direction of the diffraction pattern for a given primary beam energy and angle of incidence [14].

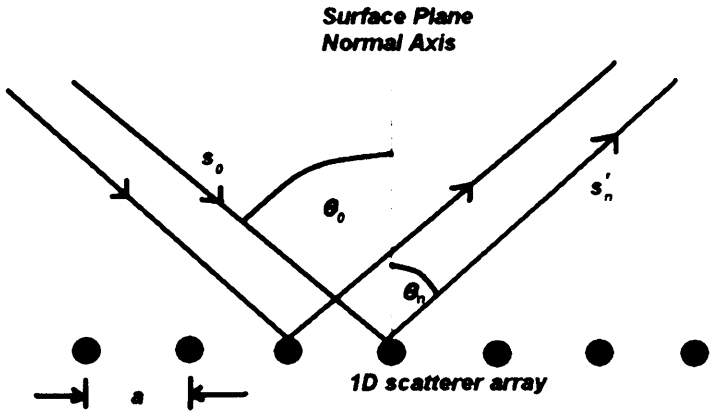

Fig. 17: Laue diffraction on a 2D model metal surface [35].

Typical LEED apparatus is shown in Fig. 18 (see page 72). The energy of the incident beam is varied between E = 0-1 keV. Beams are produced using an electron gun and are fired at the earthed sample. Backscattered electrons collide with a set of concentric grids around the gun. Backscattered electrons are either elastic (which form the diffraction pattern) or inelastic (not required, but constitute 99% of the total flux [36]). G4 is earthed, as is the innermost grid G1 to ensure that there are no E-fields in this region. So elastically scattered electrons are accelerated towards the phosphor detector S, which has a high positive potential of 5-6 keV. Thus the diffracted beams are energetic enough to induce fluorescence in S and give a highlighted diffraction pattern of bright spots. The inner grids, G2 and G3 are at a negative variable potential of the value –E +/- 0-10 V. These grids act as a filter to repel the inelastically scattered electrons which could otherwise obscure the LEED pattern. The diffraction pattern can be viewed by the naked eye, or camera to give recordable quantitative results. The relative spot positions give a direct indication of the 2-D ordering of the surface and adsorbate adlayer unit cells. The variation in spot intensities with beam energy give information on the surface geometry, such as bond lengths and angles of the surface and/or adsorbates. In these experiments, the relative positions of the spots were of more significance than the intensities of the diffraction spots, and in-depth quantitative analysis of intensities was not attempted.

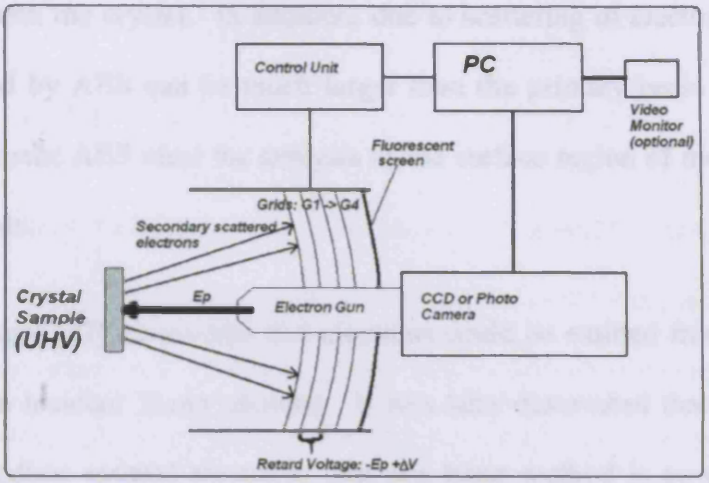

Fig. 18: LEED grids and electron gun for use in a UHV analysis chamber. Often these systems are combined with AES apparatus for use with the same phosphorescent screen and electron beam.

2.7 Auger Electron Spectroscopy (AES)

AES is a significant technique in characterizing surface chemical composition. Thus it can be used to quantify contamination and elemental ratios in surfaces. It has been called the most important surface analysis technique for conducting samples [36]. Auger electrons emitted in the Auger process are part of the secondary electron spectrum, and have characteristic kinetic energies that can be associated with specific atomic types. In the experiments described in the following chapters, AES was used to determine carbon contamination and buildup through organic molecule decomposition on Pd (110), as well as surface composition of Au:Pd alloy surfaces produced by metal vapour deposition (MVD). AES was chosen for these tasks partly because of its sensitivity: Auger electrons give information essentially on the first 2-10 atomic layers. Compared to emitted X-rays from electron bombardment, Auger electrons of kinetic energies less than 2 keV have a smaller escape depth of only a few monolayers. This is because of their larger ionization

cross section with the crystal. In addition, due to scattering of electrons, the size of the region analysed by AES can be much larger than the primary beam flux region itself. These factors make AES ideal for analysis of the surface region of model catalysts such as single crystals.

In 1923, P. Auger [37] discovered that electrons could be emitted from a gas sample by ionization from incident X-ray photons. It was later discovered that incident electrons would also produce emitted electrons, and this latter method is now called the Auger process. Nowadays, AES relies on a primary electron beam of 3-30 keV energy for ionization that can be focused using LEED optics. In one example four grids in the LEED optics are used as a Retarding Field Analyser (RFA) which acts as a high-pass filter, allowing only electrons of sufficient energy to overcome a retarding voltage to pass to the detector. On bombardment, primary, backscattered and characteristic Auger electrons are produced, along with X-rays that can also be useful for analysis. Auger processes are defined by three letters which give information on the energies of the core hole, the 'down' electron and the Auger electron respectively. For example, the Auger process is illustrated for a $KL_1L_{2,3}$ transition in Fig. 19 (see page 75). An incident electron excites a surface atom resulting in photoemission of a core electron, leaving a core level vacancy. This vacancy can be filled by a more weakly bound 'down' electron in a higher energy shell, releasing a quantum of energy ΔE. This quantum of energy can leave the atom as a photon – this phenomenon is known as X-ray fluorescence. However, in the Auger process, ΔE is transferred to another (Auger) electron which leaves the atom and is detected with a characteristic kinetic energy E_{kin}, which is expressed by:

$$E_{kin} = (E_K - EL_1) - (EL_{2,3} - \Phi) \quad (2.15)$$

Where Φ is the work function i.e. the minimum energy needed to expel an electron from the uppermost energy level in the solid to a region infinitely far away at zero potential energy. The first part of this equation is the energy available to the Auger electron from the 'down' electron and is the difference in binding energy between the core hole and the 'down' electron's initial energy level. The second half of the equation is the energy needed to overcome the potential barrier for Auger electron emission.

In the alternative to the Auger process, X-ray fluorescence, the release of a photon rather than an Auger electron produces a singly ionized ion from the original atom. The photon has energy E_K-E_{L1}. Thus, the Auger process is a more useful method of determining surface composition. It is often combined with LEED to obtain a complete picture of surface structure and chemistry. When a surface is bombarded by an electron beam in AES, there is a large secondary electron background: only a small fraction of secondary electrons are Auger electrons. Secondary electrons are produced by multiple collisions in solids, and can collide with other electrons, producing more secondary electrons with lower energies in a 'chain reaction'.

The energy distribution of the secondary electrons against energy constitutes an 'N(E)' curve [10,38]. Differentiation of this distribution to a dN(E)/dE curve is possible, and this overcomes the problem of the secondary electron background interfering with Auger signals. This is because the small Auger peaks are now more noticeable on the plot, and

their peak to peak height is directly proportional to the area under an N(E) curve. Thus 'peak to peak' heights can be used as a measure of surface concentration of a particular element, provided a suitable point of reference is available. This is discussed further in the section on Au:Pd alloy preparation, where 'peak to peak' height ratios were used to determine the composition of surface alloys. AES has a lot in common with X-ray photoelectron spectroscopy (XPS): the area under an N(E) curve gives an indication of surface concentration, and the energies of the curve peaks contain specific information on the chemical environment of the atoms. However, such quantitative analysis of oxidation states was not used significantly during the course of these experiments.

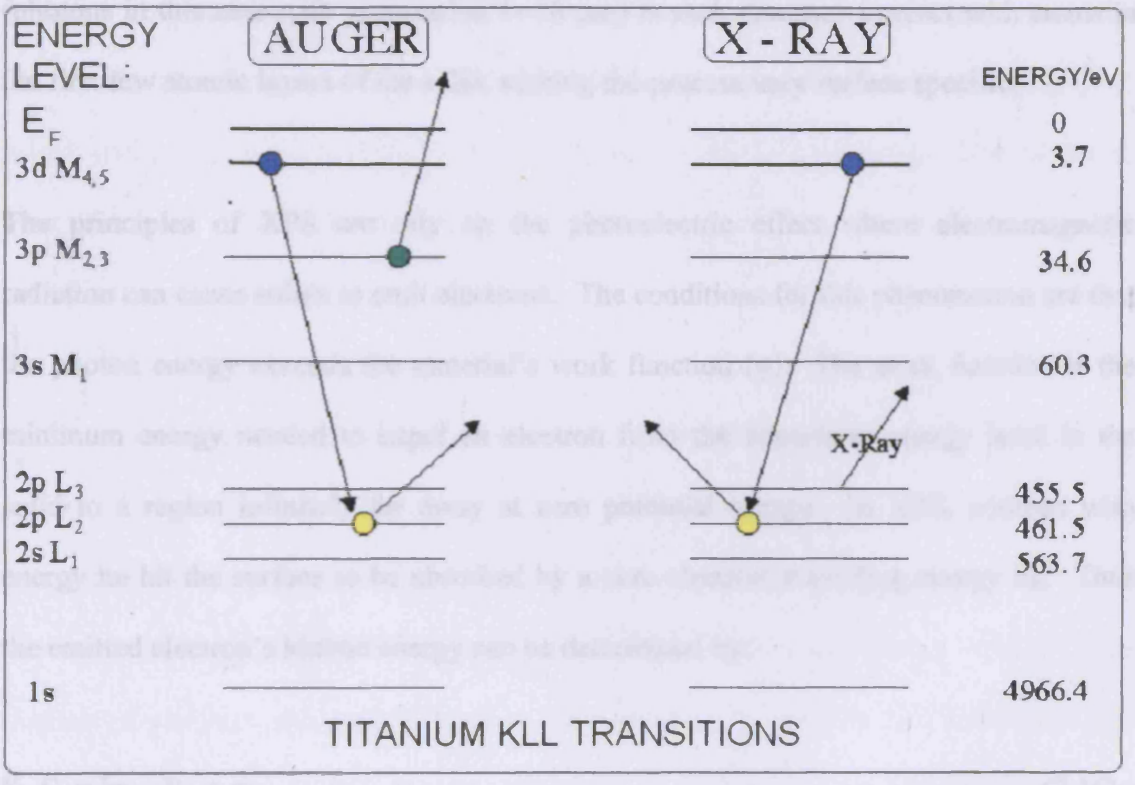

Fig 19 (left): An example KLL Auger process for a Ti atom. An electron with an energy specific to its previous orbital environment is expelled and analysed.

Fig. 20 (right): An example KLL XPS transition process for a Ti atom. X-Ray radiation is expelled and analysed. Its energy (frequency) gives an indication of the chemical environment of the atom.

2.8 X-Ray Photoelectron Spectroscopy (XPS)

A set of experiments were undertaken as an extension to the work on ethylene/Pd(110) systems with M. Bowker, A. McDowall and F. Grillo at Cardiff University. The results obtained contribute only a small part of the thesis but some basic information on the versatile technique of XPS is required. More detailed accounts are provided in the following literature [10,14,39,40]. Like AES, it allows understanding of the chemical composition and oxidation states involved in the surface-adsorbate region of a sample, as discovered by Siegbahn et. al. [41]. Like AES, the energy of the incident particles (photons in this case with penetration 1- 10 μm) is such that they interact with atoms in the first few atomic layers of the solid, making the process very surface specific.

The principles of XPS are rely on the photoelectric effect where electromagnetic radiation can cause solids to emit electrons. The conditions for this phenomenon are that the photon energy exceeds the material's work function (φ). The work function is the minimum energy needed to expel an electron from the uppermost energy level in the solid to a region infinitely far away at zero potential energy. In XPS, photons with energy hυ hit the surface to be absorbed by a core electron at binding energy E_B. Thus the emitted electron's kinetic energy can be determined by:

$$K.E. = h\upsilon - E_B + \varphi \qquad (2.16)$$

K. E. can be determined experimentally. The work function (φ) is generally calculated from system calibrations. Hence E_B is easily obtained and is measured from the Fermi level of the solid (the highest occupied energy level). Thus for a given $h\upsilon$ and E_B, electron photoemission is elementally specific, provided the core levels are well-defined. Generally E_B increases with atomic number Z. The photoemission process is shown schematically for a KLL transition in Fig. 20 (see page 75).

Note that in XPS, Koopmans' Theorem, which states that E_B is the same as the negative orbital energy of the photoelectron, does not generally hold. Koopmans' Theorem assumes that all other electrons in the system remain unchanged before and after photoemission. However, due to a 'relaxation shift' where electrons fall in energy to lower states to screen the hole created by photoemission, more energy is available to photoelectrons. This additional energy is not larger than a few eV, which means that orbitals can still be determined.

In XPS nowadays, the incident radiation usually consists of soft X-rays with $h\upsilon \approx 1.2 - 1.4$ keV from either a synchrotron radiation source or a Kα source (Al or Mg). Synchrotron sources allow a much larger variation in $h\upsilon$ from about 10 eV to 10 keV. An electrostatic energy analyser measures the electron energy distribution, which is the number of electrons detected N(E) as a function of K.E.. The analyser consists of two concentric hemispheres which have a potential between them and are isolated electrically. The analyser acts as an 'energy pass filter', allowing electrons with specific K. E. to enter

and be detected. Usually, XPS spectra are displayed as a function of E_B rather than K.E. to allow for simpler chemical identification.

Looking at E_B for the core levels of a surface-adsorbate species' atoms and molecules allows the chemical bonding of the system to be deduced. 'Chemical shifts' of 0-10 eV are variations in formal oxidation states that produce variation of the positions of XPS spectrum peaks. For instance, higher oxidation states produce peaks at higher binding energies. These 'shifts' give information on the chemical environments of a particular atom. The 'shifts' are very useful for analysing carbon species in the decomposition of organic molecules on surfaces, which may help in defining reaction intermediates.

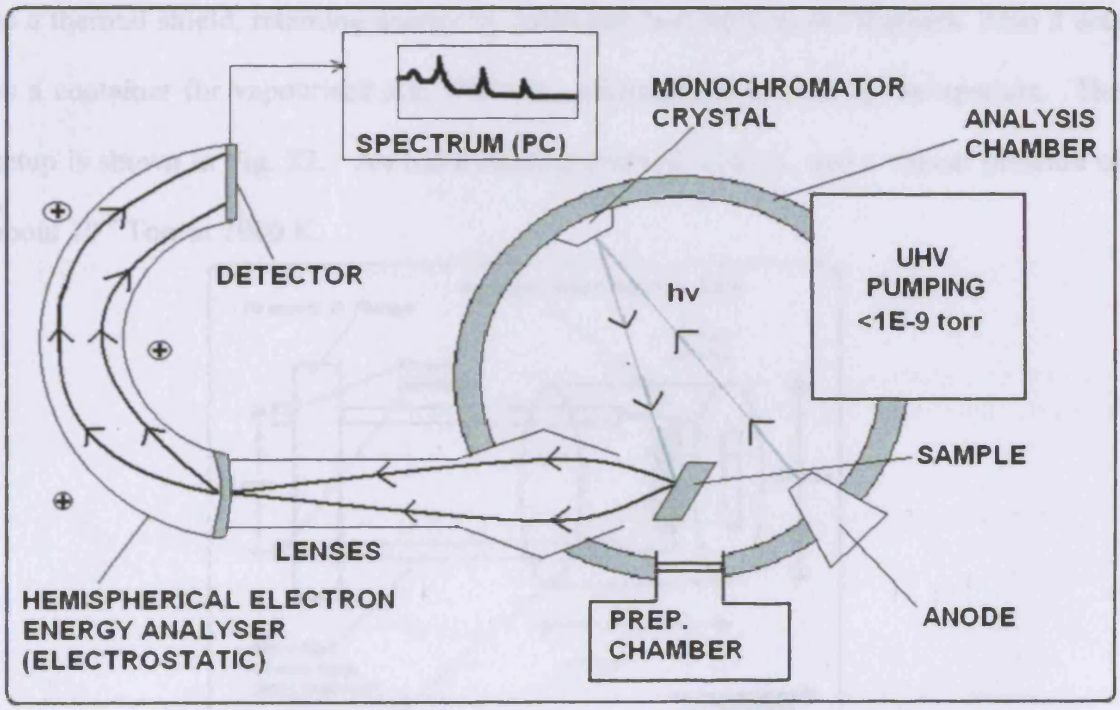

Fig 21: A typical XPS hemisphere analyser and apparatus.

A schematic of the apparatus used in XPS is shown in Fig. 21. The source used in the work in this thesis was a conventional monochromatic Mg Kα source with hυ = 1.2356 keV. The analyser was a conventional seven-channel analyser. The anode voltage was 15 keV, and the filament and emission currents were 4.7 A and 20 mA respectively.

2.9 Pd/Au Bimetallic Catalyst Preparation

To create the Au/Pd (110) model catalysts used in these experiments, Au was deposited via metal vapour deposition (MVD) from an in-house constructed Au evaporator, comprising an Au wire wound tightly round a W filament. The source is enclosed in a stainless steel cylindrical metal case with a rectangular aperture at one end. The case acts as a thermal shield, retaining energy by reflecting heat back to the filament. Also it acts as a container for vapourised Au, which is collimated to a beam by the aperture. The setup is shown in Fig. 22. Au has a melting point of 1340 K, and a vapour pressure of about 10^{-9} Torr at 1000 K.

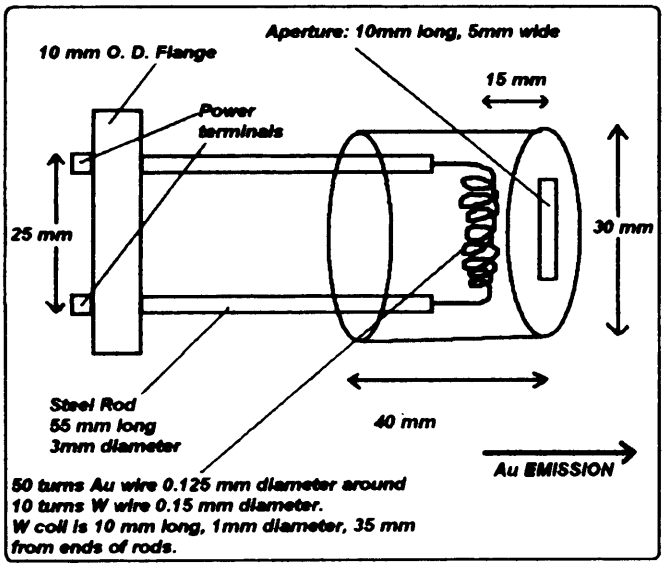

Fig.22: A diagram of a custom made MVD doser for gold.

REFERENCES:

[1] L. Dunnoyer, *Le Radium*, **8** (1911) 142.

[2] M. Knudsen, *Ann. Phys.* **48** (1915) 1113.

[3] R. W. Wood., *Philos. Mag.* **30** (1915) 300.

[4] O. Z. Stern, *Phys. 2* (1920) 49.

[5] J. T. Stuckless, N. Al-Sarraf, C. Wartnaby, D. A. King, *J. Chem. Phys.*, **99** (1993) 2202.

[6] B. Poelsema, S. T. de Zwart, G. Comsa, *Phys. Rev. Lett.*, **49** (1982) 578.

[7] M. Bowker, Q. Guo, Y. Li, R. W. Joyner, *Surf. Sci.*, **257** (1991) 33.

[8] G. Comsa, *Surf. Sci.*, **299** (1994) 77.

[9] M. Bowker, *Appl. Catal. A: General* **160** (1997) 89.

[10] G. Attard, C. Barnes, '*Surfaces*', p76, Oxford Chemistry Primers, OUP, (1998).

[11] D. A. King, M. G. Wells, *Surf. Sci.*, **29** (1972) 454.

[12] P Alnot, A. Cassuto, D. A. King, *Farad. Disc. Chem. Soc.*, **87** (1989) 219.

[13] S. L. M. Schroeder, M. Gottfried, '*Temperature Programmed Desorption and Thermal Desorption Spectroscopy*', (2002), Advanced Physical Chemistry Laboratory, FU Berlin.

[14] D.P. Woodruff, T. A. Delchar, '*Modern Techniques of Surface Science*', CUP, 2nd Edition, (1994).

[15] P. A. Redhead, *Vacuum*, **12** (1962) 203.

[16] M. Bowker, from '*Cohesion & Structure of Surfaces*' by K. Binder et.al., (1995) Elsevier.

[17] M. Bowker, D. A. King, *Surf. Sci.*, **94** (1980) 564.

[18] M. Bowker, P. D. A. Pudney, C. J. Barnes, *J. Vac. Sci. Technol.* A, **8 (2)** (1990) 816.

[19] M. Bowker, C. Morgan, J. Couves, *Surf. Sci.*, **55** (2004) 145.

[20] B. Klink, K. Lass, Internal Report, University of Reading

[21] See for instance (i) '*Mass Spectroscopy: Principles and Applications*', I. Howe, D. H. Williams, R. D. Bowden, McGraw-Hill, New York (1981) 2nd Ed., or (ii)B. Tissue, report on www.chem.vt.edu/chem-ed/ms/quadrupo.html (2000), or (iii) Anglo Scientific Instruments website at www.a-s-i.demon.co.uk.

[22] J. W. He, P. R. Norton, *Surf. Sci.*, **195** (1988) L199.

[23] M. Milun, P. Oervan, M. Vajic, K. Wandelt, *Surf. Sci.*, **211** (1989) 887.

[24] T. Matsushima, *Surf. Sci.*, **217** (1989) 155.

[25] M. Nishijama, J. Yoshinobu, T. Sekitani, M. Onchi, *J. Chem. Phys.*, **90** (1989) 5114.

[26] P. Hu, L. Morales de la Garza, R. Raval, D. A. King, *Surf. Sci.* **249** (1991) 1.

[27] R. D. Ramsier, Q. Gao, Neergaard Waltenburg, J. T. Yates Jr., *J. Chem. Phys.*, **100** (1994) 6837.

[28] T. Matsushima, K. Shobatake., Y. Ohno, K. Tabayashi, *J. Chem. Phys.*, **97** (1992) 273.

[29] J. Goschnick., M. Grunze, J. Loboda-Cackovic, J. H. Block, *Surf. Sci.*, **189** (1987) 137.

[30] J. Goschnick, M. Wolf, M. Grunze, W. N. Unertl, J. H. Block, J. Loboda-Cackovic, *Surf. Sci.*, **178** (1986) 831.

[31] See for instance '*Compilation of Mass Spectral data*', A. Cornu, R. Massot, London, Philadelphia-Heyden, (1979) 2nd Ed.

[32] C. J. Davisson., L. H. Germer., *Phys. Rev.*, **30** (1927) 705.

[33] E. J. Scheiber, L. H. Germer, C. D. Hartman, *Rev. Sci, Inst.*, **31** (1960) 112.

[34] Queen Mary University, London, Chemistry Department Website: http://www.chem.qmw.ac.uk/surfaces/scc/scat6_2.htm

[35] L. J. Clarke, '*Surface Crystallography: An Introduction to Low Energy Electron Diffraction*' Chester Wiley (1985) p6.

[36] J. Vickerman (Ed.), '*Surface Aanalysis: The Principal Techniques*', Wiley (1997).

[37] P. Auger, *J. Phys. Radium* **6** (1925) 205.

[38] C. L. Hedberg (Ed.), '*Handbook of Auger Electron Spectroscopy*', 3rd. Ed., Physical Electronics Inc., (1995).

[39] J. F. Moulder, W. K. Stickle, P. E. Sobel, K. D. Bomben, '*Handbook of X-Ray Photoelectron Spectroscopy*', Perkin-Elmer Corp., (1992).

[40] D. Briggs, M. P. Seah (Eds.), '*Practical Surface Science Analysis Vol. 1: Auger and X-Ray Photoelectron Spectroscopy*', Perkin-Elmer Corp., (1990).

[41] K. Siegbahn., '*ESCA: Atomic, Molecular and Solid State Structure studied by means of Electron Spectroscopy*' ,Almqvist & Wiksells, Uppsala, (1967).

[42] A. Roth, 'Vacuum Technology', A. Roth, North-Holland, 1976.

3 THE INTERACTION OF Pd (110) WITH O_2, ETHENE AND ACETIC ACID

3 INTERACTION OF Pd (110) WITH O_2, ETHENE AND ACETIC ACID

This chapter is concerned primarily with the interaction of the three starting materials for the heterogeneous ethene acetoxylation synthesis of VAM described in Chapter 1 i.e. oxygen, ethene and acetic acid. These molecules are relatively simple compared to VAM, and there is much literature on their interaction with Pd surfaces and nanoparticulate systems. On Pd (110), these molecules chemisorb and may decompose at higher temperatures in UHV to either recombine or give new products, some of which can be observed using QMS, LEED and/or AES. Chapter 4 uses the information described in this chapter to describe the interaction of the product VAM molecule with Pd (110). In addition, Chapter 4 considers the importance of two molecules that are found to have significance in the VAM decomposition: carbon monoxide and acetaldehyde. These two molecules are also by-products of industrial VAM synthesis.

3.1 Oxygen on Pd (110)

3.1.1 Introduction

Diatomic oxygen has been found to dissociate on all platinum group metals at room temperature [1,2]. Its relatively low gas phase dissociation energy (498 kJ/mol) means that, at room temperature, it will dissociatively adsorb on these surfaces, whereas CO, with a dissociation energy of 1076 kJ/mol does not [3]. On Pd (110), oxygen will adsorb molecularly at 120 K to give a pseudo-(2x1) adsorbate phase, and

begin to dissociate above 200 K [4,5]. The LEED pattern changes to an ordered c(2x4) on heating to 470 K. This structure can also be produced by dosing oxygen on clean surfaces above 280 K [6], and induces a (1x2) reconstruction in the Pd selvedge. It is the only oxygen structure formed under these conditions and corresponds to a saturation coverage of 0.5 ML (monolayers) [5, 7-10]. At 400 K, an additional (2x3) – 1D phase with a saturation coverage of 0.23 ML can be formed at low exposures [6, 11], reconstructing the Pd selvedge to (1x3) as determined by STM [7]. Dissociated surface oxygen can diffuse into the subsurface and bulk of Pd (110) and Pd (111) surfaces. This has also been observed for certain forms of surface carbon from decomposition of organic molecules described in this work, and has great significance to the findings of this thesis. Milun et al. [10], doing TPD experiments on the O_2/Pd(110) system showed two β-states of desorption at around 800 K arising from recombination of dissociated oxygen on the surface. The lower temperature state (β_1) was attributed to desorption of oxygen in the subsurface [4,12,13], and occurs at coverages exceeding 0.5 ML [14]. There is a tendency for more oxygen to enter the subsurface at low adsorption temperatures. Sticking experiments performed by Goschnick et al. on Pd (110) by measurement of backscattered surface molecules found that oxygen sticks well, with an S_0 of 0.86 +/- 0.03 at room temperature [5]. Molecular beam, XPS and TPD work on O_2/Pd (110) by Jones et al. determined S_0 to be 0.44 at room temperature, decreasing to 0.33 +/- 0.02 at 700 K, and found that greater desorption from the subsurface occurred at greater dosing pressures, and that diffusion into the subsurface accompanies surface Pd reconstruction with increasing temperature [15]. At temperatures below 300 K, the saturation coverage was deduced to be greater than 0.5 ML. The differences in S_0 between the findings of Goschnick et al. and Jones et al. are attributed to backscattering methods being less precise and

susceptible to variation in pumping speed, surface shielding by the mass spectrometer and changing oxygen-QMS sensitivity at high pressures. Most TPD spectra in the literature agree that the two β desorption states occur at around 690 and 770 K, with peak shapes implying second order desorption kinetics common with associative desorption [4,12,13,16]. The desorption energy of the β_2 peak by itself varies from 201 to 335 kJ/mol with decreasing coverage, as calculated by Ertl et al. [17]. However, by sticking and TPD analysis Yagi et al. [18] suggested first-order associative desorption kinetics, affected by lateral interaction and added-row reconstruction. Yagi et al. also suggested that the mechanism of dissociation was precursor-trapping, and that S_0 was independent of surface temperature. Junell et al., using MBSS (molecular beam surface scattering) experiments, determined that S_0 and the adsorption kinetics will depend strongly on translational energy: at low energies a strongly attractive molecularly chemisorbed precursor state occurs, at higher energies molecules tend to dissociate via a direct activated adsorption channel [19]. In contrast to Yagi et al., they found that S_0 decreases with surface temperature at low translational energies e.g. those associated with thermal beams. It would be of interest to perform thermal molecular beam sticking experiments for oxygen on Pd (110), to compare adsorption data with those of Yagi et al. and Junell et al. (see Section 3.1.2).

On the close-packed Pd (111) surface, oxygen TPD from dosing at 100 K shows four desorption states occurring at 125, 150, 200 and 800 K, and a saturation coverage of 0.62 ML [20]. The first three states are attributed to chemisorbed molecular oxygen: as with the Pd (110) surface, on Pd (111) O_2 dissociates above 200 K. The fourth (β) state is due to associative desorption of oxygen atoms [2]. Adsorption below 300 K

gives LEED structures of (2x2) at 0.25 ML and ($\sqrt{3}$x$\sqrt{3}$)R30° at 0.33 ML [21]. Above 300 K a (2x2) superstructure associated with the β states forms with a coverage of 0.25 ML [2,20,21]. This is the only structure forming under these conditions. Klotzer et al. found that adsorption below 0.25 ML coverage was precursor mediated, while above 0.25 ML it was activated with a change in surface phase, and indicated auto catalytic desorption kinetics [22]. Zheng et al. found that the oxygen coverage could be increased from 0.25 ML up to 0.37 ML above 500 K, and could be increased further using NO_2 as an oxidant [23]. At high temperatures (> 470 K) and pressures (> $1x10^{-4}$ Pa), in O/Pd(111), subsurface diffusion of oxygen occurs [24]. Using TPD data, Conrad et al found S_0 to be 0.3 [21], while Guo et al found S_0 to vary with coverage: 0.14 at 0 ML and 0.87 at 0.05 ML [20]. Engel et al. used thermal molecular beams to determine that S_0 decreases with temperature and linearly with coverage: 0.5 at 420 K and 0.3 at 667 K [25] . Uvdal et al. with supersonic beams found S_0 to be 0.63 at 0.083 eV and 0.58 at 0.69 eV translational beam energies at 300 K [26]. Thermal molecular beam work by Jones et al. found S_0 to be 0.27 +/- 0.02 at room temperature which decreases linearly with coverage, and non-linearly with temperature: falling to 0.2 +/- 0.01 at 465 K. S_0 was therefore found to be significantly larger on the rougher Pd (110) [15]. The reasons for the differences between the findings of Jones et al., Conrad et al and Guo et al. have not been explained. TPD analysis from O_2 dosing at room temperature shows that the β peak obeys second order desorption kinetics by decreasing in desorption temperature at high coverages, and has a desorption energy of around 230 kJ/mol for a 1L dose [2,15]. Leisenberger et al. have performed molecular sticking at temperatures up at 1000 K and found that the surface could be dosed to 1 ML coverage where the subsurface was completely saturated, and that subsurface oxygen cannot be removed

by CO. Compared to Pd (110), the lack of reconstruction of Pd (111) on addition of oxygen is associated with the absence of a β_2 subsurface oxygen desorption peak in TPD spectra [27]. Comparatively little work has been published on adsorption of oxygen on Pd (100). However, S_0 is expected to be significantly lower on this surface compared to Pd(110), as Pd (100) is less openly packed [28]. At low coverages [29] at room temperature (2x2) and c(2x2) structures form that desorb at 800 and 700 K, forming one atom high islands at saturation. Above 475 K the surface reconstructs via a (5x5) reconstruction to a ($\sqrt{5}$x$\sqrt{5}$)R27° reconstruction similar to PdO(001). Under these conditions an additional desorption at 650 K is observed. At higher temperatures and pressures, PdO forms, causing the LEED pattern to fade, an additional low temperature desorption to occur, and three dimensional structures to form on the surface (i.e. surface roughening). Surface XRD experiments (Lundgren et al. [30]) have shown a strong kinetic hindrance to formation of bulk PdO at temperatures up to 625 K.

3.1.2 Results and Discussion

3.1.2 a) LEED Results

a) b)

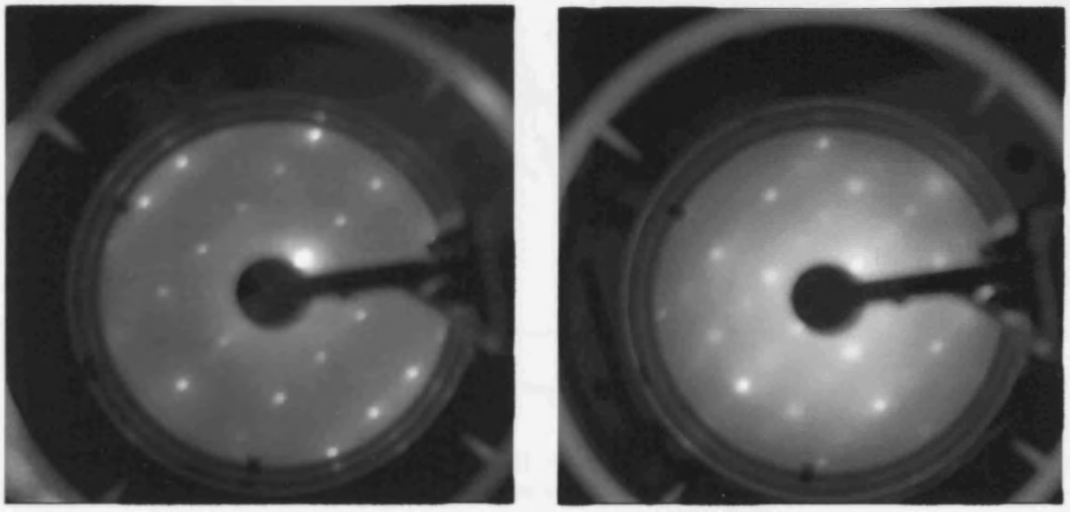

Fig. 1: LEED pictures for a) clean Pd (110) showing the (1x1) pattern at room temperature and 127 eV beam energy, and b) c(2x4)-O formed by dosing 5 L oxygen on clean Pd (110) at 318 K, viewed at 80 eV beam energy.

Fig 1 shows the c(2x4) oxygen surface phase obtained at 332 K by dosing clean Pd(110) to saturation. This result agrees with the pattern reported by He et al. and Ertl et al. who found that this phase forms at high coverages above 280 K [4,12,17]. Based on LEED and TPD studies by these groups, the absolute coverage for this phase has been estimated to be 0.5 +/- 0.05 ML. Formation of this overlayer, and its comparison with the clean Pd (110) (1x1) surface can be used as an indication of crystal cleanliness, although oxygen TPD and/or molecular beam tests were used in this thesis (see Chapter 2) as they were considered more convenient. The structure of the oxygen phase depends on both coverage and temperature, and structures have been found to include (1x2), (1x3), c(2x4), c(2x6), 1D-(2x3) and 'complex' [7] but were not observed in this report as they are associated with very high exposures and coverages.

3.1.2 b) Molecular Beam Sticking Measurements

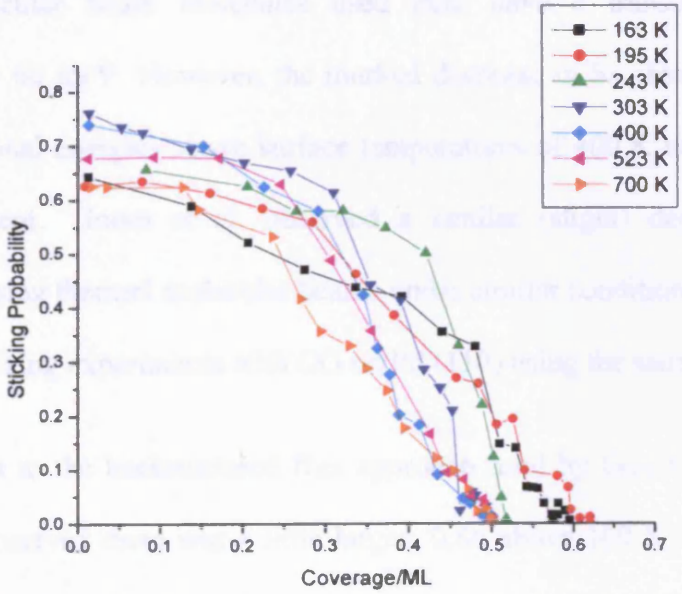

Fig. 2: Sticking Probability vs Coverage for O_2 on Pd (110) at various substrate temperatures from 163 to 700 K. The beam source pressure was 20 mbar.

Figure 2 shows sticking probability vs. coverage data obtained over temperatures between 163 and 700 K using the molecular beam reactor. S_0 varies only slightly with

sample temperature: from 0.63 +/- 0.02 at low temperatures to 0.78 +/- 0.02 at 303 K. At 700 K, S_0 has decreased more significantly to 0.59 +/- 0.02. The saturation coverage (0.5 ML) was assigned by consideration of LEED data and is considered independent of temperature between 200 and 700 K, which is just below the desorption temperature of the β_1 peak. At 303 K the saturation coverage was assumed to be exactly 0.5 ML. For the lowest temperature measurements, the saturation coverage was determined to be 0.62 at 195 K and 0.59 at 163 K, and may not be at complete saturation under these conditions. The overall profile shape remains largely unaffected by temperature, although the higher temperature profiles are slightly different in shape.

These results vary from most other reports in the literature, although there is some agreement with Junell et al. [19] who reported room temperature values of 0.74 and 0.84 for S_0 with translational energies of 44 meV and 153 meV respectively. The thermal molecular beam molecules used here have a translational energy of approximately 60 meV. However, the marked decrease in S_0 observed by Junell for such translational energies above surface temperatures of 400 K was not observed to the same extent. Jones et al. observed a similar (slight) decrease in S_0 with temperature using thermal molecular beams under similar conditions. Jones et al. also performed sticking experiments with CO on Pd (110) using the same equipment.

In comparison to the backscattered flux approach used by Goschnick et al. [5], the value of S_0 observed there was a little larger: 0.86 above 160 K. The method used here is considered more precise due to a greater degree of control over the molecular beam characteristics compared to direct leaking experiments. Comparison with similar molecular beam experiments on Rh (110) where S_0 was found to be 0.62 at

310 K and largely temperature independent, shows some similarity [31]. However, it was found that S(t) decreases more slowly on Rh (110) over time compared to Pd (110), due to the nature of the reconstructions occurring on the Rh surface, increasing its reactivity. S_0 for oxygen on Pt (110) is significantly lower and has been estimated to be 0.13 at 300 K by Wilf et al., occurring via a dissociative adsorption [32]. However, Klink et al. used the same molecular beam system to the one used in this thesis (see Chapter 2) to investigate O_2 sticking on Pt (110) and observed a value of about 0.5 for S_0 at room temperature [33].

3.1.2 c) Temperature Programmed Desorption

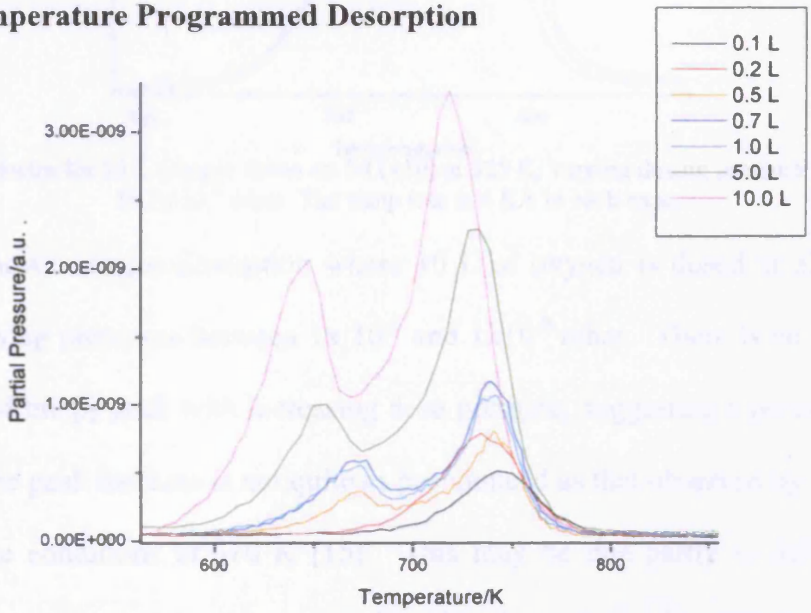

Fig. 3: TPD spectra of O_2 on Pd (110) from 273 K for various exposures from 0.1 L to 10.0 L. The ramp rate was 2.7 K/s and the dosing pressure 1 x 10^{-8} mbar in all cases.

Using different exposures of O_2 at 274 K from 0.1 L to 10 L, the TPD spectrum in Fig 3.was obtained, which agrees well with findings of He et al. and Bondzie et al. [4,12,13]. There are two desorption states, a β_1 peak at 675 K and a β_2 peak at 745 K (at an average ramp rate of 2.7 K/s) which increase in size at higher exposures. The desorption temperatures for both states decrease with increasing coverage. The lower temperature peak is associated with desorption of oxygen from the subsurface. The second peak is more symmetrical and is attributed to second order desorption kinetics

associated with recombination mechanisms. The 0.2 L peak indicates a desorption energy of 306 kJ/mol by consideration of an Arrhenius equation (see Chapter 2). At 10 L exposure the system had not reached saturation.

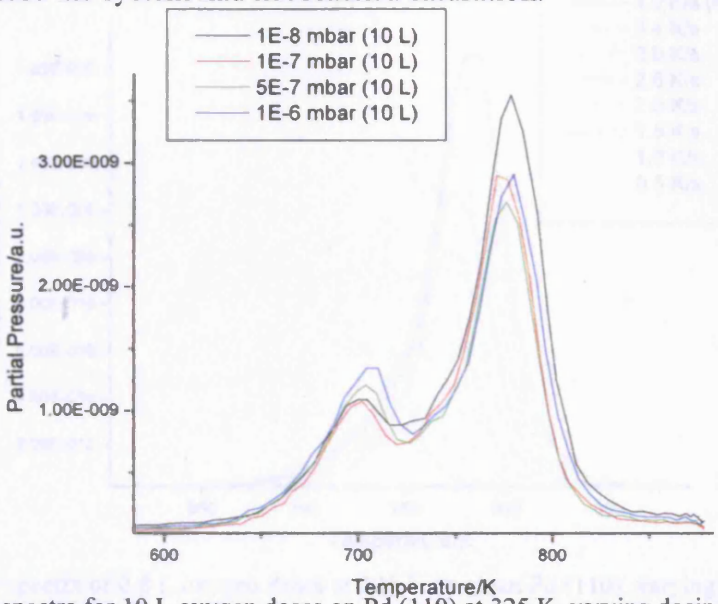

Fig. 4: TPD spectra for 10 L oxygen doses on Pd (110) at 325 K, varying dosing pressure from 1 x 10^{-8} to 1x 10^{-6} mbar. The ramp rate is 4 K/s in each case.

Figure 4. shows oxygen desorption where 10 L of oxygen is dosed at 325 K, with different dosing pressures between 1x 10^{-6} and 1x10^{-8} mbar. There is an increase in magnitude of the β_2 peak with increasing dose pressure, suggesting a pressure-dosing effect, but the peak increase is not quite as pronounced as that observed by Jones et al. for the same conditions at 310 K [15]. This may be due partly to differences in surface temperature, and there is a possibility that the surfaces shown in Fig. 4 may be contaminated by subsurface oxygen between runs so that the β_1 peak is already nearly saturated, even at the lowest pressure dosing. The variation in β_1 peak size with dosing pressure is proposed to be due to a more disordered extent of reconstruction of the surface as the coverage of oxygen increases with increased flux [15]. It is to be noted that the beta peak temperature values have changed due to the change in ramp rate as described in the literature and as shown in Figure 5 for dosing of 0.8 L at 473 K. Increasing the ramp rate results in increased peak integral and desorption

temperature, as described by Yagi et al. using analysis by the Polanyi-Wigner equation [18].

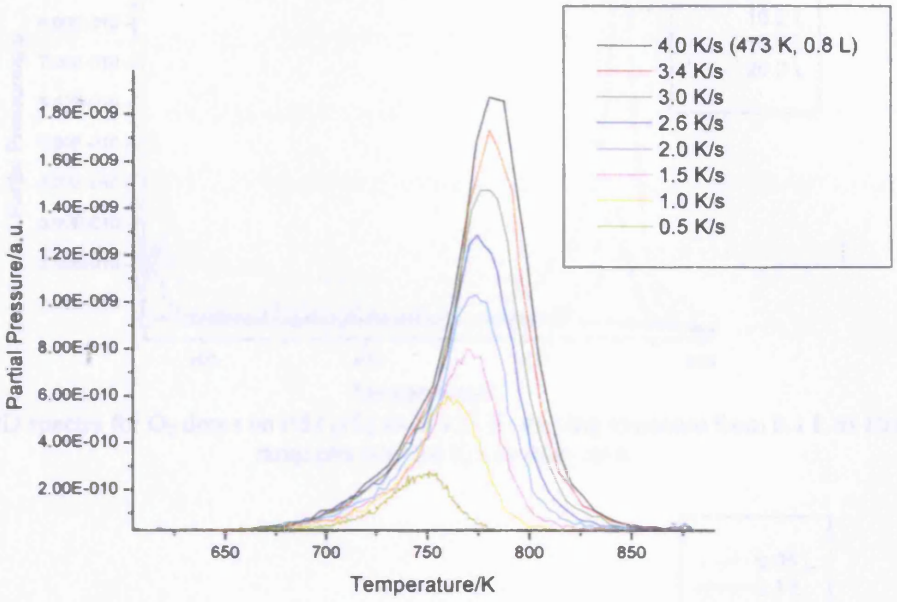

Fig. 5: TPD spectra of 0.8 L oxygen doses at 325 K on clean Pd (110), varying ramp rate from 0.5 K/s to 4.0 K/s.

Cooled TPD experiments at 123 K for O_2 exposures between 0.1 and 20 L at a ramp rate of 1.2 K/s in Figure 6 show no β_1 peak, but reveal a molecular desorption state at 137 K. He et al. and Milun et al. still observed the subsurface desorption under these conditions above 0.8 L [4,10,12]. A longer exposure would have been required to reach saturation for the data in Figure 6. Figure 7 shows a similar set of experiments but for dosing temperatures of 473 K and coverages between 0.05 L and 20 L. These data agree with data found in the literature for similar coverages and temperatures between 310 and 510 K where the β_1 state emerges after the β_2 state is fully saturated (between 15 and 20 L of exposure). The amplitude of the β_1 peak is small, even at 20 L exposure which suggests that the subsurface is not saturated. Indeed, Milun et al. found that at 510 K that an exposure of 2000 L still did not saturate the subsurface [10].

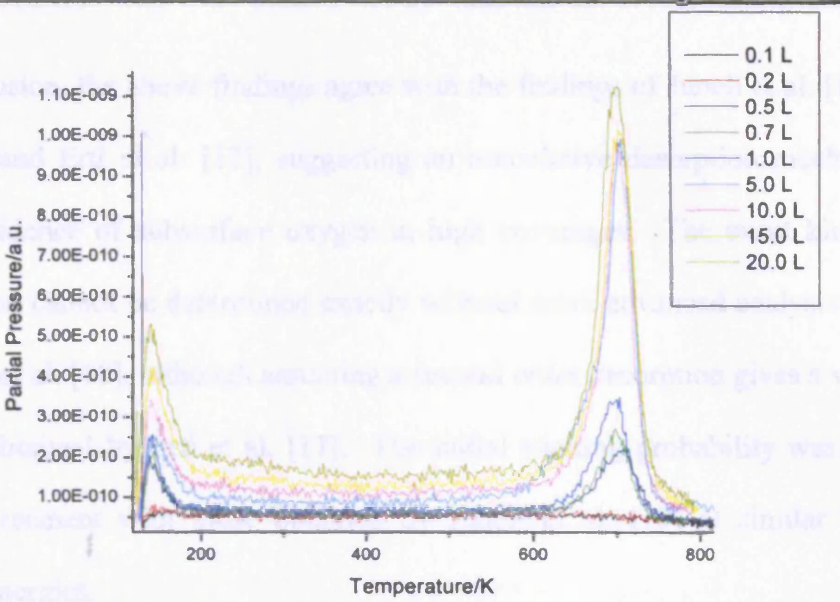

Fig. 6: TPD spectra for O_2 doses on Pd (110) from 123 K, varying exposure from 0.1 L to 10.0 L. The ramp rate was 1.6 K/s in each case.

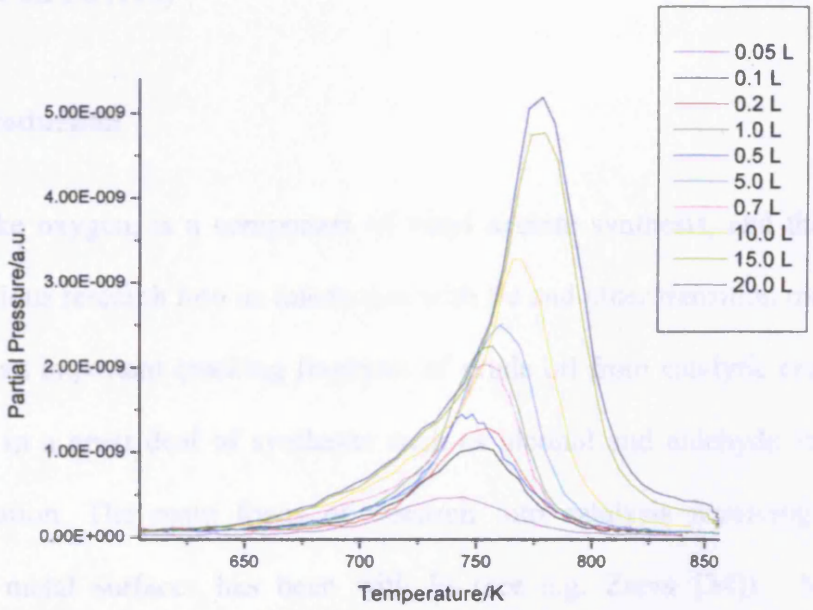

Fig. 7: TPD spectra for O_2 doses on Pd (110) from 473 K, varying exposure from 0.05 L to 20.0 L. The ramp rate was 4.0 K/s in each case.

Consideration of the standard Arrhenius kinetics equations and data in Fig. 5 suggests that a plot of ln (β/T^2) against 1/T will give a straight line of gradient –E/R, where E is the desorption energy, T is the temperature at standard pressure, and β is the ramp rate in K/s. Hence the desorption energy was calculated to be 296 (+/- 3) kJ/mol. This value agreed with findings by Engel et al., who found E to vary with coverage between about 260 and 330 kJ/mol in a similar temperature range [25].

In conclusion, the above findings agree with the findings of Junell et al. [19], Jones et al. [15] and Ertl et al. [17], suggesting an associative desorption mechanism, with some evidence of subsurface oxygen at high coverages. The exact kinetics of the desorption cannot be determined exactly without more advanced analysis as provided by Yagi et al. [18], although assuming a second order desorption gives a value similar to that obtained by Ertl et al. [17]. The initial sticking probability was high and in close agreement with those obtained by Junell et al. [19] at similar translational kinetic energies.

3.2 Ethene on Pd (110)

3.2.1. Introduction

Ethene, like oxygen, is a component of vinyl acetate synthesis, and there has been some previous research into its interaction with Pd and other transition metal surfaces. Ethene is an important cracking fragment of crude oil from catalytic cracking and is thus used in a great deal of syntheses such as alcohol and aldehyde formation and polymerisation. The main focus of research into catalysis involving ethene and transition metal surfaces has been with Pt (see e.g. Zaera [34]). Madix et al., investigating the interaction of ethene and Pd (100) using TPD and EELS at low temperature, found two forms of ethene bonding [35,36]. One, a π-bonded species desorbs from the surface at 300K. At the same temperature, the other species, a di- σ bonded molecule dehydrogenates to methyne (-CH) species which dehydrogenates to surface carbon above 350 K. Low temperature EELS analysis of ethene on Pd (110) indicated that the π – species predominated at 110 K, with di-σ forming with higher coverages [37]. Kawai et al. investigated the low coverage π-bonded species by STM and characterised a c(2x2) structure at 250 K [38-42]. This data was supported by

Nishijima et al. who characterised a saturation surface consisting of about 0.5 ML of the π-bonding species which desorbs gradually at 260 K [43,44]. At 300 K, the remaining 0.38 ML of adsorbed molecules dehydrogenate, apparently to di-bonded ethynyl ($-C_2H$) with sp^2/sp^3 hybridised C centres. The exact nature of the carbon bonding was not elucidated. The ethynyl then dehydrogenates further at 480 K to leave surface carbon. It is generally accepted that the carbon goes subsurface but an alternative is that the carbon forms large thin pillars or islands on the surface and this might be compatible with the data. The presence of carbon from decomposition of organic molecules has been found to have strong effect on surface reactivity of Pd (110) and Pd/silica systems. In other systems, especially model dispersed Pd systems such as the $Pd/Al_2O_3/NiAl$ (110) catalysts, surface carbon has been found to be a crucial product of ethene decomposition [45]. In this case, surface carbon deactivates the dehydrogenation of di-σ bonded ethene, but does not inhibit ethene decomposition. Alkylidyne (-RH) was formed as an intermediate, and occurred on facets of Pd nanoparticles resembling the (111) surface. Another key investigation by Bloxham, Haq and Raval into the decomposition of 1,2-dichloroethene on Pd (110) using a molecular beam discovered steady state decomposition of the molecule above 473 K, apparently without poisoning by surface carbon [46]

3.2.2 Results and Discussion

3.2.2 a) Ethene Interaction with Pd (110)

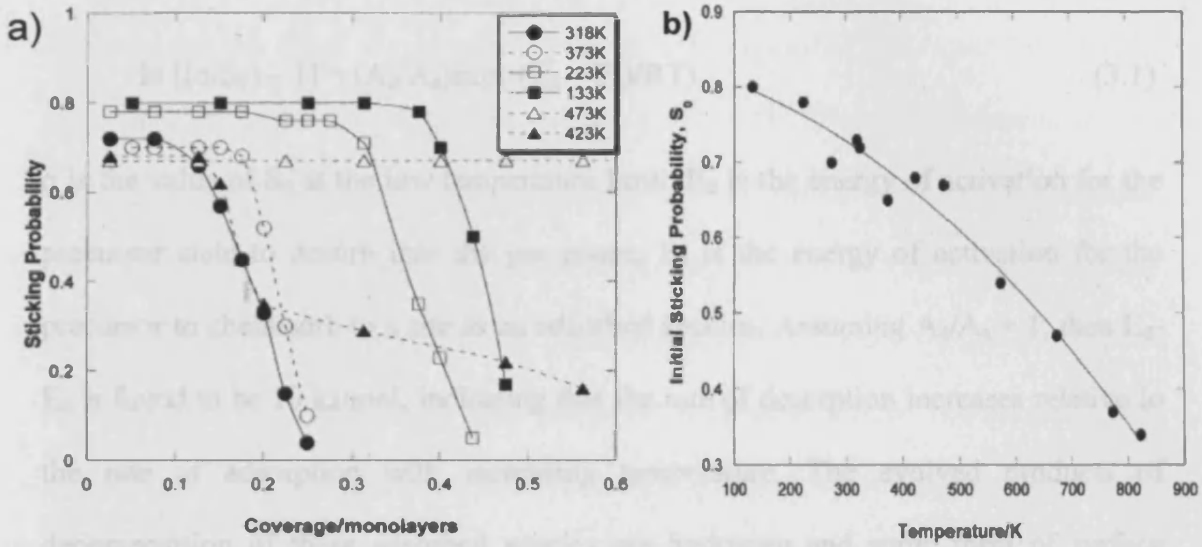

Fig. 8: a) Sticking probability (S) for ethene adsorption as a function of amount adsorbed on the surface at several adsorption temperatures. The lines are interpolated curve fits. b) Dependence of the initial sticking probability (S_0) upon adsorption temperature.

Molecular beam sticking measurements for ethene on clean Pd (110) are given in Figure 8 in terms of their dependence on surface coverage and temperature. Ethene sticks with a high S_0 at all temperatures between 133 and 473 K, from 0.80 at 133 K to 0.64 at 423 K. Saturation occurs at about 0.25 ML coverage at room temperature. The presence of a plateau in S(t), which decreases eventually with increased coverage, constrasts strongly with the Langmuirian behaviour exhibited by molecules such as oxygen and CO on Pd (110). It indicates that the adsorption involves an intermediate species (a precursor), and is described extensively in the literature [47-53] e.g. it occurs in the reverse-spillover mechanism of CO oxidation in some supported nanoparticle systems. The intermediate tends to diffuse readily over surface sites as it is only held weakly on the surface [53]. It will diffuse uninhibited regardless of whether surface sites are occupied or not, and despite its short lifetime will thus prolong an increased adsorption rate. The 'lifetimes' of the plateaux in Figure 8 a)

seem to decrease with increased temperature. Using an equation highlighted by King et al.,[47] Arrhenius analysis of the S_0 vs temperature data in Figure 8 b) will provide information on the adsorption and desorption energy barriers:

$$\ln [(\alpha/S_0) - 1] = (A_d/A_a)\exp(-(E_d - E_a)/RT) \quad (3.1)$$

α is the value of S_0 at the low temperature limit, E_d is the energy of activation for the precursor state to desorb into the gas phase, E_a is the energy of activation for the precursor to chemisorb to a site as an adsorbed species. Assuming $A_d/A_a = 1$, then E_d-E_a is found to be 10 kJ/mol, indicating that the rate of desorption increases relative to the rate of adsorption with increasing temperature. The evolved products of decomposition of these adsorbed species are hydrogen and some form of surface species described as 'C_xH_y'. At temperatures below 273 K, H_2 does not desorb. At 320 K, desorption is significantly slower than the rate of ethene sticking, as shown in Figure 9.

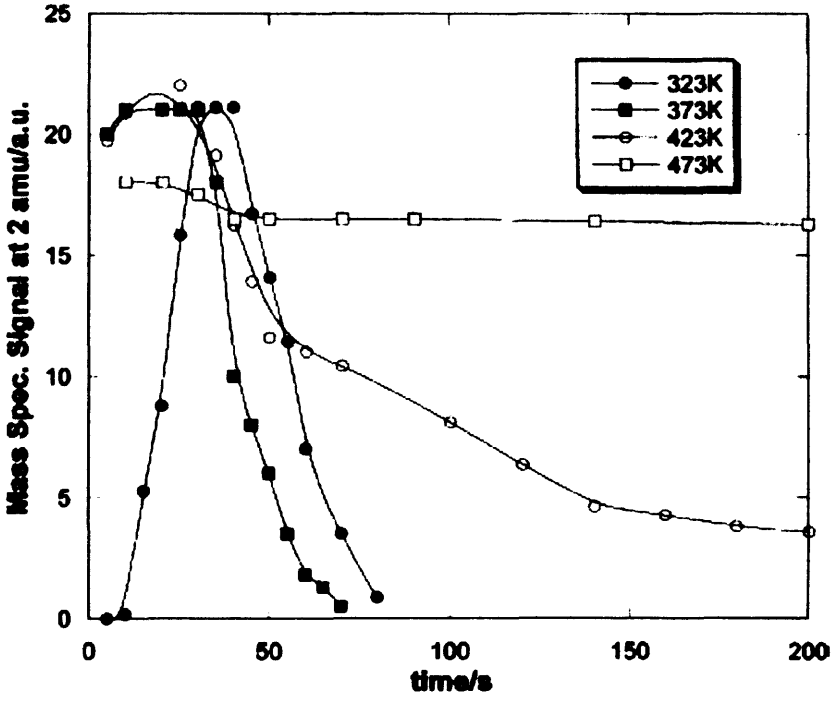

Fig. 9: H_2 evolution during the adsorption of ethene at several temperatures. There is no hydrogen evolution below 270 K. All of the curves are for continuous exposure of the surface to the beam (which begins at time zero). The lines are smoothed curve fits.

When the beam was blocked during the adsorption, the slope of the decrease in hydrogen production appears to obey first-order kinetics, suggesting that the rate determining step (RDS) is due to intermediate decomposition. Hydrogen desorption, which is not the RDS, would give a second order decay of hydrogen decrease, as implied by the findings of Cattania et al. [43,44,54]. The decay constant of the hydrogen dropoff induced by beam chopping is 0.2 s^{-1}, and the half life is 3 seconds. The main hydrogen desorption in a TPD experiment occurs at 310 K and is second-order in nature. This is supported by Nishijima et al. [43]. Sticking at 423 K shows that decomposition leading to desorption of hydrogen is now immediate. This suggests a very low residual concentration of hydrogen containing species on the surface (i.e. y is now lower in the formula C_xH_y). C_xH_y can take various possible forms, including (progressively) C_2H_4, C_2H_3, C_2H_2, C_2H, C_2 and C. Several of these occur as intermediates in other systems. The relative stability of one type of C_xH_y to another in the ethene/Pd(110) system cannot be easily deduced. This is compounded by the fact that hydrogen, present as 90 % of the background gas in the analysis chamber will tend to adsorb on the clean region of the crystal outside the beam exposure area (which is only 10 % of the surface of the crystal). However, low temperature and room temperature TPDs of ethene on clean Pd (110) were taken (Figure 10) and agree with data obtained previously in literature [43,44].

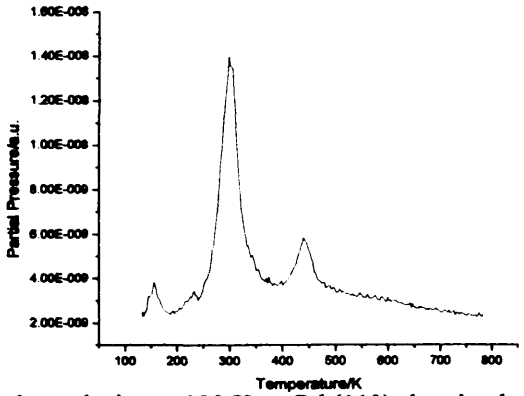

Fig. 10: TPD spectrum of ethene dosing at 133 K on Pd (110) showing hydrogen (mass 2) evolution at 300 and 425 K. The evolution at 150 K is due to hydrogen desorption from heater filaments. Hydrogen is the only product evolved.

To help elucidate the extent of dehydrogenation at 320 K and estimate the extent of background H_2 contamination, molecular experiments involving ethene-d_4 (C_2D_4) were performed at 318 K as shown in Figure 11 (see page 101). There was immediate desorption of HD and D_2 in the ratio 1:8, indicating that before the experiment commenced the surface was already contaminated by approximately 0.05 ML of H atoms. H_2 was not an immediate product, so HD was formed by the reaction. The HD desorption peak reached a maximum before the D_2 desorption peak (see * on Fig. 11), suggesting H atoms in the beam area have reacted. On heating, only a small amount of D_2 evolved at 320 K from heating as the tail of the isothermal decomposition peak (see ** on Fig.11.). A second, larger desorption occurred due to association of adsorbed D atoms. If these atoms are associated with carbon present, then, from the ratio of the D_2 desorbed during isothermal adsorption and the 320 K peak to the D_2 desorbed in the 460 K peak (5.3 (+/-0.5):1) then the carbonaceous layer has a formula of x = 2 and y = 0.7. This could be present as a combination of surface carbon and ethynyl (C_2D) groups, or perhaps as C_6D_2 oligomers. Nishijima et al. [43,44], using RAIRS and TPD, determined the C_xH_y layer at 400 K to consist completely of C_2H. However, the TPDs performed by Nishijima showed varying ratios for the integrals for the two H_2 desorptions at low temperature (P_1) and high temperature (P_2). These ratios had a mean value of 3.8:1, which compares well with the value of 4.2 (+/- 0.4):1 obtained from the data in Figure 10. Both ratios can be compared with the ratio of 3:1 expected for pure ethynyl at 420 K. Thus it may be that Nishijima et al. were convinced by the similarity in ratios to infer that ethynyl is the dominant species in these conditions. However, the values of the ratios suggest that more investigation involving deuterated species may be required to confirm this. In addition, the EELS data provided by Nishijima et al. might not account for the

presence of any surface carbon: some intensity in the carbon region occurs at 350 K but this can be attributed to an ethynyl species as well [see papers 43,44].

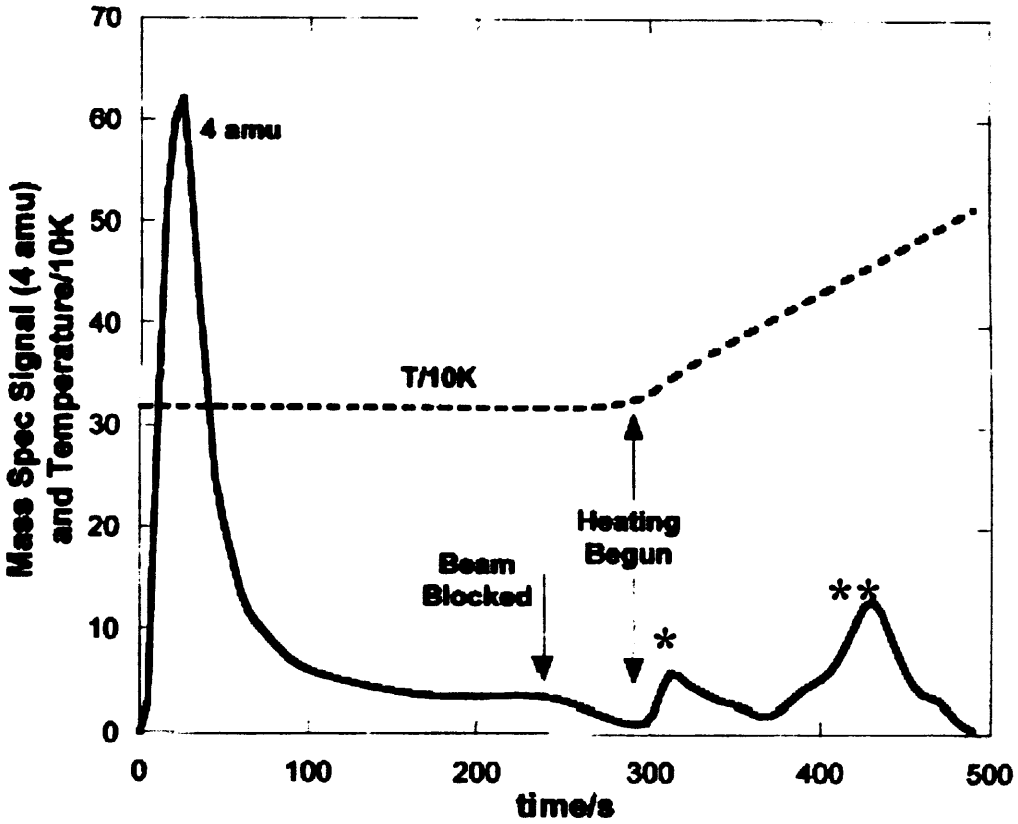

Fig. 11: Adsorption experiment at 318 K for C_2D_4 on Pd (110), showing only D_2 evolution during isothermal adsorption and subsequent temperature-programmed desorption, heating beginning at 300 s.

After complete heating then, the saturation coverage of 0.25 ML will fully decompose to about 0.5 ML of surface carbon. This is supported by LEED data, which gave a faint c(2x2) structure after adsorption at 473 K, implying 0.5 ML of adsorbate (figure 12). This structure persisted until 553 K, where a general disordered background was recovered. At low temperatures, ethene adsorbs molecularly to coverages > 0.25 ML. On heating this excess ethene desorbs at 220 and 300 K to leave a molecular 0.25 ML layer on the surface, supported by Nishijima et al.. Figure 8 indicates that the coverage is about 0.33 ML, so there is good agreement. At higher temperatures, the adsorption and hydrogen evolution becomes more continuous in nature, resulting in a steady state decomposition and carbon deposition and uptake on the surface. Some such sticking experiments were performed for 1 hour at 473 K on the surface,

depositing over 20 ML of carbon. Surprisingly, however, the AES signal for carbon did not suggest that the surface was covered in carbon, as the signal not 1:1 but was relatively small, taking into consideration the C and Pd (MNN) overlaps at about 275 eV. This, coupled with a consistently high sticking probability throughout the whole beam experiment, suggested that a great deal of the surface carbon has dissolved into the bulk beyond AES measurement (i.e. beyond 2-10 atomic layers).. This has been noted previously by Perkins et al. and Raval et al. with other alkenes on Pd (110) [46,55].

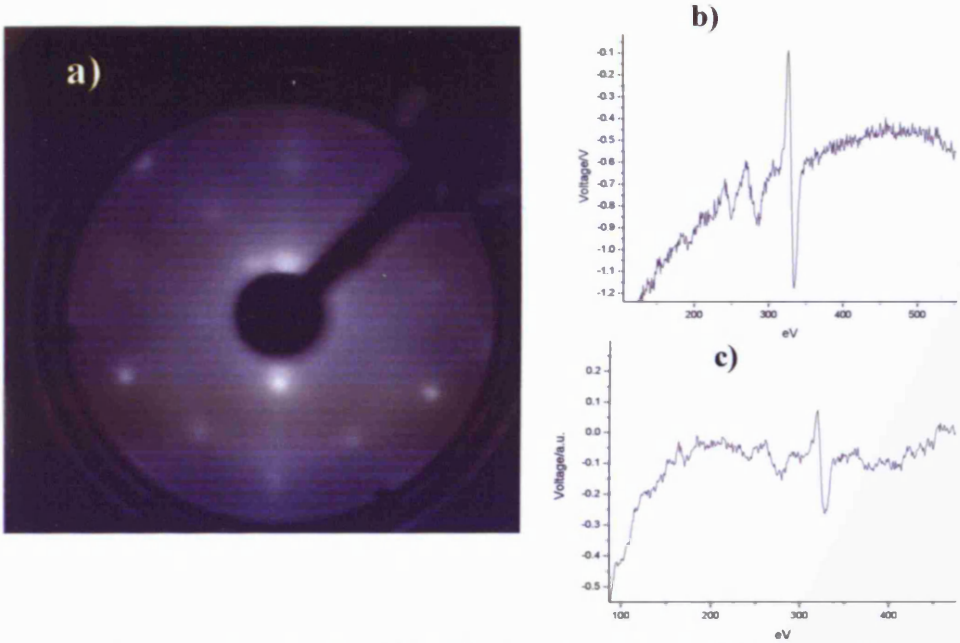

Fig. 12: a) LEED pattern for 1hr of 1 x 10^{-8} mbar ethene on clean Pd (110) at 473 K, producing a c(2x2) pattern. b) an AES spectrum for clean Pd (110), c) an AES spectrum after the condition described in (a) are applied – there is no significant variation in the C:Pd peak height ratio.

Sticking at the intermediate temperature of 423 K shows properties of both transient and continuous sticking and reaction. Saturating still occurs but does so after an extended period, implying that the dissolution of carbon into the bulk is less extensive than at higher temperatures. The behaviour at this temperature implies that the transient (carbon layer formation) and continuous (dissolution into crystal bulk) behaviours are in competition. This is supported by the data in Figure 13, which shows the dependence of beam source pressure (flux) on the adsorption kinetics.

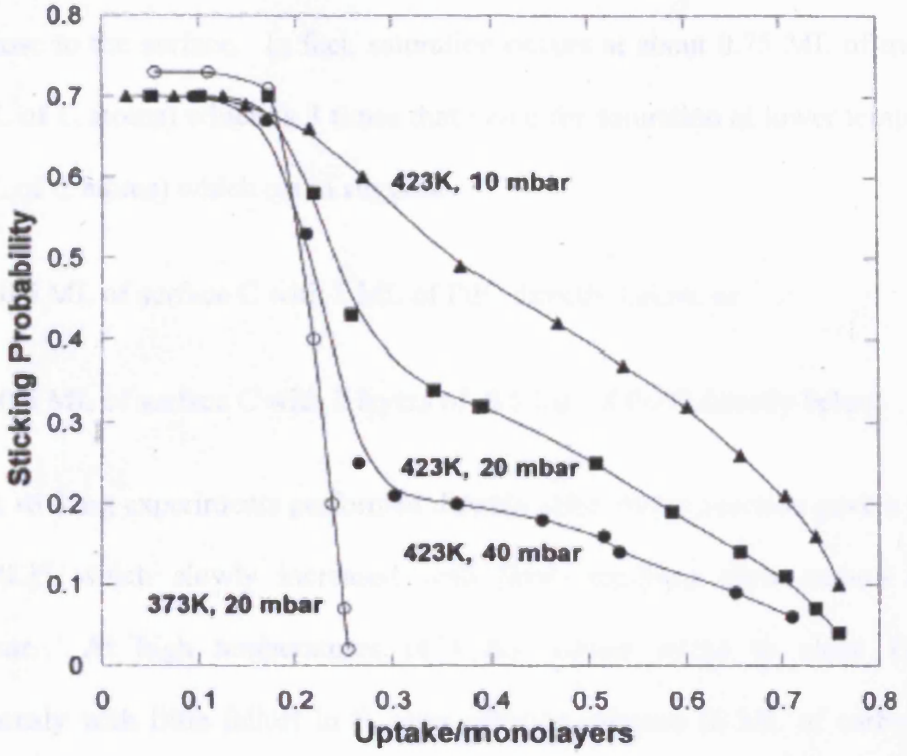

Fig. 13: Sticking probability dependence on uptake of ethene at 423 K at three different beam pressures. The usual beam source pressure, and that used in the other beam experiments shown in this paper, is 20 mbar. Data at 373 K are shown for comparison. The lines are smoothed curve fits.

The overall uptake in each case is more or less the same, but the profile shape is different in each case. At high source pressures, the sticking rate decreases rapidly with increasing coverage, to a much lower plateau value of S (t). At lower pressures, the first plateau only decreases slowly, and is still considerable (0.1-0.2) at saturation. This effect is probably due to the effect of subsurface diffusion of carbon in this intermediate temperature range, and the shape change in the curves is due to competition between adsorption and subsurface diffusion. At higher pressures, the surface layer builds up more quickly and there is less time for a layer to go subsurface, so the sticking drops to a lower value at a given time, due to the lower availability of surface sites for adsorption. The fact that saturation will occur with any

pressure between 10-40 mbar at 423 K, may be due to a saturation of a selvedge layer quite close to the surface. In fact, saturation occurs at about 0.75 ML of molecules (1.5 ML of C atoms) which is 3 times that value for saturation at lower temperatures (0.5 ML of C atoms) which could suggest:

- 0.5 ML of surface C with 1 ML of PdC directly below, or
- 0.5 ML of surface C with 2 layers of 0.5 ML of Pd/C directly below.

Oxygen sticking experiments performed directly after ethene reaction gave a value of S_0 of 0.25 which slowly increased with time, implying slow carbon cleanoff behaviour. At high temperatures (473 K), ethene sticks to clean Pd (110) continuously with little falloff in S, even after 18 minutes (6 ML of carbon atoms buildup) (Figure 14), presumably due to more facile diffusion into the bulk at this temperature.

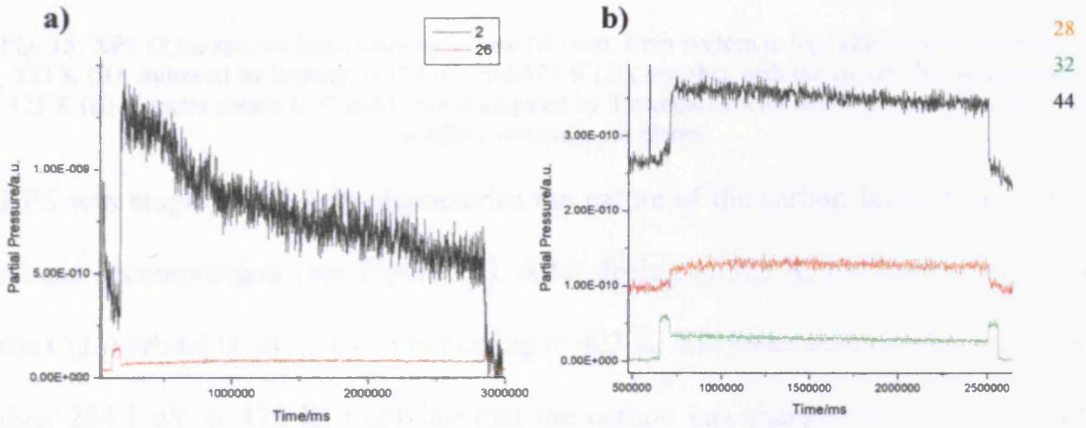

Fig. 14: a) Beam experiment for ethene sticking on clean Pd (110) at 473 K. Hydrogen is the only product and is produced continuously under these conditions. b) Oxygen sticking at the same temperature directly after (a). Oxygen sticks continuously, and CO and CO_2 are produced continuously over this time period.

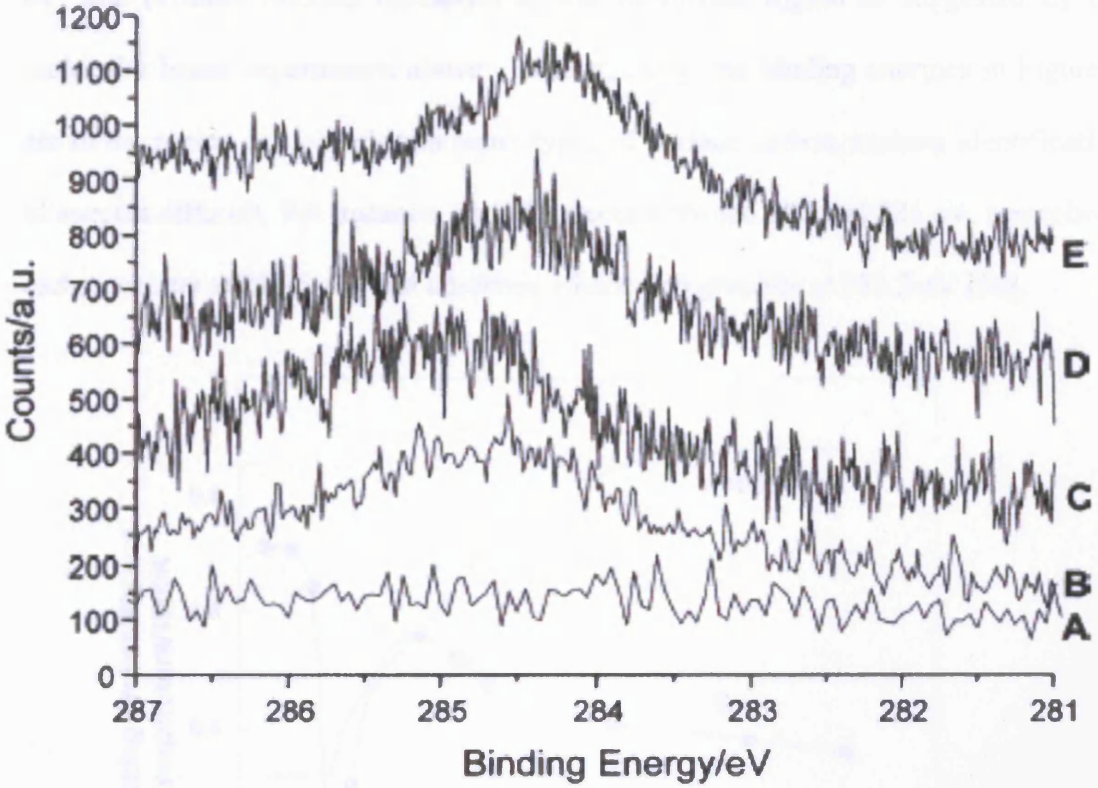

Fig. 15: XPS C(1s) spectra before dosing ethene (A) and, from bottom to top, after ethene adsorption at 323 K (B), followed by heating to 373 (C) and 473 K (D), together with the signal after adsorption at 423 K (E). Spectra counts in C and D are multiplied by 3 compared with the others and each spectrum is offset vertically for clarity.

XPS was employed to help characterise the nature of the carbon layers formed from ethene decomposition (see Figure 15). After dosing at 323 K, the binding energy of the C(1s) orbital is 284.5 eV. On heating to 423 K, this value shifts to about 284.3 eV then 284.1 eV at 473 K, implying that the carbon has changed its electronic state. Even after heating to 373 K, the signal has shifted, which suggests that some carbon has been lost and presumably already gone subsurface under the top layer. There is probably a change in binding site, although carbon is probably not in the surface troughs, as this would not bring about a significant shift. This is because electrons are sampled normal to the surface and are thus not 'shadowed' by any Pd atoms in that

position. Adsorption at 423 K (E) gives a bigger signal with a binding energy of 284.3 eV, due to more buildup of carbon in the subsurface region as suggested by the molecular beam experiments above. Unfortunately, the binding energies in Figure 8 are in the region associated with many types of surface carbon, making identification of species difficult. For instance, carbides occur between 282 and 284 eV, amorphous carbon occurs at 284.5 eV, and adsorbed ethene and graphite at 283.5 eV [56].

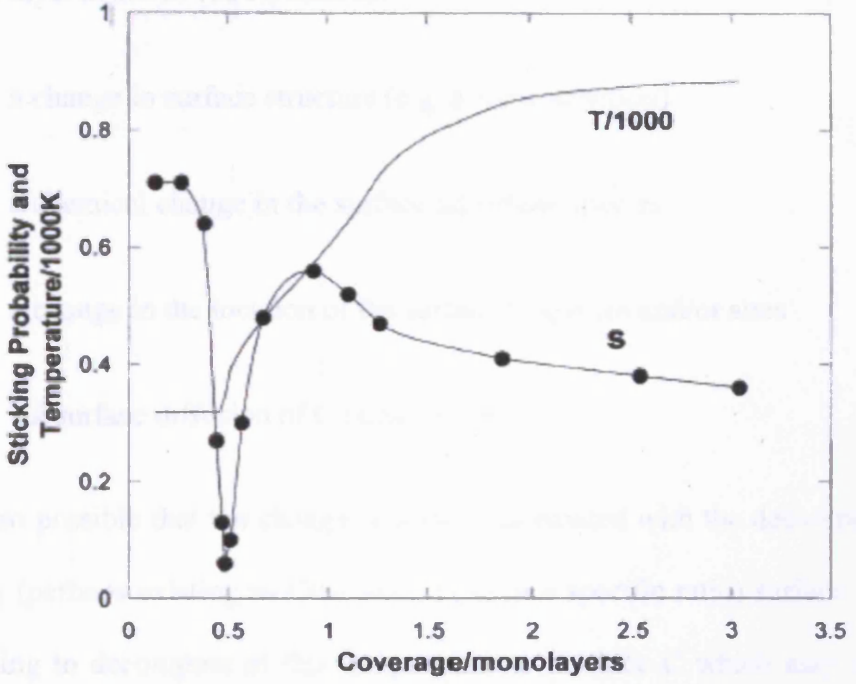

Fig. 16: Temperature-programmed adsorption (TPA) measurement for ethene adsorption on the Pd(110) surface, with the beam on during heating. This shows the ethene sticking probability dependence upon coverage of *carbon atoms* for the isothermal period and the TPA period, with the temperature profile also.

Figure 16 shows a temperature programmed adsorption (TPA) for ethene on Pd (110), which involves non-isothermal adsorption and sticking. The total carbon uptake in this reaction is 3 ML, which is 6 times the saturation coverage of carbon formed from conventional sticking with ethene at room temperature. Clearly much of this carbon uptake must dissolve into the crystal bulk, as ethene sticking continues to be high. At 320 K, isothermal uptake occurs as expected with $S_0 = 0.70$, with adsorption stopping at 0.25 ML coverage (0.5 ML coverage of atoms). Upon heating above 400 K, ethene

begins to stick again, producing hydrogen, with a maximum value for S of 0.55 at 570 K. Thereafter, S decreases as described above (Figure 9) but now the surface is contaminated with either surface carbon or an ethene fragment, which has no apparent effect on the reaction with ethene at this temperature (although it clearly impedes the reaction at lower temperatures). The reason for the resumption of sticking at specifically 400 K is not completely clear, but probably indicates a change in the carbon layer at about 400 K, such as:

- a change in surface structure (e.g. a reconstruction)
- a chemical change in the surface adsorbate species
- a change in the location of the surface C species and/or sites
- subsurface diffusion of C begins to occur.

It is also possible that the change is closely associated with the decomposition of the $CCH_{0.7}$ (perhaps existing as C(a) and CH(a) in a specific ratio) surface intermediate, beginning to decompose at this temperature to produce C which may move to new sites, that do not block ethene adsorption. This movement then exposes more sites to ethene adsorption. These sites to which the blocking species move may be directly below the surface layer, or in the <011> troughs on the surface. Deeper diffusion into the bulk, which appears more activated at about 400 K, will free more sites for adsorption. The ordered c (2x2) LEED pattern (Figure 12) at this temperature implies that at least 0.5 ML of carbon still exists in the top layer or immediate subsurface.

3.2.2 b) Oxygen Interaction with Ethene/Pd (110)

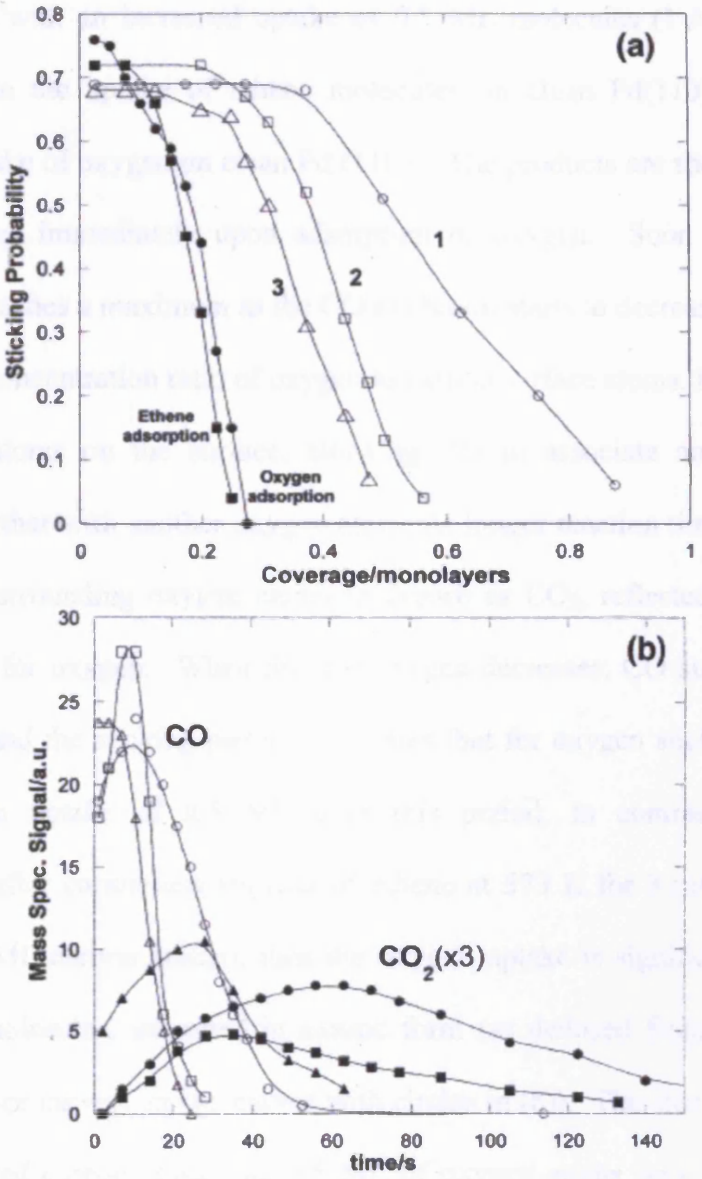

Fig. 17: (a) Sticking probability curves for separate ethene and oxygen adsorption on Pd(110) at 318 K as a function of coverage, and for oxygen adsorption at 573 K after the dosing of ethene (curves 1-3): curve 1, oxygen adsorption after dosing ethene for 180 s at 573 K; curve 2, after ethene dosing for 90 s at 573 K; curve 3, after dosing ethene to saturation (0.25 ML of molecules) at 318 K. The lines are smoothed curve fits. (b) Product evolution as a function of temperature for the experiments of (a): filled data points are CO_2; open points are CO; circles, ethene dosed at 573 K for 180 s; squares, ethene dosed at 573 K for 90 s; triangles, ethene dosed at 318 K to saturation. The lines are smoothed curve fits.

Figure 17 a) shows the dependence of S(t) on coverage of incident molecules for ethene and oxygen adsorbing independently on clean Pd (110), as well as sticking

profiles for oxygen after the adsorption of ethene. Postadsorption of oxygen at 573 K after preadsorption of ethene to saturation at 320 K (curve 3 in (a), curves with triangles in (b)) shows that oxygen sticks well on the carbon layer as well as on the clean surface, with an increased uptake of 0.5 ML molecules (1 ML of C atoms), which is twice the uptake of ethene molecules on clean Pd(110), and twice the saturation uptake of oxygen on clean Pd (110). The products are shown in Figure 17 b). CO evolves immediately upon adsorption of oxygen. Soon afterwards, CO_2 evolves and reaches a maximum as the CO evolution starts to decrease. This is due to the changing concentration ratio of oxygen to carbon surface atoms. Initially, there are few oxygen atoms on the surface, allowing CO to associate and desorb before associating further with another oxygen atom. At longer reaction times, CO will tend to scavenge surrounding oxygen atoms to desorb as CO_2, reflected as a plateau of constant S (t) for oxygen. When S(t) for oxygen decreases, CO and CO_2 evolution have ceased, and the sticking profile resembles that for oxygen sticking on clean Pd (110) with an uptake of 0.5 ML over this period. In contrast, if oxygen is postadsorbed after continuous sticking of ethene at 573 K for 3 minutes (S = 0.55, uptake = 2.5 ML carbon atoms), then the oxygen uptake is significantly larger: 0.9 ML oxygen molecules, adsorbed in atomic form (as deduced from the integrals in Figure 17 a) (see curve 1 in (a), curves with circles in (b)). This does not account for all the deposited carbon: assuming 0.5 ML of oxygen atoms were adsorbed on the surface, then only 1.25 ML of carbon atoms were recovered. A carbon atom yield of about 6 times the oxygen uptake on the clean surface might have been expected: cleanoff of 2.5 ML of carbon atoms, plus 0.5 ML of oxygen atoms. As shown in Figure 17 b), CO desorbs first, followed by CO_2. Also in Figure 17, another experiment where 2-2.5 times the normal ethene uptake (1-1.25 ML carbon atoms)

were preadsorbed, is shown, The oxygen uptake in this case was 2-2.5 times the normal uptake (1-1.25 ML oxygen atoms) on clean Pd (110), and again is assumed to include the 0.5 ML adsorbed oxygen atoms. So in this case, as in the previous case, the full (expected) amount of carbon was not recovered during cleanoff, suggesting some carbon is either very strongly bound or is no longer accessible at the surface.

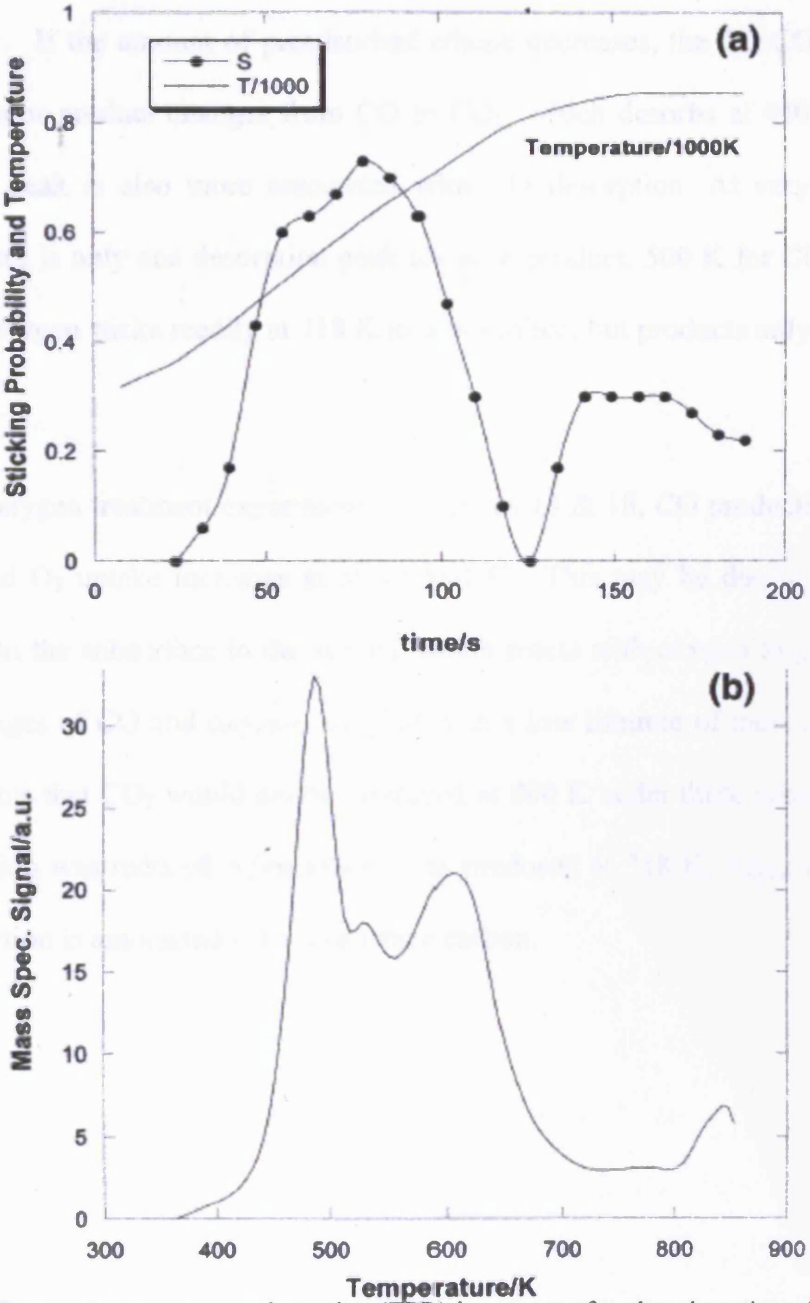

Fig. 18: (a) Temperature-programmed reaction (TPR) in oxygen after the adsorption of ethene at 318 K, shown in terms of the sticking probability of oxygen as a function of time, together with the temperature profile. (b) Evolution of CO as a function of temperature during the experiment of Figure 18a. Only a small amount of CO_2 was evolved and is not shown here for clarity.

Figure 18 shows a TPR of oxygen on Pd (110) with ethene preadsorbed at 318 K. The adsorbed C_xH_y inhibits oxygen sticking completely at this temperature. Oxygen uptake commences at 400 K, accompanying rapid CO_2 evolution, then CO evolution. Two desorption peaks occur for each of the products, e.g. CO desorbs at 500 and 600 K. At 720 K, oxygen sticking decreases, implying the surface has been cleaned off completely. If the amount of preadsorbed ethene decreases, the CO:CO_2 ratio falls, and the major product changes from CO to CO_2, which desorbs at 440 and 500 K. The latter peak is also more associated with CO desorption. At very low ethene dosing, there is only one desorption peak for each product: 500 K for CO and 440 K for CO_2. Oxygen sticks readily at 318 K to this surface, but products only desorb after heating.

In all the oxygen treatment experiments in Figures 17 & 18, CO production increases slightly and O_2 uptake increases at about 800 K. This may be due to diffusion of carbon from the subsurface to the surface which reacts with oxygen to give CO. The low coverages of CO and oxygen, coupled with a low lifetime of most adsorbates at 800 K means that CO_2 would not be produced at 800 K under these conditions. This CO evolution was reduced when ethene was predosed at 318 K, suggesting that the CO production is associated with subsurface carbon.

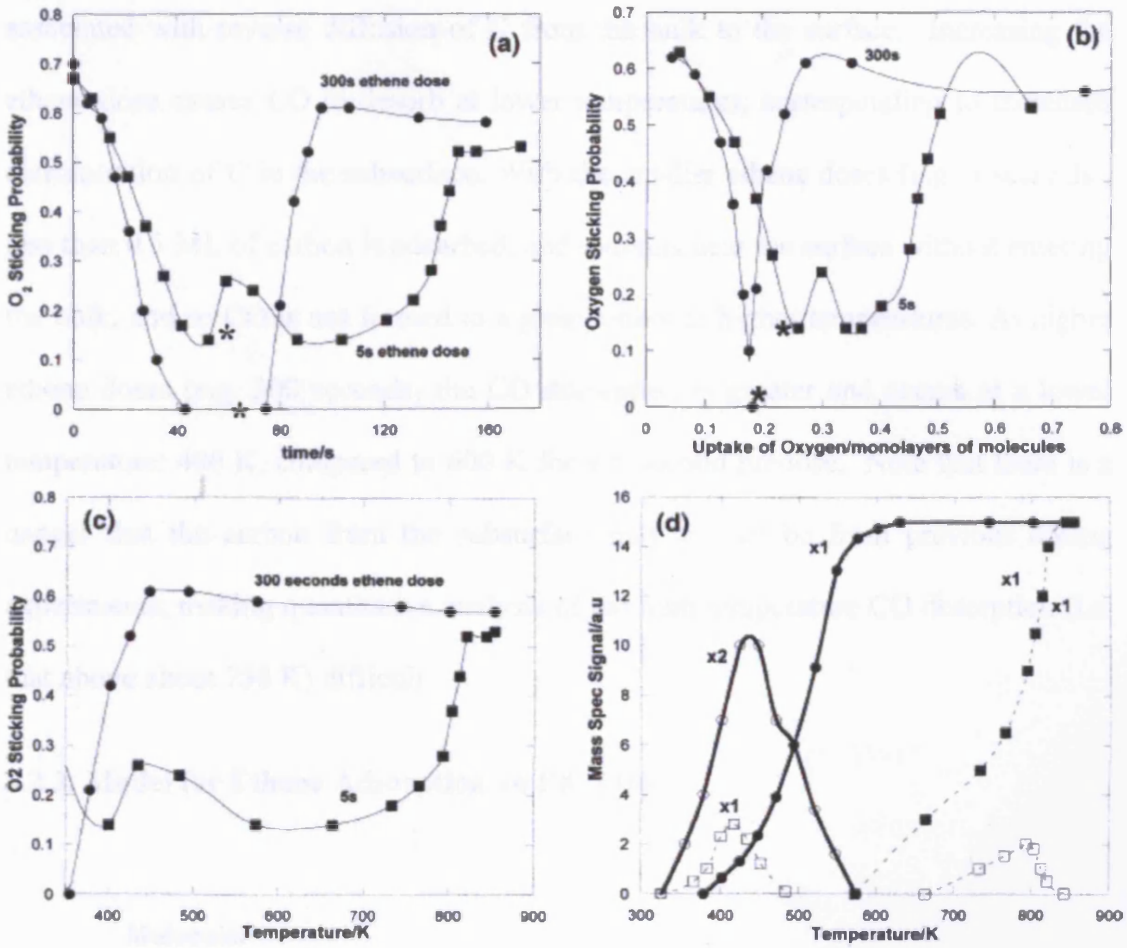

Fig. 19: (a) TPR in oxygen after the adsorption of ethene at 573 K for various ethene adsorption times, showing the sticking probability for oxygen as a function of time. The asterisks note the time at which heating was begun for the different experiments; before this point the surface was held at 318 K. (b) Same data as (a), represented in terms of oxygen uptake onto the surface. The uptake has only been shown until 0.8 monolayer for clarity, but for this experiment the total oxygen uptake for the 300 s dose was 1.35 monolayers and for the 5 s dose 0.9 monolayers. (c) Data for (a) represented as a function of temperature during heating. (d) Product evolution as a function of temperature for the same experiments shown in (a)-(c). Filled points are for CO, and open points for CO_2; otherwise the symbols are as for (a)-(c). Data with the solid curve fit are for the 300 s ethene predose at 573 K; the dotted curve fit is for the 5 s predose.

Figure 19 concerns ethene preadsorption at higher temperature (573 K). Parts a-c show the same data in different forms: as S(t) dependence on time, oxygen uptake and temperature. Oxygen was adsorbed after cooling to 320 K and then the system was heated. Figures 18 and 19 show similar trends: oxygen sticking is not blocked by preadsorbed ethene at high temperatures and coverages up to at least 6 ML of carbon atoms. Figure 19 d) shows that the first product to evolve is CO_2 between 350 and 500 K. In Figure 19, a great deal more CO is produced at high temperatures

associated with reverse diffusion of C from the bulk to the surface. Increasing the ethene dose causes CO to desorb at lower temperatures, corresponding to increased concentration of C in the subsurface. With the smaller ethene doses (e.g. 5 seconds), less than 0.5 ML of carbon is adsorbed, and remains near the surface without entering the bulk, and so CO is not formed to a great extent at higher temperatures. At higher ethene doses (e.g. 300 seconds) the CO desorption is greater and occurs at a lower temperature: 400 K, compared to 600 K for a 5 second predose. Note that there is a danger that the carbon from the subsurface may in fact be from previous dosing experiments, making quantitative analysis of the high temperature CO desorption (i.e. that above about 750 K) difficult.

3.2.3. Model for Ethene Adsorption on Pd (110)

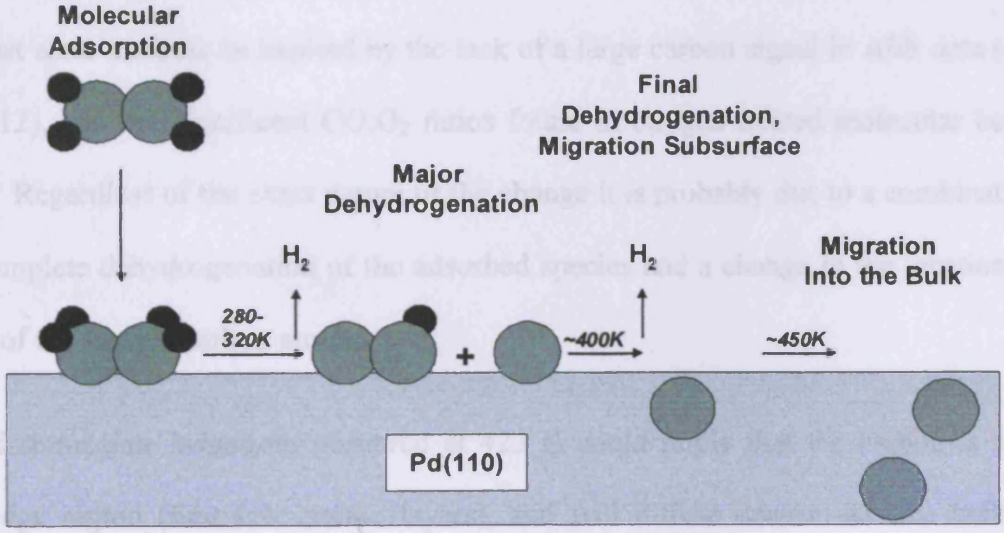

Fig. 20: Schematic model summarizing the adsorption and dehydrogenation of ethene on Pd (110).

Figure 20 shows the proposed model for the behaviour observed above. Ethene adsorbs molecularly at very low temperatures and does not dissociate [37-44]. Dehydrogenation occurs on heating at 270 K. Other dehydrogenated species may

occur at this temperature but cannot be isolated using the above data. By around 320 K, ethene has completely dehydrogenated to what is most likely to be a mixture of surface carbon and ethyne species. A significant change in the system occurs at 400 K: at lower temperatures, the saturated surface inhibits adsorption of oxygen and ethene, and at higher temperatures they can stick efficiently. The nature of this change may be associated with surface reconstruction of the sort shown on formation of c(2x4)-O with a missing row (1x2) reconstruction [4,12,15]. However, this reconstruction was not observed using LEED. The change could be due to carbon loss from the surface region, which certainly occurs above 450 K where carbon multilayers can be deposited. An alternative explanation may be that the carbon poisoned sites are beginning to position, possibly resulting in movement of surface carbon to the bottom of the (110) troughs, exposing active sites above about 430 K. However, a large amount of carbon can be adsorbed at this temperature, and much of it must enter the bulk as implied by the lack of a large carbon signal in AES data (see Fig. 12), and the significant $CO:O_2$ ratios found in oxygen treated molecular beam data. Regardless of the exact nature of the change it is probably due to a combination of complete dehydrogenation of the adsorbed species and a change in the location of sites of the surface carbon atoms.

The intermediate behaviour observed at 423 K could imply that the carbon is in a selvedge region (first few atomic layers), and will diffuse deeper into the bulk at higher temperatures, as deduced by the data in Figure 13. This carbon will diffuse back into the surface at higher temperatures where it can be cleaned off by oxygen quite quickly, this implies that the diffused bulk carbon is retrieveable. Much of the bulk-diffused carbon retrieval is however very slow, as it cannot all be recovered in

oxygen clean off at high temperatures in the timescale of the molecular beam experiments.

The above variations in surface carbon behaviour may explain the lack of ordered structures observed on the surface by LEED with varying coverage and temperature. At low temperatures, dehydrogenation and molecular adsorption occurs to varying extents, and the species are arranged in a disordered fashion. A weak c(2x2) pattern occurring between 473 and 553 K suggests 0.5 ML of carbon occurring in the surface region.

The most significant observation in these studies is possibly the fact that carbon does not poison subsequent reaction at temperatures above 450 K. Reactions with ethene and oxygen under these conditions occur with a high steady state uptake and sticking. Carbon buildup in the bulk inevitably occurs, and may have a more poisoning effect in smaller catalysts, where the volume of the nanoparticulate palladium is much smaller than that of the Pd (110) crystal used in these experiments, and hence saturation of Pd with carbon will occur much more rapidly.

3.3 ACETIC ACID ON Pd (110)

3.3.1 Introduction

The chemistry of acetic acid and its interaction with transition metal surfaces has been well documented [57-66]. The most common method of bonding occurs via a bidentate bond through both oxygen atoms [66]. This occurs in an orientation normal to most (110) surfaces [67,68]. HREELS investigations on acetic acid/Pd(111) at low temperature have suggested that the nature of the bonding may be monodentate [69]

although bidentate bonding may also occur. On most (111) and (110) surfaces, acetic acid dehydrogenates during TPD, depositing surface carbon species [57-62]:

$$CHCOOH \rightarrow CH_3COO(a) + H(a) \quad (3.2)$$

$$CH_3COO(a) \rightarrow C(a) + 3H(a) + CO_2 \quad (3.3)$$

$$2H(a) \rightarrow H_2 \quad (3.4)$$

On Pd (110) the acetate species decomposes at 350 K [60-61], and is bound more strongly than formate which decomposes at 230 K [70]. This is because acetate is a stronger conjugate base than formate and is therefore more stable on a (110) surface. Similar behaviour is observed on Cu (110) [62-64] and Rh (110) [71]. The kinetics of acetate decomposition is also different from that of formate on these surfaces. TPD studies of formate decomposition often show typical first order decomposition behaviour. However, in certain cases, acetate will decompose in a more unusual way. For acetate decomposition on Ni single crystals [57], Madix et al. observed a form of autocatalytic decomposition or 'surface explosion' [72]. This has since been found to occur on many surfaces [59-63, 71,73-75] such as Pd (110) and Rh (110) [71] and can even occur on dispersed Rh nanoparticulate systems on alumina [73]. The kinetics of autocatalytic decomposition have been investigated extensively but have not yet been fully elucidated. TPD investigations have already been conducted for the acetic acid/Pd (110) system [62] and are discussed in relation to the findings given here.

3.3.2.a) Molecular Beam Sticking Experiments: Adsorption and Decomposition

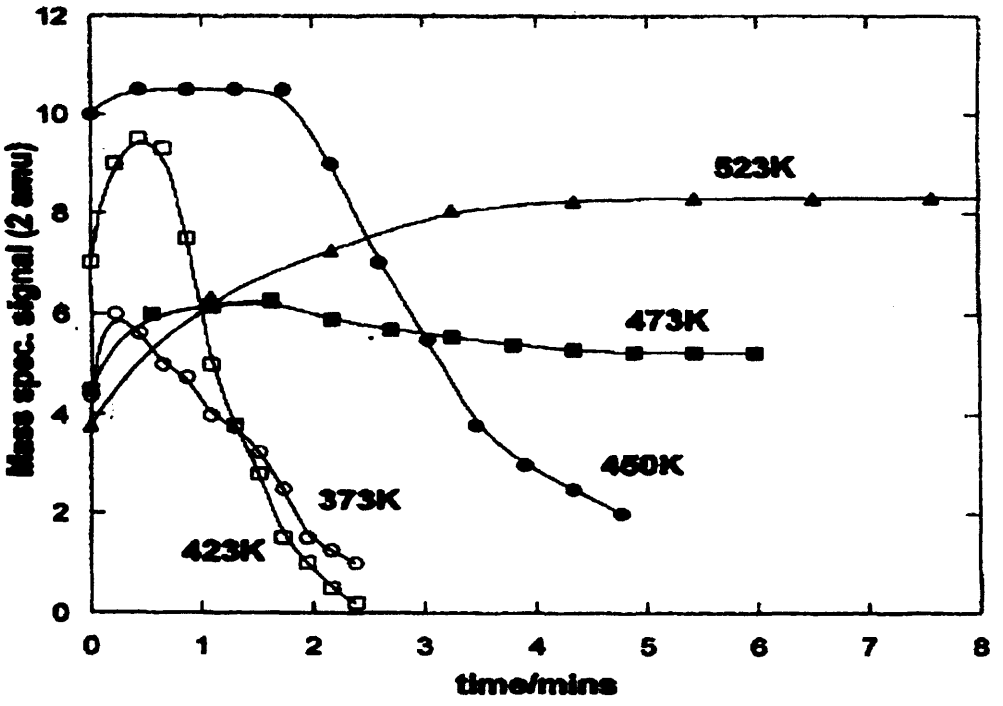

Fig. 21: Hydrogen production during reaction of acetic acid with clean Pd (110) at different crystal temperatures. The reaction appears to be continuous above 450 K. In subsequent TPD experiments after the conclusion of these runs acetate decomposition was identified for the two lowest temperature experiments, but none was present for 450 K and above. CO_2 is also a product, but this has been omitted for clarity.

Figure 21 shows the hydrogen production during beam reaction of acetic acid with clean Pd (110) at different crystal temperatures. Below 320 K, only dihydrogen is desorbed as a product, CO_2 desorbs coincidentally with hydrogen at higher temperatures. After each molecular beam run, TPD was conducted, producing narrow hydrogen desorption peaks of FWHM 10-25 K, indicative of autocatalytic decomposition. However, as the beam exposure region is only about 10 % of the total crystal area, the signal-to-noise ratio was significantly worse than TPDs obtained by direct leaking (see section 3.3.3 below). As the adsorption temperature increases, the desorption peak shifts to a higher temperature: the peak occurs at 430 K for 373 K adsorption, and 475 K for 423 K adsorption. At adsorption temperatures of 450 K and above, transient desorption did not occur, and the acetate decomposed in a steady state, despite continual deposition of surface carbon from the acetate methyl group.

Even after 10 monolayers of deposition, the desorption rate remains unaffected. This suggests that the carbon deposited has no inhibiting effect on the surface active sites, and has probably diffused in a facile manner into the subsurface, as described above for ethene. Figure 22 shows a carbon cleanoff experiment using oxygen at 473 K, indicating that the deposited carbon is easily removed with a high oxygen uptake. The sticking of oxygen is immediate, producing carbon oxides which desorb immediately. The initial evolution of CO, followed by CO_2 reflects variation in C:O concentration at the surface over time, (compare with experiments with ethene in Figure 19). Initially, carbon coverage is high and oxygen coverage is low, but CO_2 coverage increases as surface CO begins to react with surface oxygen. The acetate is stabilised at temperatures below 450 K where the sticking and desorption is transient, and is adsorbed on a carbonaceous layer as evidenced by the increased decomposition temperature with respect to acetate on the clean surface, shown more clearly in the TPD results below.

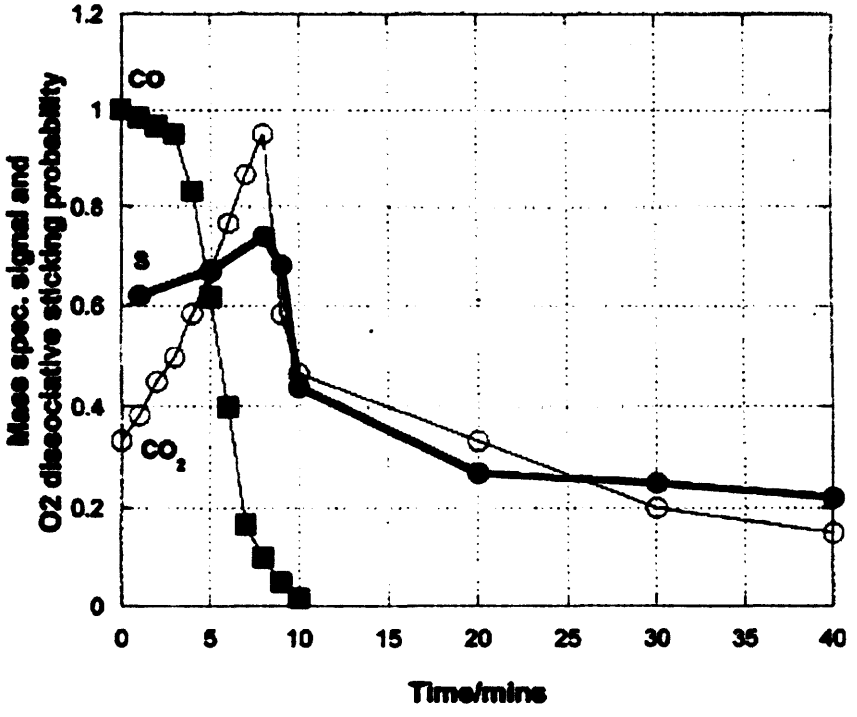

Fig. 22: Showing a carbon clean-off experiment using an oxygen molecular beam. The surface was exposed to acetic acid for 15 min at 473 K, the oxygen being introduced at time zero on the plot. The product observed immediately is CO, followed by CO_2.

3.3.2.b) Temperature Programmed Desorption from Background Dosing

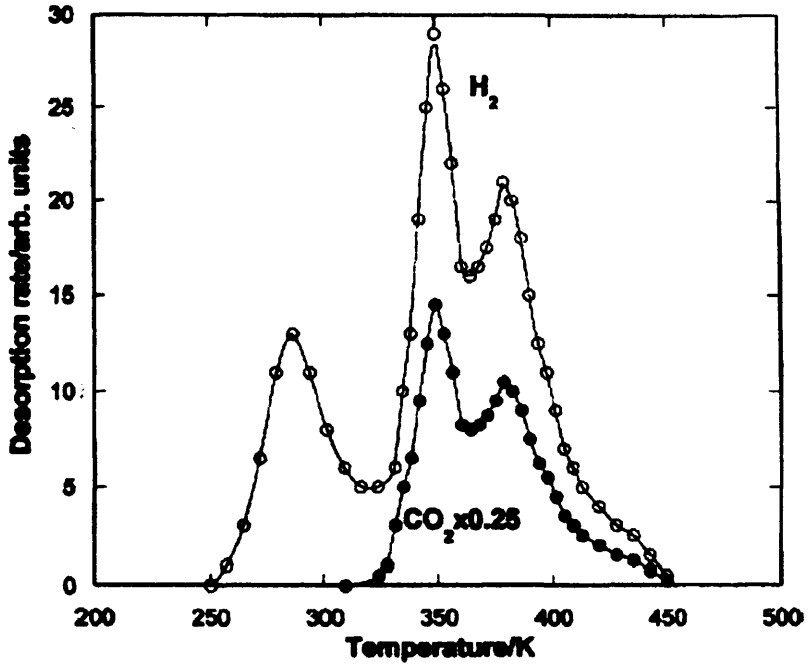

Fig. 23: TPD from the clean surface dosed with 2 L of acetic acid at 220 K, showing products from acetic acid decomposition.

Figure 23 shows the desorption of products from dosing acetic acid on Pd (110) at 220 K. At 290 K, hydrogen desorbs in a desorption-limited peak, i.e. the desorption of H_2 into the gas phase in the rate determining step. Between 325 and 400 K, hydrogen and CO_2 desorb coincidentally in a double peaked structure. This two-peak structure arises from acetate decomposition, the rate determining step in product evolution being the decomposition of acetate, not desorption itself. The second peak may arise from deposition of surface carbon arising from the first peak at 350 K, which stabilises the remaining acetate layer. The 290 K peak occurs from association of acidic hydrogens previously cleaved from the acetic acid molecule (see equation 3.2 above). This TPD cannot be repeated unless the surface is completely cleaned by sputtering and annealing cycles, as the surface carbon product of methyl decomposition is still present at the surface. This surface carbon affects subsequent acetic acid and decomposition significantly, as shown in hydrogen desorptions in

Figure 24. The initial adsorption (B), performed at 323 K, is similar to the low temperature TPD observed in Figure 23. However, here some acetic acid has decomposed, resulting in a reduced leading peak at 325 K. On subsequent dosings and desorptions, the peaks gradually merge into a single feature, each at a progressively higher temperature. The peak also becomes much narrower, with a FWHM of 32 K on the third run (D), to 20 K on the sixth (E). A final experiment (F), where 12 L of acetic acid is decomposed to carbon at 473 K, followed by cooling to 323 K, dosing of 2 L acetic acid and TPD, involves a much narrower desorption peak of FWHM 10 K at a much higher peak temperature of 452 K. These data are indicative of an autocatalytic decomposition as observed in previous work on acetic acid decomposition on Pd (110) and Rh (110). This temperature shift suggests that the carbon present stabilises the acetate to decompose at higher temperatures. CO dosing on the c(2x2) carbon surface (Figure 25) from acetic acid decomposition shows that the CO saturation coverage at 320 K falls by about a half, and the CO desorption temperature shifts from 450 to 430 K, indicating surface carbon is present.

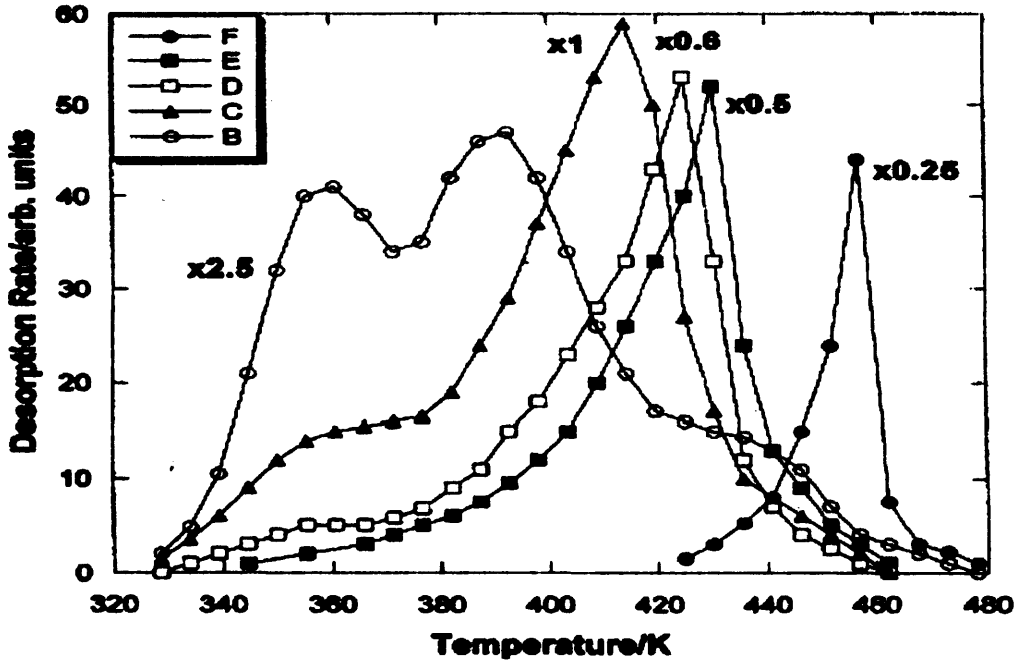

Fig. 24: TPD (at 44 amu) from the clean surface dosed with 2 L of acetic acid at 323 K, followed by repeated doses and TPD, after heating each time to only 530 K. The first TPD is curve B, the second curve C, the third curve D, while curve E is the 6th dose and desorption. Curve F is a new experiment for which the surface was dosed with 12 L acetic acid at 473 K, which deposits C on the surface, followed by 2 L at 323 K. Magnitudes of each curve have been multiplied by a certain factor for clarity.

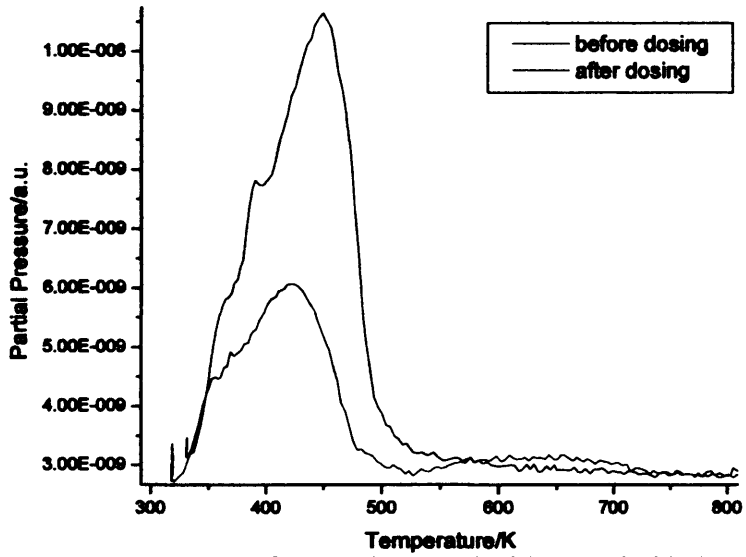

Fig. 25: Room temperature TPDs of CO on C-covered Pd (110). The black trace shows a triple-peak desorption produced by 2 L of CO on clean Pd (110). The red trace shows a TPD from a similar dose on c(2x2) produced by dosing 5 L of ethene on Pd (110) at 330 K, then heating to 473 K and cooling. The main peak temperature decreases from 450 K to 425 K on treatment with acetic acid, so the carbon layer reduces the CO-Pd chemisorption bonding strength.

3.3.2.c) Autocatalytic Decomposition

In Figure 24, the peaks are sufficiently narrow to suggest a surface explosion phenomenon, but the FWHM of such peaks are usually narrower on other relevant surfaces, for instance, the value can be as low as 6 K for formic and acetic acid on Ni (110) [57,77,78], and 5 K on Rh (110) [59]. The surface explosion has been attributed to a homogeneous second order autocatalytic phenomenon by Bowker et al.. Arrhenius analysis of Curve F in Figure 24 using:

$$-d\theta/dt = A.\theta. \exp(-E/RT) \quad (3.5)$$

gives kinetic parameters of unrealistic values. An alternative equation incorporating a (1-θ) preexponential term is required to explain the kinetic parameters [76]:

$$d\theta/dt = A.\theta. (1 - \theta) \exp(-E/RT) \quad (3.6)$$

Using normal desorption the desorption activation energy E is determined from a plot of ln (rate) vs. (1/T) for rates measured on the lower temperature side of the desorption curve where the coverage is essentially constant. For a 'typical' TPD desorption of E = 100 kJ/mol and preexponential factor A = 10^{14} s^{-1}, and coverage of 1 ML, an Arrhenius plot of gives a straight line at the low coverage side of the TPD curve, where 1/T is high, giving correct values of E and A on analysis.

In the case of autocatalytic decomposition, the additional (1-θ) term has great significance. At the low temperature end of the desorption curve (1-θ) may be very small, but increases extremely rapidly with temperature as the reaction occurs at high coverage. Thus there are now two important factors determining the rate of desorption. The associated Arrhenius plot of ln (rate) vs. (1/T) gives a curved line, making determination of E and A difficult. In this case, E is more easily approximated

using the Redhead method (see Section 2.1.5), assuming A = 10^{14} s^{-1}. Redhead analysis of curve F gives E = 124 kJ/mol and A =$10^{13}s^{-1}$ compares well with analysis of the same data using autocatalytic kinetics (see Figure 26) with θ_0 = 0.98 gives E = 118 kJ/mol, A = $10^{13}s^{-1}$ and results in a FWHM of 10 K, and a peak temperature of 455 K.

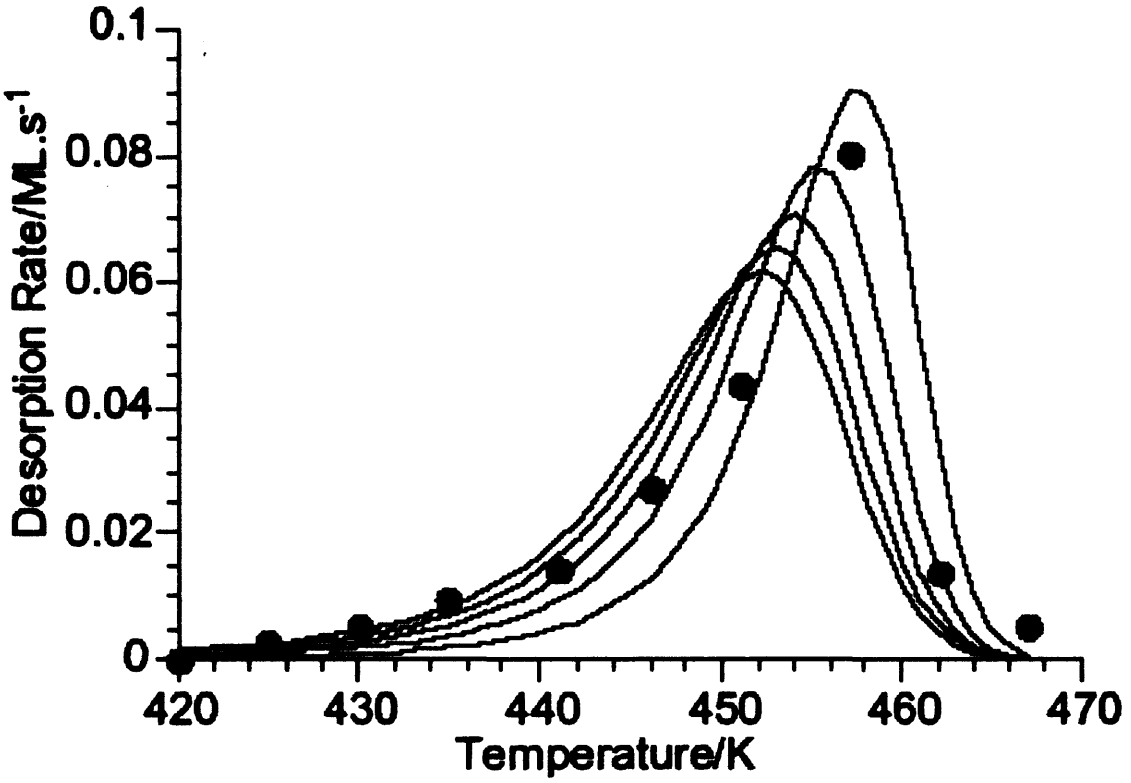

Fig. 26: Modelling of the experimental TPD, the parameters used are shown in the text. Data points are the experiment while the solid lines are the modelled curves using autocatalytic kinetics using Eq. (3.6) in the text and starting coverages ranging from 0.95 to 0.99 (highest temperature peak).

The desorption profiles of the surface explosions depend strongly on the amount of surface carbon present as shown in Figure 24, which itself appears to induce the explosion phenomenon. Hence experimental conditions such as dose exposure and temperature are critical. Also, starting coverage θ_0 and A strongly affect peak width, and as these are fitted, the overall modelled desorption is not exact. This model resembles that proposed by Madix et al. [57,77,78], but differs in terms of the source of the kinetics. In the case described here, reaction initiates by acetate decomposition

at vacant adjacent sites (comparable to Madix's initiation sites [57]) which are initially low in coverage. The vacancies in the adlayer formed by acetate decomposition diffuse quickly and are randomised. This mobile system mediates the reaction, and the vacancies are of an average homogeneous distribution during the process. In contrast to Madix's model, it is apparent here that the surface explosion must occur in the presence of a co-adsorbate such as C or CO. For instance, with decomposition on Rh (110), the coadsorbates could be C, N and/or O, which all induced surface explosions [58-60]. Such coadsorbates appear to block sites for acetate (or formate) decomposition, which are associated with the (1-θ) term in the Arrhenius-like equation above. Thus the coadsorbates seem to be stabilisers for the acetate intermediate to 'explode'. This model is similar to that suggested by Madix et al., although the effects of adsorbate islands were considered important in that research.

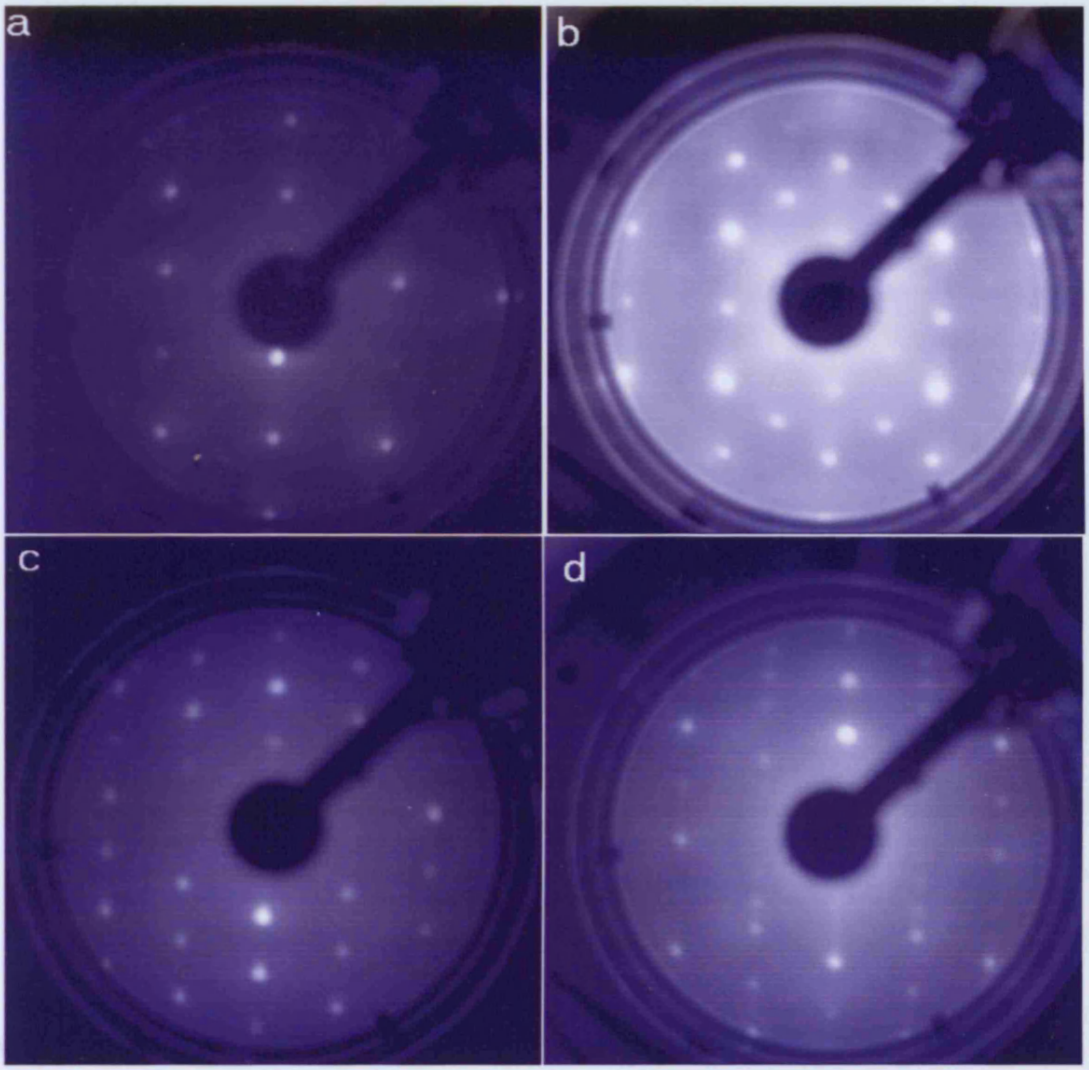

Fig. 27: LEED patterns observed during acetic acid treatments. (a) Clean surface (124 eV); (b) c(2 x 2) after acetic acid dosing at 473 K (157 eV); (c) c(2 x 4) after acetic acid adsorption at 373 K onto a preformed c(2 x 2)-C surface layer (62 eV); (d) mixed c(2 x 2), c(2 x 4) structure observed at 423 K (64 eV).

3.3.2.d) LEED results

LEED was employed to help determine the surface on which steady-state acetic acid decomposition above 450 K occurs. Dosing acetic acid on clean Pd (110) (see Figure 27 a)) produced a high background intensity in addition to the usual (1x1) expected for clean Pd (110). Dosing 5 L acetic acid at 473 K produced a relatively sharp and well-defined c(2x2) pattern (see Figure 27 b)) which is attributed to surface carbon, as

acetate would have either decomposed or desorbed at this temperature. This surface appears to be stable up to at least 573 K and over time (at least 10 minutes). Hence steady state decomposition of acetate might be able to occur on this surface, although this would have to be confirmed by dosing acid and performing LEED experiments simultaneously. Dosing acetic acid at 373 K on this surface produces a sharp c(2x4) pattern, where the acetate is presumably bound to Pd metal atoms (see Figure 27 c)). This structure can also be formed by dosing acetic acid at 400 K, where presumably a layer of carbon forms initially as acetate decomposes on clean Pd (110). If acetic acid is dosed at 420 K, the c(2x4) structure is more unstable, and a mixed c(2x2) and c(2x4) pattern is often seen (see Figure 27 d)). If this system is left over time, the extent of c(2x2) structure increases, presumably due to acetate decomposition. However, this degradation could also be due to electron beam enhanced decomposition. The 'extra' carbon from the c(2x4) structure is either now in a disordered structural state, or has been lost from the active surface, and presumably dissolves into the crystal bulk. From AES studies of the acetic acid/Pd(110) system similar to those obtained for ethene/Pd (110) in Figure 12, carbon coverage is estimated to be 0.7 +/- 0.4 ML of atoms. This coverage does not increase at high temperature and acetic acid exposure, despite the apparent deposition of several monolayers of C, as evidenced by the molecular beam experiments. Hence the latter explanation of the fate of the extra carbon is more likely.

So the c(2x2) adlayer is still very reactive to subsequent acetic acid deposition at 473 K: there is no significant decrease in adsorption probability over time, as observed by hydrogen desorption. Hence, many of the Pd surface atoms may be exposed for acetate binding and decomposition. The adsorbed layer would consist of a mix of acetate and surface carbon, possibly involving a surface reconstruction as observed

for formate on Cu(110) [63-65]. The carbon atoms may be in (110) troughs or subsurface, but this cannot be confirmed from the above AES and LEED data alone, and research into the system by STM and/or XPS would be beneficial in this respect. In the latter case, the acetate decomposition carbon C1s peak electronic shift could be correlated with the exact surface coverage of carbon, which at the moment can only be estimated at 0.5 ML.

3.3.3. Model for Acetic Acid Adsorption on Pd (110)

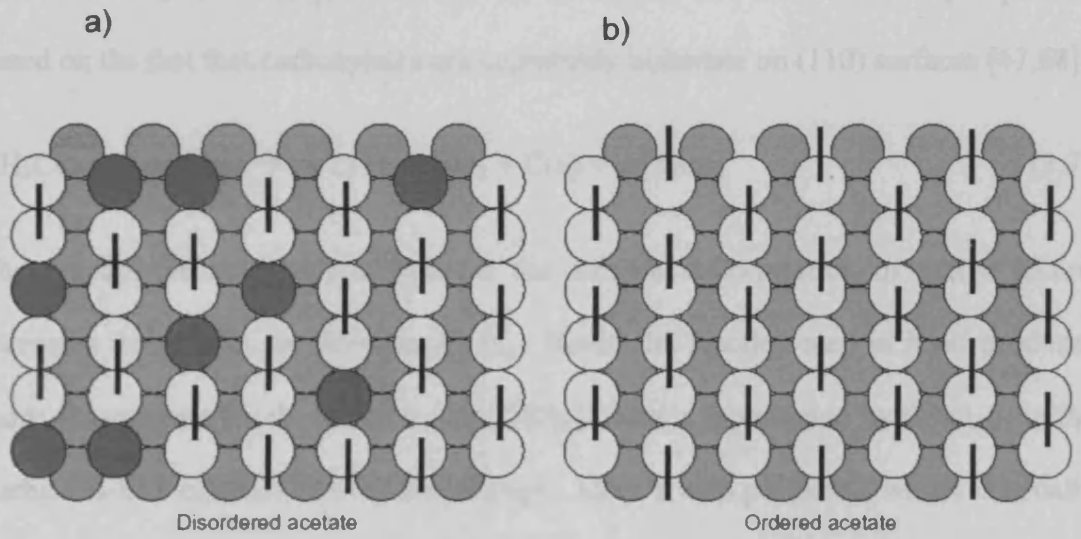

Fig. 28: Schematic models of the surface layer after acetic acid adsorption on the clean surface (a) and the C covered surface (b), with acetate being shown bound to two adjacent surface Pd atoms. The figure simply shows much more order for the coadsorbed surface, though the detailed structure of this system is not yet known.

A model for the surface explosion on a Pd (110) surface is proposed in Figure 28. Figure 28 a) shows the acetate species as bars on the clean surface and it is shown as adsorbing randomly as suggested by the above LEED patterns. Acetate tends to bind to two adjacent metal sites, but cannot fill every site under these conditions as the distribution is not ordered, leaving exposed atoms (dark circles). Two free sites are required for acetate adsorption and bonding, so acetate will not bond to a single metal site which is hindered sterically by other acetate species. These exposed sites act as

active sites for subsequent decomposition of adjacent acetates as the surface is heated. Only a few of these exposed sites are required on the surface to initiate first-order desorption kinetics. Figure 28 (b) shows a more ordered acetate array with no isolated metal sites, hence acetate decomposition is slowed (stabilised). As soon as free sites appear from decomposition, 'explosive' decomposition is initiated. However, to confirm this model completely, the structure of the acetate species present needs to be determined.

The autocatalytic decomposition can be written as a chemical/vacancy equation, based on the fact that carboxylates are commonly bidentate on (110) surfaces [67,68]:

$$CH_3COO(a) + [Site] \rightarrow (3/2)\, H_2 + CO_2 + C(a) + 2\,[Sites] \qquad (3.7)$$

The reaction is autocatalytic because the surface concentration of active [Sites] increases throughout the decomposition. Hence the reaction step in itself produces more components for the reaction. The '[Site]' term is represented by the (1-θ) in the Arrhenius-like equation above. Surprisingly, C(a) is also produced, which is usually expected to block sites and inhibit reaction. In fact, C(a) is an essential component of the explosion phenomenon. Although C is produced, it will block only one site, compared to acetate decomposition which frees two new sites. Also C(a) apparently dissolves into the crystal bulk above 450 K so will probably not have a poisoning effect beyond its interaction in the surface c(2x2) layer.

Why small coadsorbates such as C, CO, N, O or S are required for this and similar phenomena is not entirely clear. These species may behave like templates, increasing ordering of molecules in the adsorbate layer which may inhibit their own decomposition, as indicated in Figure 28 b) [58,60]. Thus the c(2x2) carbon layer observed in LEED may be such a template that can form an ordered c(2x4) layer of

acetate. Hence there are few free sites, and (1-θ) changes significantly early in desorption. Alternatively, without a coadsorbate, the acetate is probably more disordered, the surface resembling at in Figure 28 a). Thus the decomposition will be facile as the (1-θ) term will always be relatively large, and changes relatively little at the low temperature end of the desorption curve, thus making the kinetics resemble those represented by 'normal' Arrhenius equations.

REFERENCES:

[1] H. Conrad, J. Kuppers, F. Nitschke, A. Plagge, *Surf. Sci.*, **69** (1977) 668.

[2] T. Matsushima, *Surf. Sci.*, **157** (1985) 297.

[3] D. R. Lide (Ed.), '*Handbook of Chemistry & Physics*', 73rd Ed, CRC Press Inc., USA, 9-129.

[4] J. –W. He, U. Memmert, P. R. Norton, *J. Chem. Phys.*,**90** (1989) 5088.

[5] J. Goschnick, M. Wolf, M. Grunze, W. N. Unertl, J. H. Block, J. Loboda-Cackovic, *Surf. Sci.*,**178** (1986) 831.

[6] J. –W. He, U. Memmert, K. Griffiths, P. R. Norton, *J. Chem. Phys.*, **90** (1989) 5082.

[7] R. A. Bennett, S. Poulston, I. Z. Jones, M. Bowker, *Surf. Sci.*, **401** (1998) 72.

[8] H. Niehus, C. Achete, *Surf. Sci.*, **369** (1996) 9.

[9] H. Tanaka, J. Yoshinobu, M. Kawai, *Surf. Sci.*,**369** (1996) 55.

[10] M. Milun, P. Pervan, M. Vajic, *Surf. Sci.*, **211** (1989) 887.

[11] M. Jo, Y. Kuwahara, M. Onchi, M. Nishijima, *Chem. Phys. Lett.*, **31** (1986), 106.

[12] J. –W. He, P. R. Norton, *Surf. Sci.*,**204** (1988) 26.

[13] V. A. Bondzie, P. Kleban, D. J. Dwyer, *Surf. Sci.*,**347** (1996) 319.

[14] S. Ladas, R. Imbhil, G. Ertl, *Surf. Sci.*, **219** (1989) 88.

[15] M. Bowker, I. Z. Jones, R. A. Bennett, S. Poulston, *Studies in Surf. Sci. & Catal.*,**116** (1998) 431.

[16] M. Bowker, Chapter 4., '*Cohesion & Structure of Surfaces*', D. G. Pettifor (Ed.), Elsevier Science (1995), 285.

[17] G. Ertl, P. Rau, *Surf. Sci.*, **15** (1969) 443.

[18] K. Yagi, D. Sekiba, H. Fukutani, *Surf. Sci.*, **442** (1999) 307.

[19] P. Junell, K. Honkala, M. Hirsimaki, M. Valden, K. Laasonen, *Surf. Sci.*, **546** (2003), L797.

[20] X. Guo, A. Hoffman, J. T. Yates Jr., *J. Chem. Phys.*, **90 (10)** (1989) 5787.

[21] H. Conrad, G. Ertl, J. Kuppers, E. E. Latta, *Surf. Sci.*,**65** (1977) 245.

[22] B. Klotzer, K. Hayek, C. Konvicka, E. Lundgren, P. Varga, *Surf. Sci.*, **482** (2001), 237.

[23] G. Zheng, E. I. Altman, *Surf. Sci.*, **462** (2000) 151.

[24] E. H. Voogt, A. J. M. Mens, O. L. J. Gijzeman, J. W. Geus, *Surf. Sci.*,**373** (1997) , 210.

[25] T. Engel, G. Ertl, *J. Chem. Phys.*,**69 (3)** (1978) 1297.

[26] P. Sjovall, P. Uvdal, *Chem. Phys. Lett.*,**282** (1998) 355.

[27] F. P. Leisenberger, G. Koller, M. Sock, S. Surney, M. G. Ramsey, F. P. Netzer, B. Klotzer, K. Hayek, *Surf. Sci.*, **445** (2000) 380.

[28] S. L. Chang, P. A. Thiel, J. W. Evans, *Surf. Sci.*, **205** (1988) 117.

[29] G. Zheng, E. I. Altman, Surf. Sci., **504** (2002) 253.

[30] E. Lundgren, J., Gustafson, A. Mikkelsen, J. N. Andersen, A. Stierle, H. Dosch, M. Todorova, J. Rogal, K. Reuter, M. Scheffler, *Phys. Rev. Lett.*, **92 (4)** (2004) 46101.

[31] M. Bowker, Q. Guo, R. Joyner, *Surf. Sci.*,**253** (1991) 33.

[32] M. Wilf, P. T. Dawson, *Surf. Sci.*,**65** (1977) 399.

[33] B. Klink & K. Lass, Internal Report, University of Reading (1999).

[34] see for instance, F. Zaera, *Langmuir*,**12** (1996) 88.

[35] E. Stuve, R. J. Madix, C. R. Brundle, *Surf. Sci.*,**152/3** (1985) 532.

[36] E. Stuve, R. J. Madix, *Surf. Sci.*, **160** (1985) 293.

[37] M. Chesters, G. McDougall, M. Pemble, N. Sheppard, *Appl. Surf. Sci.*, **22/3** (1985), 369.

[38] H. Okuyama,. S. Ichihara, H. Kato, J. Yoshinobu, M. Kawai, *Chem. Phys. Lett.*, **310** (1999) 451.

[39] H. Okuyama, S. Ichihara, H. Ogasawara, H. Kato, T. Komeda, M. Kawai, J. Yoshinobu, *J. Chem. Phys.*, **112** (2000) 5948.

[40] H. Okuyama, H. Kato, M. Kawai, J. Yoshinobu, *J. Chem. Phys.*, **113** (2000) 2866.

[41] H. Pichierri, T. Iitaka, T. Ebisuzaki, M. Kawai, D. M. Bird, *J. Phys. Chem.*, **105** (2001), 8149.

[42] S. Ichihara, H. Okuyama, H. Kato, M. Kawai, K. Domen,. *Chem. Lett.*, (2000), 112.

[43] M. Nishijima, J. Yoshinobu, T. Sekitani, M. Onchi, *J. Chem. Phys.*, **90** (1989) 5114.

[44] T. Sekitani, T. Takaoka, M. Fujisawa, M. Nishijima, *J. Phys. Chem.*, **96** (1992) 8462.

[45] S. Shaikhutdinov, M. Frank, M. Baumer, S. Jackson, R. Oldman, H. – J. Freund, *Catal. Lett.*, **80** (2002), 115.

[46] L. Bloxham, S. Haq, C. Mitchell, R. Raval, *Surf. Sci.*, **489** (2001), 1.

[47] D. A. King, M. G. Wells, *Proc. R. Soc. London, Ser. A.*, **339** (1974), 245.

[48] P. Kisliuk, *J. Phys. Chem. Solids*, **3** (1957) 95.

[49] P. Kisliuk, *Phys. Chem. Solids*, **5** (1958) 78.

[50] D. A. King, *Surf. Sci.*, **64** (1977) 43.

[51] D. A. King, *CRC Crit. Rev. Solid State Mater. Sci.*, **7** (1979) 167.

[52] A. Cassuto, D. A. King, *Surf. Sci.*, **388** (1981) 102.

[53] M. Bowker, *Surf. Rev. Letts.*, **1** (1994) 549.

[54] M. G. Cattania, V. Penka, R. J. Behm, K. Christman, G. Ertl, *Surf. Sci.*, **126** (1983) 382.

[55] N. Perkins, Thesis & internal reports, University of Reading (2001), 43.

[56] J. F. Moulder, W. K. Stickle, P. E. Sobol, K. D. Bomben, '*Handbook of X-Ray Photoelectron Spectroscopy*', Perkin-Elmer Corp., (1992).

[57] R.J. Madix, J. Falconer, A. Suzko, *Surf. Sci.*, **54** (1976) 6.

[58] M. Bowker, Y. Li, *Catal. Lett.*,**10** (1991) 249.

[59] Y. Li, M. Bowker, *J. Catal.*, **142** (1993) 630.

[60] Y. Li, M. Bowker, *Surf. Sci.*,**285** (1993) 219.

[61] T. J. Cassidy, M. D. Allen, Y. Li, M. Bowker, *Catalysis Letters,* **21** (1993) 321.

[62] N. Aas, M. Bowker, *J. Chem. Soc. Faraday Trans.*,**89** (1993) 1249.

[63] M. Bowker, R.J. Madix, *Appl. Surf. Sci.*, **8** (1981) 299.

[64] M. Bowker, R.J. Madix, *Vacuum*, **31** (1981) 711.

[65] S. York, S. Haq, K. Kilway, J. Philip, F. Liebsle, *Surf. Sci.*, **522** (2003) 34.

[66] see for instance, B. Sexton, *Chem. Phys. Lett.*, **65** (1979) 469 and J. Davis, M. Barteau, *Surf. Sci.*, **256** (1991) 50.

[67] S. Bao, G. Liu, D.P. Woodruff., *Surf. Sci.*,**203** (1988) 89.

[68] P. Baumann, H.P. Bonzel, G. Pirug, J. Werner, *Chem. Phys. Lett.*,**260** (1996) 215.

[69] R. Haley, M. Tikhov, R.M. Lambert, *Catal. Lett.*, **76** (2001) 125.

[70] N. Aas, Y. Li, M. Bowker, *J. Phys.: Condens. Matter*, **3** (1991) S281.

[71] T. Cassidy, M.D. Allen, Y. Li, M. Bowker, *Catal. Lett.*, **21** (1993) 321.

[72] See, for instance A. Frost, R.G. Pearson, '*Kinetics and Mechanism*', 2nd Edition., Wiley International, N.Y., (1961), p. 19.

[73] M. Bowker, T. Cassidy, M.D. Allen, Y. Li, *Surf. Sci.*,**307-9** (1994) 143.

[74] J.W. He, P.R. Norton, *Surf. Sci.*,**195** (1988) L199.

[75] M. Milun, P. Oervan, M. Vajic, K. Wandelt, *Surf. Sci.*,**211** (1989) 887.

[76] M. Bowker, C. Morgan, J. Couves, *Surf. Sci.*, **555** (2004) 145.

[77] J. McCarty, J. Falconer, R.J. Madix, *J. Catal.*, **30** (1973) 235.

[78] J. Falconer, R.J. Madix, *Surf. Sci.*, **46** (1974) 473.

4 THE INTERACTION OF Pd (110) WITH CARBON MONOXIDE, ACETALDEHYDE AND VINYL ACETATE

CHAPTER 4: THE INTERACTION OF Pd (110) WITH CARBON MONOXIDE, ACETALDEHYDE AND VINYL ACETATE

4.1 Overview

The interaction of vinyl acetate with simple model catalysts such as single crystal surfaces has not been investigated in great detail in published literature. Hence in this study, its adsorption and decomposition on the Pd (110) surface has been considered with respect to the findings of the previous chapter, that is, the interaction of ethene and acetic acid with the surface. Vinyl acetate can be viewed as a vinyl group (an ethene group missing one hydrogen atom) attached to an acetate group (the conjugate base group of acetic acid) via a single C (sp^2 hybridised) – O bond. However, it is not clear at this stage whether these particular groups would manifest themselves on the surface, or whether vinyl acetate prefers to decompose via other routes. For instance, it may be that the molecule cleaves on the other side of the oxygen atom, producing acetyl and $OCHCH_2$ groups. The presence of acetyl and $OCHCH_2$ would be confirmed by CO, methane and H_2 desorptions similar to those obtained by decomposition of acetaldehyde on the surface. Therefore, before vinyl acetate is considered, it would be of interest to investigate the interactions of acetaldehyde with the surface. As will be shown later the properties of adsorbed carbon monoxide are relevant to this work, and will be presented in the next section. The fact that CO and acetaldehyde species are also significant by-products in the formation of vinyl acetate on industrial catalysts [see for instance 1-3] added extra relevance to their study here. The formation of vinyl acetate from oxygen, acetic acid and ethene on Pd (110) was not investigated as it would be unfavourable thermodynamically in UHV. Instead vinyl acetate decomposition, which occurs readily at low pressures in this system, was

studied with the intention of relating it to the reverse formation process. It is possible that ethene will react with adsorbed acetate from acetic acid decomposition, and this is discussed in Chapter 6.

4.2 Carbon Monoxide on Pd (110)

4.2.1 Introduction

In surface science, carbon monoxide has been studied on many systems, and its interaction with oxygen on metal surfaces is considered a model heterogeneous catalytic process. Its popularity is partly due to its role as a surface probe: it is a simple small molecule that adsorbs molecularly in a manner specific to the type of late transition metal surface. On some other transition metals, CO will adsorb dissociatively [4]. In addition, carbon monoxide has been studied extensively in pollution control systems, where it oxidises readily to carbon dioxide which will desorb from many surfaces. Carbon monoxide plays a significant role in surface spectroscopy such as infrared spectroscopy where the C=O vibrational frequency is straightforward to monitor in a variety of structural and chemical environments.

The CO/Pd (110) system has been studied extensively with LEED [5-9], XPS [10-13], EELS [13-15], TPD [7,8,16-17], molecular beam measurements [11,12], work function studies [8,18] and RAIRS [19-21]. On Pd (110), CO induces a specific range of reconstructions and deconstructions over varying temperatures and overpressures, confirmed by high resolution XPS studies [10]. At 300K, CO is observed in LEED as a disordered background on a (1x1) surface phase up to 0.3 ML coverage. The

molecules are adsorbed in a disordered manner. RAIRS investigations gave a symmetrical band at 1912 cm^{-1} at 0.3 ML, corresponding to a shift of about 30 cm^{-1} from free CO [19-21]. At higher coverages up to 0.75 ML, a (4x2) structure forms which has been associated with a (1x2) missing row substrate reconstruction [18,20,21]. This structure is most clear at 0.75 ML, implying a complete reconstruction at this coverage [9]. RAIRS analysis implies that the CO has adsorbed into several site types. At coverages > 0.75 ML , the surface deconstructs back to the (1x1) termination. At 1 ML, a (2x1) p2mg phase forms with a RAIRS band at 2003 cm^{-1}. [13,20,21]. EELS analysis confirms that CO adsorbs in alternate tilted atop sites, due to nearest neighbour CO-CO repulsion [13,22]. In addition, many low temperature studies have been performed. RAIRS studies at 180 K found no reconstructions from (1x1) [20]. However, RAIRS and LEED studies at 300 K suggested CO induced reconstructions to (1x2) missing row, then back to (1x1) bulk truncation as CO coverage reaches saturation [20,21]. Low adsorption temperature TPD spectra show five desorption peaks, the highest peak at 480 K: an α_3 peak at 338 K occurs due to the overlayer transition from (2x1) to (4x2) [8]. At 102 K, using a backscatter CO flux technique, the sticking probability has been found to be about 1.0, and does not change with temperature [17]. Using a more direct molecular beam approach, S_0 has been determined as 0.45 and the saturation coverage 0.92 ML at 201 K. At 470 K, S_0 was found to drop suddenly to 0.38 +/- 0.02. The saturation coverage decreased continuously with increasing temperature, reaching 0.10 +/- 0.02 at 470 K [11,12]. This trend resembled that found with studies performed on Rh (110) in the same manner, where S_0 was 0.68 at low temperature [23]. These studies implied a precursor weakly held CO state as an adsorption intermediate at low temperatures on Pd (110). XPS studies on this system gave binding energy shifts

during CO uptake at 180 K, which were seen as changing intermolecular interactions with increasing coverages. Kinetic analysis of the Pd (110) sticking curves obtained at 327 K gave a precursor state parameter of 0.13 (K_p), showing that CO is more mobile on Pd (110) than Rh (110) (where K_p = 0.3) prior to adsorption [11,12]. Clearly, the surface changes considerably on addition of CO, resulting in unusual effects such as Pd atom displacement and adsorbed CO diffusion, which implies adsorption and desorption kinetics that are not straightforward. It has been proposed from TPD and sticking data that the desorption process involves a mobile intermediate state where CO molecules in a specific molecular state desorb via a mobile state before leaving the surface [24].

On the Pd (111) surface, low temperature, high coverage TPD spectra show three desorption states, the highest peak at 480 K [25,26]. Direct-leak adsorption experiments have determined a value of S_0 of about 1.0 at room temperature [28]. The slow dropoff in S with time suggested a precursor effect was present. IR analysis shows that CO adsorbs in hollow sites at low coverages < 0.3 ML, in bridge sites up to 0.5 ML, and in atop and bridge sites at coverages higher than 0.5 ML [28,29]. Saturation coverages and LEED patterns have been determined for several temperatures: a ($\sqrt{3}$x$\sqrt{3}$)R30° at 0.33 ML, a c(4x2) at 0.5 ML (the saturation coverage at 300 K), a c($\sqrt{3}$x5)rect at 0.6 ML, a (4$\sqrt{3}$x8)rect at 0.63 ML, a split (2x2) at 0.67 ML (the saturation coverage at 200 K), and a (2x2) at 0.75 ML (the saturation coverage at 90 K) [30-32]. Several studies have indicated that the initial isosteric adsorption energy of the CO/Pd(111) system is about 142 kJ/mol [17,27,28].

4.2.2 Molecular Beam and TPD Experiments

Sticking measurements by molecular beam for the CO/Pd(110) system are given in Fig. 1, giving the CO sticking probability variation with coverage and surface temperature. The initial sticking probability is 0.70 (+/- 0.02) at 330 K, and by comparison with LEED data in the literature, the uptake corresponds to a saturation coverage of 0.75 ML associated with a c(2x2) CO/Pd (110) unit cell. S_0 is not affected by temperature until 493 K, where S_0 falls to 0.52 (+/- 0.02). The saturation coverage falls with increasing temperature, to 0.14 ML at 473 K and 0.03 ML at 493 K. This is because CO desorption is prevalent at temperatures close to 480 K, as shown in Fig. 2. Jones et. al. reported a similar trend using a similar molecular beam system [11,12]. The value of S_0 at room temperature found here is significantly lower than that observed by Goschnick et. al. [17] and Yagi-Watanabe et. al. (where S_0 = 0.95) [24], but is considered to be more reliable, as the backscattering method [17,24] using differentially pumped mass spectrometers is considered less direct compared to molecular beam studies. Fig. 1 shows, that between 330 and 438 K, S(t) varies only slowly with coverage until the coverage exceeds 50% of the saturation coverage. Jones et. al. have suggested this behaviour implies a precursor weakly bound CO intermediate in the adsorption process. Kisliuk et. al. [33] have proposed a kinetic model for such precursor states, where:

$$S = \frac{S_0}{[(1+ ((K_p\theta/(1-\theta))]} \quad (4.1)$$

If the precursor state parameter K_p is unity, then simple Langmuir kinetics dominate. If $K_p<1$, then the precursor state is mobile to a significant extent. Applying this

equation to the curve for 330 K in Fig. 1 gives a value of K_p of about 0.15. At higher temperatures, K_p approaches unity, due to the decreasing diffusion lifetimes of the precursors. The K_p value at 330K is similar to that found by Jones for the same system, suggesting that the CO precursor is much more mobile in this system than for other systems, such as CO/Rh(110) where K_p is found to be 0.30 [23].

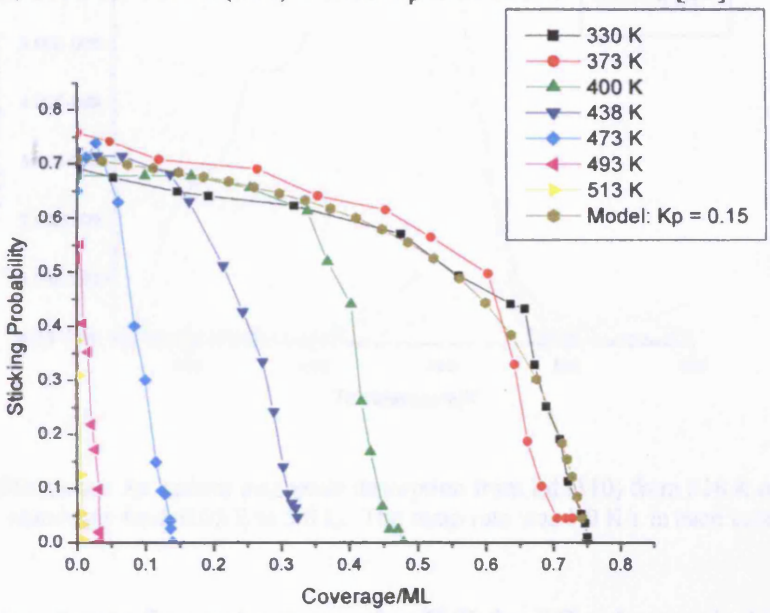

Figure 1: Sticking probability vs. Coverage curves for carbon monoxide on Pd (110) across a range of temperatures from 330 to 513 K. The gas line source pressure was 20 mbar in each case. Results were calibrated from LEED data in literature where saturation was found to be 0.75 ML at 330 K. Also included is a Kisliuk model curve for the data at 330 K using a K_p value of 0.15.

Fig. 2 shows TPD spectra for CO/Pd(110) which behave identically to other data in the literature [8,33]. After 0.05 L exposure, a single β_2 peak occurs at 467 K, and shifts to lower temperatures as the exposure (and thus coverage) increases. This shift is attributed to increasing repulsive interactions between adjacent CO molecules, as well as the increased influence of precursor states at higher coverages [34]. This is manifested as a coverage term in the expression for heat of CO adsorption. At the highest coverage investigated (5 L exposure), two additional features are observed at about 330 (α_3) and 375 K (β_1). The feature at 330 K is associated with the α_3 state which is more prominent at higher coverages in TPD conducted from 200 K, as found in the literature. This 330 K peak is associated with a reconstruction of the substrate

from (1x1) to missing-row (1x2) at high CO coverages. This also occurs on CO/Rh (110) at a higher threshold temperature [23].

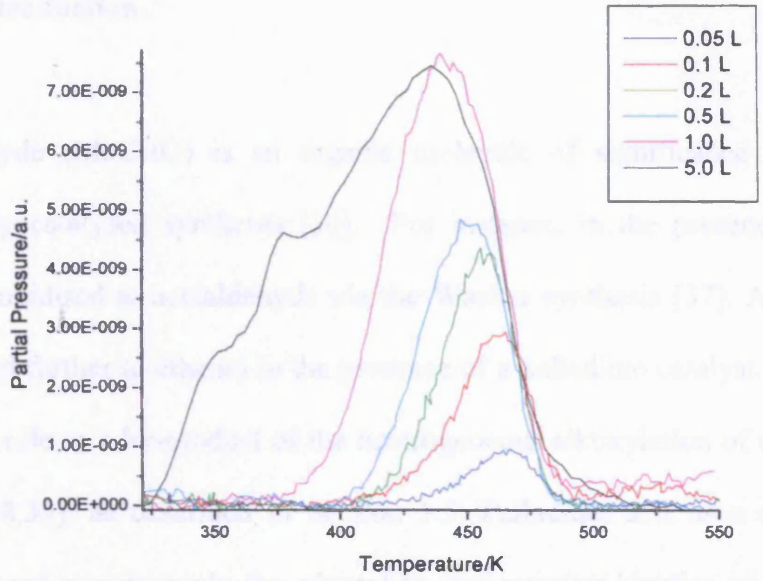

Figure 2: TPD spectra for carbon monoxide desorption from Pd (110) from 318 K over a range of coverages from 0.05 L to 5.0 L. The ramp rate was 1.0 K/s in each case.

If we assume a simple first order desorption [35] for CO, where A is 10^{13} s^{-1}, then by an iterative method, E_d was found to be 126.7 (+/- 4) kJ/mol for the 0.05 L desorption, decreasing to 119.4 (+/- 4) kJ/mol for the 1.0 L desorption. However, the rate of desorption of CO from the CO/Pd (110) surface cannot be written as a simple power law equation because there is a coverage dependence on the pre-exponential factor and E_d. This is confirmed in literature [24], and the applicability of the Kisliuk model also confirms this [33]. A multi-step desorption process of the sort suggested by Yagi-Watanabe et. al. [24] may be a more applicable model to apply to the process, although this was not considered further.

4.3 Acetaldehyde on Pd (110)

4.3.1 Introduction

Acetaldehyde (MeCHO) is an organic molecule of significance in a variety of industrially catalysed syntheses [36]. For instance, in the presence of palladium, ethene is oxidised to acetaldehyde via the Wacker synthesis [37]. Acetaldehyde can be oxidised further to ethanol in the presence of a palladium catalyst. It also plays an important role as a by-product of the heterogeneous alkoxylation of ethylene to vinyl acetate [38,39], as described in Section 1.5. Palladium acts as a catalyst in these reactions, and consequently the adsorption and reaction kinetics of acetaldehyde on palladium have been studied previously by surface science techniques. Using TPD and EELS analysis, Barteau et. al. [40,41] have reported low temperature adsorption of acetaldehyde on Pd (110) and Pd (111). Below 200 K, acetaldehyde bonds in two forms: in a weakly bonding monodentate fashion through its oxygen atom (the $\eta 1$ (O) arrangement), and as a more strongly π-bonded bidentate moiety via the carbonyl group (the planar $\eta 2$ (C,O) arrangement). The $\eta 1$ species desorbs above 200 K, leaving the $\eta 2$ state which decomposes (decarbonylates) at higher temperatures. Barteau suggested a ketene (CH_2CO) intermediate undergoes C-C cleavage to give adsorbed methylene and carbon monoxide [42]. However, in contrast, Shekhar et. al. recently questioned the existence of a surface methylene species, partly because such a species cannot be isolated satisfactorily at present [43].

4.3.2 **Molecular Beam and TPD Experiments**

Desorption experiments were performed by dosing acetaldehyde on clean Pd (110) as shown in Figures 3 and 4. Dosing at 173 K produces methane at 270 K and CO at 450 K, as well as small amounts of hydrogen. In contrast, dosing at 313 K produces CO, but negligible amounts of methane. Thus, there is a strong selectivity for methane production, and hence decarbonylation of acetaldehyde to methyl, at temperatures below 313 K. If acetaldehyde is dosed at low temperature on a surface which has been predosed at high temperature with 5×10^{-6} mbar seconds of acetaldehyde, then the amount of methane desorption increases significantly. The methane desorption is now broader, but still occurs at a lower temperature (300 K) than the CO desorption peak which optimises at 390 K. In addition, hydrogen does not now desorb with the methane, neither does it desorb at 320 K as would be expected for H_2 on clean Pd (110). This implies that the product of acetaldehyde decomposition on the surface at 373 K (presumably some kind of surface carbon, as CO is unstable on the surface at this temperature) has stabilised the methyl species formed from subsequent dosings of acetaldehyde. Thus the methyl groups are more likely to hydrogenate and desorb as methane, than decompose to surface carbon.

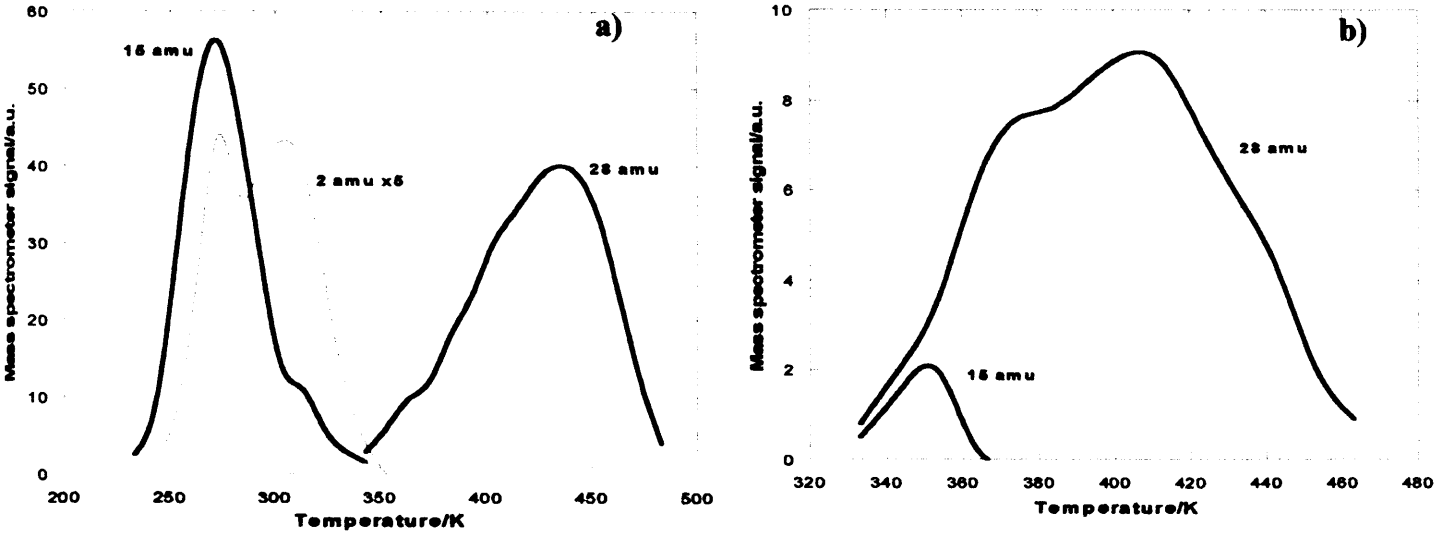

Figure 3: TPD spectra for acetaldehyde after dosing the Pd(110) with 10 L of acetaldehyde at a) 173K and b) 313K. Note that, although the hydrogen evolution appears large in fig a), the mass spectrometer is much more sensitive to it, than it is to the other products.

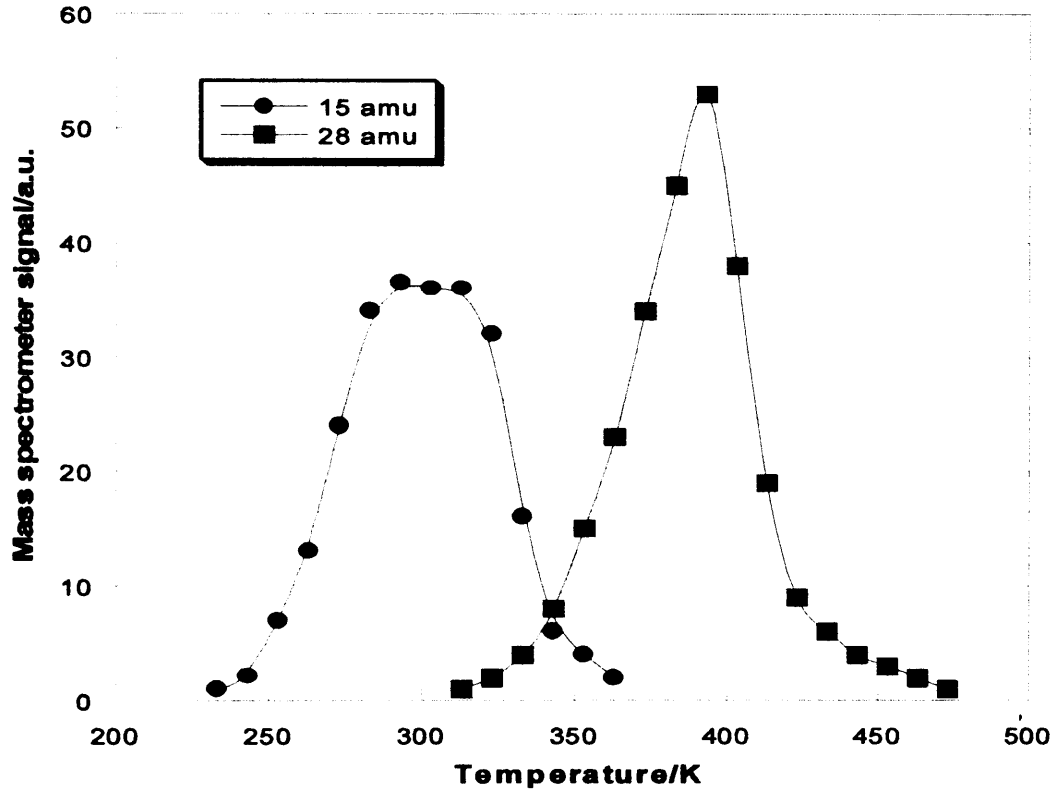

Figure 4: Temperature programmed desorption after dosing 10 L of acetaldehyde at 173 K onto a surface already treated with 10 L of acetaldehyde at 373 K. Ramp rate = 1K/s.

Figure 5 shows isothermal adsorption measurements for acetaldehyde on clean Pd (110) carried out using the molecular beam reactor. The sticking probability is

measured using the mass 29 signal. S_0 is high and decreases with increasing temperature: from 0.80 (+/- 0.02) at 273 K to 0.64 (+/- 0.02) at 473 K, implying efficient adsorption across this temperature range. These data support the low temperature desorption spectrum in Fig. 3, as methane evolution is slow below 240 K, and is produced rapidly and transiently at 273 K. The transient nature of methane evolution is attributed to surface carbon monoxide accumulation, inhibiting adsorption and decomposition of incident acetaldehyde. By 300 K, the carbon monoxide has a greater tendency to desorb at high coverage (see Fig. 2), so the evolution of methane and sticking of acetaldehyde becomes steady-state in nature. A TPD performed after isothermal sticking at 300 K gives a low temperature shoulder in the mass 28 desorption peak (see Fig. 6 on p148) , as the surface carbon destabilises CO. By 370 K, the extent of steady-state adsorption and decomposition has increased. Arrhenius analysis for the steady state methane evolution between 270 and 350 K indicates that the decarbonylation has an activation energy of about 26 (+/- 1) kJ/mol, assuming an initial rate method. This relatively small positive value is likely to be the apparent activation energy from several kinetic steps. Note that the 'initial rate method', that is the assumption that the concentrations of CH_3 (a) and H (a) are constant in the decarbonylation rate equation: rate = $k[CH_3][H]$, is not really applicable, as both concentrations are probably inversely proportional to surface temperature. In addition, the surface structure and chemistry varies significantly over this temperature range, for instance, the concentration of surface carbon is changing and this affects adsorbed methyl stability for dehydrogenation. Hence, Arrhenius analysis is probably not suitable for these conditions. The rate determining step for the overall reaction is likely to be desorption of CO for three main reasons:

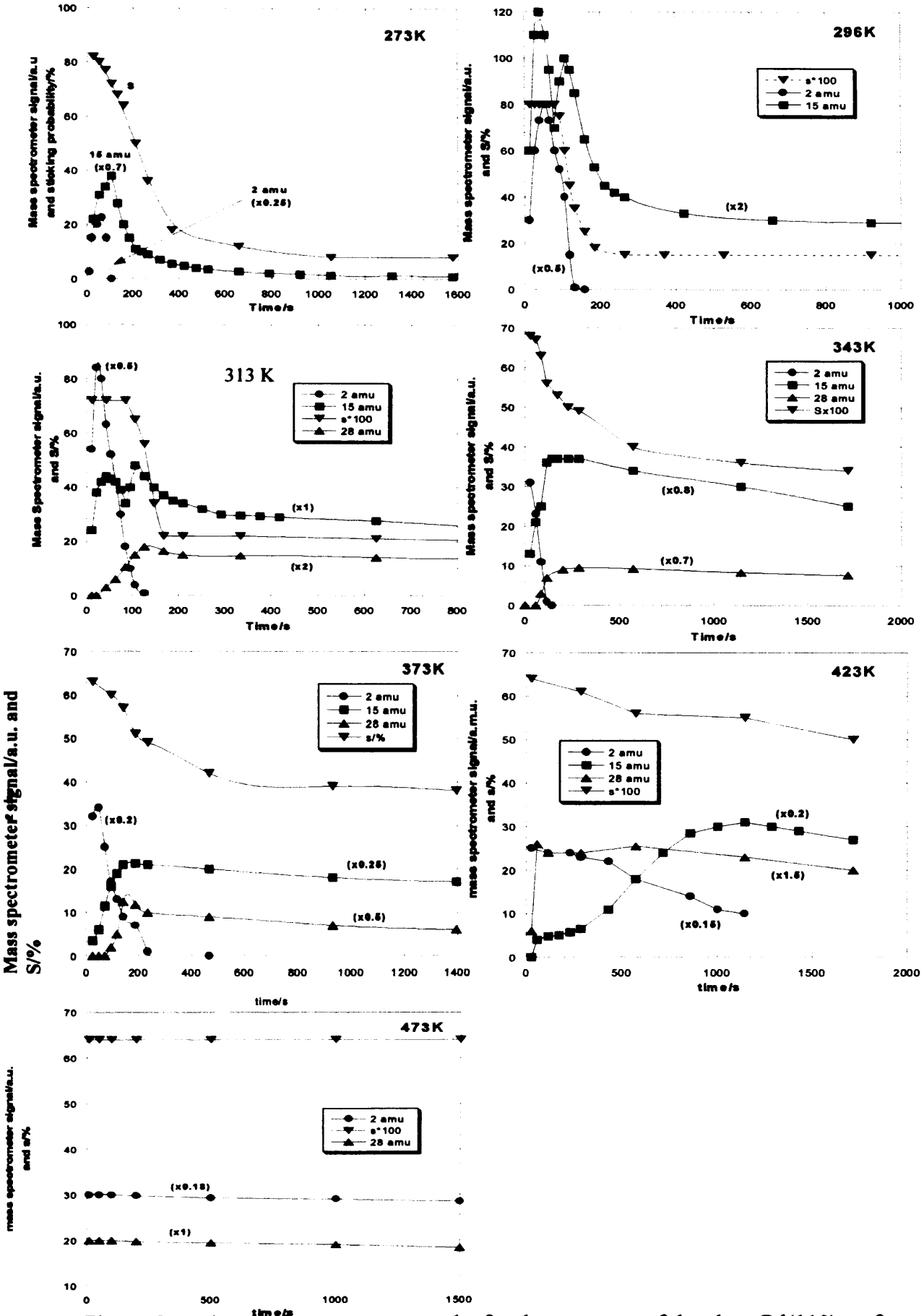

Figure 5: Molecular beam reactor results for the exposure of the clean Pd(110) surface to acetaldehyde at a variety of adsorption temperatures, as indicated.

- Its evolution is much slower than that of methane, which evolves quickly at temperatures as low as 273 K.
- CO is relatively strongly adsorbed on the surface.
- The evolution of CO is slow at the lower temperatures

At temperatures above 370 K, methane evolution is more delayed, accompanying a change in the reaction from partial to complete dehydrogenation. Above 473 K, CO and H_2 are the only products, and evolve continuously: S(t) is unchanged after 25 minutes of adsorption. The adsorption and desorption data suggest that methane production from acetaldehyde decomposition occurs via:

$CH_3CHO \rightarrow CH_3CHO(a)$ (4.2)

$CH_3CHO(a) \rightarrow CH_3(a) + H(a) + CO(a)$ (4.3)

$CH_3(a) + H(a) \rightarrow CH_4$ (4.4)

$CH_3(a) \rightarrow C(a) + 3H(a)$ (4.5)

$H(a) + H(a) \rightarrow H_2$ (4.6)

$CO(a) \rightarrow CO$ (4.7)

The first three steps occur quickly at 300 K and above. The second step is proposed elsewhere to occur in two stages [40,41] : loss of alpha hydrogen to form an acetyl species, then C-C scission, although there is no direct evidence to support this phenomenon in these experiments. The third step, production and evolution of methane, is dependent on methyl group stability to dehydrogenation (step 4.5). Molecular beam reactions involving deuterated d_4-acetaldehyde, as shown in Fig. 7, helped to prove the nature of step (4.5). Inevitably, the surface was contaminated by surface ambient hydrogen (95% of the UHV chamber base pressure), inducing immediate and rapid production of CD_3H, which evolves transiently, accompanying

transient acetaldehyde sticking. After the surface hydrogen is expended, CD_4 is produced. This behaviour is echoed in immediate and rapid production of HD which is gradually replaced by D_2 production, especially at 313 K. The high initial rate of these hydrogenous products is due to an optimal concentration of surface hydrogen initially, which is gradually depleted through desorption. At 343 K, the yield ratio of D_2 to H(a) is 3:1, and H_2 is not produced. This shows that step (4.4) is fast, probably limited by availability of H(a). From integrating the yield in the 313 K experiment, where the initial coverage of H(a) is expected to be higher, the initial hydrogen coverage is found to be 0.05 ML. At 313 K, there are more hydrogenated products, the initial 'transient' sticking period is longer, and the steady state rate of methane production is much lower than that at 343 K. The lack of CD_2H_2 as a product at either temperature implies that methylene is not a significant intermediate (or product). Although CD_2H_2 has mass 18 as the molecular ion, the mass 18 QMS signal is also a major cracking fragment of CD_4, by consideration of the amount of mass 20 present and hence CD_4 production, the entire mass 18 signal can be attributed to CD_4 only. Thus, the initial major products of this reaction are CD_3H and CD_4. These data thus suggest, in agreement with Shekhar et. al. [43], that methyl, not methylene, is the major intermediate. The initial non-steady state period for these deuterated reactants has a corresponding period of high S(t) for non-deuterated reactants as shown in Fig. 5. CD_3H is produced before HD and D_2, thus showing that hydrogenation of methyl is more favourable than the formation of hydrogen in this reaction. Fig. 5 shows that above 343 K, the adsorbed methyl species become destabilised, associated with an evolution of hydrogen and reduction in initial methane evolution. Accumulation of surface carbon and CO from acetaldehyde decomposition stabilises the methyl group, reducing hydrogen evolution and increasing methyl production with time to a

continuous state. Hydrogen production drops quickly to zero under these conditions. Between 313 and 343 K, CO reaches steady-state production at a relatively slow rate. The LEED data (Fig. 8) below implies that carbon is deposited from dehydrogenation of acetaldehyde. Despite this, the overall reaction continues at a steady-state. This implies that, as in the case of ethene and acetic acid decomposition on the clean surface (Chapter 3), the adsorbed carbon is either beneath the surface plane, possibly in troughs or directly below surface atoms, as it does not block the reaction.

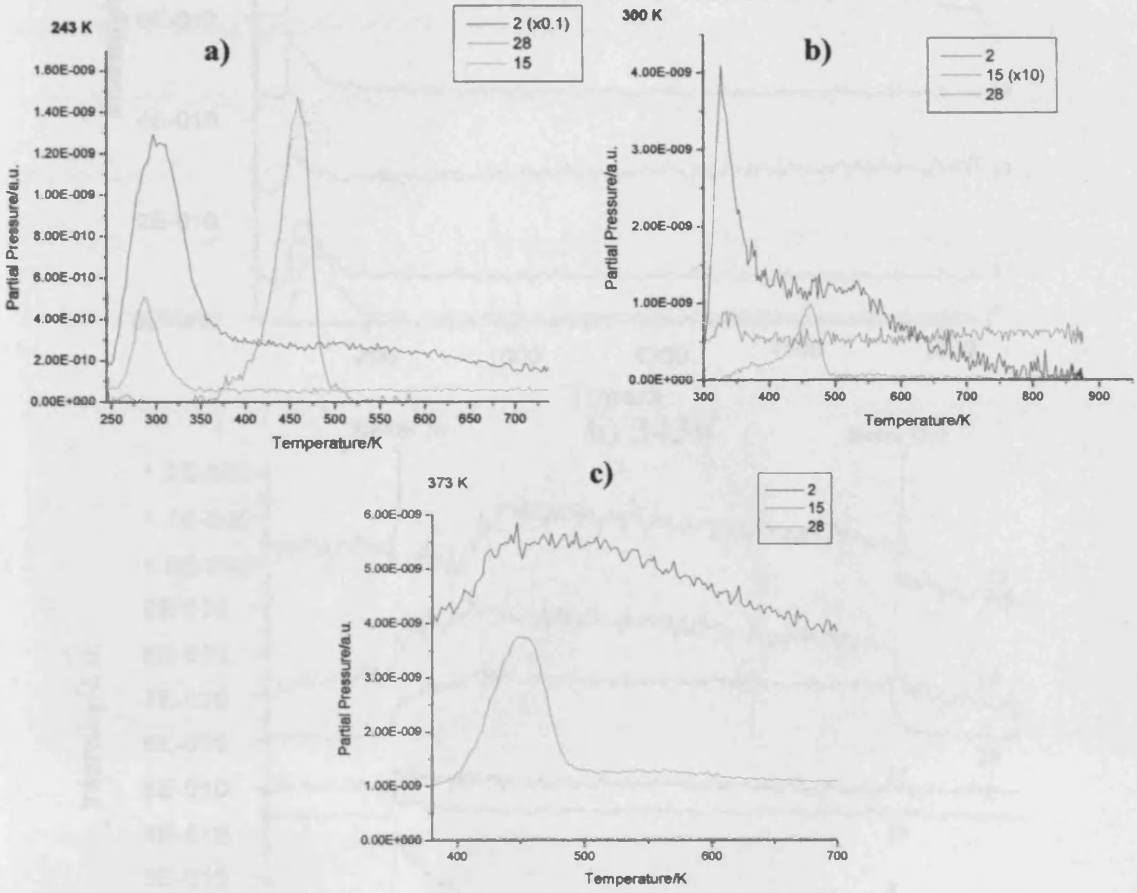

Figure 6: TPD spectra performed after molecular beam reactor experiments for the exposure of the clean Pd (110) surface to acetaldehyde to a variety of adsorption temperatures,a) 243 K, b) 300 K and 373 K. There is evidence of a low temperature (350 K) shoulder to the CO desorption in b) which suggests stabilisation of CO on the surface that does not occur in a) or c).

Note that at 473 K, where dehydrogenation is steady-state in nature, the sticking probability has been observed to remain at 0.64 for at least one hour, where the beam flux is about 0.8 ML a minute. Hence around 30 ML of carbon is deposited over the

course of a one hour experiment, yet it has no apparent effect on subsequent acetaldehyde sticking. This phenomenon was also found for the organic molecules investigated in Chapter 3, and has also seen in molecular beam sticking measurements for ethanol and 1,2-dichloroethene on Pd (110) [44-46].

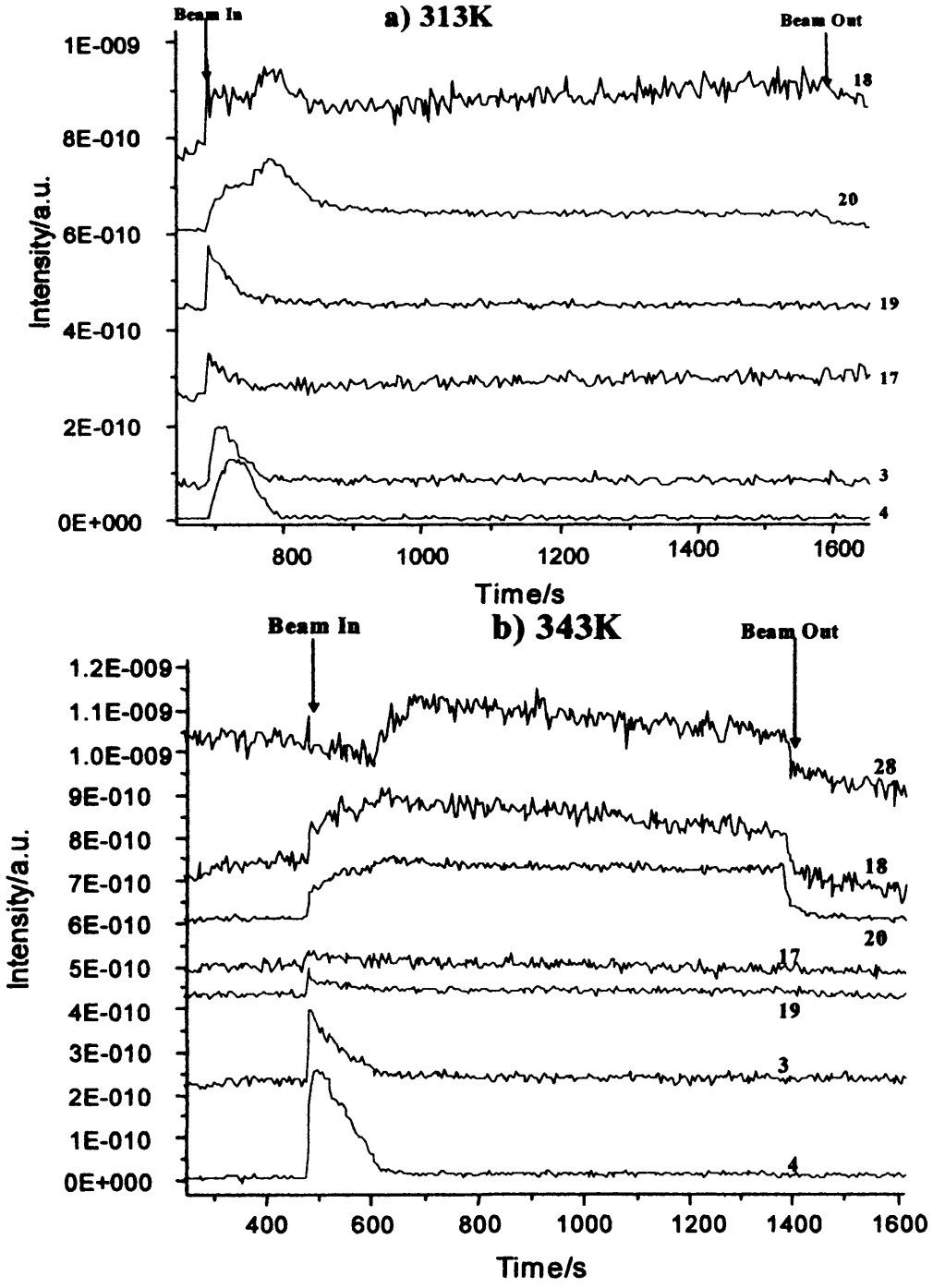

Figure 7: The reaction of CD_3CDO with the Pd(110) surface. The surface had become contaminated with some hydrogen from the background, hence the evolution of hydrogenated products early in the reaction. a) 313K and b) 343K adsorption temperature.

4.3.3. LEED experiments

It is of interest to characterise the carbon layer mentioned above structurally, for instance through LEED experiments (Fig. 8). Dosing at 320 K (B) gives a mostly disordered surface with a faint c(2x2) feature, and 'smearing' in the [001] direction, perhaps indicating a missing row structure with variable missing row periodicity. At higher temperatures, dosing produces a sharper c(2x2) pattern with streaking in the principal crystallographic directions. The c(2x2) is probably a result of the surface carbon produced by acetaldehyde decomposition, as mentioned in the previous sections. This is an ordered layer on which the reaction occurs above 320 K where the methyl group is stabilised, as indicated by the double peak desorption of methane observed in Fig. 5, and continuous desorption of methane at temperatures above 320 K.

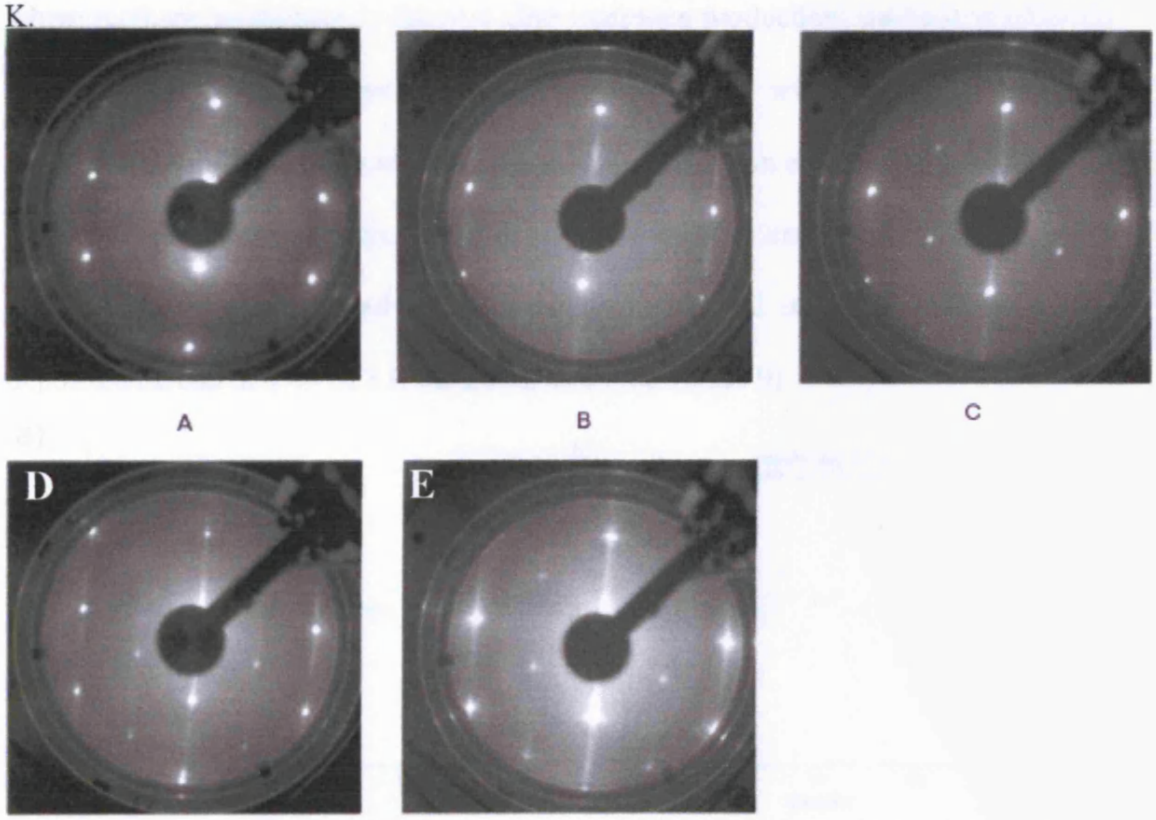

Figure 8: LEED patterns from the clean and C-covered surface of Pd(110). A is the (1x1) pattern from the clean surface at 320K (58ev); B is after dosing $2x10^{-6}$ mbar.s of acetaldehyde at 320K (49eV); C (48eV), D (56eV) and E (50eV) are the same dose onto the previously clean surface at 373K, 403K and 423K respectively, the patterns being taken at the adsorption temperature.

4.3.4 Model for Decomposition of Acetaldehyde on Pd (110)

Figs. 5 & 8 and equation steps 1-6 above provide a coherent model for the reaction. Above 473 K, the stabilised methyl groups are no longer stable enough to support methane formation, and dehydrogenation of methyl by C-H cleavage (step 4.5) is swift, eliminating step (4.4), because the steady state coverage of methyl and adsorbed hydrogen is greatly decreased.

This implies the following overall reaction:

$$CH_3CHO_a \rightarrow 2H_2 + CO + C_{(a)} \qquad (4.8)$$

Surface carbon slows methyl dehydrogenation significantly, as evidenced by Fig. 5 where methane production is delayed after hydrogen production: methane production is initially zero but increases to a maximum plateau over time. Despite this modification of the reaction kinetics, the overall reaction in equation (4.8) still occurs readily at high temperatures on a surface covered by carbon in this way. AES experiments were performed to determine the structural state and location of the deposited carbon at 473- 523 K on the surface (see Figure 9).

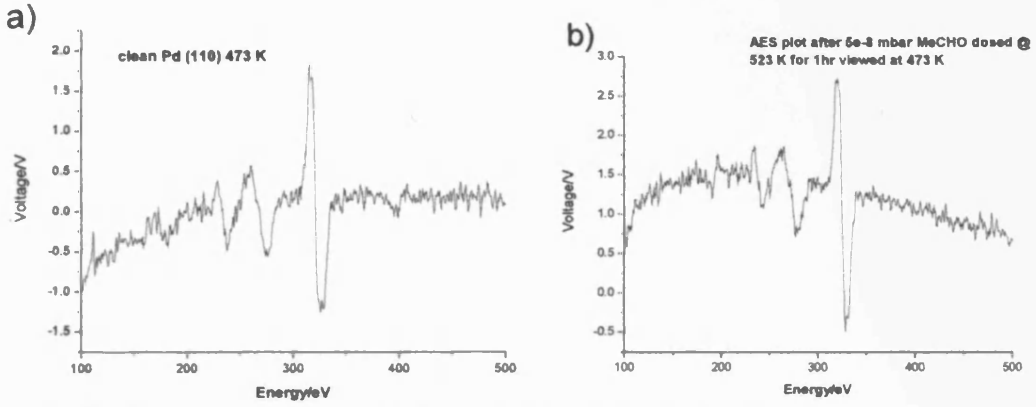

Figure 9: AES spectra for a) clean Pd (110) at 473 K, b) Pd (110) after dosing 100 L acetaldehyde at 5 x 10^{-8} mbar for 1hour at 523 K, viewed at 473 K. Only 0.5 ML of carbon atoms remains on the surface.

The data in Figure 9 indicates that dosing 100 L acetaldehyde which decomposes to carbon between room temperature and 473 K, produces a relatively small carbon signal at 275 eV, suggesting that most of the carbon deposited has diffused into the bulk under these conditions. If all the carbon had remained on the surface, about 50 ML would have been observed. However, taking into account C and Pd (MNN) overlapping at 275 eV and C and Pd sensitivity factors, the C:Pd ratio is significantly smaller: only about 0.5 ML of carbon remains on the surface. This, coupled with a consistently high sticking probability throughout the whole beam experiment at 473 K, suggested that a great deal of the surface carbon has dissolved into the bulk

The sticking behaviour of acetaldehyde on clean Pd (110) at 423 K requires specific discussion – here carbon eventually accumulates such that it poisons adsorption step 1 in the above decomposition process. Hence, methane evolution is initially slow, increases to a high maximum as the methyl group becomes stabilised, then decreases. This behaviour is anomalous in the observed range of experiments: at temperatures above 423 K it appears that the carbon will diffuse subsurface and allow total dehydrogenation of acetaldehyde pseudo-continuously. On a single crystal catalyst such as Pd (110) this process will continue indefinitely.

4.4 Vinyl Acetate Adsorption and Decomposition on Pd (110)

4.4.1 Introduction

Vinyl acetate monomer (VA) is a versatile petrochemical intermediate used in the manufacture of adhesives, coatings, paints, and many other useful substances as described in Section 1.3 (on page 9). The VAM production process has advanced significantly over the past four decades. The original production relied on the homogeneously catalysed reaction of acetic acid and ethylene in the presence of palladium and Cu (II) chloride [38,47]. The catalyst has since become a metal oxide supported palladium catalyst as part of a heterogeneous system to help reduce corrosion and unwanted by-products. Hoescht [48] and Bayer [49] have developed industrial synthesis processes based on Pd only and on Pd-Au bimetallic catalysts respectively. Companies such as BP use catalysts comprising Pd-Au binary systems with promoters such as potassium acetate. An in-depth consideration of the industrial VAM formation mechanism is given in Section 1.4 (on page 13). The fundamental interactions of VAM and the starting materials are not completely elucidated yet. There have been several studies related to the general system, but none have involved direct analysis of vinyl acetate structure and reactivity under UHV conditions. The adsorption and reaction of the heterogeneous process starting materials oxygen, ethene and acetic acid, as well as a key by-product, acetaldehyde, have been reported in previous publications [50-52]. Those findings can help to determine more about the VAM production mechanism. In this section, the reaction of VAM with Pd (110) is reported.

4.4.2 TPD Experiments

Fig. 10 shows the results of TPD experiments carried out by adsorbing 5 L VAM at low temperature (133 K) and at room temperature (323 K). The low temperature adsorption (Fig. 10 a)) shows molecular VAM desorption at 210 K, a large methane desorption at 273 K, and a broad coincident CO and H_2 evolution at 400 K. The overall products are thus methane, CO and H_2 in relative temperatures and quantities similar to those obtained by acetaldehyde decomposition on clean Pd (110) [52], and thus indicate a high selectivity for the splitting of VAM into the acetaldehyde-like acetyl CH_3CO (which decomposes to CH_3 and CO) and $OCHCH_2$ at low temperatures. The relatively large amount of methane produced suggests that the $OCHCH_2$ species may isomerise to CH_3CHO in the presence of adsorbed hydrogen, which is likely to be present as a result of the decomposition of the vinyl group. In the room temperature case, (Fig. 10 b)) there are significant amounts of CO_2 present, and the FWHM of the CO_2 and H_2 maxima are quite narrow (about 15 K) which may suggest that decomposition of VAM to acetate and vinyl occurs under these conditions, producing an autocatalytic surface 'explosion' phenomenon similar to that described in detail in Chapter 3 for acetic acid on Pd (110) [51,53]. Varying the dose of vinyl acetate between 2 and 30 L at this temperature had no effect on the relative integrals of mass 2: mass 15: mass:28: mass 44 ratios, suggesting that at this temperature, the crystal is saturated by 2 L of vinyl acetate.

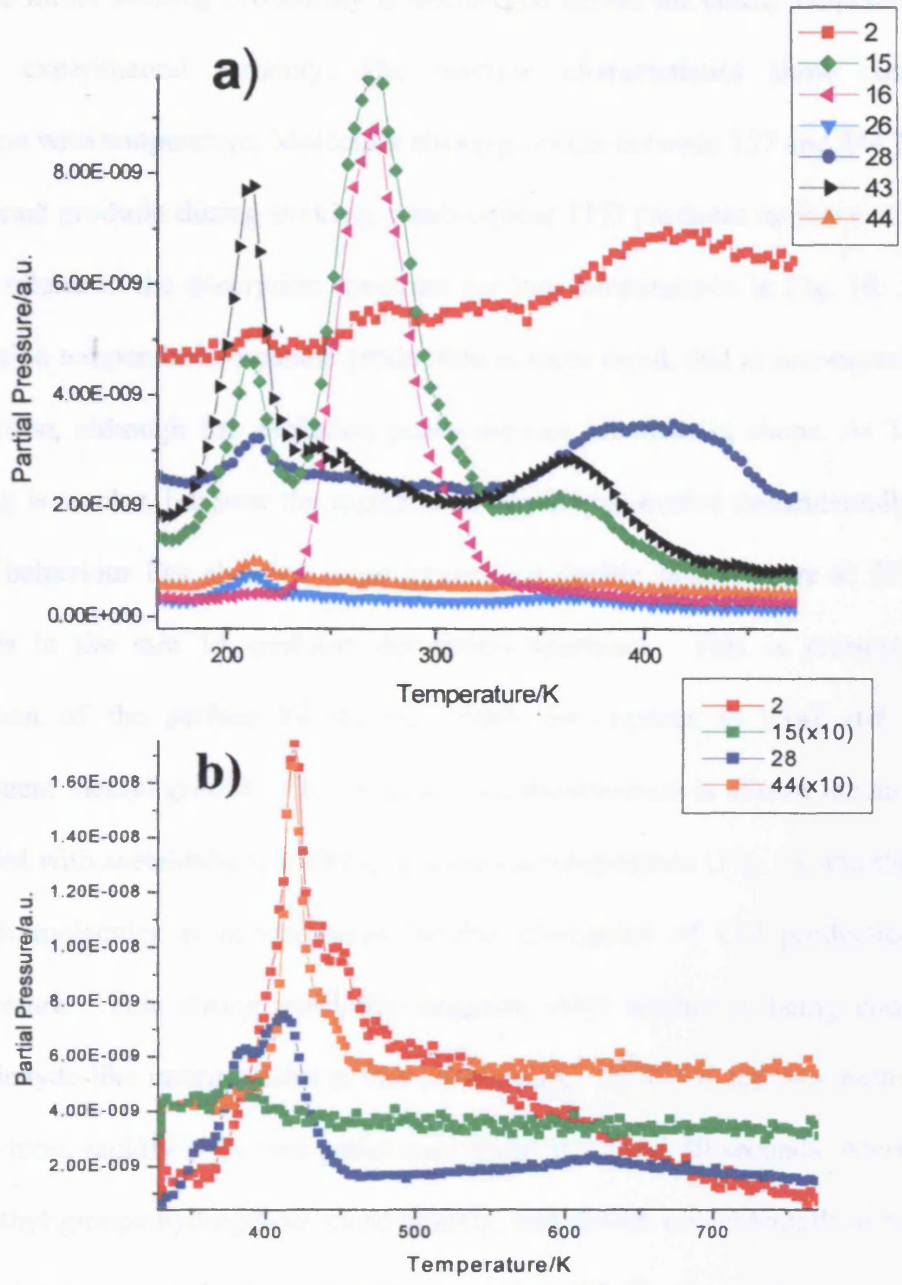

Figure 10: TPD spectra for 5 L Vinyl Acetate on Pd (110) from experiments at a) 133 K and b) 323 K. Ramp rate: 1K/s.

4.4.3 Molecular Beam Sticking Experiments

Figs. 11 and 12 show molecular beam studies over a range of reaction temperatures from 157 to 473 K. S_0 is very high, varying from 0.71 at 157 K , to 0.80 between 248 K and 473 K. The errors associated with these values are quite high due to the very

small mass 43 signal: the error in S(t) is between +/- 0.05 and +/- 0.10, which suggest that the initial sticking probability is unchanged across the entire temperature range within experimental certainty. The reaction characteristics show considerable variation with temperature. Molecular sticking occurs between 157 and 244 K with no significant products during sticking, a subsequent TPD produces methane, H_2 and CO which relates to the desorption spectrum for low temperatures in Fig. 10. At 273 K adsorption temperature, methane production is more rapid, and is accompanied by H_2 production, although the evolution peaks are not identical in shape. At 313 K the sticking is similar, but now the methane and hydrogen evolve coincidentally. At 323 K the behaviour has changed more: there is a double peak feature at 50 and 100 seconds in the m/e 15 methane desorption spectrum. This is probably due to saturation of the surface by methyl which decomposes to C(a) and stabilises subsequent methyl groups. This double peak phenomenon is almost identical to that observed with acetaldehyde sticking at a similar temperature (Fig. 5), and the sticking of both molecules is accompanied by the emergence of CO production at this temperature. This strong similarity suggests vinyl acetate is being converted to acetaldehyde-like intermediates at this temperature. At 333 K the two methane peaks evolve more rapidly – the two peaks now occur at 12 and 50 seconds. Above 393 K, the methyl groups hydrogenate more quickly, and desorb coincidentally with CO in a single desorption peak. At temperatures above 405 K, the sticking continues for longer but is still transient. As the temperature increases, the amount of methane produced decreases until only H_2 and CO are seen as products at 473 K, where the sticking and production is continuous. This behaviour reflects strongly the adsorption behaviour of acetaldehyde on Pd (110), and relates to the surface carbon layer going subsurface or moving to a site where it cannot poison subsequent VAM sticking.

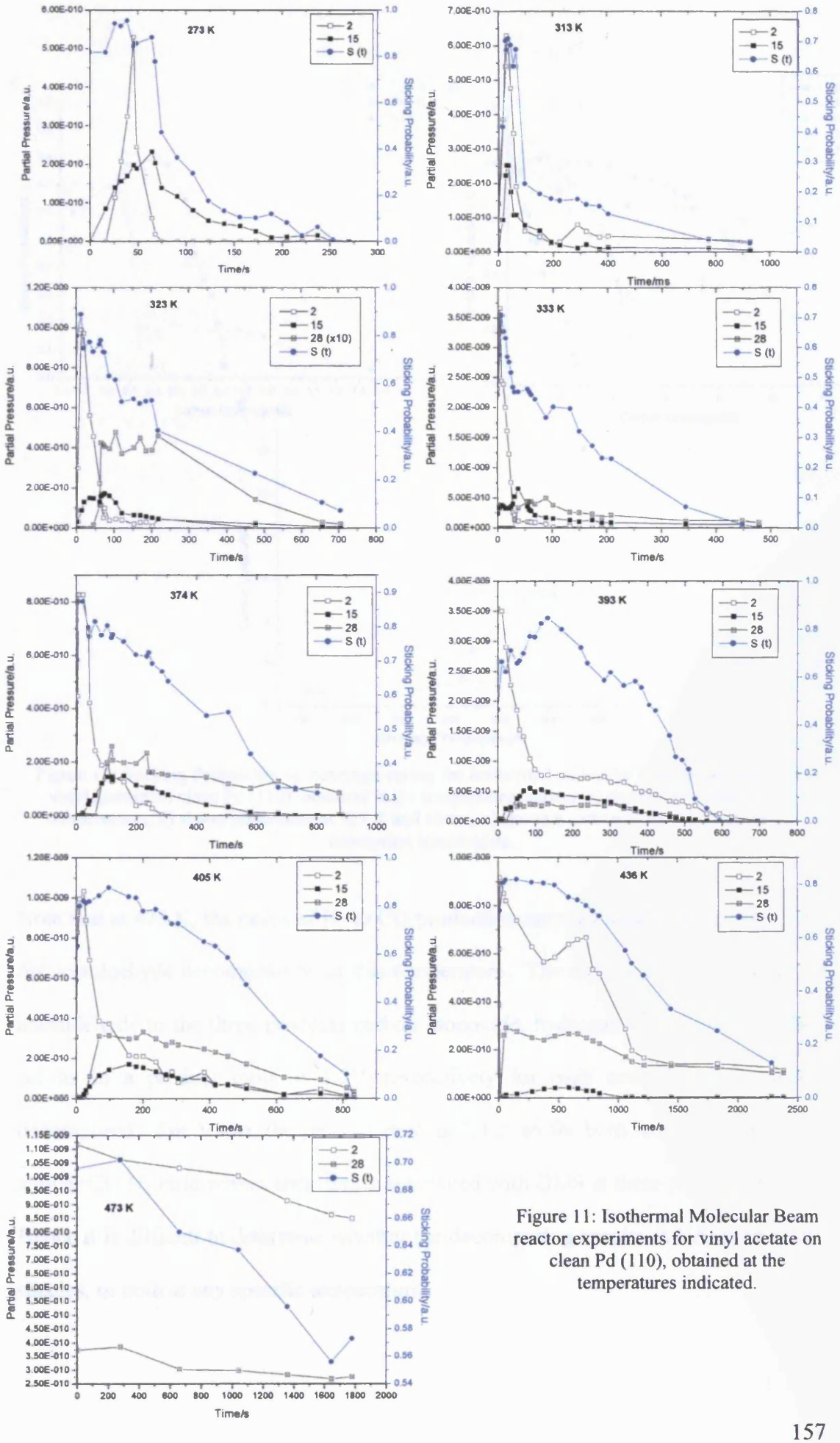

Figure 11: Isothermal Molecular Beam reactor experiments for vinyl acetate on clean Pd (110), obtained at the temperatures indicated.

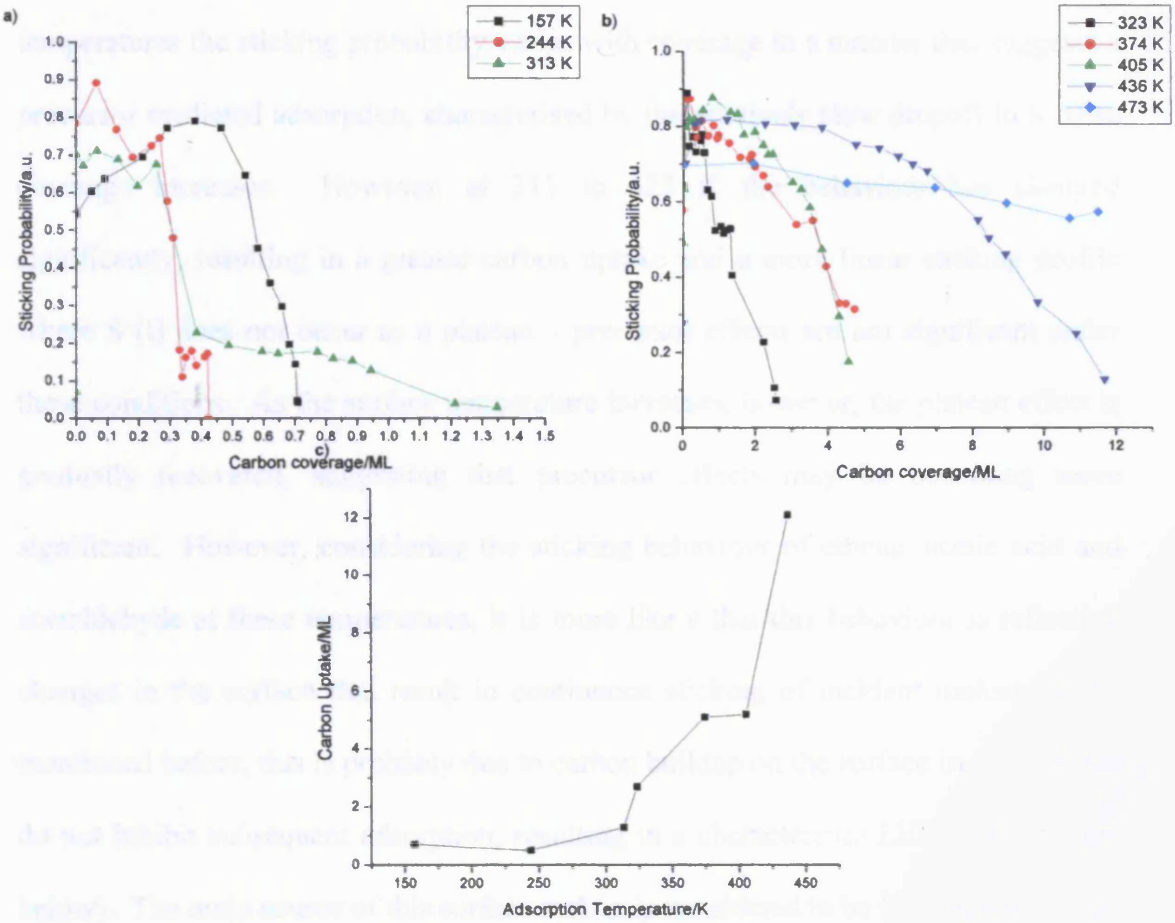

Figure 12: Sticking Probability vs. coverage curves for isothermal molecular beam experiments for vinyl acetate on clean Pd (110), obtained at the temperatures shown. a) shows adsorption at low temperatures, b) shows adsorption at 323 K and above, c) shows a carbon atom uptake curve vs. adsorption temperature.

Note that at 473 K, the ratios of H_2 to CO production are very similar to that observed for acetaldehyde decomposition at this temperature. The complete decomposition of acetaldehyde to the three products carbon monoxide, hydrogen and adsorbed carbon results in a product ratio of 1:2:1 respectively for each acetaldehyde molecule decomposed. For VAM, the product ratio is 2:3:2, so for both molecules there is a similar CO:H_2 ratio within error limits associated with QMS at these partial pressures. Hence it is difficult to determine whether the decomposing species is VAM, an acetyl species, or both at any specific temperature.

The sticking profiles shown in Figure 12 are of interest, showing that at low temperatures the sticking probability varies with coverage in a manner that suggests a precursor mediated adsorption, characterised by the relatively slow dropoff in S (t) as coverage increases. However, at 313 to 323 K the behaviour has changed significantly, resulting in a greater carbon uptake and a more linear sticking profile where S (t) does not occur as a plateau – precursor effects are not significant under these conditions. As the surface temperature increases, however, the plateau effect is gradually recovered, suggesting that precursor effects may be becoming more significant. However, considering the sticking behaviour of ethene, acetic acid and acetaldehyde at these temperatures, it is more likely that this behaviour is reflecting changes in the surface that result in continuous sticking of incident molecules. As mentioned before, this is probably due to carbon buildup on the surface in regions that do not inhibit subsequent adsorption, resulting in a characteristic LEED pattern (see below). The main source of this surface carbon is considered to be from acetyl groups as mentioned above. The absence of any useful LEED data (see below) at temperatures below 473 K makes it impossible to determine the exact saturation coverage across this range. As fig. 12 c) shows, the carbon uptake from VAM increases significantly from 1ML at 323 K to 12 ML at 423 K, becoming an essentially continuous uptake at 473 K. This transition temperature, where the uptake increases at 323 K may be significant: it is where the double peak of methane is observed in sticking experiments, and where CO begins to be produced. Hence 323 K probably relates to the thermally induced onset of decomposition of the acetyl species to methane and CO which may expose Pd sites to subsequent VAM adsorption.

4.4.4. LEED experiments

LEED patterns of VAM on Pd (110) at room temperature and below showed only a high disordered background over the (1x1) unit cell . Adsorption at 473 K produced a c(2x2) overlayer which is likely to be C(a) from VAM decomposition (see Figure 13). The overlayer may also contain some CO(a), although a significant amount of CO will have desorbed from the surface at 473 K. This pattern appears to decrease in intensity on cooling to room temperature which may correspond to a shift in the position of these atoms in the active sites on the surface with temperature changes. Unfortunately, as ethene, acetic acid and acetaldehyde all produce similar patterns under these conditions, these patterns do not give solid evidence on which pathway has occurred, although it does indicate the presence of an ordered carbonaceous structure on which reactions can continue, at least at temperatures above 420 K.

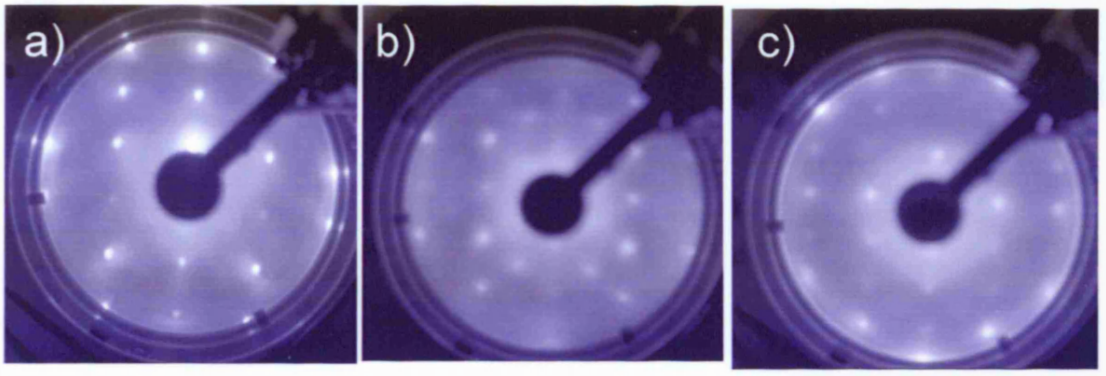

Figure 13: LEED patterns for Pd (110) observed under the following conditions: a) clean at 318 K at 150 eV, b) after dosing 100 L VA at 473 K, observed at 473 K at 153 eV, c) directly after b) but cooled to 318 K and observed at 217 eV.

4.4.5 Models for VAM Decomposition on Pd (110)

VAM appears to decompose via two different pathways, which depend on coverage and substrate temperature:

1) Vinyl Cleavage:

$CH_3COOCHCH_2 \rightarrow CH_3COO(a) + CHCH_2(a)$ (4.9)

$CH_3COO(a) \rightarrow C\ (a) + 3H(a) + CO_2$ (4.10)

$2H(a) \rightarrow H_2$ (4.11)

$CHCH_2(a) \rightarrow$ 'CCH'(a) + '2H' (a) (4.12)

$2H(a) \rightarrow H_2$ (4.13)

By comparison with molecular beam data for deuterated d_4-ethene adsorption on Pd (110) (Section 3.2.2.a)), not all $CHCH_2$ is completely dehydrogenated at temperatures below 400 K, so the 'CCH' in step 11 could be closer to $CCH_{0.7}$. According to the above TPD data, this pathway appears to occur at coverages between 2 and 30 L for VAM adsorbed at 313-323 K, but is surpressed by the 'Acetyl cleavage' mechanism at higher temperatures (see below). However, there is no evidence for the 'Vinyl cleavage' mechanism occurring from the molecular beam sticking data between 313 K and 323 K – the data suggests that vinyl acetate decomposes in a manner similar to acetaldehyde under these conditions. It is proposed that at very low coverages, under conditions similar to those obtained from molecular beam (about 0.2 L), the 'Vinyl-cleavage' mechanism is not preferred, and acetyl is formed, at higher coverages (somewhere between 0.2 and 2 L) the reverse is true. The reason for this is that TPD

performed after the sticking experiments in Fig. 11 at 313-323 K did not produce a characteristic autocatalytic decomposition associated with Vinyl cleavage.

2) Acetyl cleavage:

$CH_3COOCHCH_2 \rightarrow CH_3CO\ (a) + OCHCH_2\ (a)$ (4.14)

$OCHCH_2\ (a) \rightarrow CH_3CO\ (a)$ (4.15)

$CH_3CO(a) \rightarrow CH_3\ (a) + CO\ (a)$ (4.16)

$CH_3(a) + H(a) \rightarrow CH_4$ (4.17)

$CH_3(a) \rightarrow C\ (a) + 3H\ (a)$ (4.18)

$CO\ (a) \rightarrow CO\ (g)$ (4.19)

$2\ H\ (a) \rightarrow H_2\ (g)$ (4.20)

This pathway resembles acetaldehyde decomposition on Pd (110). Step (4.15) involves a hydride transfer (intramolecular rearrangement) step. The Acetyl cleavage route appears to be favoured at temperatures above 323 K, where CO_2 is not observed in TPD's from VAM dosed above 323 K, CO_2 being with the Vinyl cleavage mechanism. As in the acetaldehyde decomposition (see above), steps (4.16) and (4.17) would be rapid above about 300-320 K, and the residence time of acetyl on the surface would be short. At temperatures above 473 K, again in a manner similar to acetaldehyde decomposition, step (4.18) becomes very swift compared to step (4.16) which is essentially eliminated.

The data above suggests that both decomposition routes are possible and should both occur to an extent under most conditions where VAM decomposes, in order for

$OCHCH_2$ to isomerise to CH_3CO and produce methane in the large quantities observed in Fig. 10. At temperatures above 323 K, and at low coverages between 300 and 323 K, there is a greater tendency towards the Acetyl cleavage pathway, and in fact the Vinyl cleavage only appears to occur significantly at high coverages between 300 and 323 K. Why the Acetyl cleavage pathway is dominant under most conditions is not clear, but may be due to a combination of energetic and structural factors – the nature of the $O\text{-}COCH_3$ cleavage may be more exothermic than the alternative cleavage and/or produce species that are more stable on the surface.

An important question is, why would the Vinyl cleavage pathway only be favourable under such specific conditions? The answer may lie in the formation of a layer on the surface, presumably from acetaldehyde decomposition, that can stabilise acetate formation, allowing decomposition at around 423 K in an autocatalytic manner. From TPD experiments for acetic acid on clean Pd (110) (see Chapter 3), acetic acid begins to form H (a) and acetate groups at this temperature, and conversion of acetaldehyde to adsorbed methane, hydrogen and CO begins to become rapid above 300 K, these species begin to desorb at about 320 K (see Figure 10 a)), and some methane will decompose to C(a) and adsorbed hydrogen. It is proposed then, that a 'template' for autocatalytic decomposition is being formed on the surface at 300-320 K and at coverages above about 0.2 L. This template probably consists of a critical concentration of CO which has not desorbed at this temperature: some C(a) from methane decomposition may also contribute. Evidence for a stabilising layer is given by the 'double peak' phenomenon occurring in the mass 15 signal for sticking experiments between 313 and 333 K in Figure 11 – in that particular case methane is being stabilised, but at higher coverages it may be more favourable to stabilise acetate

over methane, resulting in the favourability of the Vinyl cleavage mechanism. At higher temperatures, acetyl decomposes quickly and CO desorbs quickly, and the carbon layer becomes less capable of stabilising acetate, perhaps because of diffusion of C(a) into the bulk, so the autocatalytic decomposition will not occur. At temperatures between 273 and 300 K, most of the adsorbed species are acetyl which will decompose slowly to CO and methane but will not desorb – forming a saturated surface which is not conducive to the formation of a 'template' structure which would favour acetate stabilisation and autocatalytic decomposition, hence the Vinyl cleavage mechanism is not favoured.

REFERENCES:

[1] L. H. Little, N. Sheppard, P. J. C. Yates, *Proc. Roy. Soc.*, **242** (1960) A259.

[2] E. A. Crathorne, D. MacGowan, S. R. Morris, A. P. Rawlinson, *J. Catal.*, **149** (1994) 254.

[3] J. M. Davidson, P. M. Mitchell, N. S. Raghavan, *Front. Chem. React. Eng.*, **1** (1984) 300.

[4] see for instance, J. M. Thomas, W. J. Thomas, '*The Principles and Practice of Heterogeneous Catalysis*', (1996), VCH Publishers Inc., 207.

[5] H. Conrad, G. Ertl, J. Koch, E. E. Latta, *Surf. Sci.*, **43** (1975) 462.

[6] R. M. Lambert, *Surf. Sci.*, **49** (1974) 325.

[7] J. Goschnick, M. Wolf, M. Grunze, W.N. Unertl, J. H. Block, J. Loboda-Cockovic, *Surf. Sci.*,**178** (1986) 831.

[8] J. W. He, P. R. Norton, *J. Chem. Phys.*, **89** (1988) 1170.

[9] P. Hu, L. Morales de la Garza, R. Raval, D. A. King, *Surf. Sci.*,**249** (1991) 1.

[10] M. G. Ramsey, F. P. Leisenberger, F. P. Netzer, A. J. Roberts, A. J. Roberts, R. Raval, *Surf. Sci.*, **385** (1997) 207.

[11] I. Z. Jones, R. A. Bennett, M. Bowker, *Surf. Sci.*,**402** (1998) 595.

[12] I. Z. Jones, R. A. Bennett, M. Bowker, *Surf. Sci.*, **438** (1999) 235.

[13] M. A. Chesters, G. S. Mc Dougall, M. E. Pemble, N. Sheppard, *Surf. Sci.*, **164** (1985) 425.

[14] H. Kato, M. Kawai, J. Yoshinobu, *Phys. Rev. Lett.*, **82** (1999) 1899.

[15] H. Kato, J. Yoshinobu, M. Kawai, *Surf. Sci.*, **427** (1999) 69.

[16] M. Ehsasi, C. Seidel, H. Ruppender, W. Drachsel, J. H. Block, *Surf. Sci.*, **210** (1989) L198.

[17] J. Goschnick, M. Grunze, J. Loboda-Cackovic, J. H. Block, *Surf. Sci.*, **198/190** (1987), 137.

[18] J. W. He, U. Memmert, K. Griffiths, W. N. Lennard, P. R. Norton, *Surf. Sci.*, **202** (1988) L555.

[19] R. Raval, M. A. Harrison, D. A. King, *Surf. Sci.*, **211/212** (1989) 61.

[20] R. Raval, S. Haq, M. A. Harrison, G. Blyholder, D. A. King, *Chem. Phys. Lett.*, **167** (1990) 391.

[21] R. Raval, S. Haq, G. Blyholder, D. A. King, *J. Electron. Spectrosc. Relat. Phenom.*, **54/55** (1990) 629.

[22] A. Wander, P. Hu., D. A. King, *Chem. Phys. Lett.*, **201** (1993) 393.

[23] M. Bowker, Q. Guo, R. Joyner, *Surf. Sci.*, **33** (1991)253.

[24] K. Yagi-Watanabe, H. Fukutani, *J. Chem. Phys.*, **112 (17)** (2000)7652.

[25] X. Guo, J. T. Yates Jr., *J. Chem. Phys.*, **90 (11)** (1989)6761.

[26] W. K. Kuhn, J. Szanyi, D. W. Goodman, *Surf. Sci.*, **274** (1992) L611.

[27] T. Engel, *J. Chem. Phys.*, **69 (1)** (1978) 373.

[28] H. Conrad, G. Ertl, J. Koch, E. E. Latta, *Surf. Sci.*, **43** (1974)462.

[29] E. H. Voogt, L. Coulier, O. L. J. Gijzeman, J. W. Geus, *J. Catal.*, **169** (1997) 359.

[30] F. M. Hoffman, *Surf. Sci. Rep.*, **3** (1983) 107.

[31] H. Conrad, G. Ertl, J. Kuppers, *Surf. Sci.*, **76** (1978) 323.

[32] H. Ohtani, M. A. van Hove, G. A. Somorjai, *Surf. Sci.*, **187** (1987) 372.

[33] P. Kisliuk, *J. Phys. Chem. Solids*, **3** (1957) 95.

[34] D. A. King, *Surf. Sci.*, **64** (1977) 43.

[35] G. Attard, C. Barnes, '*Surfaces*', (1998), OUP, p78.

[36] See, for instance, S. Nishimura, *"Handbook of Heterogeneous Catalytic Hydrogenation for Organic Synthesis"*, Wiley, NY, (2001).

[37] J.F. Waller, *J. Mol. Catal.*, **31**(1985)123

[38] See, for instance, *Chem. Week, 101* **73** (1967); British Patent 964001, 969162

[39] E. Crathorne, D. MacGowan, S. Morris and A. Rawlinson, *J. Catal.* **149** (1994) 254 .

[40] J. Davis, M.A. Barteau, *J. Am. Chem. Soc.*,**111** (1989)1782.

[41] M. Mavrikakis and M.A. Barteau, *J. Mol. Catal. A*, **131** (1998)135.

[42] G. van der Lee and V. Ponec, *Catal. Rev. Sci. Eng.*, **29** (1987)183.

[43] R. Shekhar, M.A. Barteau, R. Plank and J.Vohs, *J. Phys. Chem. B*, **101** (1997) 7939.

[44] M. Bowker, R. Holroyd, R. Sharpe, J. Corneille, S. Francis, and D.W. Goodman, *Surf. Sci.*, **370** (1997) 113-24.

[45] R. Holroyd, R. Bennett, I. Jones and M. Bowker, *J. Chem. Phys.*, **110** (1999) 8703-13.

[46] L. Bloxham, S. Haq, C. Mitchell and R. Raval, *Surf. Sci.* **489** (2001) 1.

[47] I. Moiseev, M. N.Vargaftic, Y. K. Syrkin, *Dokl. Akad. Nauk. USSR*, **133** (1960) 377.

[48] *Eur. Chem. News.*, **11** (1967) 40.

[49] *World Pet. Cong. Proc.*, **5** (1968) 41.

[50] M. Bowker, C. Morgan, N. Perkins, R. Holroyd, E. Fourre, F. Grillo, A. MacDowall, *J. Phys. Chem.*, **109 (6)** (2005) 2377.

[51] M. Bowker, C. Morgan, J. Couves, *Surf. Sci.*, **555** (2004) 145.

[52] M. Bowker, C. Morgan, PCCP, submitted.

[53] N. Aas , M. Bowker, *J. Chem. Soc. Farad. Trans.*, **89** (1993) 1249.

5 THE INTERACTION OF Au/Pd(110) BIMETALLIC SURFACES WITH VAM SYNTHESIS REACTANTS AND PRODUCTS

5 INTERACTION OF Au/Pd(110) BIMETALLIC SURFACES WITH VAM SYNTHESIS REACTANTS AND PRODUCTS

5.1 Introduction

The role of Au in the industrial synthesis of vinyl acetate has been described extensively in Sections 1.6 and 1.7 and is described in brief here. Provine et al. showed that Au enhances the selectivity of the acetoxylation of ethene to vinyl acetate, and suppresses the oxidation of the starting materials to carbonaceous oxides [1]. Carbide formation in used Pd-Au catalysts was initially investigated by Bonarowska et al. [2-3]. Han et al. have investigated Pd-Au/SiO_2 mixed metal catalysts with XPS and XRD, and found that the alloying of Au with Pd is very effective in preventing carbide formation on the Pd catalysts for VAM synthesis [4]. Activity for acetoxylation is also enhanced by the presence of Au in VAM synthesis catalysts, it is improved by a factor of 5-7 [5]. The effects of ageing of Pd-Au-K/SiO_2 VAM synthesis catalysts has been studied by MacLeod et al., using XPS, DRIFTS and TPR [6]. The fresh catalysts were found to contain Pd-Au alloy particles 4-5 nm in diameter which sintered on ageing but did not change in Pd/Au composition. It is clear then that Pd-Au alloying is significant in forming an effective VAM synthesis catalyst [1-6]. Studies of model catalysts in UHV can therefore prove complementary to the above studies. The Pd-Au model catalysts can be obtained in a variety of ways, including producing nanoparticulate arrays of Pd and Au on a metal oxide support, using prepared bulk PdAu alloys in a variety of compositions, or depositing either Pd on Au or Au on Pd crystals using MOCVD or MVD. The last of these catalyst preparation methods was employed as it would provide a convenient comparison to

the results of the previous two Chapters involving adsorption, reaction and decomposition of simple molecules on a clean Pd (110) surface, with reference to VAM synthesis.

5.2 Previous Research

This chapter is associated mainly with the formation of Au films on a Pd (110) surface. This bulk film/surface is shown to reconstruct, and the extent of reconstruction is governed by the coverage of Au and the surface and selvedge morphology. Significant research has already been conducted on this system, including LEED [7], AES [7-9], CO TPD[8], MEIS [10-11] and theoretical analysis [12], to determine the growth mode (the coverage dependent morphology), structure, and the reactivity of the Au films. Unlike Pd (110), bulk Au (110) is relatively unreactive in UHV: CO does not adsorb to it [13], and O_2 only does so at high temperatures under specific conditions [14-15]. Pd and Au are both fcc metals, exhibit a lattice mismatch of 4.8 % [16] and are miscible at all alloy compositions [17]. Like Pt and Ir, Au (110) displays a series of (1xn) missing row reconstructions [18-28] where n can take values of 2 or 3 or above, in contrast to Pd (110) which does not reconstruct at all. The reason for the missing row reconstructions in Au has been elucidated by Ho et al. [25], where the reconstructions are driven by a need for s-p surface electrons to lower their kinetic energy. This is achieved by increasing surface area. The relatively high lattice mismatch between Pd and Au means that thicker Au layers will induce misfit dislocations (defects) that relieve the strain. The strain energy associated with films of increasing depth has an effect of the growth mode[10-11]. Schmitz et al. [8-9] investigated the Au/Pd (110) system produced from MVD at

130 K, using LEED, AES and CO TDS. They found that the growth mode was Stransky Krastanov (SK) (layer by layer growth up to a critical thickness, then island formation) with a critical coverage of 2 ML, corresponding to a complete covering of the Pd lower layer by Au (1 ML of Au coverage leaves the Pd ridge atoms exposed). They used a cross calibration of CO TDS and AES to determine absolute coverages of Au (0 to 7 ML). In contrast, Vos et al., using MEIS studies and MVD at 300 K determined the growth mode to be layer-by-layer only, and suggested misfit dislocations at higher coverage. However, Vos et al. attributed the apparent differences in growth mode to differences in MVD dosing temperature and coverages (up to 3.5 nm thickness). Kaukasoina et al. [7] continued the work of Schmitz et al., and found a (1x1) LEED pattern at coverages below 1.5 ML. At higher coverages, a range of LEED patterns were observed, dependent on annealing temperature and coverage. Annealing these films between 310 and 640 K produced streaky patterns with fractional-order spots. These spots varied continuously from ½-order to 1/3-order as the coverage increased from 1.5 to 4 ML. These streaks were attributed to a mix of relatively small (1x2) and (1x3) domains whose populations varied with coverage. In contrast, if a high coverage Au film was annealed at 640 K, a very sharp (1x2) pattern was observed and this pattern was also attributed to 1.5 ML coverage at lower temperatures. In addition, the LEED patterns become less bright as coverage increases. Thermal dissolution of Au into the bulk occurs at 740-770 K at coverages > 2 ML, and at lower temperatures for lower coverages. The dissolution accompanies a shift from a (1x2) to a (1x1) LEED pattern. These trends were unaffected by varying deposition temperature between 130 and 300 K. Kaukasoina et al. investigated the geometric structure of a (1x2) film annealed at 640 K, and using dynamical LEED analysis [7] found intermixed layers beneath two layers of essentially pure gold, with

a specific optimum geometry: the topmost layer was of the missing row type, the second layer row-paired, and the third layer rumpled. Both Vos et al. [10-11] and Schmitz et al. observed that the streaky (1xz) LEED patterns are not due to alloy formation, as they initially occur well below the temperatures where Pd and Au interdiffuse. However, the sharp (1x2) pattern, which occurs at 640 K (after the (1xz) pattern has changed from a blurred (1x3) to a blurred (1x2) pattern) could be due to a PdAu alloy. The reactivity of these surfaces has not been investigated thoroughly, although the (1x1) and (1xz) bulk terminations are expected to be inhibited by the presence of Au, and the extent of reactivity is probably dependent on Au coverage. Vos et al., investigating film thicknesses between 0.4 nm (about 3 ML) and 3.5 nm (about 23 ML) in the 573-673 K range found significant interdiffusion, with Pd being the diffusing species. Annealing in this temperature range improved the Au layer crystalline quality [10-11]. Nieminen, performing theoretical analysis of the system, supported the experimental data provided by Schmitz et al. in terms of the (1x1) to (1x3) reconstructions obtained with temperature, and the SK growth mode [12].

Au deposition on another Pd surface, (111) has also been studied extensively by Kuk et al. using ISS, AES and LEED [29]. This system behaves quite differently from Au/Pd(110) structurally. Using MVD at 300 K, the growth mode was found to be layer-by-layer, with Au atoms in the first layer filling Pd (111) fcc sites. At 1 ML coverage the structure shifts rapidly from a pseudomorphic single layer to an overlayer with a high defect concentration [29]. In the topmost layer of the substrate, the spacing between Pd atoms in the [111] direction had increased during deposition [29]. Jaklevic investigated the same system with electron reflection spectroscopy, and

found that bulk Au grew at coverages above 3 ML, forming a ($\sqrt{3}$ x 22 +/- 1) reconstruction which has been observed on Au (111) above 4 ML coverage [30].

5.3 Growth of Au Films on Pd (110) using MVD, LEED and AES

In order to form gold films on the Pd (110) surface, an MVD evaporator was constructed as described in Section 2.9. The end of the evaporator was about 15 cm from the crystal surface during dosing. The cylindrical case reflects heat back onto the filament, thus insulating the doser contents from the main chamber and reducing heat dissipation. In addition, it contains and controls the gold vapour which leaves the aperture as a localised beam. It was assumed that a constant supply of power to the filament produces a constant Au flux, in order to control the extent of dosing with time. Deposition was performed at a crystal temperature of 300 K, and the power supplied was 1.2 A and 5 V (6 W) in each case, unless otherwise mentioned.

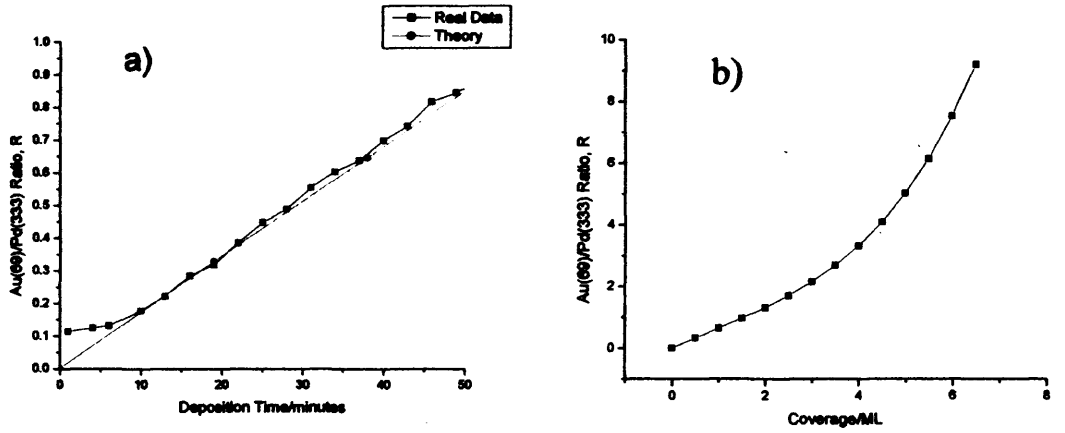

Fig. 1: a) Experimental data for MVD (black), showing variation in Au(69eV) to Pd (333 eV) ratio, R with deposition time, compared to theoretical data (red) suggested by Lu et. al.[31] and Seah et. al [32-33]., assuming 1 ML corresponds to 38 minutes deposition (R=0.65) and a regular layer-by-layer deposition. According to this comparison, the Au coverage does not reach 2 ML of Au, so the possibility of SK growth at 2ML or above cannot be investigated. Fig. 1b) Theoretical results for layer-by-layer growth Au film production profiles, using an RFA analyser, using Equation (5.1) described below and parameters described in the text.

The amount of Au present in the first 3-10 atomic layers was quantified using AES and LEED as described in Chapter 2. AES data were recorded as the peak to peak amplitudes of the derivative Pd_{330}(MNN) and Au_{69}(NVV) Auger transitions after Au depositions, at a beam energy of 3 keV and normal beam incidence. Then the peak heights were measured and expressed as a ratio R of the Au_{69}(NVV)/ Pd_{330}(MNN) signals. The results are given in Fig. 1. Layer-by-layer growth can reveal linear segments intersecting at points where successive layers are completed, but this need not necessarily happen in this growth mode. Using equations which describe substrate and overlayer signal intensities as a function of film thickness [31], it is possible to obtain estimates for the film thickness from the Au_{69}/Pd_{330} ratios obtained:

$$R = [I_a (1 - \exp(-nd_a/\lambda_a))]/[I_s (\exp(-nd_a/\lambda_s))] \quad (5.1)$$

Where I_a and I_s are the Auger electrons signals from the pure, clean adsorbate (of infinite thickness) and substrate respectively at normal incidence, n is the number of adsorbate layers, d_a is the thickness of an adsorbate layer, and λ_s and λ_a are the inelastic mean free paths (IMFPs) of the substrate and adsorbate respectively defined by Seah et al. [32,33]. When using an RFA, which is less accurate than a cylindrical mirror analyser (CMA), it is better to measure a ratio of the adsorbate and substrate signals, rather than just the signal intensity from either Pd or Au [31, 34], as the intensity of a particular peak is very sensitive to crystal position and so may vary considerably between readings. In addition, monitoring a ratio eliminates the need to consider relative Auger sensitivities between Au and Pd. The value of I_a/I_s was found to be 0.68, which is very similar to that obtained by a CMA at 3 keV in the literature (0.70). Elsewhere, in similar comparisons between Co and Cu using STM to cross-

calibrate, the difference in I_a/I_s for an RFA and CMA was larger [35]. I_a was calculated as an extrapolated average over several experiments using very thick Au films obtained from extended deposition times where the Pd signal was minimized. However, there is a large inherent error in the values of I_a and I_s determined between AES spectra, due partly to the limitations of an RFA mentioned above, and also due to the large increase in electron emission at energies below 100 eV which has significance for the Au (69) signal. Hence, by considerations of error, I_a/I_s has an error of +/- 0.1, despite eliminating much of the individual errors in I_a and I_s by considering them as a ratio. Using inelastic mean free paths for Au and Pd of 2 and 5 Å respectively, and a d_a of 2 Å, the theoretical results in Fig. 1 b) were obtained, and suggest that 1 ML of Au forms at R = 0. 65 and 2 ML of Au forms at R = 1.32. These theoretical IMFP values do not resemble those in the literature (4 and 7 Å for Au and Pd respectively [36-37]) but the theoretical trend in R in Fig. 1 b) is linear up to 3 ML, and fits the practical data in Fig 1a) well. It has been suggested in the literature that the growth mode is either completely layer-by-layer [10-11], or SK with a critical thickness of 2 ML [8-9]. Fig. 1 shows that the slope increases smoothly above 2 ML thickness, but there is not a sharp decrease as expected with SK growth [38] hence this data cannot prove conclusively which growth mode is occurring. The slope in Fig 1a) for the experimental data is essentially linear (within error limits) across the time range investigated, with additional Au present at times close to zero. The exact reason for this is not clear, but can be attributed to experimental error in manual control of the power source, or Au being present in trace amounts from previous experiments. Assuming 1 ML (corresponding to R=0.65 in Fig 1 b)) is obtained at 38 minutes of deposition gives a good agreement in slope with the graph obtained by theory, as shown in Fig. 1 a), suggesting that between 10 and 38 minutes the flux

associated with the MVD evaporator is 4.4 x 10^{-4} ML (3.22 x 10^{11} atoms) per second, assuming linear growth in this time region. Note that 1 ML is defined as one adatom per surface Pd atom, or 9.35 x 10^{14} atoms cm^{-2}.

a)

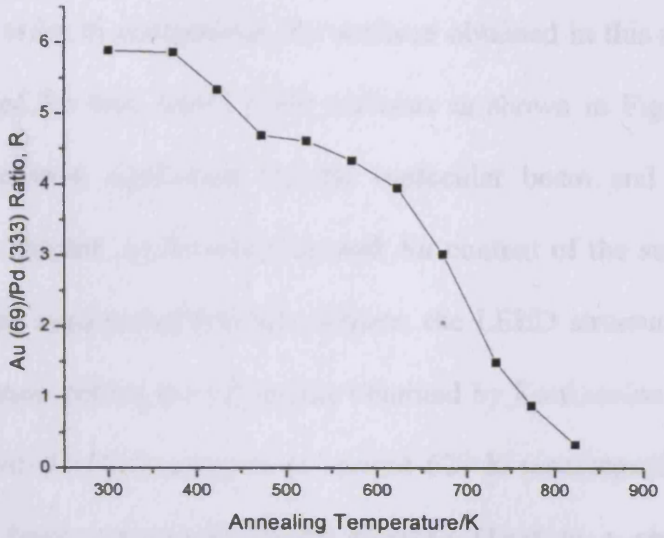

b)

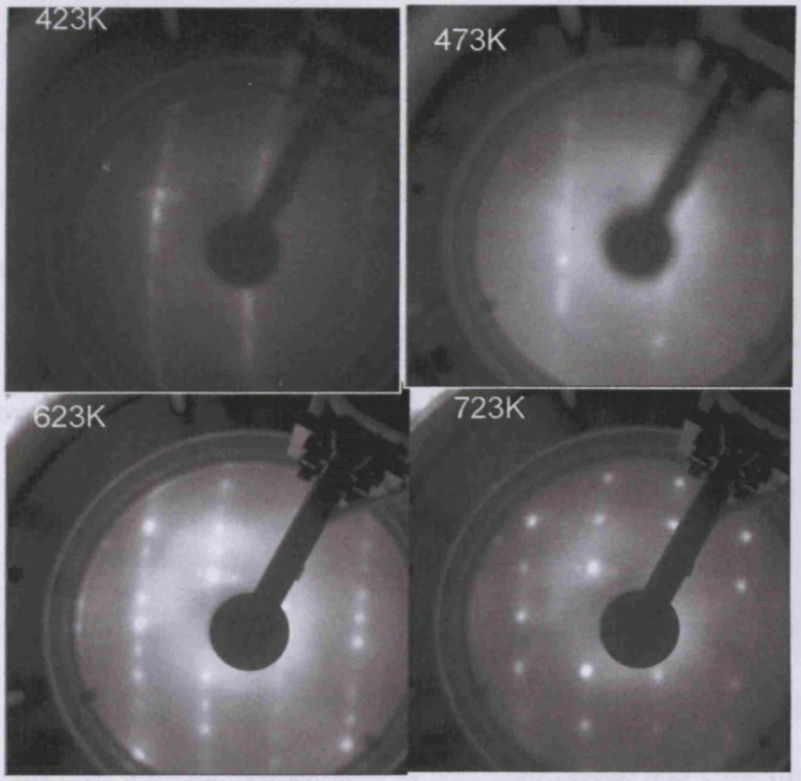

Fig. 2: a) Experimental data for the effects of annealing a thick Au film (5-6 ML) at various temperatures for 5 minutes, observing R at 300 K complements LEED patterns obtained in Fig. 2 b). A sharp dropoff in R (and hence Au coverage) occurs above 623 K, suggesting formation of an alloy, and extensive dissolution at this temperature. LEED beam energies are 87 eV (423 K), 84 eV (473 K), 172 eV (623 K) and 186 eV (723 K).

It has been suggested that at high annealing temperatures, gold may dissipate into the crystal bulk, the exact temperature depending on Au coverage and structure (see above). The structures arising have specific LEED structures as recorded by Schmitz et al. [8-9]. In order to characterise the surfaces obtained in this report, these trends were investigated for two Au/Pd (110) surfaces as shown in Figs. 2 and 3. These experiments are very significant for the molecular beam and TPD experiments reported in this chapter, as the structure and Au content of the surface needed to be defined. For the unannealed 5-6 ML surface, the LEED structures and Au content against temperature resembled the results obtained by Kaukasoina et al. and Schmitz et al.. Significant dissolution occurs at around 623 K (accompanied by a change in LEED pattern from a vertically [110] streaked (1xz) to a sharp (1x2) pattern) compared to 640 K in the literature. In Fig. 2b) there is a thermal progression from a blurred (1xz) (where z is 2 or 3) which alters continuously with coverage between z=3 at 7 ML and z=2 at 2 ML to a sharp (1x2) pattern and after annealing at 623 K for 5 minutes (which may suggest a 1.5 - 2 ML coverage as predicted by Kaukasoina et al. [7] to a (1x1) pattern after 723 K annealing (which suggests an Au coverage of 1.5 ML or below according to Schmitz et al [8-9]). The latter two patterns may be due to alloy formation, but the former two are definitely not alloys, as they occur at temperatures below significant Au dissolution into the bulk. Note that for the unannealed surface, there is some dropoff in Au signal even at around 400 K (Fig. 2), but this is not observed for the annealed 0.78 +/- 0.13 ML surface (Fig. 3). With a 640 K preannealed surface, the dropoff is less significant, and dissolution occurs at around 650 K, becoming very significant at 723 K (Fig. 3). This (1x1) LEED structure could be due to the formation of an Au/Pd alloy where Au and Pd form an intermixed layer, although this could also be due to a bulk-type Au layer on the

surface, and the exact structure cannot be proven on this data alone. The (1xz) structure observed with the unannealed high coverage surface cannot be due to alloying, as it occurs at temperatures far below significant Au dissolution. Hence, on annealed surfaces up to about 1 ML Au concentration, TPD and molecular beam experiments can be performed up to 723 K without a significant change in Au concentration. This is most significant for oxygen sticking and TPD experiments, as the desorption temperature is around 800 K for oxygen on clean Pd (110). *Unless otherwise stated, the following adsorption and desorption experiments were performed on surfaces that were obtained by MVD dosing then annealing at 640 – 723 K until a suitable surface was obtained as determined by AES and/or LEED.* The significant error in R has a large effect on the estimate of Au coverage in the 0-1 ML region, so the errors associated with each surface Au is important and is mentioned in each of the following experiments.

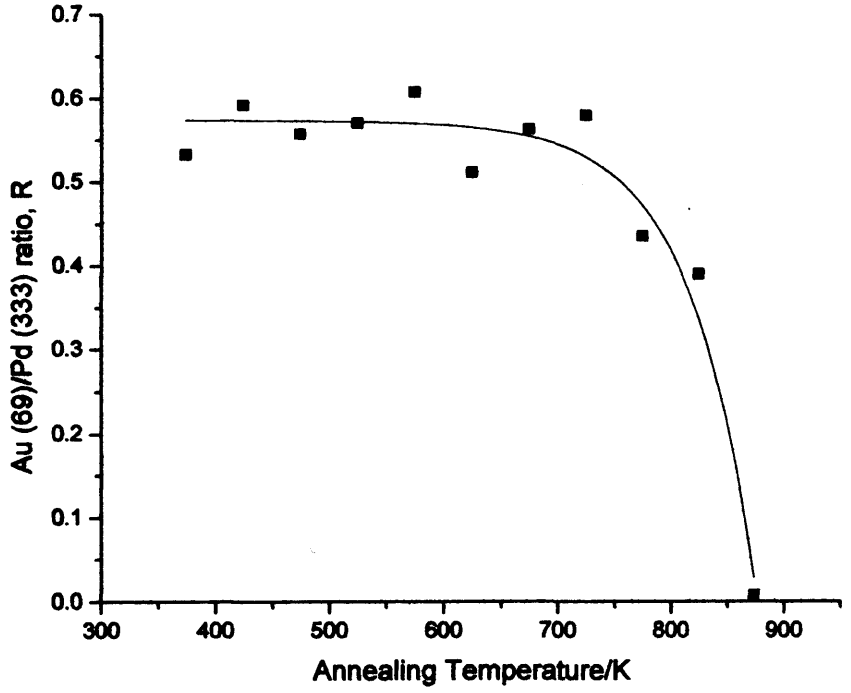

Fig. 3: Experimental data for the effects of annealing a 0.78 +/- 0.13 ML Au film at various temperatures for 5 minutes, then determining R at 300 K. A sharp dropoff in R (and hence Au coverage) occurs above 723 K, suggesting dissolution of Au into the bulk.

5.4 CO Adsorption and Desorption on Au/Pd (110)

Of the six molecules investigated on the following sections, only one has been studied on the Au/Pd(110) system previously. CO TPD experiments were performed by Schmitz et al. who found three specific desorption states at 225, 190 and about 440 K [9]. The first two desorptions were associated with adsorption on first and second layers of a Pd-modified Au surface respectively. The high temperature state reached a minimum intensity when 1 ML of Au was adsorbed and is therefore associated with desorption from Pd. CO interacts only very weakly with bulk Au surfaces, and CO is unstable in vacuum on Au even at very low temperatures. Note that Schmitz et al. used low temperature annealing techniques to obtain their results and did not heat their crystal above the temperatures required to desorb CO (about 440 K).

Experiments using the molecular beam reactor were performed (see Fig. 4) to complement the results obtained by Schmitz et al. and the adsorption and desorption of CO on clean Pd (110) as described in Section 4.2. A quick and efficient method of investigating desorption was employed by performing TPD's directly after the surface was saturated by a molecular beam during an adsorption experiment. Considering the dimensions of the crystal and molecular beam flux spot (about 10% of the crystal area), the saturation coverages for these molecular beaming experiments, is thus about 0.05 – 0.08 ML, depending on the molecules adsorbed, corresponding to saturation of the beam flux spot, with the rest of the crystal essentially clean. However, as adsorption only occurs on about 10 % of the crystal, the rest of the crystal is prone to contamination from background CO and H_2. These 'molecular beam TPD experiments' do, however, provide a quick method of cleaning off CO and

other molecules adsorbed during experiments, and provide useful semi-quantitative data, and minimise the number of heating cycles of the crystal which may cause diffusion of Au into the bulk at high temperatures.

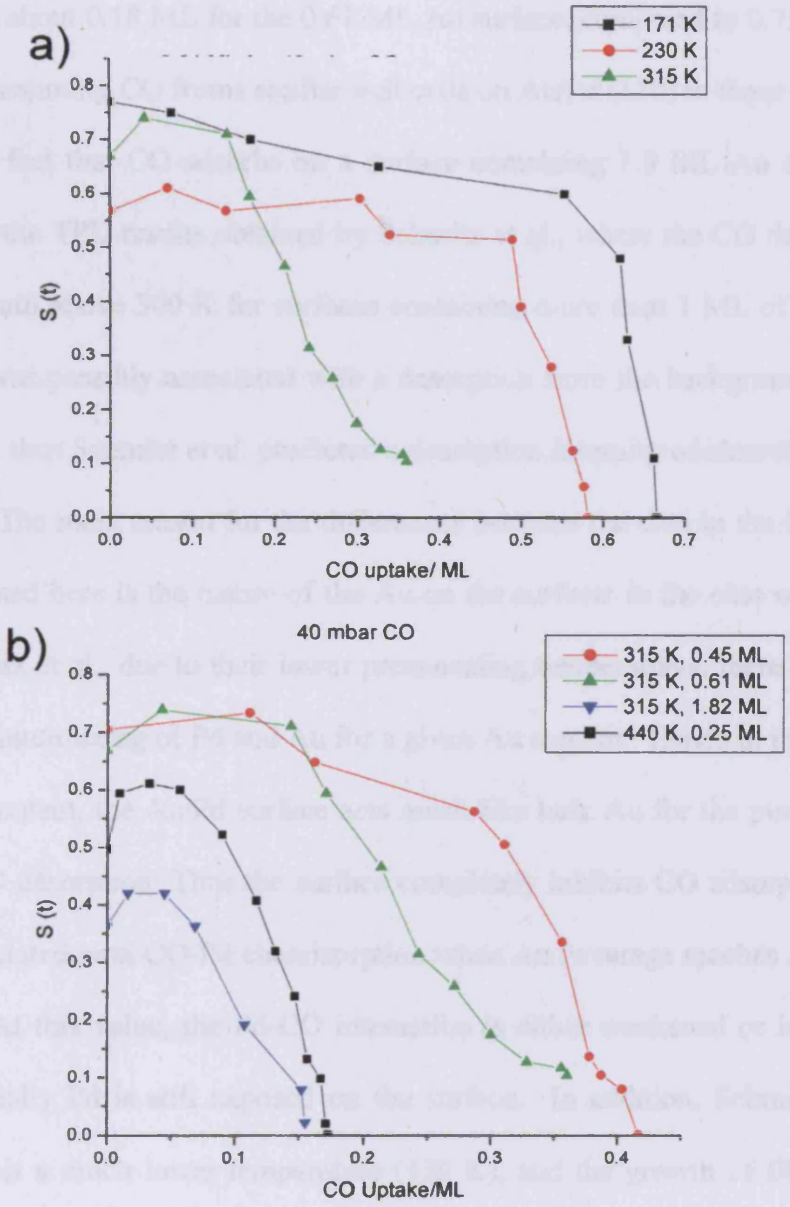

Fig. 4 a) Sticking profiles for a 0.44 ML Au coverage surface at three different substrate temperatures. Fig. 4 b) Sticking profiles at 315 K for three different Au coverages 0.45, 0.61 and 1.82 ML and a lower Au coverage (0.25 ML) at a higher substrate temperature (440 K). The error in each Au coverage is +/- 0.15. The CO beam source pressure is 40 mbar in each case.

At 315 K, CO adsorbs readily on surfaces with an Au coverage of between about 0.3 and 1.8 ML, prepared by dosing Au from MVD and annealing at 523 K for 5 minutes,

all giving sharp (1x1) LEED patterns. The initial sticking probability is high (0.60 to 0.70), and comparable to that for CO on clean Pd (110), which is observed to be 0.70. However, the saturation coverage is greatly reduced: about 0.15 ML for the 0.25 ML Au surface, and about 0.18 ML for the 0.61 ML Au surface, compared to 0.75 ML on clean Pd (110) assuming CO forms similar unit cells on Au/Pd (110) to those on clean Pd (110). The fact that CO adsorbs on a surface containing 1.8 ML Au disagrees somewhat with the TPD results obtained by Schmitz et al., where the CO desorption was at a minimum above 300 K for surfaces containing more than 1 ML of Au, and this minimum was possibly associated with a desorption from the background rather than the crystal, thus Schmitz et al. predicted a desorption intensity of almost zero for such surfaces. The main reason for the differences between the data in the literature and those obtained here is the nature of the Au on the surface: in the case of the Au dosed by Schmitz et al., due to their lower preannealing temperatures, there was less opportunity for intermixing of Pd and Au for a given Au content. Hence in their case, at a given Au content, the Au/Pd surface acts much like bulk Au for the purposes of the > 300 K CO desorption. Thus the surface completely inhibits CO adsorption and desorption associated with CO-Pd chemisorption when Au coverage reaches a critical value (1 ML). At this value, the Pd-CO interaction is either weakened or inhibited, although potentially Pd is still exposed on the surface. In addition, Schmitz et al. dosed their Au at a much lower temperature (130 K), and the growth of films may well vary between 130 K and 300 K. However, in the surfaces used to obtain the data in Fig. 4, Au is detected by AES, but does not inhibit CO-Pd chemisorption to the same extent, and suggests modification of Pd adsorption properties, rather than inhibition. This may suggest on some regions of the crystal an alloy structure has formed on the upper layers, producing a mixture of Pd and Au atomic sites, as well as

Au occurring as bulk Au on the uppermost layer. At low temperatures for the 0.61 ML Au/Pd(110) surface, the initial sticking probability and saturation coverage increase significantly, as seen in low temperature sticking profiles for CO on clean Pd (110) in literature [39-40]. The overall shapes of the sticking profiles are very similar to those obtained in Section 4.2.2, suggesting that the Kisliuk model is applicable to explain the adsorption process [41], that the presence of Au in the surface has not affected the overall mechanism of adsorption, and that it may be simply a site blocker.

Consideration of the molecular beam TPD spectra from the above experiments reveals that the mean CO desorption peak position has shifted slightly from 470 to 460 K. (see Fig. 5). However, in the 0.61 ML Au case, the shift is far more significant: from 470 to 420 K, and occurs at the same temperature as that observed by Schmitz et al. for Au coverages of about 1 ML. Hence, Au modification weakens the CO binding compared to clean Pd (110).

While S_0 is largely unaffected by Au content (for exceptions, see below), the saturation coverage decreases with increasing Au content to about 0.15 ML CO coverage at about 1.82 ML Au coverage (R = 1.18) where presumably about 0.18 ML is still exposed Pd (although there is a significant error associated with this). This may suggest that the CO uptake is a good measure of the amount of Pd remaining exposed, not accounting for possible diffusion of Au into the bulk on preannealing. Note that all Au coverages above 2 ML investigated gave no sticking for CO under the conditions tested. In summary then, for CO adsorption and desorption, the presence of Au appears to inhibit sticking and weaken Pd-CO chemisorption as predicted in Chapter 1 and by Schmitz et al., although the critical value where

chemisorption falls to zero is closer to 2 ML in the studies here. This difference in critical Au content is attributed to partial intermixing of Pd and Au in the studies here, and this may perhaps be quantified in future studies by measuring CO uptake against more Au coverages.

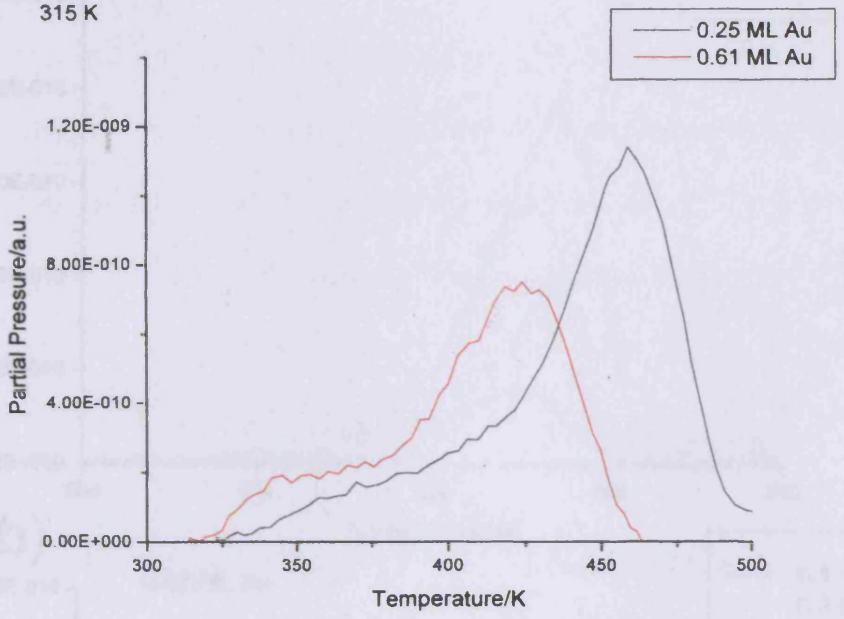

Fig. 5: CO molecular beam TPDs after sticking to saturation for two surface Au concentrations R = 0.16 (0.25 ML) and 0.39 (0.61 ML). CO was adsorbed at room temperature.

5.5 O_2 Adsorption and Desorption on Au/Pd (110)

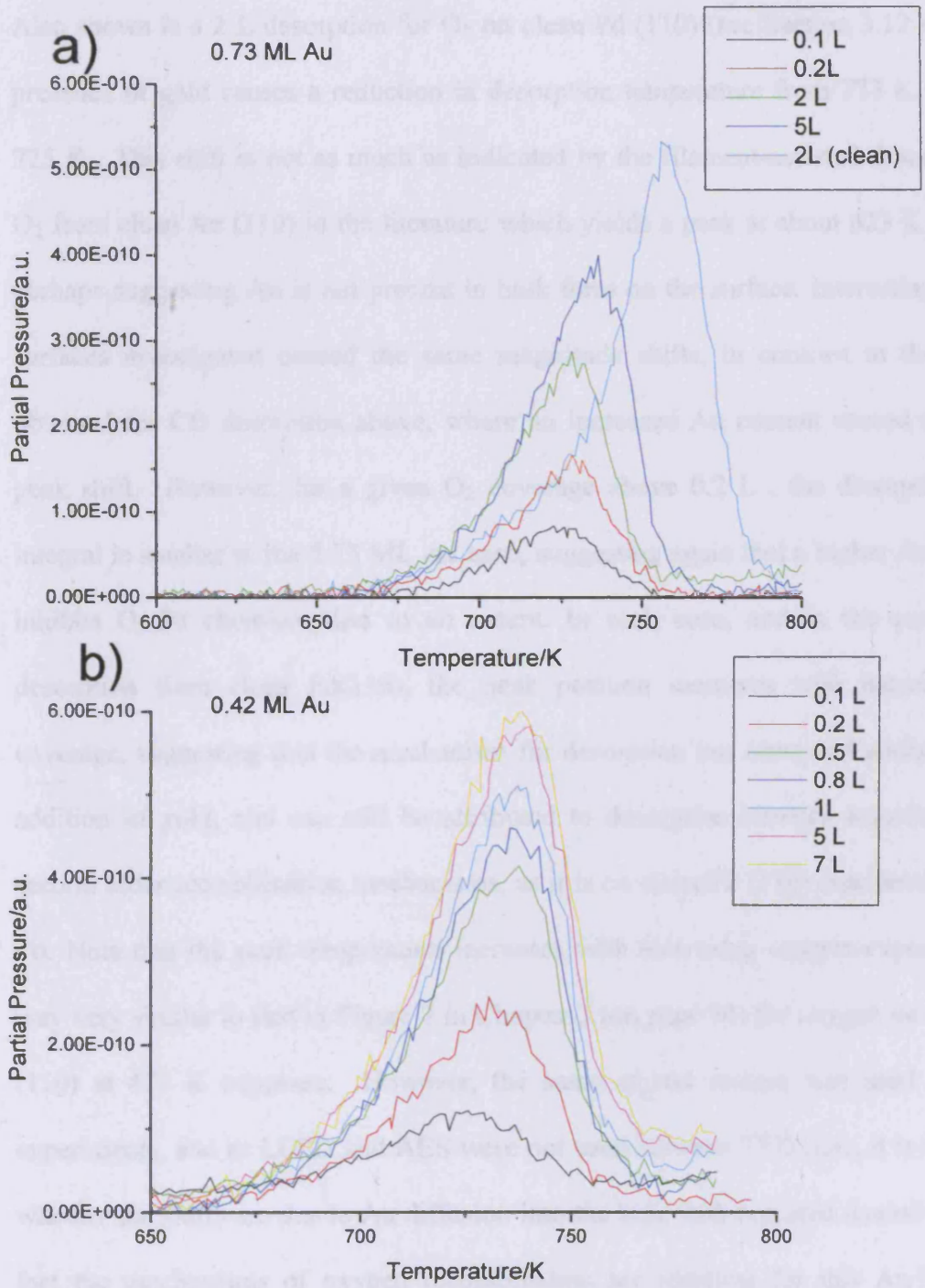

Fig. 6: a) Oxygen TPDs from room temperature for a 0.73 ML Au coverage at various oxygen exposures, compared to a TPD for a clean Pd (110) crystal exposed to 2 L of oxygen at room temperature. TPD runs were performed from lowest coverage to highest. Fig. 6 b) Oxygen TPDs from room temperature for a 0.42 ML Au coverage at various oxygen exposures.

Fig. 6 shows TPD spectra obtained in the usual direct leak manner for two Au/Pd(110) surfaces of 0.73 ML (R = 0.49) and 0.42 ML (R = 0.27) Au respectively. Also shown is a 2 L desorption for O_2 on clean Pd (110) (see Section 3.12 c)). The presence of gold causes a reduction in desorption temperature from 773 K to about 725 K. This shift is not as much as indicated by the filament-assisted desorption of O_2 from clean Au (110) in the literature which yields a peak at about 623 K [13-14], perhaps suggesting Au is not present in bulk form on the surface. Interestingly, both surfaces investigated caused the same magnitude shifts, in contrast to the results obtained for CO desorption above, where an increased Au content caused a greater peak shift. However, for a given O_2 coverage above 0.2 L , the desorption peak integral is smaller in the 0.73 ML Au case, suggesting again that a higher Au content inhibits O_2-Pd chemisorption to an extent. In each case, and in the case of O_2 desorption from clean Pd(110), the peak position increases with increasing O_2 coverage, suggesting that the mechanism for desorption has remained unchanged on addition of gold, and can still be attributed to desorption kinetics associated with second order recombination mechanisms, as it is on clean Pd (110) (see Section 3.1.2 c)). Note that the peak temperature increases with increasing oxygen exposure in a way very similar to that in Figure 7 in Chapter 3 (on page 94) for oxygen on clean Pd (110) at 473 K exposure. However, the same crystal surface was used between experiments, and as LEED and AES were not used between TPD runs, it is not clear whether the shifts are due to Au diffusion into the bulk with repeated annealing, or in fact the mechanisms of oxygen recombination are identical for this Au/Pd (110) surface and a clean Pd (110) as shown in Figure 7 in Chapter 3. Between (p94) TPD runs, it is expected that some of the Au was lost, as the extreme temperatures reached were 800 K (even if they were reached instantaneously). AES data taken before and

after the experiments showed a definite decrease in Au content of about 10 - 20 %. However, these decreases were difficult to avoid due to the high temperatures required.

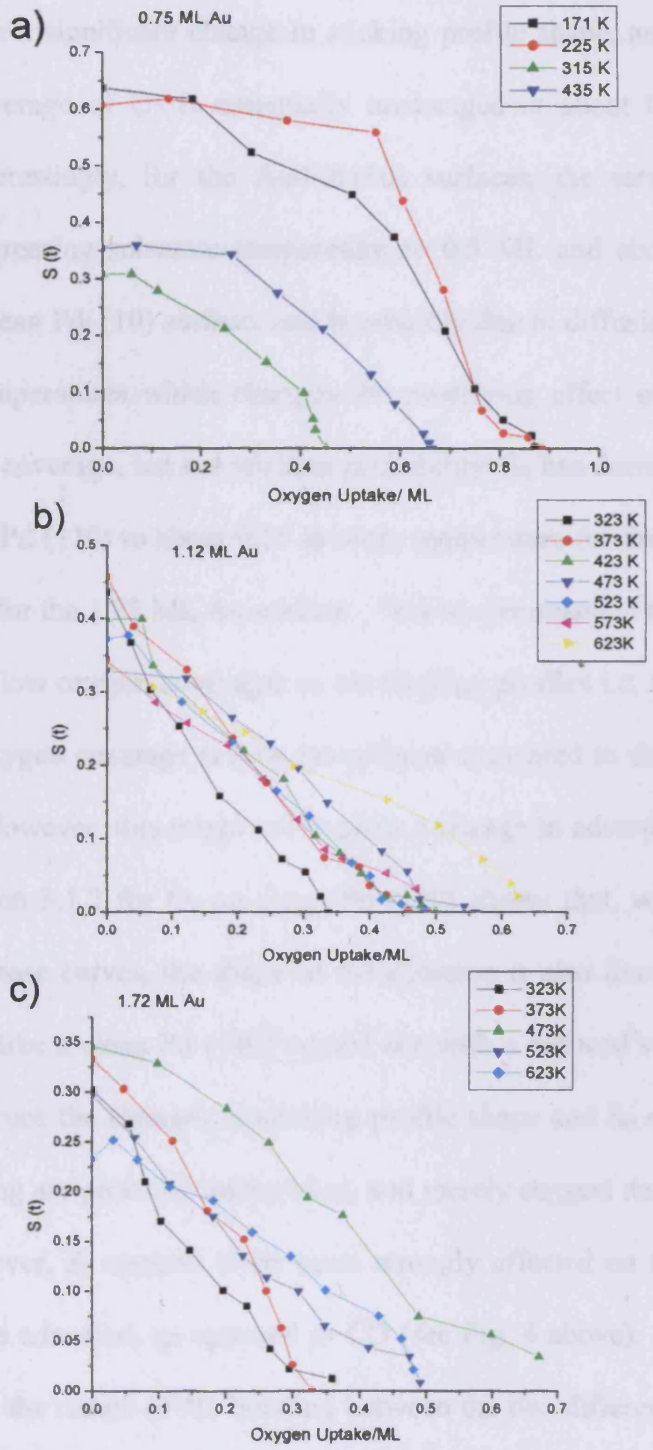

Fig. 7 a) Oxygen sticking profiles for a 0.75 ML Au coverage at various substrate temperatures (40 mbar) b) Oxygen sticking profiles for a 1.12 ML Au coverage at various substrate temperatures (20 mbar) c) Oxygen sticking profiles for a 1.72 ML Au coverage at various substrate temperatures (20 mbar). Sticking experiments were performed in order from lowest temperature to highest, with flashes to 750 K between runs.

Fig. 7 shows sticking profiles varying with temperature for O_2 on Au/Pd(110) for 0.75, 1.12 and 1.72 ML Au coverage. In comparison with sticking on the clean surface, Au causes a significant change in sticking profile shape, and S_0. However, the saturation coverage of O_2 is essentially unchanged at about 0.5 ML at room temperature. Interestingly, for the Au/Pd(110) surfaces, the saturation coverage increases with increasing substrate temperature to 0.5 ML and above – this is not observed on the clean Pd(110) surface, and is possibly due to diffusion of Au into the bulk at higher temperatures which changes the modifying effect of Au: increasing oxygen saturation coverage, but not sticking probability. S_0 has decreased from about 0.6 - 0.8 on clean Pd (110) to about 0.35 at room temperature for the first two Au/Pd surfaces and 0.30 for the 1.72 ML Au surface. This is accompanied by the absence of a small plateau at low oxygen coverages in the sticking profiles i.e. the decrease in S with increasing oxygen coverage is now more linear compared to that for oxygen on clean Pd (110). However, this might not suggest a change in adsorption mechanism, as Fig. 2 in Section 3.1.2 for O_2 on clean Pd (110) shows that, when S(t) reaches about 0.3-0.4 in those curves, the shape of the decrease is also linear, so the crystal may be behaving like a clean Pd (110) crystal but with a reduced surface area from Au inhibition. Hence the changes in sticking profile shape and S_0 on adding Au by MVD and annealing are probably interrelated, and merely suggest an inhibiting effect due to Au. However, S_0 appears to be more strongly affected on the 0.43 ML Au surface when O_2 is adsorbed, as opposed to CO (see Fig. 4 above). The reasons for this may be due to the nature of the bonding between the two different molecules and the modified sites on the same Au/Pd(110) surface. A LEED pattern for 2 L of oxygen adsorbed on the 1.72 ML Au surface showed only a high background and no ordered structure, even though about 0.32 ML of oxygen may be present in the

crystallographic unit cell. In addition, above 1.93 ML (R=1.29) Au content, O_2 did not stick at all, implying that the surface is saturated with Au, preventing any O_2 adsorption. This sudden change is adsorption behaviour across a relatively small change in R (Au content) shows similarities to the sudden reduction in CO uptake noticed by Schmitz et al. on Au/Pd (110) at 1 ML Au coverage. However, at above 1.72 ML Au content, acetaldehyde was found to adsorb and react (see below), suggesting that the nature of the surface is not a simple bulk termination of Au, but behaves specifically towards different molecules. An alternative explanation is that the AES and LEED data cannot provide enough information on the surface Au structure and composition, and the amount of pre-annealing may have a strong effect on reactivity for surfaces with similar R values.

5.6 Ethene Adsorption and Decomposition on Au/Pd (110)

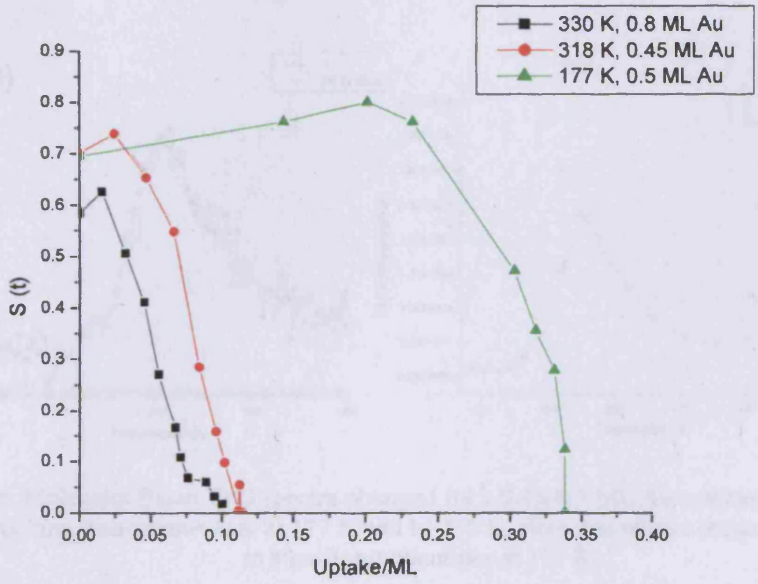

Fig. 8: Sticking profiles for ethene sticking on an Au/Pd(110) where R =0.29-0.34 (about 0.45-0.5 ML) between 318 and 330 K, and a similar sticking profile at 177K where R = 0.54 (about 0.8 ML).

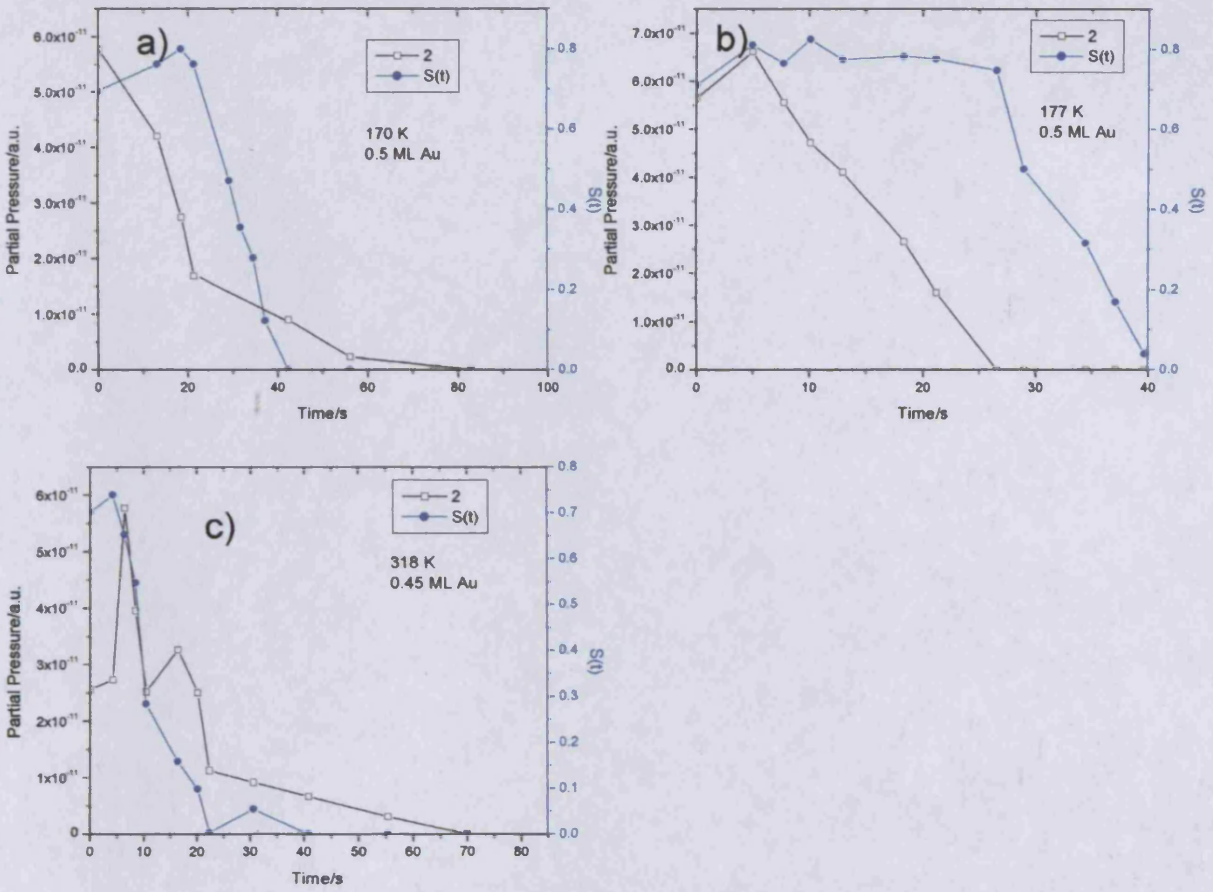

Fig. 9: a) to c) Sticking curves vs. time for ethene sticking on a 0.45-0.5 ML Au coverage surface at temperatures indicated. H_2 is the only product.

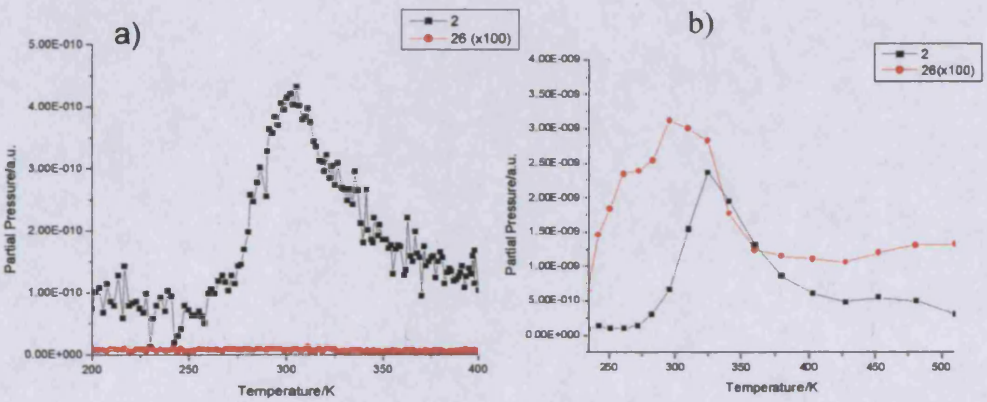

Fig. 10: Molecular Beam TPD spectra obtained for a 0.45-0.5 ML Au coverage surface from isothermal sticking measurements at a) 177 K and b) 230 K. Note that ethene (mass 26) is not produced in significant quantities at 177 K.

Adsorption and desorption of ethene was investigated on a 1 ML Au/Pd(110) surface as shown in Figs 8-10. As the adsorption temperature increases, the sticking profile changes significantly, the value of S_0 remains unchanged but the saturation coverage

decreases by a factor of about 3. Increasing the Au content from 0.45 to 0.8 ML causes S_0 and the saturation coverage to decrease only slightly. Comparing the data in Fig. 8 a) to that for ethene on clean Pd (110) under similar conditions (see Section 3.2.2. Figure 8), the shape of the sticking profile and S_0 are very similar (0.7), however the saturation coverage has decreased significantly from 0.25 ML for clean Pd (110) to 0.10 ML for 0.45-0.5 ML Au (see Figure 8 in this Chapter). Comparing Fig. 9 c) to Figure 9 in Section 3.2.2 shows that H_2 desorbs more rapidly in the experiment with Au dosed. This phenomenon may be due to the fact that the dosing source pressures are different in the two experiments (20 mbar in Section 3, 40 mbar here), but may also imply that dehydrogenation occurs more readily at room temperature on the Au treated surface, but this is not likely, as in all other experiments, the presence of Au reduced reactivity. Comparing Fig. 10 in this chapter with Fig. 10 in Section 3.2.2. for ethene on clean Pd (110), the main decomposition peak temperature is unchanged, but the H_2 yield is much smaller for the Au treated surface, supporting the much reduced saturation coverage implied for this surface in Figure 8. For a 0.45 ML Au covered surface at room temperature, it appears that the Au content has had a much greater effect on saturation coverage reduction in the case of ethene compared to oxygen and CO sticking (see above).

5.7 Acetaldehyde Adsorption and Desorption on Au/Pd (110)

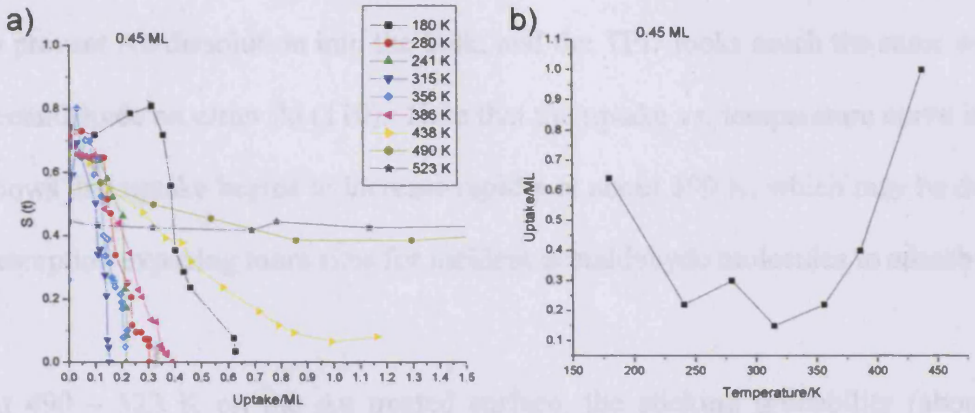

Fig. 11: a) Sticking Profiles for sticking on a R= 0.27 surface (about 0.45 ML Au coverage). b) Actaldehyde Uptake vs. Substrate Temperature for the same surface.

Figures 11 and 12 show sticking data for 40 mbar acetaldehyde on a 0.45 ML Au surface at a variety of substrate temperatures. Comparison of these data with those for acetaldehyde sticking on clean Pd (110) (see Figure 5, in Section 4.3.2) yields some very interesting results. As in the case of ethene, oxygen and CO, Au treatment reduces S_0 and the saturation coverage at temperatures from about 180 K to room temperature. S_0 has only decreased slightly from about 0.75 +/- 0.02 at room temperature for clean Pd (110) to about 0.68 +/- 0.04 for the Au treated surface, and the saturation coverage had fallen from 0.5 ML to about 0.3 ML on the Au treated surface. The yields of H_2 and methane and CO, where they occur, are reduced, corresponding to the drop in saturation coverage. Again, the source pressures are different in the two experiments: in these (40 mbar) experiments the evolution appears to be more rapid as adsorption is twice as fast. Also of interest is that CO only begins to evolve at 386 K which is significantly higher than the 313 K threshold found for clean Pd (110), and as CO is bound more weakly on the Au/Pd(110) surface (see above), this suggests that the surface is less reactive to acetaldehyde decomposition, hence the acetaldehyde will chemisorb but not decompose until a higher temperature

is reached. This cannot be confirmed completely as the molecular beam TPD associated with these experiments (Figure 15 a)) was cut short at about 450 K in order to prevent Au dissolution into the bulk, and the TPD looks much the same as that for acetaldehyde on clean Pd (110). Note that the uptake vs. temperature curve in Fig. 11 shows that uptake begins to increase rapidly at about 390 K, which may be due to CO desorption exposing more sites for incident acetaldehyde molecules to adsorb on.

At 490 – 523 K on the Au treated surface, the sticking probability (about 0.4) is significantly lower than that on clean Pd (110) (about 0.65). The yields of H_2 and CO are lower, as may be expected from the reduced saturation coverages at lower temperatures, and continuous sticking begins to occur at a slightly higher temperature (490 K) compared to the clean surface (see Fig. 5 in Section 4.3.2). It appears that this decreased steady state sticking probability may be due to the augmented Au/Pd surface's ability to prevent carbon diffusion into the bulk more rapidly, allowing less incident acetaldehyde to stick at a particular time. However this cannot be confirmed without LEED and AES data to confirm the structure and concentration (if any) of carbon at the surface at this temperature, and the reduced value of S may be due simply to Au inhibition at the surface.

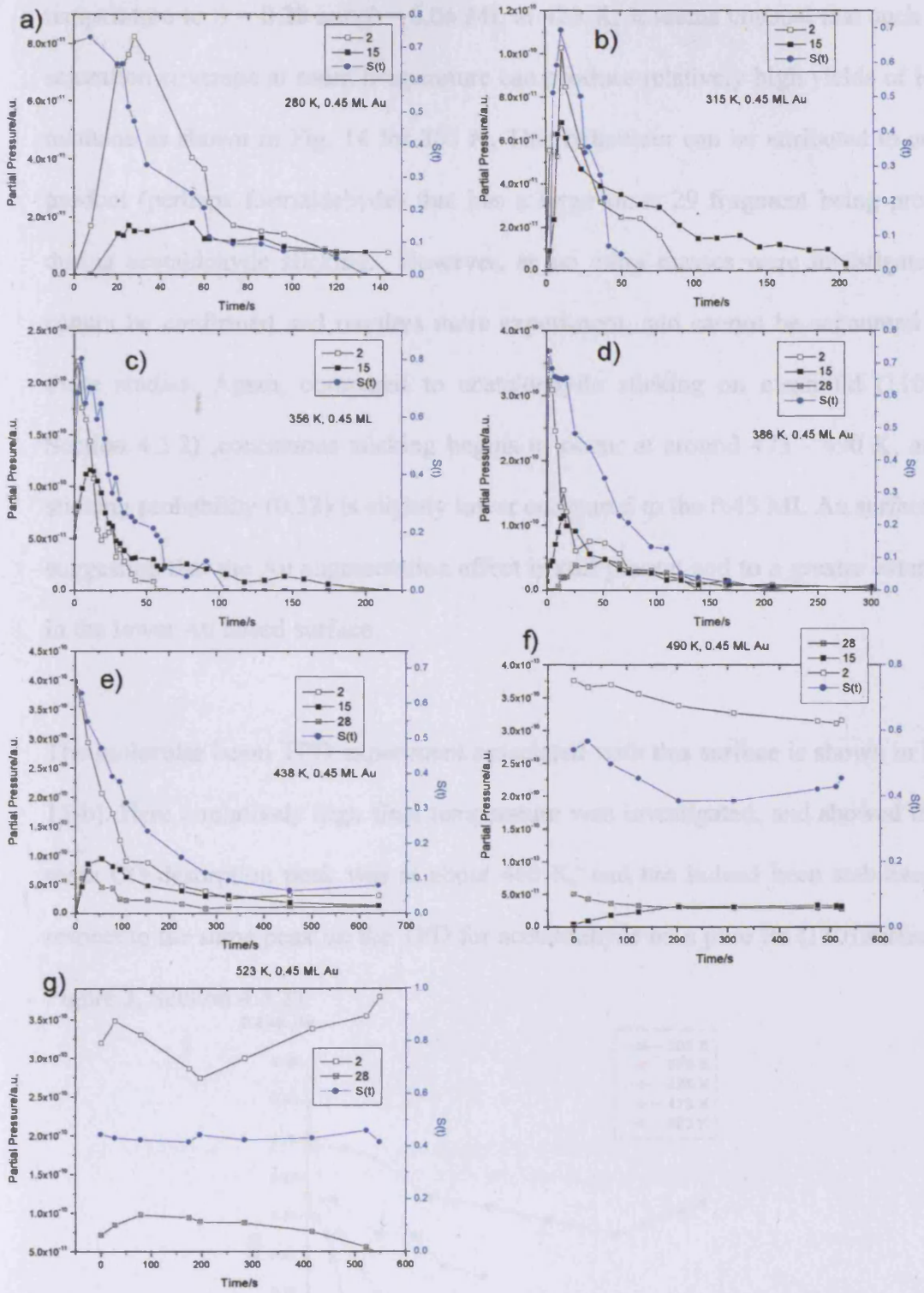

Fig. 12 Isothermal sticking measurements for acetaldehyde sticking on Au/Pd (110) (0.45 ML Au, R=0.27) at various substrate temperatures between 280 and 523 K

On a surface with a far greater Au content (R = 1.49, 2.2 ML), surprisingly, acetaldehyde still sticks to the surface at room temperature, but with a lower S_0 (0.15) and saturation coverage (0.02 ML) (see Figure 13), which both increase with substrate

temperature to S = 0.28 and θ = 0.06 ML at 423 K. It seems unusual that such a low saturation coverage at room temperature can produce relatively high yields of H_2 and methane as shown in Fig. 14 for 303 K. This behaviour can be attributed to another product (perhaps formaldehyde) that has a large mass 29 fragment being produced during acetaldehyde sticking. However, as no extra masses were investigated this cannot be confirmed and requires more experiment, and cannot be accounted for in these studies. Again, compared to acetaldehyde sticking on clean Pd (110) (see Section 4.3.2) ,continuous sticking begins to occur at around 473 - 490 K, and the sticking probability (0.32) is slightly lower compared to the 0.45 ML Au surface (0.4) suggesting that the Au augmentation effect is still present and to a greater extent than in the lower Au dosed surface.

The molecular beam TPD experiment associated with this surface is shown in Figure 15 b). Here a relatively high final temperature was investigated, and showed that the main CO desorption peak was at about 460 K, and has indeed been stabilised with respect to the same peak on the TPD for acetaldehyde on a pure Pd (110) surface (see Figure 3, Section 4.3.2).

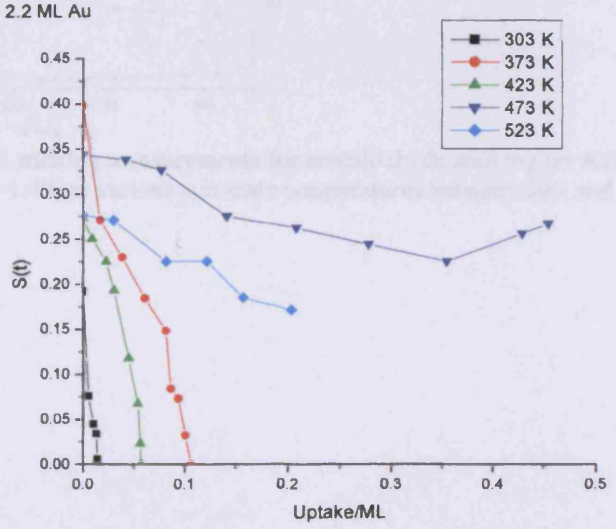

Fig. 13 Sticking Profiles for acetaldehyde sticking on a R= 1.49 surface (about 2.2 ML).

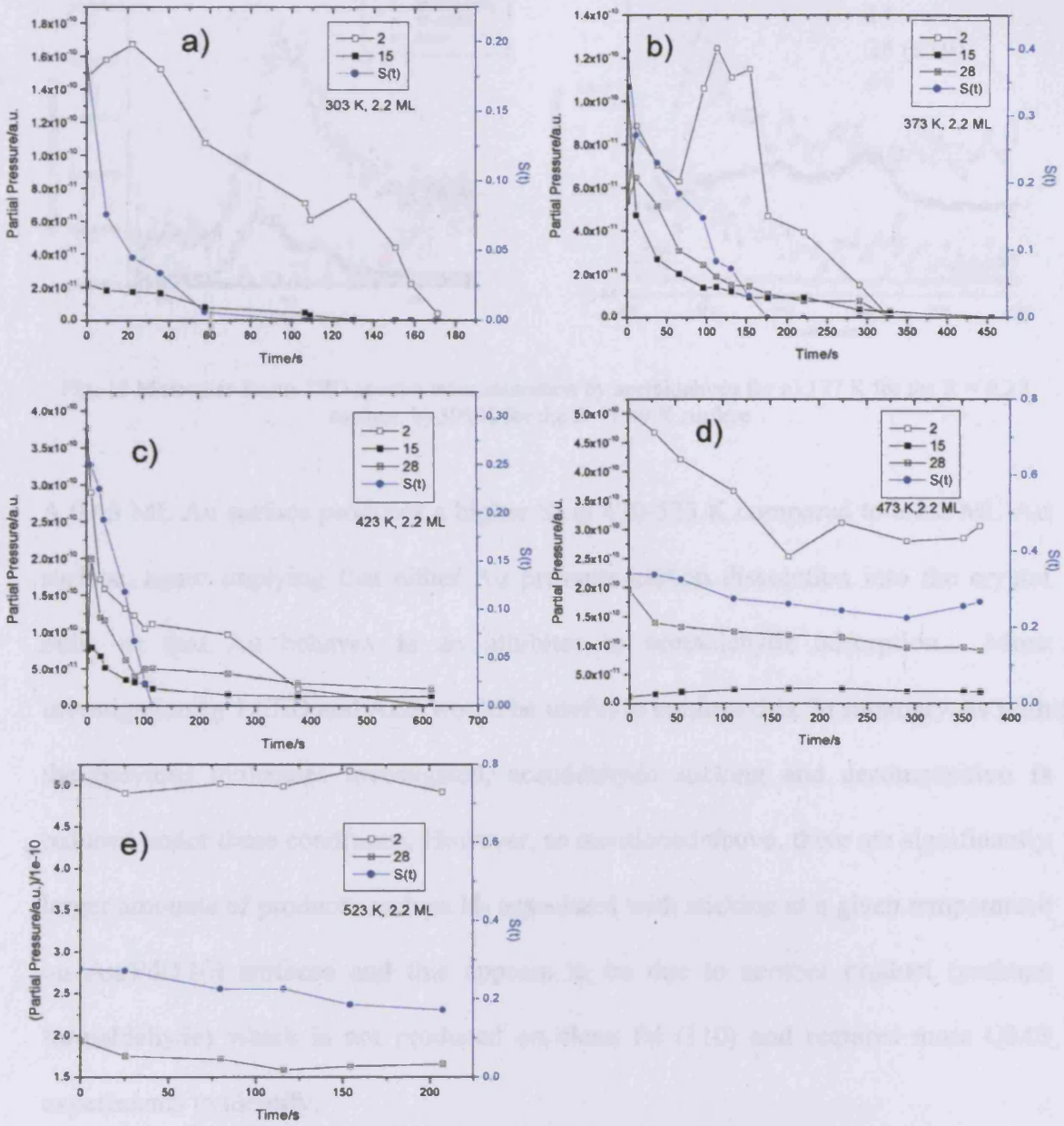

Fig. 14 Isothermal sticking measurements for acetaldehyde sticking on Au/Pd (110) (2.2 ML Au, R=1.49) at various substrate temperatures between 303 and 523 K.

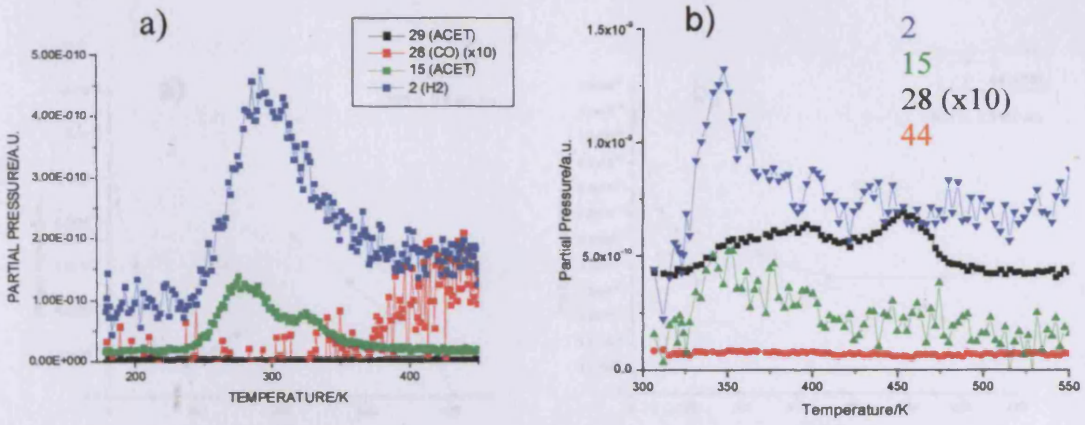

Fig. 15 Molecular Beam TPD spectra from saturation by acetaldehyde for a) 177 K for the R = 0.27 surface, b) 300 K for the R =1.49 K surface.

A 0.45 ML Au surface produces a higher S_0 at 470-523 K compared to a 2.2 ML Au surface, again implying that either Au prevents carbon dissolution into the crystal bulk, or that Au behaves as an inhibitor to acetaldehyde adsorption. More investigation by LEED and AES would be useful to confirm this. In summary, as with the previous molecules investigated, acetaldehyde sticking and decomposition is reduced under these conditions. However, as mentioned above, there are significantly larger amounts of products such as H_2 associated with sticking at a given temperature on Au/Pd(110) surfaces and this appears to be due to another product (perhaps formaldehyde) which is not produced on clean Pd (110) and requires more QMS experiments to identify.

5.8 Acetic Acid Adsorption on Au/Pd(110)

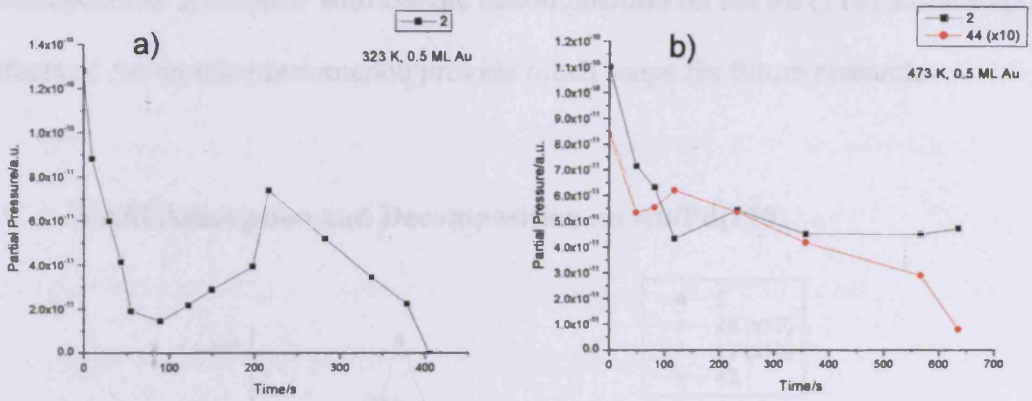

Fig. 16: Acetic Acid sticking curves for an R= 0.34 (0.5 ML) surface at a) 323 K and b) 473 K.

Only a cursory investigation of acetic acid adsorption on a 0.5 ML Au/Pd (110) was performed and the results are shown in Figure 16. The sticking of acetic acid cannot be measured directly using this equipment setup, and only the products H_2 and CO_2 can be detected. The yield of H_2 at both temperatures 323 K and 473 K is small compared to those obtained for clean Pd (110) adsorption (see Figure 21 in Section 3.2.2), suggesting that the saturation coverage is probably low. At 323 K, no CO_2 is produced, and H_2 shows a double peak isothermal desorption which does not occur on clean Pd (110). The reason for this double peak is not clear, although it should be noted that the H_2 partial pressure error is quite large at this relatively low partial pressure. If this feature is real it may imply that acetic acid is stabilised by a layer of acetate on the surface and may decompose at a relatively late time near saturation coverage. This experiment requires repetition and further investigation. At 473 K the desorption of H_2 appears to be continuous, but CO_2 appears to drop off at around 500 seconds. The reason for this phenomenon, which does not occur on clean Pd (110), cannot be determined without TPD experiments which need to be done for future work. The overall shape of the H_2 desorption is very similar to that observed for acetic

acid on clean Pd (110) in Figure 5 in Section 3.2.2. The characteristic autocatalytic decomposition associated with acetate decomposition on the Pd (110) surface and the effects of Au on this phenomenon provide much scope for future research.

5.9 VAM Adsorption and Decomposition on Au/Pd(110)

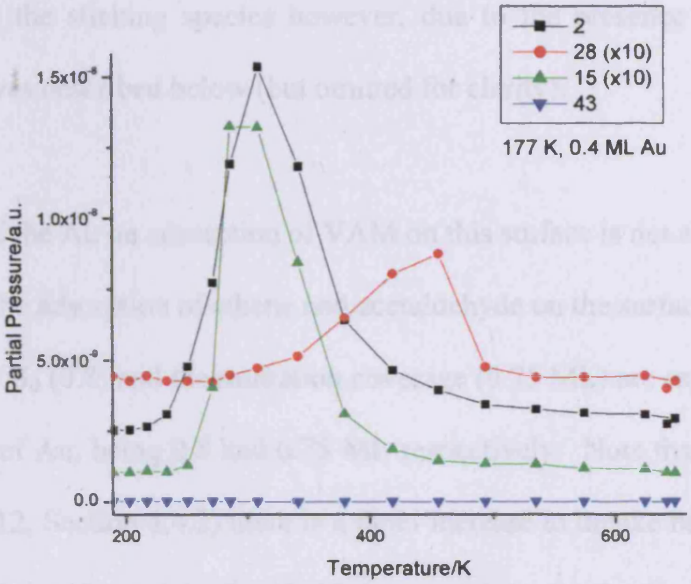

Fig. 17: Molecular Beam TPD for VAM sticking at 177 K where R =0.24 (about 0.4 ML).

A low temperature molecular beam experiment performed on a 0.4 ML Au/Pd(110) surface dosed to saturation with VAM at 177 K shows the results in Figure 17. This TPD resembles an acetaldehyde decomposition on Pd (110) and Au/Pd (110) surfaces described in Figure 3 in Section 4.3.2 and Figure 15 in this Chapter more than the VAM TPD observed on clean Pd in Figure 10 a) from 133 K in Section 4.4.2. In Figure 17, H_2 is a major product at about 300 K, but is much smaller (by a factor of about 13) in Figure 10 a) in Section 4.4.2, but it is possible that there may be significant background H_2 in this particular experiment shown in Fig. 17 often associated with low temperature dosing. There is also no VAM desorption at 200 and 350 K in Figure 17, and the methane signal at 300 K is greatly reduced (by a factor of

about 7). The reason for the contrasts in spectra may be due to the effects of gold dosing, however, the fact that the TPD here is a low coverage molecular beam (about 0.05 ML VAM over the whole crystal) may also be significant. In addition, as mentioned in Chapter 4, the acetyl cleavage mechanism is favoured under these conditions, which were never investigated fully for VAM on clean Pd (110). VAM is undoubtedly the sticking species however, due to the presence of mass 86 in the sticking curves described below (but omitted for clarity).

The effect of the Au on adsorption of VAM on this surface is not as straightforward as it was with the adsorption of ethene and acetaldehyde on the surface (see Figure 18) - The value of S_0 (0.8) and the saturation coverage (0.75 ML) are essentially unchanged on addition of Au, being 0.8 and 0.75 ML respectively. Note that on clean Pd (110) (see Figure 12, Section 4.4.2) there is a rapid increase in uptake between 313 and 323 K which had significance for the VAM decomposition mechanisms proposed, but this phenomenon was not investigated for the Au/Pd(110) surface, and is an opportunity for future research. The evolution of products in the Au treated system changes somewhat compared to the clean surface: at 273 K, 15 is the only product, and there is a distinct delay in H_2 production compared to 15 production at 308 K. In fact the 308 K sticking profile in Figure 19 resembles that for 273 K on the clean Pd (110) surface (see Figure 12, Section 4.4.2). It appears then that H_2 is a decomposition product from acetyl decomposition which is stabilised on Au/Pd(110) surface compared to the clean surface, and this is supported by the positions of the 15 peak relative to the 2 peak in Figure 17. Compared to the clean surface, the mass 2 peak at 273 K has shifted to about 303 K on addition of Au (see Figure 12, Section 4.4.2). The continuous sticking observed at 490 K in Figure 19 c) is also different to that

observed for the clean surface at 473 K. The addition of Au has had little effect on continuous sticking probability (from 0.60 on the clean surface to 0.67 on Pd/Au), and this increase is within the experimental errors in S_0 (+/- 0.1). Note that also, mass 15 is still produced in small quantities at 490 K which may mean that methyl groups are stabilised to higher temperatures on the Au/Pd surface, although the yield of methane is quite small.

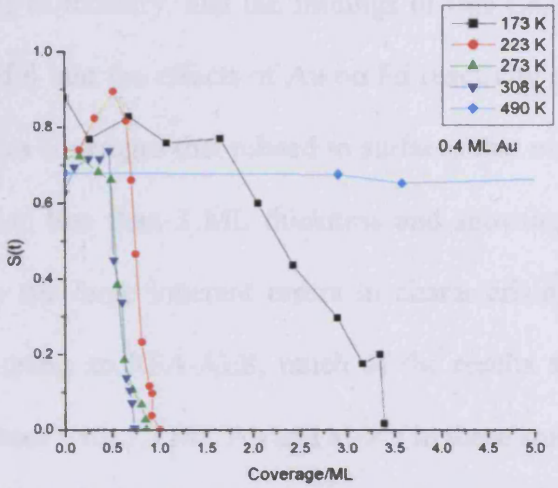

Fig. 18 Sticking Profiles for VAM sticking on a R= 0.24 surface (about 0.4 ML).

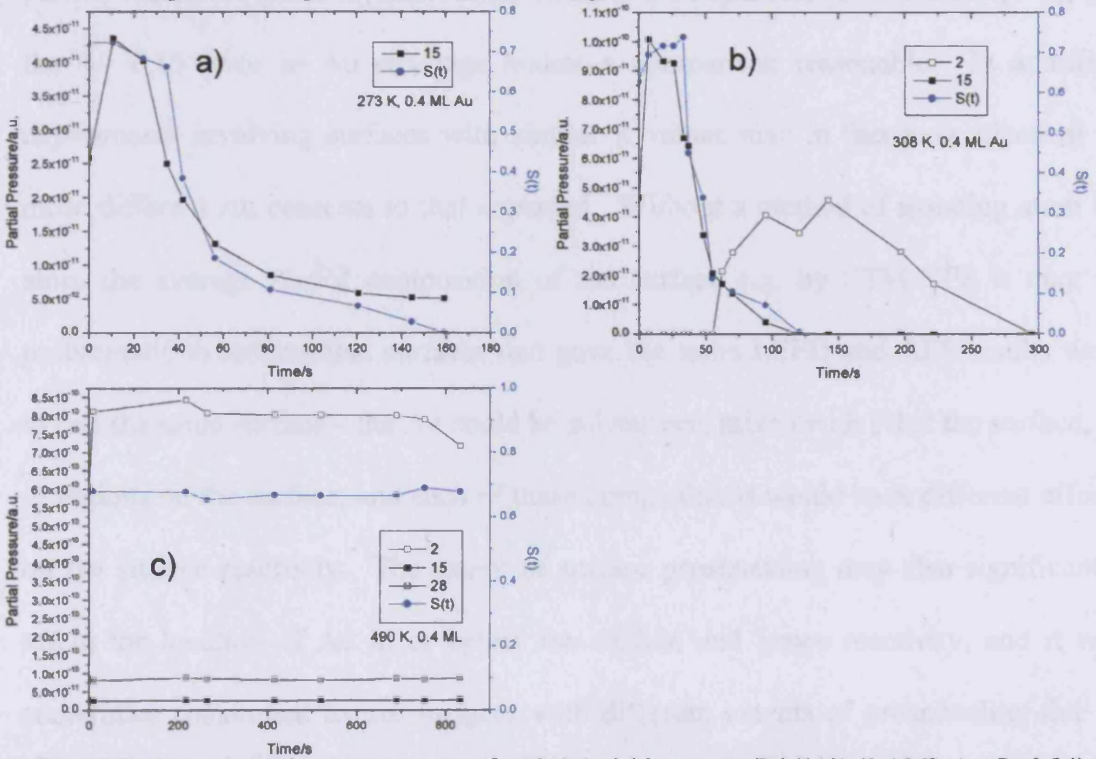

Fig. 19 Isothermal sticking measurements for VAM sticking on Au/Pd (110) (0.4 ML Au, R=0.24) at various substrate temperatures between 273 and 490 K.

5.10 The Bimetallic Au/Pd(110) System

In spite of the relative complexity of some of the molecules investigated in this chapter compared to CO, some such as VAM and acetaldehyde are still useful probe molecules for the Au/Pd(110) system investigated. They also have specific relevance to VAM synthesis in industry, and the findings of this Chapter, while only cursory, have been insightful into the effects of Au on Pd reactivity and selectivity. It was of interest to study Au coverages that related to surfaces that may be alloys as suggested in the literature i.e. less than 2 ML thickness and showing (1x1) and (1x2) LEED patterns. Due to the large inherent errors in characterising the Au content of the surfaces from R using an RFA-AES, much of the results are only qualitative. For instance, the surfaces with 1.3 ML Au and above in these studies showed (1x2) LEED pattern which are generally associated with 1.5-2 ML surfaces in literature [7-9], but the +/- 0.15 error in Au coverage makes a comparison reasonable. In addition, experiments involving surfaces with similar R values may in fact have identical or more different Au contents to that expected. Without a method of isolating atom by atom the average Au:Pd composition of the surface e.g. by STM-XPS it may be problematic to assume that surfaces that gave the same LEED and AES results were in fact the same surface – the Au could be subsurface, mixed with Pd at the surface, or in regions on the surface, and each of these compositions would have different effects on the surface reactivity. The extent of surface preannealing may also significantly affect the location of Au in or below the surface and hence reactivity, and it was sometimes convenient to use surfaces with different extents of preannealing due to time constraints. In the case of the (1x1) structures, Pd/Au alloys could have formed (and this was inferred by the fact that sticking of all the molecules was modified up to

about 1-2 ML at room temperature) by Au occupying the troughs between upper Pd rows, which would still leave an exposed array of Pd rows comprising 50% of the surface, assuming that the Au was completely inhibiting to sticking and chemisorption of the molecules shown in this chapter. Alternatively, in surfaces where the coverage of Au above 2 ML, Au may have completely covered the surface, but the presence of Pd below the surface may have kept the surface reactive. A missing-row version of this structure is proposed in literature by Kaukasoina et al. [7] for 2 ML (1x2) structures prepared by annealing to 640 K which was found to be the threshold for dissolution into the bulk [7]. Other alternative models for fcc (110) (1x2) structures [42] were considered not so favourable. Another alternative is that Au intermixes with Pd atoms completely, occupying Pd sites randomly across the Pd (110) surface. This process is possible as, while it would involve direct substitution of metal atoms in the lattice, the formation of Pd/Au alloys is exothermic. More investigation of these surfaces is needed to confirm their structures, although the experiments in this chapter strongly suggest modification of Pd reactivity by Au as well as partial inhibition of active sites.

Of most interest are the changes in S_0 for continuous sticking of acetaldehyde and vinyl acetate at temperatures above 473 K on Au/Pd (110) surfaces. It would be useful to determine if a carbon layer is present on the surface under these conditions, and how the structure and composition of the surface layer, if any, differs from that on the pure Pd (110) surface under these conditions. Although Au does not inhibit carbon deposition for acetaldehyde adsorption significantly (see Figures 12-14), the effect on continuous sticking of acetic acid and ethene (and potentially ethanol and other related molecules) may be different. It would be of interest manipulate the Au

content of these surfaces more carefully to find a more exhaustive range of reactivity against Au content, which will have significance to the industrial production (and unwanted decomposition) of VAM using Pd/Au catalysts.

REFERENCES:

[1] M. Neurock, W. D. Provine, D. A. Dixon, G. W. Coulston, J. J. Lerou, R. A. van Santen, *Chem. Eng. Sci.*, **51** (1996) 1691.

[2] M. Bonarowska, J. Pielaszek, V. A. Semikolenov, Z. Karpinski, *J. Catal.*, **209** (2002) 528.

[3] M. Bonarowska, A. Malinowksi, W. Jusczy, Z. Karpinski, *Appl. Catal. B. : Environ.*, **30** (2001) 187.

[4] Y. F. Han, D. Kumar, C. Sivadinarayana, A. Clearfield, D. W. Goodman, *Catal. Lett.*, **94 (3-4)** (2004) 131.

[5] W. D. Provine, P. L. Mills, J. J. Lerou, *Stud. Surf. Catal.*, **101** (1996) 191.

[6] N. MacLeod, J. M. Keel, R. M. Lambert, *Appl. Catal. General A*, **261** (2004) 37.

[7] P. Kaukasoina, M. Lindroos, O. L. Warren, P. A. Thiel, *Surf. Sci.*, **318,** (1994) 243.

[8] P. J. Schmitz, H. C. Kang, W. Y. Leung, P. A. Thiel, *Surf. Sci.*, **248** (1991) 287.

[9] P. J. Schmitz, W. Y. Leung, H. C. Kang, P. A. Thiel, *Phys. Rev. B*, **43 (11),** (1991), 8834.

[10] M. Vos, I. V. Mitchell, *Nucl. Instr. & Meth. In Phys. Res.*, B72 (1992) 447.

[11] M. Vos, I. V. Mitchell, *Phys. Rev. B*, **45 (16),** (1992) 9398.

[12] J. A. Nieminen, *Phys. Rev. Lett.*, **74 (19),** (1995), 3856.

[13] D. A. Outka, R. J. Madix, *Surf. Sci.*, **179** (1987) 351.

[14] N. D. S. Canning, D. Outka, R. J. Madix, *Surf. Sci.*, **141** (1984) 240.

[15] A. G. Sault, R. J. Madix, *Surf. Sci.*, **169** (1986) 347.

[16] C. Kittel, '*Introduction to Solid State Physics*', 5th Ed., Wiley, New York, (1976).

[17] E. G. Allison, G. C. Bond, *Cat. Rev.*, **7** (1972) 233.

[18] W. Moritz, D. Wolf, *Surf. Sci.*, **88** (1979) L29.

[19] G. Binnig, H. Rohrer, C. Gerber, E. Weibel, *Surf. Sci*, **131** (1983) L379.

[20] G. A. Held, J. L. Jordan-Sweet, P. M. Horn, A. Mak, R. J. Birgeneau, *Solid State Commun.*, **72** (1989) 37.

[21] D. G. Fedak, N. A. Gkostein, *Acta. Metall.*, **15** (1967) 827.

[22] D. Wolf, H. Jagadzinski, W. Moritz, *Surf. Sci*, **77** (1978) 265.

[23] J. R Noonan, H. L. Davies, *J. Vac. Sci. Technol*, **16** (1979) 587.

[24] P. L. Estrup, '*Chemistry and Physics of Solid Surfaces*', Vol. 5, Springer, Berlin, (1984) p205.

[25] K. M. Ho, K. P. Bohnen, *Phys. Rev. Lett.*, **59** (1987) 1833.

[26] J. Moller, K. L. Snowdon, W. Heiland, *Surf. Sci.*, **178** (1986) 475.

[27] M. Copel, T. Gustafsson, *Phys. Rev. Lett.*, **57** (1986) 723.

[28] I. K. Robinson, *Phys. Rev. B,* **33 (6)** (1986) 3830.

[29] Y. Kuk, L. C. Feldman, P. J. Silverman, *Phys. Rev. Lett.*, **50** (1983) 511.

[30] R. C. Jacklevic, *Phys. Rev. B*, **30** (1984) 5494.

[31] S. H. Lu, J. Quinn, D. Tian, F. Jona, *Surf. Sci.*, **209** (1989) 364.

[32] M.P. Seah, *Surf. Sci.*, **32** (1972) 703.

[33] M. P. Seah, I. S. Gilmore, *Surf. Interface Anal.*, **31** (2001) 835.

[34] P. W. Palmberg, G. E. Riach, R. E. Weber, N. C. MacDonald, '*Handbook of Auger Electron Spectroscopy*', Physical Electronics, Eden Prairi, (1972).

[35] U. Ramsperger, A. Vaterlaus, P. Pfaffi, U. Maier, D. Pescia, *Phys. Rev. B*, **53 (12)** (1996) 8001.

[36] P. W. Palmberg, *Anal. Chem*, **45** (1973) 549A.

[37] S. Xinyin, D. J. Frankel, J. C. Hermanson, G. J. Lapeyre, R. J. Smith, *Phys. Rev. B,* **32** (1985) 2120.

[38] G. Attard, C. Barnes, '*Surfaces*', OUP, (1998), p46.

[39] R. Holroyd, R. Bennett, I. Jones and M. Bowker, *J. Chem. Phys.*, **110** (1999) 8703-13.

[40] I. Z. Jones, PhD Thesis, University of Reading, (1999).

[41] P. Kisliuk, *J. Phys. Chem. Solids,* **3,** (1957) , 95.

[42] C. J. Barnes, M. Lindroos, D. A. King, *Surf. Sci.,* **201** (1988) 108.

6 CONCLUSIONS AND FUTURE WORK

6 CONCLUSIONS AND FUTURE WORK

6.1 Introduction

This work has been successful in providing models for the adsorption and decomposition of VA and related molecules on specific Pd-based catalysts under UHV conditions. To an extent these findings can be related to the mechanism for industrial synthesis of VAM, however there are major differences between the conditions used industrially and in this work and these need to be considered and addressed. In Chapter 1 the unknown aspects of VAM synthesis were highlighted and implied the following questions: what is the structure and composition of the active catalyst surface, how are the products and by-products formed, and what are the reaction intermediates? The effects of Au on the Pd catalyst are also not completely understood and need to be elucidated. This study has helped in providing relevant information to consider these aspects of VAM synthesis.

6.1.1. Interactions with Pd

In Chapter 3 it was determined that oxygen adsorbed dissociatively with a high initial sticking probability (0.7) and desorbed associatively by second order desorption kinetics. Other molecules investigated also stuck well to clean Pd (110), with S_0 being between 0.5 and 0.9. The oxygen saturation coverage was about 0.5 ML at room temperature, and there was evidence of subsurface oxygen which diffused to the surface at high temperature. Ethene adsorbs dissociatively at room temperature and above, leaving an ethynyl-like species which inhibits adsorption of other molecules such as oxygen. However, at temperatures above 400 K, this species decomposes to carbon which allows subsequent (and continuous) sticking of either oxygen or ethene.

This change is associated with a dissolution of this carbon into the bulk, which may accompany a rearrangement of carbon atoms on the surface, leaving exposed sites. Acetic acid forms acetate species and adsorbed hydrogen on Pd (110) at room temperature. With acetic acid adsorption on the clean surface, a phenomenon occurs above about 450 K, where the acetate species decomposes to carbon dioxide and hydrogen in a second order autocatalytic decomposition process. Comparing these results to the full scale VAM synthesis is not straightforward: catalyst dimension differences aside, the reaction conditions are very different. As the industrial reaction temperature is usually around 440 K, there is probably a significant proportion of acetate and vinyl on the surface, and the vinyl is likely to inhibit reaction with acetic acid. It has been suggested in the literature that gas phase ethene reacts with a surface acetate complex to yield VA, and chemisorbed ethene will be activated towards decomposition by-products such as water and carbon dioxide. However, carbon dioxide is only found in low amounts in an industrial reactor, which suggests that acetate is stabilised against decomposition, and that ethene chemisorbing on this surface does not decompose in significant quantities. The stability of acetate may be affected by additional promoters not considered here such as Na and K acetate, as acetate was found to decompose at about 420 K on clean Pd (110) under UHV this is certainly a possibility. There are also other factors to consider such as pressure differences between UHV and industrial synthesis and differences in the atomic arrangement of the active catalyst.

Consideration of VAM decomposition on Pd (110) suggests that the acetyl species is a more favourable intermediate than vinyl under most of the UHV conditions available, despite the fact that the role of vinyl has been considered significant in

certain microreactor studies. However, the forward synthesis of VAM may differ significantly from the reverse decomposition studied. Also, the results of Chapter 4 imply that vinyl must be produced to an extent to provide hydrogen atoms for formation of acetyl to produce the quantities of methane observed. This methane is produced by the decomposition of acetyl to methyl and CO, and subsequent hydrogenation of methyl. However, it was suggested in Chapter 4 that the presence of a stable acetate template from acetic acid decomposition is important for vinyl production. Thus the effects of promoters such as Na and K acetate may be important here in bringing conditions optimal for vinyl production about, by affecting the stability of ethene and/or acetate.

Studies of two potential industrial by-products of VAM synthesis, acetaldehyde and carbon monoxide (subsequently oxidised to CO_2), as well as acetic acid on Pd (110) have provided some useful information on the formation of these by-products. In these studies carbon dioxide can be formed from decomposition of acetate species. The primary by-product in industrial VAM synthesis is carbon dioxide which can be formed by oxidising carbon monoxide from acetaldehyde and VAM decomposition. As the industrial synthesis is performed at about 440 K, which is incidentally the desorption temperature of CO on Pd (110), carbon monoxide should be present on the surface in significant quantities and is thus a major source of carbon dioxide. In industrial VAM synthesis acetaldehyde can be produced from VAM decomposition, and occurs in low quantities. While acetaldehyde was not observed as a product in VAM decomposition (Chapter 4) per se, acetyl was produced which may interact with hydrogen from ethene and acetate decomposition to form acetaldehyde. Two other significant by-products, acetic anhydride and water were not investigated in detail.

However, the acetic anhydride production pathway is in competition with that of acetaldehyde and the results thus suggest that acetyl forms at its expense in UHV. This is supported by industrial reactor data (Chapter 1) where acetaldehyde is more predominant than acetic anhydride as a by-product. Water occurs industrially both in the primary formation of VAM, and as a by-product by oxidation of hydrogen on the surface from acetic acid and VAM decomposition. While water has been found as a product of the interaction of oxygen and acetate in the literature, it was not found as a product in any of the reactions described in Chapters 3 and 4, and its absence is attributed to the lack of predosed oxygen or atmospheric oxygen in those reactions.

6.1.2. Interactions with Au/Pd (110)

In contrast to Pd, it has been confirmed that in general Au acts as an inhibitor to the reactions of the specific molecules on Au/Pd (110) surfaces. This is mainly due to the fact that pure Au does not accommodate dissociatively adsorbed oxygen, and cannot chemisorb ethene or acetic acid significantly. Thus Au does not promote decomposition of any of the molecules concerned i.e. reactants, VAM or by-products. Hence, reactants are less likely to combine and desorb as products, and any adsorbates are destabilised, tending to decompose more readily. However, the inhibiting effect of Au was not as pronounced as expected by consideration of surface Au/Pd ratios, and this has been attributed in Chapter 5 to a significant intermixing through annealing of Au and Pd in the surface layers which expose more reactive Pd to incoming molecules than predicted for a surface where Au remains unmixed.

For most adsorption systems investigated, surfaces with an Au coverage up to about 1 ML exhibit chemistry that is essentially intermediate between the unreactive Au (110) and the catalytic Pd (110) surface. With regard to oxygen adsorption, this means that a low coverage preadsorption of oxygen is possible and hence interactions with hydrocarbons such as acetate can occur, and as mentioned above, decomposition to by-products will become less likely. Oxygen is of course abundant in industrial high pressure syntheses and will probably adsorb before ethene and acetic acid decomposition. This low coverage of oxygen may act as a template to stabilise acetate intermediates without promoting oxidation and decomposition of acetate. Also, as mentioned above, the presence of oxygen may enhance the stability of the vinyl intermediate over the acetyl intermediate in VAM decomposition (and perhaps synthesis), thus ethene may preferentially decompose to vinyl which could interact with adsorbed acetate to give VAM. In these studies, Au appears to act primarily as an inhibitor to the interaction of hydrocarbons, and its role as a modifier of adsorption and reactivity is not obvious with regard to decomposition of VAM and related molecules. However, it may be that Au can affect the formation of carbon layers obtained from decomposition of these molecules at high temperatures, by limiting transport of carbon from the bulk to the surface and vice versa. It may be that the presence of more significant gold content shifts the onset of continuous sticking to slightly higher temperatures and thus confines carbon to the surface where it may interact with oxygen, thus reducing catalyst poisoning effects. However, there is no conclusive evidence from this work to support this prediction, and the hypothesis needs more structural information under these conditions to prove.

6.2 UHV vs. High Pressure Industrial Reactions

There are many differences between the industrial VAM synthesis and the molecular beam experiments performed in this study under UHV. One of the main differences is the nature of the active catalyst – the Pd is dispersed as nanoparticles on a silica support in the industrial case. These nanoparticles have been predicted to resemble Wolff polyhedra [1], and thus may display facets with fcc (110) and (111) atomic arrangements. Structurally then, UHV studies on Pd (110) may reflect the reactions occurring on such nanoparticles, although in general practical studies on many systems have found that particles are far less perfect than Wolff polyhedra and do not exhibit specific planes. However, the differences in dimensions between the Pd (110) crystal used in these studies and the much smaller Pd nanoparticles imply that saturation of Pd to PdC by formation and dissolution of surface carbon may be more pronounced in the industrial case where the particles are only of the order of 100 Pd atoms, and thus do not have significant volume for carbon dissolution. The nature of the interaction of Pd and Au in the nanoparticles is also of importance and may not reflect the Au/Pd (110) structures used in this study. It has been suggested that alloys of the two elements form, while others propose that Pd and Au are separate but modify each other electronically. More information is required on the structures both of the nanoparticulate system and the Au/Pd(110) systems in order to appreciate their differences. It was suggested in Chapter 5 that consideration of qualitative LEED and AES alone was not enough to fully characterise the nature of the Au in the systems as they cannot give atom by atom Au and Pd positions, and thus there may have been some variation in the positions and arrangement in Au atoms between different

experiments, and it is possible that Au occurs in a variety of forms in the industrial case too.

The influence of high pressures (5 atmospheres) in the industrial synthesis, compared to the very low pressures of UHV has already been commented on, and the main implications are that synthesis is less likely in UHV as suggested by Le Chatelier's principle and entropy laws. The effect of oxygen becomes an important consideration in industrial synthesis, and it seems that these conditions may explain the apparent differences in the proposed reaction intermediates for VAM synthesis in a reactor (vinyl), and VAM decomposition in low-oxygen UHV (acetyl). Preadsorption of oxygen on Pd (110) in UHV using the molecular beam reactor in this study was very problematic, and was not investigated in detail. Recent work by Goodman et. al. on VAM synthesis showed a surprisingly low turnover frequency (TOF) for VAM on Pd: 0.01 (one molecule of VAM produced per site every 100 seconds) at 5 kPa overpressure, suggesting that VAM synthesis, and hence the probability of reaction between oxygen, ethene and acetic acid will be much lower in UHV where the beam pressure is many orders of magnitude lower than in the industrial synthesis [2].

6.3 Proposed Reaction Mechanism

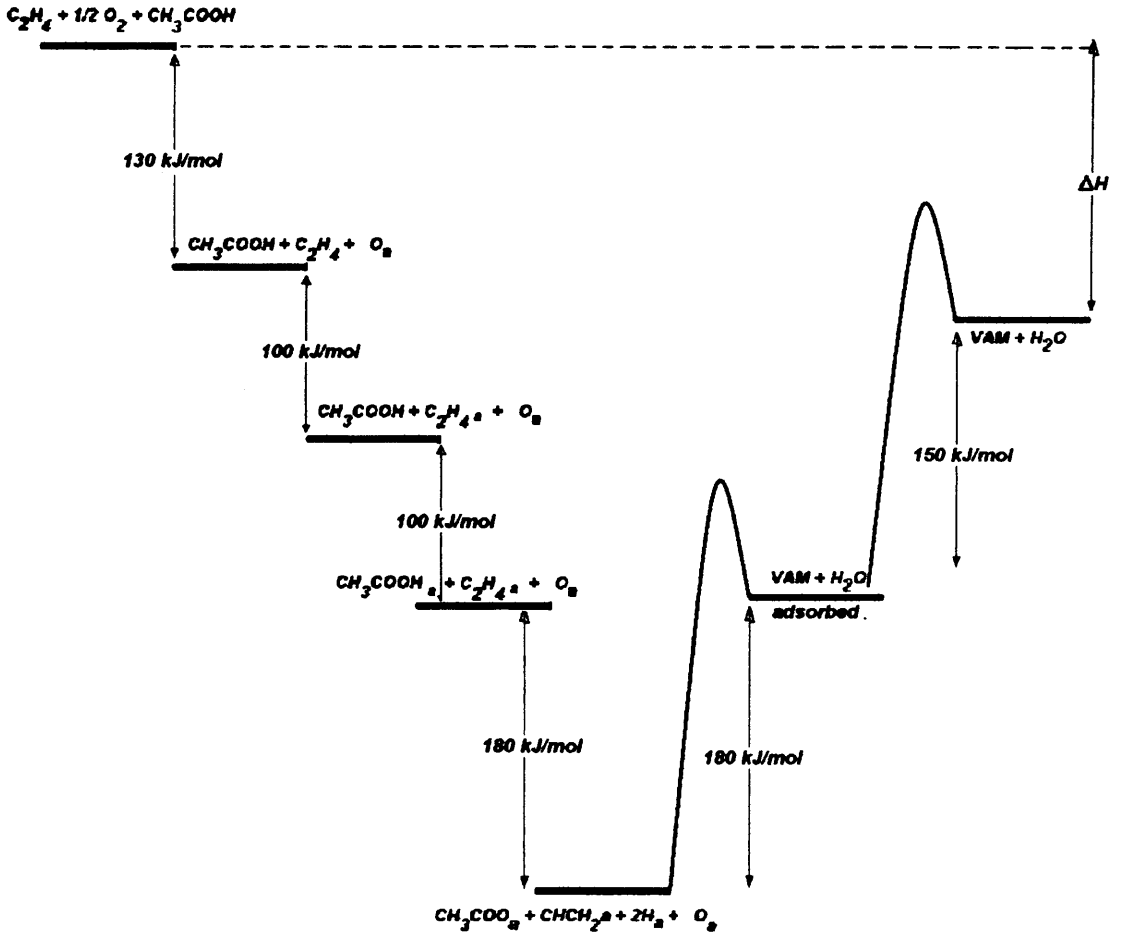

Fig. 1: An estimated energy level diagram for VAM production via a primary vinyl intermediate pathway on a clean Pd (110) surface or a Au/Pd (110) surface where Au content is less than 2 ML based on the findings of Chapters 3 to 5. The overall reaction is exothermic, with a ΔH of -176 kJ/mol [3].

Based on the above findings, both pathways of VAM production via acetyl and vinyl intermediates are potentially possible (see Chapter 4), but the former seems predominant in UHV, and the latter is predominant in industrial synthesis. It is relatively straightforward to construct an estimated energy level diagram based on either mechanism, for instance the vinyl intermediate route is shown in Fig. 1. From low temperature TPD experiments for O_2, (see Chapter 3 and comparison by values from Ertl. et. al.), ethene [4] and acetic acid (see Chapter 3) approximate values for the energies of the first three steps (adsorption of the reactants) can be estimated, and

will vary depending on the extent of chemisorption which in turn is affected by the Au content of the surface. It was mentioned in the TPD findings for VAM/Pd (110) in Chapter 4 (see Figure 10 in Section 4.4.2) that at room temperature there is a possibility that VAM recombines to an extent during decomposition (desorbing at about 350 K), so its formation is expected be reversible with a specific activation energy which is estimated to be of the order of 50 kJ/mol. VAM itself desorbs at a very low temperature from Pd (110) (less than 223 K), so its desorption with water is estimated to be low, about 150 kJ/mol, again with an activation energy required to break the chemisorption that cannot be deduced from these studies. Thus the energy of reaction for formation of adsorbed products from adsorbed starting materials is estimated to be about 180 kJ/mol. The presence of gold in the surface is expected to make desorption of these products slightly more favourable, based on the results of Chapter 5, and may also reduce the activation energy for this step. However, without detailed calorimetric analysis of low temperature TPD for these molecules on Pd (110), as well as calculated values for the reactions themselves on these surfaces, the values in Figure 1 remain only estimates. The results from Chapters 3 to 5 however suggest that the role of Au is to make the adsorption energies less favourable, and desorption of products more favourable, and they cannot provide in-depth reaction energetics values alone. More experiments are required, perhaps by theoretical computing and calorimetric methods, to attach more quantitative values to the proposed mechanism. Also, a better understanding of the actual structure of the annealed Au/Pd(110) surfaces, perhaps by STM, would allow a more reasoned estimate of the effect of Au on the adsorption and desorption energies to be made.

6.4 Future Work

Based on the findings of this study, there are several opportunities for future work. The TPD data obtained for VAM desorption should be extended in order to elucidate the conditions under which the two mechanisms for VAM decomposition may occur. Use of deuterated VAM would be useful in order to determine the exact origin of the hydrogen in the decomposition products, and the possibility of VAM recombination at room temperature. In addition, an attempt should be made to synthesise VAM in UHV by coadsorption of oxygen, ethene and acetic acid. The above conclusions suggest this is most likely achieved by preadsorption of oxygen, then acetate, then ethene, and this may require mixed beam experiments to minimise contamination by atmospheric molecules and potential desorption of preadsorbed molecules. However, as mentioned above, the product VAM is likely to occur only in very small quantities, and there may be significant by-products, especially in the case of clean Pd (110). It may be simpler to try to adsorb ethene on acetate-Pd (110) without the presence of oxygen. It is also of interest to study the interaction of an acetate layer with deuterium in order to determine the extent of rehydrogenation of acetate on the surface, and whether the acid hydrogen contributes completely to the H_2 product.

Future study should also focus more on structural analysis to complement the primarily reactivity based findings here. HREELS analysis of ethene, acetic acid, acetaldehyde and VAM would be beneficial, especially on Au/Pd (110) systems, in order to determine the exact nature of the carbon layers formed at high temperatures. NEXAFS (Near Edge X-ray Absorption Fine Structure) would also be useful in determining the adsorption bonding geometry of adsorbates, and may help to

elucidate the vinyl and acetyl pathways on Pd (110) and Au/Pd (110). Use of STM and LEIS is also required to determine how the Au/Pd (110) surfaces form and the exact atomic arrangement of atoms in such systems. The above results suggest that Au may form alloys at elevated temperatures with some of the Au subsurface, but this cannot be confirmed conclusively at present. Indeed, it has not been concluded whether the formation of the Au/Pd (110) is in any way representative of the distribution of Au and Pd on real catalysts, so an attempt to mirror a real catalyst more closely would be of interest, perhaps by producing Pd and/or Au nanoparticles on a silica (as in the real system) or titania (which is simple to analyse in STM) support. However, the distribution of such particles should be controlled as much as possible in order to give reproducible results, and this system may incorporate SMSI effects.

The role of Na and K acetate promoters has not been considered in the above studies, and they are likely to have a significant effect on the relative stability of the intermediates. The Group 1 metal could be evaporated on the Pd surface in a similar way to the MVD approach for Au in this study, and the techniques required are very similar to those mentioned in this report

Simpler and more accurate methods of quantifying the amount of Au on the surface by MVD are strongly recommended in order to elucidate the growth mode of Au on Pd (110). One possibility would be to analyse the surfaces using a more accurate CMA-AES analyser or to perform in-depth XPS analysis. Another possibility would be to perform Thermal Emission Atomic Scattering (TEAS) experiments using a He or Ar molecular beam in conjunction with an MVD beam of Au, and measuring incremental Au layer growth as a decrease in gas mass signal by QMS. A more

sensitive QMS system would also be of use to directly measure acetic acid sticking curves, as well as the possibility of Au desorption from Au/Pd(110) into the gas phase at high crystal temperatures. Due to the position and sensitivity of the QMS analyser in this study, neither of these could be observed

Lastly, the results of this study could be supported by theoretical analyses, perhaps by computer modelling. In recent years reactor studies using real catalysts for VAM synthesis have been investigated using Au/Pd systems as described in Chapter 5, however there is still much scope for research in this area. The interactions of ethene, acetic acid and acetaldehyde also require further study by these methods. The findings of this report are expected to provide useful information to such future studies.

REFERENCES:

[1] see for example C. T. Campbell, *Surf. Sci. Reports*, **27** (1997) 1.

[2] Y. F. Han, D. Kumar, C. Sivadinarayana, D. W. Goodman, *Abstr. Papers Am. Chem. Soc.*, 227: 37 – Petr, Pt. 2 (2004).

[3] D. R. Lide (Ed.), 'CRC Handbook of Chemistry & Physics', CRC, 80th Edition, (1999).

[4] M. Nishijima, J. Yoshinobu, T. Sekitani, M. Onchi, *J. Chem. Phys.*, **90** (1989) 5114.